Vol. 46 No. 3 (2025)

To be continued

ARCHIVES OF THERMODYNAMICS

ISSN: 1231-0956
ISSN: 2083-6023 (Online)

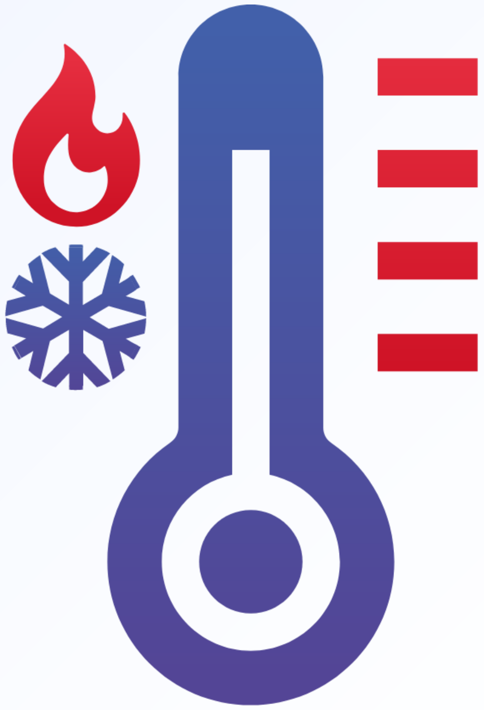

Co-published by

Institute of Fluid Flow Machinery
Polish Academy of Sciences

Committee on Thermodynamics and Combustion
Polish Academy of Sciences

WYDAWNICTWO IMP PAN

archives of thermodynamics **appears since 1980**

Aims and Scope

The aim of the quarterly journal Archives of Thermodynamics (AoT) is to disseminate knowledge between scientists and engineers worldwide and to provide a forum for original research conducted in the field of thermodynamics, heat transfer, fluid flow, combustion and energy conversion in various aspects of thermal sciences, mechanical and power engineering. Besides original research papers, review articles are also welcome.

The journal scope of interest encompasses in particular, but is not limited to:

- Classical and extended non-equilibrium thermodynamics
- Thermodynamic analysis including exergy
- Thermodynamics of heating and cooling
- Thermodynamics of nuclear power generation
- Thermodynamics in defence engineering
- Advances in thermodynamics
- Experimental, theoretical and numerical heat transfer
- Thermal and energy system analysis
- Renewable energy sources including solar energy
- Secondary fuels and fuel conversion
- Heat and momentum transfer in multiphase flows
- Nanofluids
- Energy transition
- Advanced energy carriers
- Energy storage and efficiency
- Energy in buildings
- Hydrogen energy
- Combustion and emissions
- Turbomachinery
- Thermal and energy system analysis
- Integrated energy systems
- Distributed energy generation
- Thermal incineration of wastes
- Waste heat recovery.

Supervisory Editors

- K. Badyda, Warsaw University of Technology, Poland
- M. Lackowski, Institute of Fluid Flow Machinery, Gdańsk, Poland

Honorary Editor

- J. Mikielewicz, Institute of Fluid Flow Machinery, Gdańsk, Poland

Editor-in-Chief

- P. Ocłoń, Cracow University of Technology, Cracow, Poland

Section Editors

- P. Lampart, Institute of Fluid Flow Machinery, Gdańsk, Poland
- S. Polesek-Karczewska, Institute of Fluid Flow Machinery, Gdańsk, Poland
- I. Szczygieł, Silesian University of Technology, Gliwice, Poland
- A. Szlęk, Silesian University of Technology, Gliwice, Poland

Technical Editors

- J. Frączak, Institute of Fluid Flow Machinery, Gdańsk, Poland
- S. Łopata, Institute of Fluid Flow Machinery, Gdańsk, Poland

Members of Programme Committee

- D. Kardaś, Inst. Fluid Flow Mach., Gdańsk, Poland (chairman)
- J. Badur, Inst. Fluid Flow Mach., Gdańsk, Poland
- T. Chmielniak, Silesian Univ. Tech., Gliwice, Poland
- P. Furmański, Warsaw Univ. Tech., Poland
- R. Kobyłecki, Częstochowa Univ. Tech., Poland
- S. Pietrowicz, Wrocław Univ. Sci. Tech., Poland
- J. Wajs, Gdańsk Univ. Tech., Poland

International Advisory Board

- J. Bataille, Ecole Centr. Lyon, France
- A. Bejan, Duke Univ., Durham, USA
- W. Błasiak, Royal Inst. Tech., Stockholm, Sweden
- G.P. Celata, ENEA, Rome, Italy
- L.M. Cheng, Zhejiang Univ., Hangzhou, China
- M. Colaco, Federal Univ. Rio de Janeiro, Brazil
- J.M. Delhaye, CEA, Grenoble, France
- M. Giot, Univ. Catholique Louvain, Belgium
- K. Hooman, Univ. Queensland, Australia
- D. Jackson, Univ. Manchester, UK
- D.F. Li, Kunming Univ. Sci. Tech., China
- K. Kuwagi, Okayama Univ. Science, Japan
- J.P. Meyer, Univ. Pretoria, South Africa
- S. Michaelides, Texas Christian Univ., USA
- M. Moran, Ohio State Univ., USA
- W. Muschik, Tech. Univ., Berlin, Germany
- I. Müller, Tech. Univ., Berlin, Germany
- H. Nakayama, JAEA, Japan
- S. Nizetic, Univ. Split, Croatia
- H. Orlande, Federal Univ. Rio de Janeiro, Brazil
- M. Podowski, Rensselaer Polyt. Inst., USA
- R.V. Rao, Sardar Vallabhbhai Nat. Inst. Techn., India
- A. Rusanov, Inst. Mech. Eng. Probl., Kharkiv, Ukraine
- A. Vallati, Sapienza Univ. Rome, Italy
- M.R. von Spakovsky, Virginia Polyt. Inst., USA
- H.R. Yang, Tsinghua Univ., Beijing, China

Vol. 46 No. 3 (2025)
To be continued

ARCHIVES OF THERMODYNAMICS

ISSN: 1231-0956
ISSN: 2083-6023 (Online)

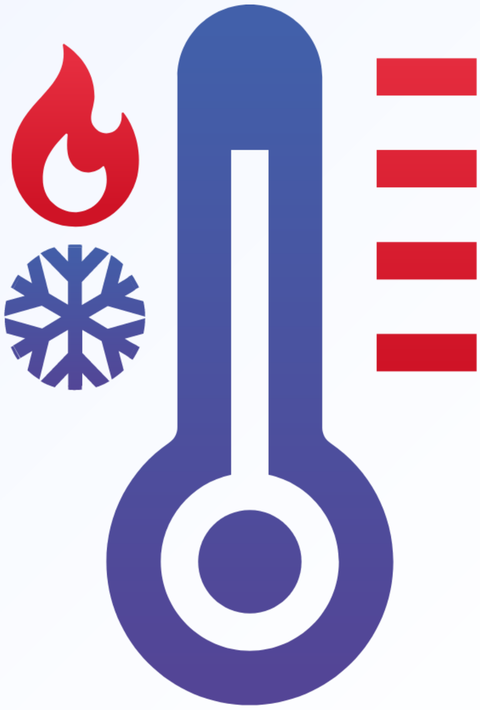

Co-published by

Institute of Fluid Flow Machinery
Polish Academy of Sciences

Committee on Thermodynamics and Combustion
Polish Academy of Sciences

WYDAWNICTWO
IMP PAN

Editorial Office
IMP PAN Publishers
Institute of Fluid Flow Machinery, Fiszera 14, 80-231 Gdańsk, Poland,
Phone: (+48) 58-341-12-71 int. 230, e-mail: redakcja(at)imp.gda(.)pl
https://www.imp.gda.pl/archives-of-thermodynamics/
Journals PAS – Electronic Library Polish Academy of Sciences
https://journals.pan.pl/ather

Subscription outside Poland

From 2024, Archives of Thermodynamics appear only in electronic version as an open access journal. However, printed archive volumes or issues are still available. The price of a full volume outside Poland is **120 EUR**. The price of a single issue is **30 EUR**. Archived volumes or issues are available on request. Orders should be sent directly to IMP PAN Publishers:
Institute of Fluid-Flow Machinery,
Fiszera 14, 80-231 Gdansk, Poland,
e-mail: redakcja(at)imp.gda.pl or jfrk(at)imp.gda(.)pl or jrybka(at)imp.gda(.)pl.
Payments should be transferred to the bank account of IMP PAN:
IBAN 28 1130 1121 0006 5498 9520 0011 at Bank Gospodarstwa Krajowego; Code SWIFT: GOSKPLPW.

Prenumerata w Polsce

Od 2024, czasopismo ukazuje się tylko w formie elektronicznej otwartej. Osiągalne są jednak wydania papierowe archiwalne. Cena pojedynczego numeru wynosi **50 PLN**. Cena rocznika **200 PLN**. Zamówienia z określeniem numeru (rocznika), nazwiskiem i adresem odbiorcy należy kierować bezpośrednio do Wydawcy:
Instytut Maszyn Przepływowych PAN
ul. Fiszera 14, 80-231 Gdańsk,
e-mail: redakcja(at)imp.gda(.)pl lub jfrk(at)imp.gda(.)pl lub jrybka(at)imp.gda(.)pl.
Wpłaty prosimy kierować na konto Instytutu Maszyn Przepływowych PAN:
nr 28 1130 1121 0006 5498 9520 0011 w Banku Gospodarstwa Krajowego.

Articles in Archives of Thermodynamics are abstracted and indexed within:

Arianta • Baidu Scholar • BazTech • Cabell's Directory • Chemical Abstracts Service (CAS) – CAplus • CNKI Scholar (China National Knowledge Infrastucture) • CNPIEC • EBSCO • Elsevier – SCOPUS • Genamics JournalSeek • Google Scholar • Inspec • Index Copernicus • J-Gate • Journal Citation Reports (ESCI) • Journal TOCs • Naviga (Softweco) • POL-index • Polymer Library • Primo Central (ExLibris) • ProQuest • ReadCube • SCImago (SJR) • TDNet • TEMA Technik und Management • Ulrich's Periodicals Directory/Ulrichsweb • Web of Science (Core Collection) • WorldCat (OCLC)

ISSN 1231-0956
ISSN 2083-6023 (Online)

Publication funding of this journal is provided by resources of the Polish Academy of Sciences and the Institute of Fluid Flow Machinery

Archives of Thermodynamics, Vol. 46, No. 3, 2025
To be continued

Contents

Co-published by
Institute of Fluid-Flow Machinery
Polish Academy of Sciences
Committee on Thermodynamics and Combustion
Polish Academy of Sciences

http://www.imp.gda.pl/archives-of-thermodynamics/

ARCHIVES
OF THERMODYNAMICS

Online monitoring of thermal loads of steam turbine components

Mariusz Banaszkiewicz

Institute of Fluid-Flow Machinery, Polish Academy of Sciences, Energy Conversion Department, ul. Fiszera 14, 80-231 Gdańsk, Poland
Author email: mbanaszkiewicz@imp.gda.pl

Received: 05.02.2025; revised: 04.06.2025; accepted: 11.06.2025

Abstract

The increasing share of renewable energy production in energy markets has resulted in the demand for more flexible operation of conventional power plants. Coal-fired units are forced to operate in a more cyclic duty with a higher number of starts, faster start-ups and increased load change rates. These unfavourable operating conditions result in additional thermal loading of steam turbine components and necessitate better monitoring of life-limiting components. The paper presents numerical investigations of thermal loading of a steam turbine valve at various operating conditions and identifies the requirements for an online monitoring method. A modified method based on Duhamel's integral is proposed and validated at different transient conditions, taking into account both convection and condensation heat transfer. It was shown that the calculation method provides reasonably accurate predictions of casing wall temperature. Relative differences between measured and calculated wall temperatures are within (−2.6%)÷(+1.5%) for the investigated start-ups with condensation and convection heat transfer conditions. Advantages of this method and its suitability for online monitoring of thermal loads of steam turbine components are discussed in detail.

Keywords: Steam turbine; Thermal loads; Condensation; Duhamel's integral

Vol. 46(2025), No. 3, 5–15; doi: 10.24425/ather.2025.154920

Cite this manuscript as: Banaszkiewicz, M. (2025). Online monitoring of thermal loads of steam turbine components. *Archives of Thermodynamics*, 46(3), 5−15.

1. Introduction

The demand for more flexible operation of conventional power plants has significantly increased during the last years. The typical operation mode of coal fired plants has shifted from a more base load oriented regime towards cyclic operation. This is due to the increasing share of fluctuating renewable energy production [1].

Consequences of this trend are an increased number of starts, faster start-ups and increased load change rates. Additionally, the minimum load for stable plant operation has to be reduced to allow low load operation of conventional units. As a result of these changes in operation mode, thermal fatigue of power plant equipment has become the main damage mechanism, which could potentially lead to component failures. This problem mainly affects the thick-walled components operating at high temperatures, like steam turbine rotors or valve casings.

In order to ensure safe and reliable operation of ageing power generation units, online monitoring of critical components has become necessary. In particular, for better understanding of the effect of changed operation mode on low cycle fatigue damage, accurate monitoring of thermal loads and stresses is essential.

The problem of thermal stress and load modelling for online monitoring of power plant equipment has been studied for many years, but has gained particular attention in recent years. Rusin et al. [2−4] proposed a new method of thermal stress modelling

Nomenclature

Bi – Biot number
c_p – specific heat, J/(kg·K)
d – hydraulic diameter, m
g – heat source, J/(m^3·s)
h – enthalpy, J/kg
H – Heaviside function,
L – length, m
Nu – Nusselt number
p – pressure, kPa
Pr – Prandtl number
r – radial co-ordinate, m
Re – Reynolds number
t – time, s
T – temperature, K

Greek symbols

α – heat transfer coefficient, W/(m^2·K)
λ – thermal conductivity, W/(m·K)
ξ – friction factor
ρ – density, kg/m^3

Subscripts and Superscripts

a – air
$cond$– condensation
$conv$– convection
f – fluid
n – time step number
sat – saturation
st – steam
$surf$– surface
w – wall

Abbreviations and Acronyms

FEM – finite element method
HS – hot start
WS – warm start

in turbine rotors employing Green's functions and Duhamel's integral, and steam temperature measurement at a critical location. Such an approach has also been adopted for monitoring of power boilers operation by Taler et al. [5], and as shown by Lee et al. [6], it can also be used for calculating stress intensity factors at transient thermal loads.

The major issue in using Green's function and Duhamel's integral method to model transient temperatures and thermal stresses in steam turbine components is the time-dependence of physical properties and heat transfer coefficients, affecting the proper evaluation of Green's functions. There are known approaches assuming determination of the influence functions at constant values of these quantities [7]. The inclusion of temperature dependent physical properties proposed by Koo et al. [8] relies on determining the weight functions for steady-state and transient operating conditions. A more important, in most cases, variation of the heat transfer coefficient can be taken into account by calculating the surface temperature using a reduced heat transfer model and employing Green's function to calculate stress response to a step change of metal surface temperature [9]. However, numerical solution of a multi-dimensional heat transfer model is complicated and time-consuming, and due to this, it cannot be used in online calculations. A full inclusion of time variability of the physical properties and heat transfer coefficients proposed by Zhang et al. [10] relies on the solution of a non-linear heat conduction problem by using the artificial parameter method and superposition rule, and replacing the time-dependent heat transfer coefficient with a constant value together with a modified fluid temperature. The effectiveness of the method has been proved by an example of a three-dimensional model of pressure vessel of a nuclear reactor.

Alternative methods of thermal stress modelling rely on using artificial neural networks [11−13] or inverse heat conduction methods [14−17]. Some researchers [18,19] investigated an approach combining direct heat conduction problems and Duhamel's integral.

This work presents numerical investigations of thermal loading of a steam turbine valve and proposes a modified method for online monitoring of wall temperature employing Duhamel's integral. The main attention is given to appropriate consideration of different heat transfer mechanisms (condensation, convection) and determination of the temperature response function for a variable heat transfer coefficient. The proposed method is validated with the help of real measurements of casing wall temperature and finite element calculations.

2. Finite element modelling of turbine valve heating process

2.1. Problem formulation

The problem under consideration is transient heat conduction in a homogeneous isotropic solid described by the Fourier-Kirchhoff differential equation [20,21]:

$$\mathrm{div}[\lambda \mathrm{grad} T(\boldsymbol{r},t)] + g(\boldsymbol{r},t) = \rho c_p \frac{\partial T(\boldsymbol{r},t)}{\partial t}, \tag{1}$$

where T is the metal temperature, g is the heat source, c_p is the specific heat, λ is the thermal conductivity and $\boldsymbol{r}$ is the spatial location.

Neglecting the heat source g and introducing the temperature Laplacian $\nabla^2 T$, Eq. (1) is rewritten in a rectangular co-ordinate system as follows:

$$\rho c_p \frac{\partial T}{\partial t} = \lambda \nabla^2 T + \frac{\partial \lambda}{\partial T}\left(\left(\frac{\partial T}{\partial x}\right)^2 + \left(\frac{\partial T}{\partial y}\right)^2 + \left(\frac{\partial T}{\partial z}\right)^2\right). \tag{2}$$

In a rectangular co-ordinate system, the temperature Laplacian is defined as follows:

$$\nabla^2 T = \frac{\partial^2 T}{\partial x^2} + \frac{\partial^2 T}{\partial y^2} + \frac{\partial^2 T}{\partial z^2}. \tag{3}$$

A uniform temperature distribution $T(\boldsymbol{r}) = T_0$ is assumed as an initial condition at $t = 0$.

For the turbine valve casings, the following boundary condition is applied:

$$\lambda \frac{\partial T}{\partial n}\bigg|_s = -\alpha\left(T_{surf} - T_{st}\right) \text{ for } t \geq 0, \tag{4}$$

where n denotes the normal direction to the surface, T_{surf} is the surface temperature, T_{st} is the steam temperature and α is the heat transfer coefficient.

The Fourier-Kirchhoff Eq. (2) is solved by means of the finite element method [22].

2.2. Heat transfer coefficients

The variation of heat transfer coefficient $\alpha(t)$ is considered by the Nusselt number Nu changing in time as a function of the Reynolds number Re and Prandtl number Pr:

$$\mathrm{Nu} = \mathrm{f}(\mathrm{Re}, \mathrm{Pr}). \tag{5}$$

The Nusselt number is defined as follows:

$$\mathrm{Nu} = \frac{\alpha d}{\lambda}, \tag{6}$$

where d denotes the hydraulic diameter.

The detailed form of Eq. (5) depends on the component geometry and flow character [23]. Practical methods of determining heat transfer coefficients are presented in [20]. The heat transfer model adopted in this study is based on the well-proven formulae for heat transfer coefficients in steam turbine components and can be employed in online calculations of temperatures and thermal stresses, which is not possible when more advanced thermal fluid-structure interaction (FSI) modelling is adopted [24–27]. Online calculations require fast and robust models which can be implemented and run on industrial computers. For typical start-up conditions and geometry of steam turbine components, the time constants of thermal processes require solving the model with new boundary conditions with a time step of around 1 minute. Start-up durations are in the range of 30 to 200 minutes, which are the required calculation times. Such times are achievable for the finite element method with convection or condensation boundary conditions, but for FSI calculations involving fluid flow and solid body simulations, these times can be several times longer. Moreover, iteration processes and time steps employed in FSI calculations adversely affect not only the calculation times but also stability and reliability of solutions. Such calculations require high performance computers while simple algorithms based for example on Duhamel's integral are easily implementable in programmable logic controllers (PLCs).

For the valve casing regions of circular cross-section, the Gnielinski correlation [28,29] is used:

$$\mathrm{Nu} = \frac{\frac{\xi}{8}(\mathrm{Re}-1000)\mathrm{Pr}}{1+12.7\sqrt{\frac{\xi}{8}}\left(\mathrm{Pr}^{2/3}-1\right)}\left[1+\left(\frac{d}{L}\right)^{2/3}\right]\left(\frac{\mathrm{Pr}_m}{\mathrm{Pr}_w}\right)^{0.11}, \tag{7}$$

where L is the pipe length and symbol ξ denotes the friction factor, for smooth tubes calculated from Filonienko's formula [30]:

$$\xi = \frac{1}{(1.82\log\mathrm{Re}-1.64)^2}. \tag{8}$$

The symbols Pr_m and Pr_w designate the Prandtl number at the bulk and wall, respectively.

For the valve main chamber, a simple power-law formula similar to those of Dittus-Boelter [31–33] and Chilton-Colburn [34] correlations is applied:

$$\mathrm{Nu} = 0.018\mathrm{Re}^{0.8}\mathrm{Pr}^{0.33}. \tag{9}$$

The factor 0.018 was established based on 3-dimensional thermal fluid-solid interaction calculations performed for this valve with time-dependent boundary conditions representing valve heating up from a cold, warm and hot state [35]. Direct simulation results using a 3-dimensional FSI method were available for design start-up conditions, assuming theoretical variations of steam temperature, pressure and mass flow rates. The primary goal of these calculations was to determine a relationship between the similarity numbers (i.e. Nusselt and Reynolds numbers) for the analysed valve geometry, which could be used in finite element calculations and online calculations for any start-up conditions (not only for the predefined design start-ups).

When the turbine starts from a cold state or during pre-warming, steam condensation can take place on valve casing inner surfaces, and condensation heat transfer should be taken into account. Steam condensation on casing surfaces can occur when steam is superheated or saturated. The film condensation mechanism is assumed. A schematic illustration of the condensation model adopted in this work is shown in Fig. 1. If the surface temperature is lower than the saturated steam temperature at the corresponding steam pressure, then steam condenses on the surface. The heat transfer to the surface is intensified as a result of water films appearing on the surface at the saturated steam temperature and the heat released due to condensation.

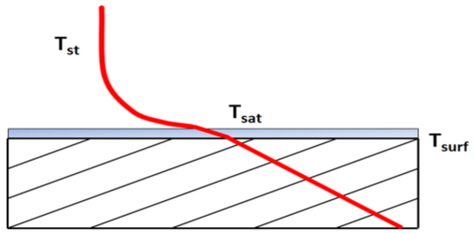

Fig. 1. Schematic illustration of film condensation model.

Condensation occurs if the following conditions are satisfied [36]:

- the metal temperature is below the saturation temperature T_{sat} at the local pressure p:

$$T_{sat} > T_{surf}, \tag{10}$$

- the heat flux from water film to metal is greater than the heat flux from steam to water film:

$$\alpha_{cond}\left(T_{sat} - T_{surf}\right) > \alpha_{conv}\left(T_{st} - T_{sat}\right). \tag{11}$$

As concluded in [23], available correlations for the Nusselt number for simple geometries, like a flat wall or pipe, can be used for estimating the condensation heat transfer coefficient usually with a large error. However, it is known that heat transfer coefficients during steam condensation assume large values reaching 120 000 W/(m^2·K) in extreme cases during nucleate condensation of steam [37,38] and, consequently, the errors of their estimation will only slightly affect the variations of temperature and thermal stress fields in turbine components. It was shown that for Biot numbers Bi > 20, the variation of heat transfer coefficient has little influence on the variation of temperature distribution [23]. Due to the lack of proper correlations for real turbine geometries and taking into account the above conclusions, the analyses of condensation heat transfer were performed with a constant heat transfer coefficient $\alpha = 11\,000$ W/(m^2·K). This value is within the range of heat transfer coefficients predicted by Shah [39] for film condensation of water inside pipes.

2.3. Numerical results and model validation

For numerical calculations of valve heating-up, a three dimensional model has been prepared. The model includes half of the valve due to the symmetry of valve geometry and flow conditions (Fig. 2). Steam enters the valve through the inlet pipe and flows into the main chamber where the flow changes direction from horizontal to vertical. Further steam flows through a converging-diverging channel and leaves the valve through the outlet pipe. Wall temperature measurement is installed in the main chamber region in the wall section perpendicular to the inlet pipe axis and containing the outlet pipe axis. The measurement point is located at a 10 mm distance from the wall inner surface where the hot junction of the measuring thermocouple is located.

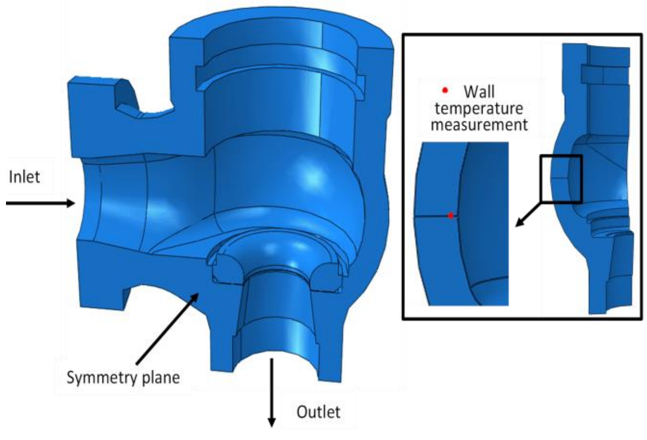

Fig. 2. Geometry model of the valve casing with shown wall temperature measurement location.

Numerical calculations have been performed using the Abaqus code [40]. Computational mesh size was approximately 94 000 second order diffusion elements with 89 546 tetrahedral and 4459 hexahedral elements. Casing material is heat resistant cast steel GS-17 CrMoV 5 11, and its physical properties as a function of temperature are given in Table 1 [35,41]. The cast steel density is constant and equal to 7850 kg/m^3.

Table 1. Physical properties of GS-17 CrMoV 5 11 cast steel at different temperatures.

Temperature, T [°C]	**20**	**100**	**200**	**300**	**400**	**500**	**550**
Thermal conductivity, λ [W/(m·K)]	50	47	46	44	41	39	37
Specific heat, c_p [kJ/(kg·K)]	0.46	0.49	0.53	0.57	0.61	0.68	0.73

Fig. 3 presents inlet steam parameters for the warm start-up with pre-warming, together with the rotor rotational speed and turbine load. Pre-warming is conducted by supplying steam to the valve chamber when the valve is in the closed position and evacuating condensate through a drain. Valve pre-warming takes place for 85 minutes until stop and control valves start to open. For the first 25 minutes, steam is at saturation and afterwards becomes superheated. During run-up and loading, the steam temperature and superheating increase, and reach maximum values at full load.

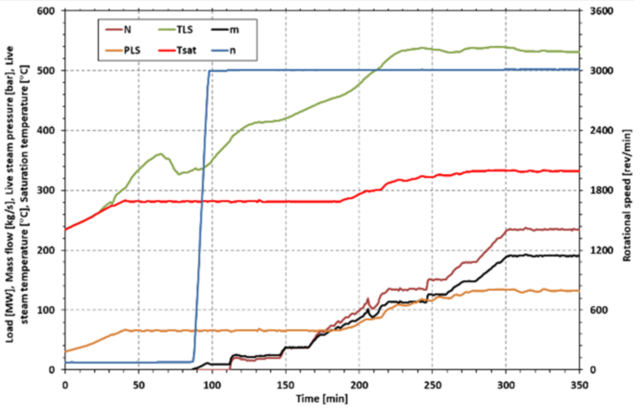

Fig. 3. Variation of inlet steam parameters, rotational speed and load during warm start-up with pre-warming.

A constant temperature of the valve casing equal to 240°C was assumed as an initial condition. Start-up simulations were carried out with time-dependent Fourier boundary conditions. Variation of fluid temperature and heat transfer coefficients for the inlet pipe and valve main chamber is presented in Fig. 4.

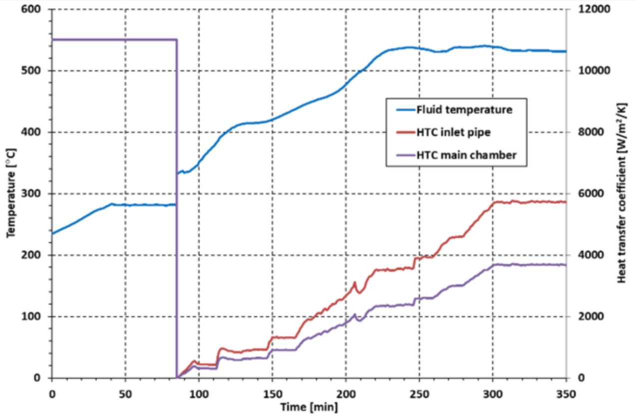

Fig. 4. Variation of temperature and heat transfer coefficients during warm start-up with pre-warming.

The calculated wall temperature at the measurement point is compared with the measured temperature in Fig. 5, which also presents steam and saturation temperatures. It is seen that the calculated wall temperature closely follows the measured value both during valve pre-warming and during start-up. The maximum deviation calculated as:

$$Deviation = \frac{Predicted\ T_{wall} - Measured\ T_{wall}}{Measured\ T_{wall}}, \qquad (12)$$

does not exceed 1.5% during pre-warming and –2.6% during steam heating.

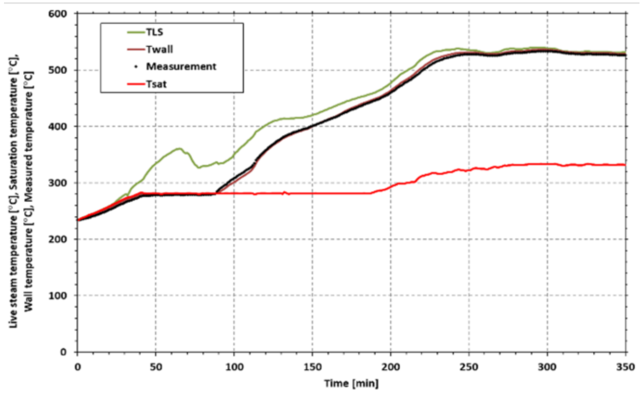

Fig. 5. Variation of steam and wall temperatures during warm start-up with pre-warming.

It is noted that condensation heat transfer prevails during the whole pre-warming phase until the beginning of run-up, and the wall temperature follows the saturation temperature. In early phases steam condensation on the valve inner surfaces takes place with saturated steam conditions and continues with superheated steam even for superheating reaching 80°C. When the valves start to open, the superheated steam flow through the valve brings about intensified heating of the valve and the wall temperature starts to increase above the saturation temperature. Since then, the casing temperatures continuously increase, slowly approaching the live steam temperature and departing the saturation temperature.

Temperature distributions in the valve casing at various phases of pre-warming and steam heating are shown in Figs. 6 and 7, respectively. Uniform temperature distribution was assumed as an initial condition for pre-warming (Fig. 6a). The first 20 minutes of pre-warming proceeds with saturated steam which condenses on the inner surfaces of the inlet pipe and main chamber. The wall surface temperature in these regions reaches 255°C (Fig. 6b), and the remaining regions are still at temperatures close to the initial. Further pre-warming takes place with superheated steam, and after 40 minutes, the wall surface temperature attains ~281°C (saturation temperature, Fig. 6c). After this time, considerable differences between surface temperature where condensation takes place and temperatures of remaining regions are still present. At the end of the pre-warming phase (Fig. 6d), temperature distribution becomes more uniform because the valve sections not being in contact with condensing steam are already heated-up via convection.

After 85 minutes of pre-warming, turbine run-up begins and steam starts to flow through the valve, bringing about intensive heating of the valve casing. The wall temperature reaches approximately 400°C after 60 minutes (Fig. 7a) and almost 500°C after 120 minutes (Fig. 7b) since the beginning of run-up. It should be noted that during the initial phases of steam heating, the temperatures of valve inlet and outlet regions tend to equalise as both regions are heated with comparable intensity by steam flow through the open valve. After 180 minutes, the nominal steam temperature is attained and the major part of the casing is at a temperature above 500°C (Fig. 7c). Since then, the temperature field is becoming more uniform while the inner surfaces being in contact with steam remain at almost constant temperature (Fig. 7d).

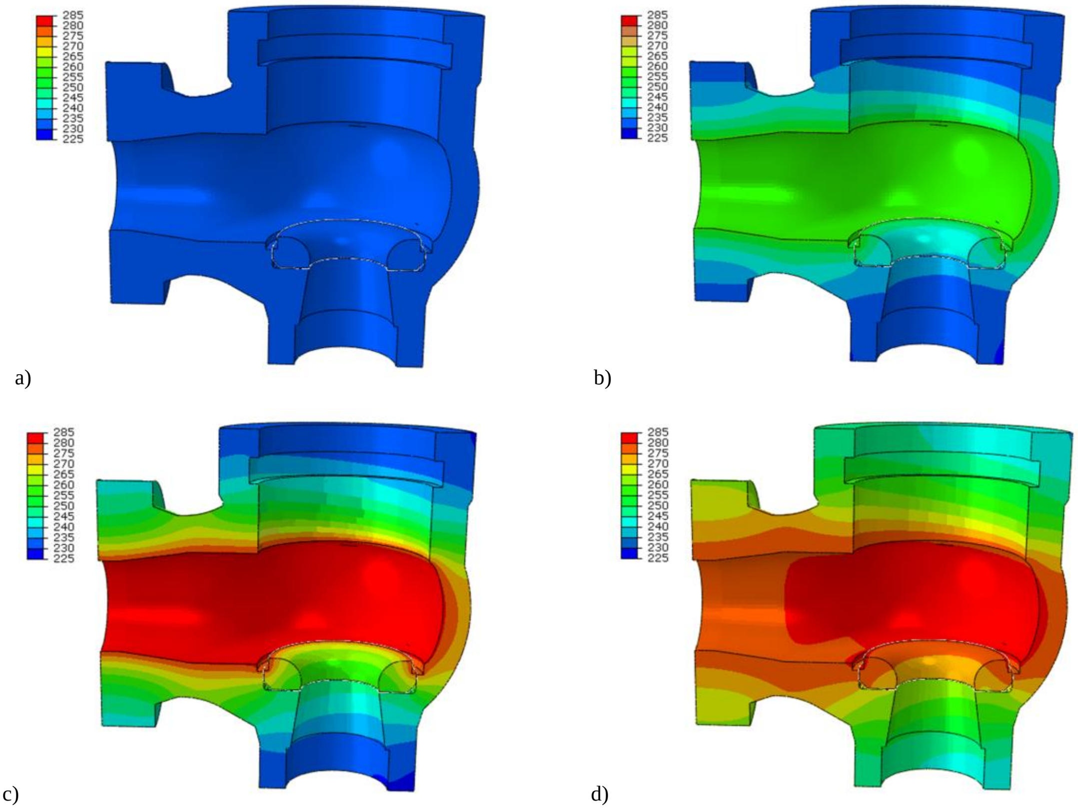

Fig. 6. Temperature distribution in the valve casing at various phases of pre-warming: a) t = 0 min, b) t = 20 min, c) t = 40 min, d) t = 85 min.

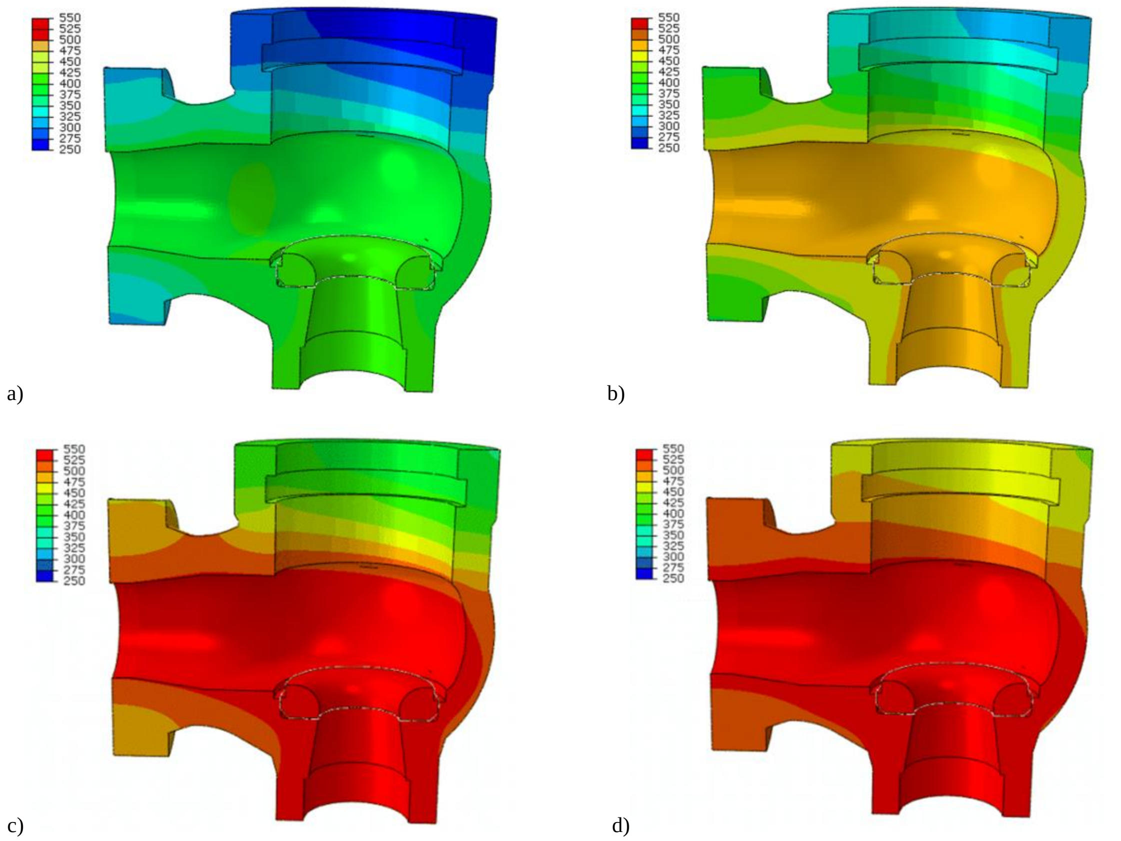

Fig. 7. Temperature distribution in the valve casing at various phases of steam heating: a) t = 60 min, b) t = 120 min, c) t = 180 min, d) t = 240 min.

3. Duhamel's integral method

3.1. Theoretical background

Duhamel's integral can be used for determining the temperature distribution in the body. For steam turbine components, a reliable and accurate measurement of surface temperature at the critical region is usually not possible, thus for on-line monitoring purposes, steam temperature measurement is used as a leading signal. Consequently, in the heat transfer model, Fourier's boundary condition (4) is applied.

Assuming that the steam temperature is described by Heaviside's function $H(t)$ [10], [42]

$$H(t) = \begin{cases} 0, & t < 0 \\ 1, & t > 0' \end{cases} \tag{13}$$

the boundary condition (4) can be written in the form [10]:

$$\lambda \frac{\partial X}{\partial n} = -\alpha\big(H(t) - X(\boldsymbol{r}, t)\big), \tag{14}$$

where $X(\boldsymbol{r}, t)$ is a solution of the direct heat conduction problem with a unit step change of steam temperature.

Using the solution $X(\boldsymbol{r}, t)$, we can calculate metal temperature for an arbitrary variation of steam temperature employing Duhamel's theorem [43]:

$$T(\boldsymbol{r}, t) = T_0 + \int_0^t X(\boldsymbol{r}, t - \tau) \frac{\partial T_{st}(\tau)}{\partial \tau} d\tau. \tag{15}$$

For simple geometries like a plate, cylinder or sphere, a solution of the one-dimensional transient heat conduction problem can be obtained analytically. In the case of more complex shapes, it is necessary to use numerical methods, e.g. the finite element method in order to obtain accurate solutions.

3.2. Numerical solution of Duhamel's integral

In order to solve Duhamel's integral given by Eq. (15), it is transformed from a continuous into discrete form:

$$T(\boldsymbol{r}, t) = T_0 + \sum_{t-t_d}^{t} X_t(\boldsymbol{r}, t - \tau) \Delta T_{st}(\tau) + X_s(\boldsymbol{r}, t), \tag{16}$$

where t_d is a cut-off time, $X_s(\boldsymbol{r},t)$ is a value of the influence function in steady state, while $X_t(\boldsymbol{r},t)$ is a transient part of the influence function.

In principle, Duhamel's integral, resulting from the superposition rule, can be applied to linear unsteady heat conduction problems. However, it has been shown in previous studies on thermal stress modelling using Duhamel's integral that it can be successfully applied to nonlinear thermoelasticity problems when the appropriately obtained solution of direct heat conduction problem $X(\boldsymbol{r}, t)$ is used [42]. This solution is obtained numerically with the assumption of time-dependent heat transfer coefficients $\alpha(t)$ and temperature-dependent specific heat $c_p(T)$ and thermal conductivity $\lambda(T)$.

It has been shown in Section 2 that for adequate modelling of thermal behaviour of turbine valves, both condensation and convection heat transfer have to be taken into account. Insofar as the condensation heat transfer coefficient can be assumed constant and high, the convection heat transfer coefficient can vary by orders of magnitude during start-up. Equation (16) is then rewritten into the form:

$$T(\boldsymbol{r},t) = T_0 + \sum_{t-t_d}^{t} X_{t,cond}(\boldsymbol{r},t-\tau)\Delta T_{sat}(\tau) + k\sum_{t-t_d}^{t} X_{t,conv}(\boldsymbol{r},t-\tau)\Delta T_{st}(\tau) + X_s(\boldsymbol{r},t), \tag{17}$$

where $X_{t,cond}$ is a temperature response function for condensation determined with a constant heat transfer coefficient, $X_{t,conv}$ is a temperature response function for convection determined with a variable heat transfer coefficient and k is a factor responsible for compensating for nonlinearity of the problem. When necessary conditions for condensation are met, then $\Delta T_{st} = 0$, and when condensation vanishes, then $\Delta T_{sat} = 0$.

In steady state conditions, the two terms with summation over time tend to zero, and the steady state term $X_s(\boldsymbol{r},t)$ is given by the following formula:

$$X(\boldsymbol{r},t) = 0.9\big(T_{st}(t-t_d) - T(t-t_d)\big)\times \left(1 + 0.1exp\left(\frac{1}{t_d-t}\right)\right). \tag{18}$$

This term is assumed to be zero at transient states and is activated and contributes to the calculation of temperature when nearly steady state conditions are reached.

4. Validation of Duhamel's integral method

Validation of the proposed method based on Duhamel's integral and described by Eq. (17) was done by performing numerical calculations of wall temperature for three different start-ups using the proposed method. The results were then compared with real measurements of the valve casing temperature and predictions of the FEM model presented in Section 2.

4.1. Temperature response function for convection and condensation

The accuracy of the proposed method depends on the form of the temperature response function, which in turn is primarily determined by the variation of the heat transfer coefficient. As it has been previously shown, the condensation heat transfer coefficient can be assumed constant and good accuracy of temperature predictions is obtained with α_{cond} = 11 000 W/(m^2·K). Figure 8 presents the temperature response functions for the wall surface and temperature measurement point located 10 mm below the surface. These functions were obtained using the finite element model of the valve presented in Section 2 and applying a step change of steam temperature from 125°C to 280°C. The temperature response was then related to the change of steam temperature (equal in this case to 155°C) to obtain a response function to a change of steam temperature by 1°C. In numerical simulations, material physical properties were temperature-dependent, and the heat transfer coefficient was kept constant.

Figure 8 also presents the temperature response functions for convection, which were obtained for variable heat transfer coefficients shown in Fig. 4. In this case, a step change of steam temperature from 280°C to 540°C was simulated, assuming temperature-dependent material properties. The shape of temperature response function reflects the variation in time of the heat transfer coefficient. It is seen from the figure that in condensation conditions, the temperature response is more rapid and regular than for convection. This behaviour results from the assumption of a constant and higher than for convection heat transfer coefficient during condensation.

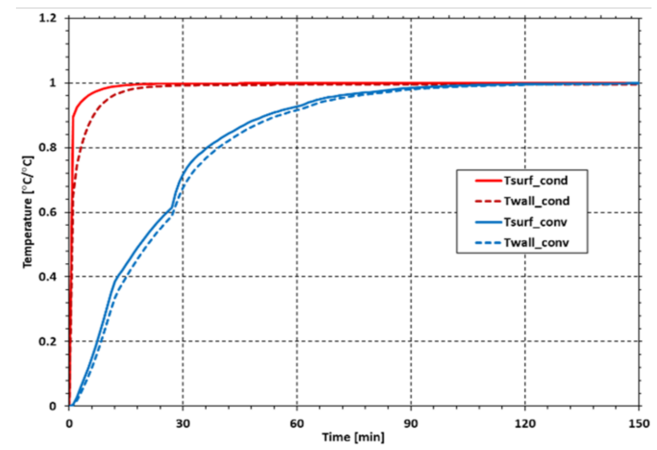

Fig. 8. Temperature response function for wall surface and measurement point location for condensation and convection.

4.2. Simulation of start-ups from various initial thermal states

The results of numerical calculations performed using Duhamel's integral were compared with wall temperature measurements and predictions of the finite element method for three different start-up conditions covering the whole range of turbine operation:

i. pre-warming from a cold state (Fig. 9),
ii. warm start with pre-warming (Fig. 10),
iii. hot start (Fig. 11).

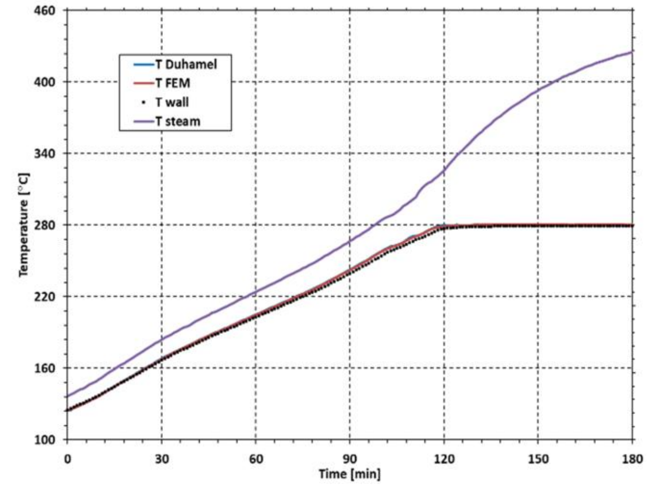

Fig. 9. Measured and calculated metal temperatures during pre-warming from a cold state.

In case i), steam condensation took place during the whole analysed period, while in case iii), only convection heat transfer was present. Case ii) included both condensation and convection. Steam condensation was modelled with the assumption of a constant heat transfer coefficient α_{cond} = 11 000 W/(m^2·K), while for forced convection, variable heat transfer coefficients were used. Thermal boundary conditions for warm start with pre-warming were presented in Fig. 4, while those calculated for the hot start are shown in Fig. 12. A constant temperature of the valve casing equal to 479°C was assumed as an initial condition for the hot start. The factor k = 1.12 accounting for nonlinearity of thermal boundary conditions was obtained by tuning for the warm start conditions and further used in hot start calculations.

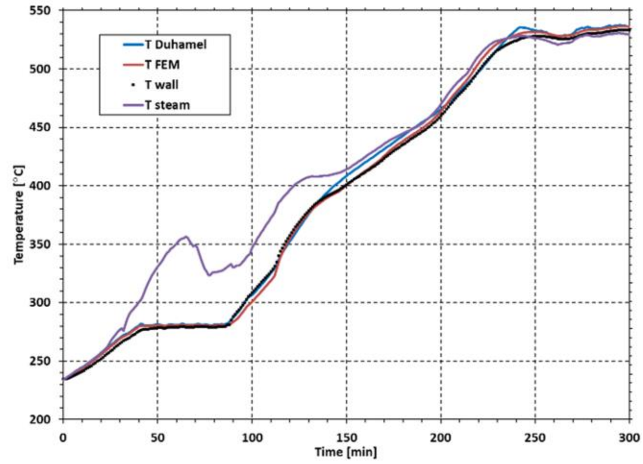

Fig. 10. Measured and calculated metal temperatures during warm start with pre-warming.

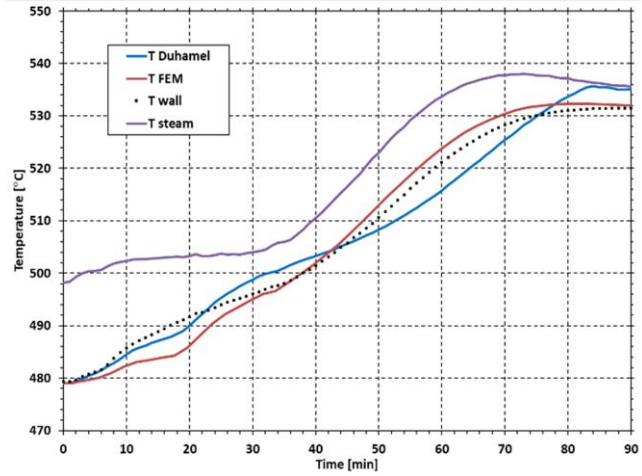

Fig. 11. Measured and calculated metal temperatures during hot start.

In all cases, very good agreement between calculations and measurements was found. At condensation conditions (Fig. 9 and Fig. 10), both methods (i.e. FEM and Duhamel's integral) predict nearly the same wall temperatures, which are very close to the measured temperature following steam saturation temperature. When the condensate film began to evaporate and convection heat transfer prevailed, larger deviations between calculated and measured temperatures were found. This is attributed mainly to inaccuracies in heat transfer coefficients determined with the help of simple correlations for pipe flows. However, the overall accuracy of the method based on Duhamel's integral can be assessed as high, taking into account the achieved deviations:

i. (−1.0%)÷(+1.5%),
ii. (−2.6%)÷(+1.5%),
iii. (−1.0%)÷(+0.8%).

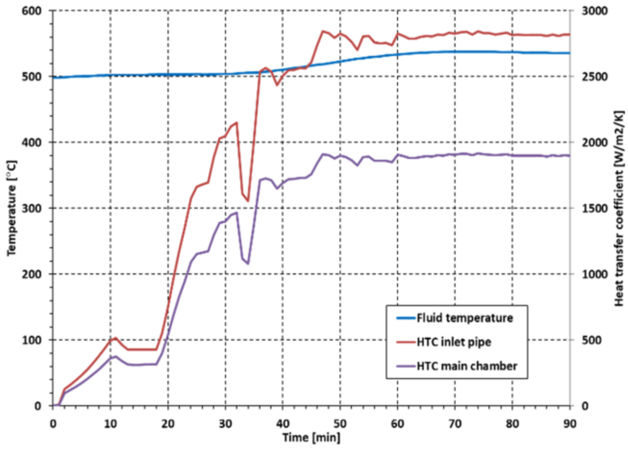

Fig. 12. Variation of temperature and heat transfer coefficients during hot start-up.

Temperature differences are also observed between the two calculation methods, in particular for forced convection. The two simulated start-ups show that Duhamel's integral tends to predict higher temperatures than FEM at lower heat transfer coefficients (lower steam velocities) and lower temperatures at higher heat transfer coefficients. Nevertheless, it should be noted that the degree of agreement between the detailed FEM calculations and predictions of the simple Duhamel's integral method is satisfactory. Finite element modelling of such complex components with nonlinear thermal boundary conditions is time consuming and results in a large amount of output data. Its use for online monitoring of power plant equipment is still impractical. However, the simple method described by Eq. (17) is fast, robust, accurate and easy to implement in industrial controllers. It considers in a simplified way the complex geometry of turbine and boiler components as well as the nonlinearity of thermal boundary conditions resulting from variation of steam temperature and heat transfer coefficient. The satisfactory accuracy of Duhamel's integral makes it very useful for online monitoring of thermal loading of turbine and boiler components.

For online checking of condensation conditions given by Eqs. (10) and (11), the wall surface temperature T_{surf} is calculated with the help of Eq. (17) and the temperature response function for the wall surface. Figure 13 presents the comparison of this temperature obtained with the help of Duhamel's integral and FEM for the warm and hot start-up. Thermal boundary conditions for the warm start are presented in Fig. 14, while for the hot start, the conditions shown in Fig. 12 were used. A constant temperature of the valve casing equal to 279°C was assumed as an initial condition for the warm start. Also for the surface temperature, reasonably good agreement between the two methods is found, in particular in the early phases of start-ups. These phases are very important because steam condensation on the valve surface can occur at the beginning of start-ups, and accurate prediction of the surface temperature is crucial in detecting steam condensation.

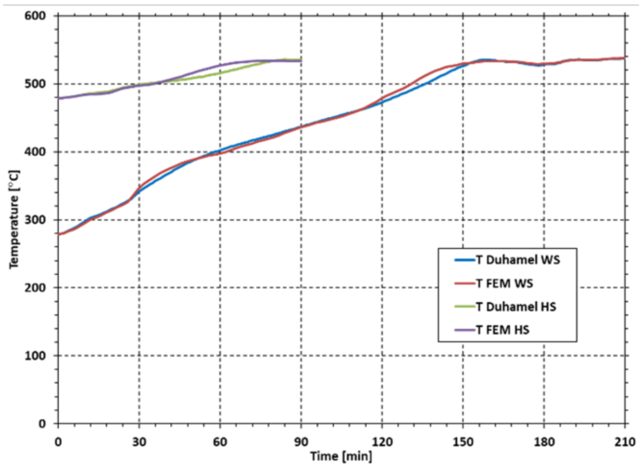

Fig. 13. Calculated wall surface temperatures during warm (WS) and hot start (HS).

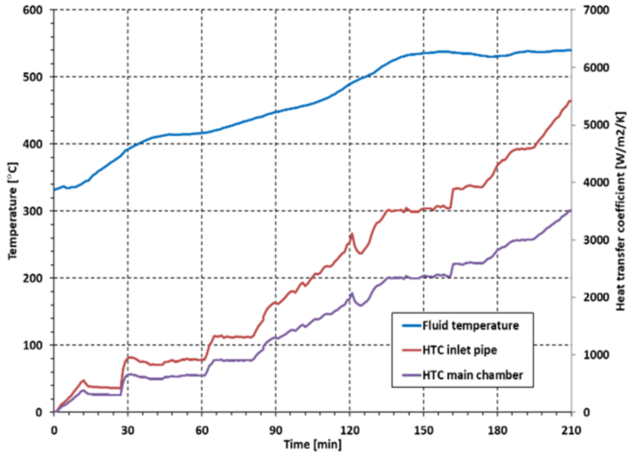

Fig. 14. Variation of temperature and heat transfer coefficients during warm start-up.

5. Summary

The paper presented numerical investigations of thermal loading of the turbine valve at various operating conditions. These included pre-warming from a cold state, warm start with pre-warming and hot start-up. Both condensation and convection heat transfer mechanisms were modelled. In the finite element modelling, it was done by applying condensation and forced convection heat transfer coefficients to the valve surfaces in contact with steam.

The proposed method for online calculation of metal temperature is based on Duhamel's integral. Different mechanisms of heat transfer are modelled in this algorithm by independent terms of Duhamel's integral. One term is responsible for condensation and the second one for convection, and each of them uses specific temperature response functions calculated with condensation and convection heat transfer coefficient, respectively.

It was shown that the calculation method provides reasonably accurate predictions of casing wall temperature. Comparison of the method predictions with the results of FEM simulations and measurements done at real operating conditions reveals the same level of accuracy as the finite element method. Relative differences between measured and calculated wall temperatures are within (−2.6%)÷(+1.5%) for the investigated start-ups with condensation and convection heat transfer conditions. This high level of accuracy was achieved by proper determination of temperature response functions which have to be calculated with a variable convection heat transfer coefficient. The quality of results is also improved by applying the constant factor k accounting for nonlinearity of thermal boundary conditions due to the variable heat transfer coefficient at convection.

The advantage of this method are fast and robust temperature calculations as well as its simple mathematical formulation, making it relatively easy for implementation in programmable logic controllers. It should also be emphasised that temperature calculations are performed using only steam temperature as an input without a need of installing metal temperature measurement in the area of interest. Turbine and valve casings are elements of complex geometry, and wall temperature measurements at critical locations are usually difficult in practical realisation. Moreover, in the case of rotating components, like rotors or blades, direct continuous measurements of metal temperature are still impractical and only short-term measurements with the help of optical probes are feasible [44]. Additional difficulty is also related to steam condensation, which reduces the accuracy of optical measurements.

References

[1] European Union. Directorate-General for Energy. (2023). *EU Energy in Figures* [accessed 22 May 2025].

[2] Rusin, A., Łukowicz, H., Lipka, M., Banaszkiewicz, M., & Radulski, W. (2005). Continuous control and optimisation of thermal stresses in the process of turbine start-up. *Proceedings of the 6th International Congress on Thermal Stresses*, 26−29 May, Vienna, Austria.

[3] Rusin, A., Radulski, W., & Banaszkiewicz, M. (2001). The Use of Duhamel's Integral in Lifetime Supervision Systems of Steam Turbines. *5th Conference on Research Problems in Power Engineering*, 4–7 December, Warsaw, Poland.

[4] Rusin, A., Łukowicz, H., Malec, A., Banaszkiewicz, M., & Lipka, M. (2003). Optimisation of Start-up Parameters of Steam Turbines. *6th Conference on Research Problems in Power Engineering*, 9–12 December, Warsaw, Poland.

[5] Taler, J., Węglowski, B., Zima, W., Duda, P., Grądziel, S., Sobota, T., Cebula, A., & Taler, D. (2008). Computer system for monitoring power boiler operation. *Proceedings of the Institution of Mechanical Engineers. Part A, Journal of Power and Energy; Journal*, 222, 13−24. doi:10.1243/09576509JPE419

[6] Lee, H.Y., Kim, J.B., & Yoo, B. (1999). Green's function approach for crack propagation problem subjected to high cycle thermal fatigue loading. *International Journal of Pressure Vessels and Piping*, 76(8), 487−494. doi: 10.1016/S0308-0161(99)00039-3

[7] Song, G., Kim, B., & Chang, S. (2011). Fatigue life evaluation for turbine rotor using Green's function. *Proceedia Engineering*, 10, 2292−2297.

[8] Koo, G.K., Kwon, J.J., & Kim, W. (2009). Green's function method with consideration of temperature dependent material properties for fatigue monitoring of nuclear power plants. *International Journal of Pressure Vessels and Piping*, 86(2−3), 187−195. doi: 10.1016/j.ijpvp.2008.09.006

[9] Botto, D., Zucca, S., & Gola, M.M. (2003). A methodology for on-line calculation of temperature and thermal stress under non-linear boundary conditions. *International Journal of Pressure Vessels and Piping*, 80(1), 21−29. doi: 10.1016/S0308-0161(02)00139-4

[10] Zhang, H.L., Liu, S., Xie, D., Xiong, Y, Yu. Y., Zhou, Y., & Guo, R. (2013). Online fatigue monitoring models with consideration of temperature dependent properties and varying heat transfer coefficients. *Hindawi Publishing Corporation*. *Science and Technology of Nuclear Installations*, ID 763175, 1−9. doi: 10.1155/2013/76317

[11] Rusin, A., Nowak, G., & Lipka, M. (2014). Practical Algorithms for Online Stress Calculations and Heating Process Control. *Journal of Thermal Stresses*, 37(11), 1286−1301. doi: 10.1080/01495739.2014.937219

[12] Nowak, G., & Rusin, A. (2016). Using the artificial neural network to control the steam turbine heating process. *Applied Thermal Engineering*. 108, 204−210. doi: 10.1016/j.applthermaleng.2016.07.129

[13] Dominiczak, K., Rządkowski, R., Radulski, W., & Szczepanik, S. (2015). *Neural networks in stress control system of steam turbine rotor*. Wydawnictwo Naukowe Instytutu Technologii Eksploatacji – PIB, 2015 (in Polish).

[14] Taler, J., Węglowski, B., & Pilarczyk, M. (2017). Monitoring of thermal stresses in pressure components using inverse heat conduction methods. *International Journal of Numerical Methods Heat & Fluid Flow*, 27, 740−756. doi: 10.1108/HFF-03-2016-0091

[15] Taler, J., Dzierwa, P., Jaremkiewicz, M., Taler, D., Kaczmarski, K., Trojan, M., Węglowski, B., & Sobota, T. (2019). Monitoring of transient 3D temperature distribution and thermal stress in pressure elements based on the wall temperature measurement. *Journal of Thermal Stresses*, 42, 698−724. doi: 10.1080/01495739.2019.1587328

[16] Pilarczyk, M., & Węglowski, B. (2019). Determination and validation of transient temperature fields within a cylindrical element using the inverse heat conduction method. *Applied Thermal Engineering*, 150, 1224−1232. doi: 10.1016/j.applthermaleng.2019.01.079

[17] Węglowski, B., & Pilarczyk, M. (2018). Experimental and numerical verification of transient spatial temperature distribution in thick-walled pressure components. *Journal of Mechanical Science and Technology*, 32, 1087−1098. doi: 10.1007/s12206-018-0211-z

[18] Banaszkiewicz, M. (2017). On-line determination of transient thermal stresses in critical steam turbine components using a two-step algorithm. *Journal of Thermal Stresses*, 40(6), 690−703. doi: 10.1080/01495739.2016.1249988

[19] Banaszkiewicz, M., & Badur, J. (2018). Practical methods for online calculations of thermoelastic stresses in steam turbine components. In *Selected Problems of Contemporary Thermomechanics*, (pp. 45−63), Intech Open. doi: 10.5772/intechopen.75876

[20] Taler, J. (1995). *Theory and practice of heat transfer processes identification*. Zakład Narodowy im. Ossolińskich (in Polish).

[21] Noda, N., Hetnarski, R.B., & Tanigawa, Y. (2003). *Thermal stresses* (2nd edition), Taylor & Francis, New York.

[22] Zienkiewicz, O.C., Taylor, R.L., & Zhu, J.Z. (2005). *The Finite Element Method: It's Basis and Fundamental*s. Elsevier Butterworth-Heinemann, Oxford.

[23] Chmielniak, T., & Kosman, G. (1990). *Thermal loads of steam turbines*. Wydawnictwa Naukowo-Techniczne (in Polish).

[24] Badur, J., Ziółkowski, P., Kornet, S., Stajnke, M., Bryk, M., Banaś, K., & Ziółkowski, P.J. (2017). The Effort of The Steam Turbine Caused by a Flood Wave Load. In *AIP Conference Proceedings. IX Polish National Conference on Applied Mechanics*, 25 November, Bydgoszcz, Poland. doi: 10.1063/1.4977675

[25] Badur, J., Ziółkowski, P., Sławiński, D., & Kornet, S. (2015). An Approach for Estimation of Water Wall Degradation Within Pulverized-Coal Boilers. *Energy*, 92, 142−152. doi: 10.1016/j.energy.2015.04.061

[26] Badur, J., Ziółkowski, P., Zakrzewski, W., Sławiński, D., Kornet, S., Kowalczyk, T., Hernet, J., Piotrowski, R., Felicjancik, J., & Ziółkowski, P.J. (2015). An advanced Thermal-FSI approach to flow heating/cooling. *Journal of Physics: Conference Series*, 530, 012039. doi: 10.1088/1742-6596/530/1/012039

[27] Banaś, K., & Badur, J. (2017). Influence of Strength Differential Effect on Material Effort of a Turbine Guide Vane Based on a Thermoelastoplastic Analysis. *Journal of Thermal Stresses*, 40(11), 1368-1385. doi: 10.1080/01495739.2017.1352463

[28] Gnielinski, V. (1975). Neue Gleichungen für den Wärme- und den Stoffübergang in turbulent durchströmten Rohren und Kanälen. *Forschung Ingenieurwes. (Engineering Research)*, 41, 8−16. doi: 10.1007/BF02559682

[29] Gnielinski, V. (1976). New equations for heat and mass transfer in the turbulent pipe and channel flow. *International Chemical Engineering*, 16, 359−368.

[30] Filonienko, G.L. (1954). Friction factor for turbulent pipe flow, *Teploenergetika*, 1(4), 40−44 (in Russian).

[31] Dittus, F.W., & Boelter, L.M.K. (1930). Heat transfer in automobile radiators of the tubular type. *The University of California Publications on Engineering*, 2, 443−461. (Reprinted in *International Communications in Heat and Mass*, 12, 3−22, 1985).

[32] Winterton, R.H.S. (1998). Where did the Dittus and Boelter equation come from?. *International Journal of Heat and Mass Transfer*, 41, 809−810. doi: 10.1016/S0017-9310(97)00177-4

[33] McAdams, W.H. (1954). *Heat Transmission* (3rd ed.), McGraw-Hill, New York.

[34] Colburn, A.P. (1933). A method of correlating forced convection heat transfer data and a comparison with fluid friction, *Transactions AIChE*, 29, 174−210. (*International Journal of Heat and Mass Transfer*, 7(12), 1359−1384. doi. 10.1016/0017-9310(64)90125-5).

[35] Badur, J., & Karcz, M. (2009). *Analysis of heat transfer conditions in stop valve chamber of 230 MW turbine*. Unpublished report.

[36] Marinescu, G., Ehrsam, A., Sell, M., & Brunner, P. (2013). Experimental investigation into thermal behaviour of steam turbine components. Part 3 – startup and the impact on LCF life. *Proceedings of ASME Turbo Expo*, 3−7 June, San Antonio, USA. doi: 10.1115/GT2013-94356

[37] Taler, J., & Duda, P. (2006). *Solving Direct and Inverse Heat Conduction Problems* (pp. 19−20), Springer, Berlin/Heidelberg.

[38] Pilarczyk, M., Weglowski, B., & Nord, L.O. (2020). A Comprehensive Thermal and Structural Transient Analysis of a Boiler's Steam Outlet Header by Means of a Dedicated Algorithm and FEM Simulation. *Energies*, 13(1), 111. doi: 10.3390/en13010111

[39] Shah, M.M. (1979). A general correlation for heat transfer during film condensation inside pipes. *International Journal of Heat and Mass Transfe*r, 22, 547−556. doi: 10.1016/0017-9310(79)90058-9

[40] *Abaqus User Manual*, ver. 6.6.

[41] DIN EN 10213. (2016). *Steel castings for pressure purposes*.

[42] Banaszkiewicz, M. (2016). On-line monitoring and control of thermal stresses in steam turbine rotors, *Applied Thermal Engineering*, 94, 763−776. doi: 10.1016/j.applthermaleng.2015.10.131

[43] Carslaw, H.S., & Jaeger, J.C. (1959). *Conduction of Heat in Solids*, Oxford University Press.

[44] Marinescu, G., Mohr, W., Ehrsam, A., Ruffino, P., & Sell, M. (2014). Experimental investigation into thermal behaviour of steam turbine components – temperature measurements with optical probes and natural cooling analysis. *Journal of Engineering for Gas Turbines and Power*, 136(2), 021602. doi: 10.1115/1.4025556

Co-published by
Institute of Fluid-Flow Machinery
Polish Academy of Sciences
Committee on Thermodynamics and Combustion
Polish Academy of Sciences

http://www.imp.gda.pl/archives-of-thermodynamics/

ARCHIVES OF THERMODYNAMICS

Steam and gas microturbines. Overview

Krzysztof Kosowski[a], Marian Piwowarski[a*], Robert Stępień[b], Wojciech Włodarski[a]

[a]Faculty of Mechanical Engineering and Ship Technology, Gdansk University of Technology, Narutowicza 11/12, 80-233 Gdansk, Poland
[b]Proturb, Poland, Fiszera 14/513, 80-231 Gdansk, Poland
*Corresponding author email: marian.piwowarski@pg.edu.pl

Received: 12.06.2025; revised: 02.09.2025; accepted: 11.09.2025

Abstract

In the contemporary energy landscape, governments are focusing on improving the efficiency of electricity generation and promoting distributed energy systems based on local and renewable sources. This has led to a substantial increase in the number of prosumer, polygeneration, and microgeneration power plants currently under development. In the case of micro-power plants, often turbine-based, particular emphasis is placed on the durability, reliability, cost-effectiveness, and efficiency of both individual components and the entire system. The construction of microturbine power plants involves several challenges, including component miniaturisation, achieving extremely high rotational speeds, efficient power transmission, maintaining adequate safety standards, reducing noise, minimising emissions of harmful compounds, and designing the electric generator. Additional difficulties concern the optimisation of thermodynamic and fluid-dynamic processes, the high-efficiency design of flow components, ensuring bearing and dynamic stability in high-speed rotating systems, miniaturising heat exchangers, and enhancing thermal processes. Despite the availability of commercial microturbine solutions, recent years have seen intensified research and development efforts. The evolution observed in this field suggests that efforts to improve efficiency, durability, reliability, and cost-effectiveness will continue, strongly supported by government involvement. Current progress and accumulated experience have enabled the development of engineering calculation methods for microturbine design, a crucial element of microgrids. This paper reviews the existing literature on microturbines, with particular attention to experimental results and examples of practical designs. It also outlines the main challenges faced by designers and engineers in developing such systems.

Keywords: Gas microturbines; Steam microturbines; Organic Rankine Cycle; Adhesion turbine

Vol. 46(2025), No. 3, 17–37; doi: 10.24425/ather.2025.154921

Cite this manuscript as: Kosowski, K., Piwowarski, M., Stępień, R., & Włodarski, W. (2025). Steam and gas microturbines. Overview. *Archives of Thermodynamics*, 46(3), 17−37.

1. Introduction

In the current 21st century, there is an increasing prevalence of trends towards miniature engineering. Their presence is evident in a variety of sectors, including the power industry, where they are employed in refrigeration, heat exchange, chemical processes, and power generation processes (microturbines, micropumps, micro-compressors, micro-valves, micro-heat exchangers, micro-motors, etc.) [1–3]. The popularity of microturbines has increased significantly over the past two decades, due to their status as relatively small devices. The characteristics of the devices under discussion are as follows: they are characterised by relatively low electrical power (ranging from 25 to 500 kW), very high rotational speeds (ranging from 50 to 120 000 rpm, with some microturbines reaching speeds of up to 1 million rpm [4,5]), and relatively good efficiencies (ranging from 20% to 30% without regeneration). These devices allow for diversification of the energy source in the region [2,6].

Nomenclature

Abbreviations and Acronyms

ACM – air cycle machine
CBC – closed Brayton cycle
CHP – combined heat and power (system)
EMG – electromagnetic generator
FBG – fibre Bragg grating
GMT – gas microturbine
GWP – global warming potential
HRSG – heat recovery steam generator
LSTM – long short-term memory
MEMS – micro-electro-mechanical systems
NZEB – net zero energy building
ODP – ozone depletion potential
ORC – organic Rankine cycle
OTEC – ocean thermal energy conversion
PLM – porous layer model
STG – steam turbine generator
TENG – triboelectric nanogenerator
VOC – volatile organic compound

The advantage of microturbines is their versatility in terms of fuel selection. In addition to conventional fuels such as natural gas and diesel, microturbines have the capacity to utilise a wide range of alternative fuels, including landfill gas, sewage treatment plant gas, flue gas, coal gasification gas, biofuels, methanol, ethanol, and hydrogen, among others [7].

At present, a significant number of corporations are engaged in conducting extensive research and development projects with the objective of constructing microturbines that exhibit enhanced efficiency, reliability, durability and cost-effectiveness. The primary objective of the activity is to achieve efficiencies in excess of 40%, with a concomitant reduction in NO_x emissions and an increase in availability (continuous operation between overhauls of more than 50000 hours), reducing investment costs (< 500 USD/kW), improving fuel flexibility (the ability to utilise several types of fuel, including biofuels, etc.). It is evident that a significant number of globally renowned corporations are engaged in addressing these issues. While some entities have already commenced the provision of microturbines to the commercial sector, ongoing research in this domain persists, with continual advancements being made. The challenges posed by the miniaturisation of components are manifold. These include, but are not limited to, difficulties with bearing and transmission at very high speeds. In addition, there is a need to ensure a proper level of safety, to reduce noise and to reduce the emission of harmful compounds into the atmosphere. A significant challenge confronting manufacturers pertains to the quality of electric generation, encompassing essential parameters such as required voltages, frequency, and power output, among others. This challenge persists during transient conditions. Concurrently, advanced research is being conducted into the use of new types of materials (synthetics, composites, ceramics, aluminium alloys, etc.) [8,9].

In the domain of micro systems, the primary concern pertains to the overall dimensions of the system. Miniaturisation facilitates the acquisition of information with greater efficiency, thereby reducing the material and energy requirements during the production process. Intelligent microsystems, equipped with microsensors and actuators, possess the capacity to interact with their environment and respond to changes therein. The utilisation of micro power supplies and microelectronics for signal processing is a prerequisite for such systems. The integration of these components enhances system efficiency, resulting in faster, more reliable, and cost-effective operation, while concurrently reducing power consumption and enabling the execution of more complex functions [10,11].

In the last two decades, there has been a marked increase in the number of articles dealing with microturbines, as evidenced by data from Elsevier's electronic journal database, which is available through the ScienceDirect platform (Fig.1).

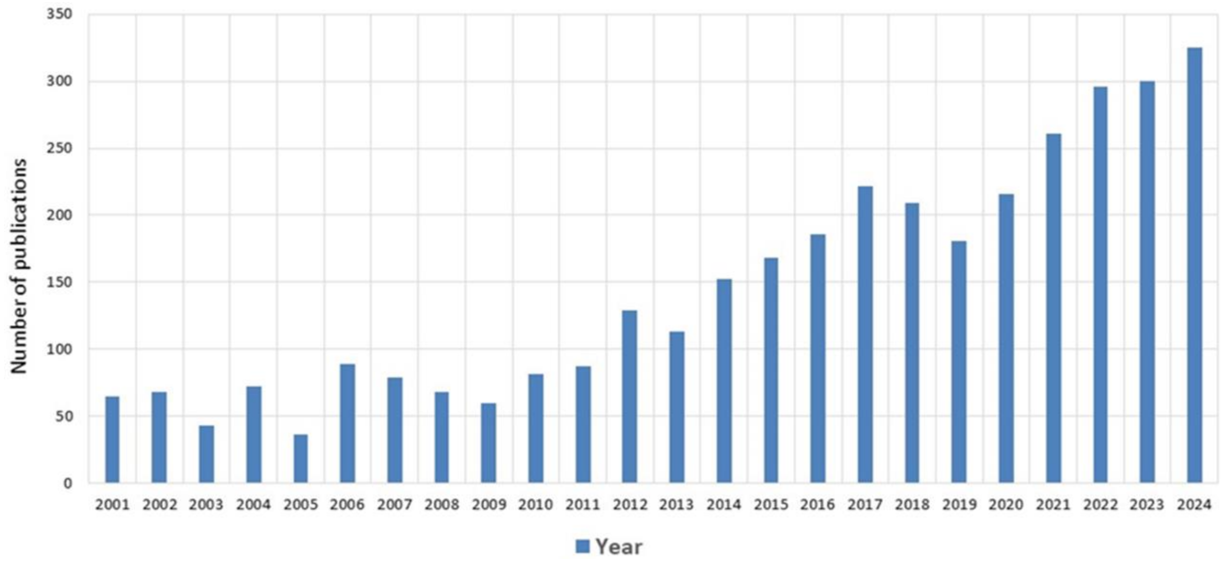

Fig. 1. Number of publications on microturbines from Elsevier's electronic journals database.

The objective of this paper is twofold: firstly, to present and systematise extant solutions for vapour and gas microturbines; and secondly, to explore the potential for future development in this area. The analyses were conducted using a range of academic databases, including Elsevier Open Access, Institute of Electrical and Electronics Engineers, and Springer, to name a few. In certain instances, the authors have encountered difficulties in accessing more detailed information due to the protection of intellectual property rights. The paper is organised into five main chapters, with each one focusing on specific aspects of these solutions. Vapour microturbines are categorised into two types: those using steam as the working medium (Rankine cycle) and those employing other working media in the Organic Rankine Cycle (ORC). The latter type of micro power plant, in particular, is undergoing significant development. The next chapter discusses gas microturbines, which are also experiencing rapid advancements. A separate chapter is dedicated to Tesla microturbines, given their ability to utilise various working media, including steam, organic vapour, air, or flue gases, which complicates their classification within a single category. Additionally, a chapter has been dedicated to microturbines (both steam and gas) that employ Microelectro-Mechanical System (MEMS) technology, in addition to the analyses presented in other chapters.

2. Steam microturbines

Steam turbines are among the most versatile and long-standing prime mover technologies still widely used today. The utilisation of steam turbines for power generation has a long history, having replaced reciprocating steam engines due to their superior efficiency and lower costs. In the extant literature, steam microturbines are referred to as devices that produce energy measured in kilowatts or even watts. Up to now, quite a few power stations have been equipped with steam microturbines. However, this knowledge and technology domain is still dynamically developing, in a similar manner to gas microturbines. The advantages of the steam microturbine are:

- a proven technology,
- broad power range,
- acceptable efficiencies (at least at nominal conditions),
- separation between combustion and power generation.

The main disadvantages are:

- low efficiency at partial load,
- relatively high costs for a small size [8].

The Rankine cycle is the most common thermodynamic cycle employed in steam turbines. This cycle constitutes the fundamental principle underlying conventional power-generating stations, Fig. 2, and it is realised in four ideal thermal processes [6]:

- heat supply at constant pressure (usually, in the boiler furnace, due to chemical reactions of fuel combustion, heat is generated and used for changing the water into steam, most frequently superheated),
- isentropic expansion (the steam of high pressure and temperature generated in the boiler enters the turbine where it expands to the low pressure of the condenser),
- heat rejection at constant pressure (in the condenser, the steam rejects its heat of condensation to a cooling system),
- isentropic compression (in the pump, the isentropic process of compression takes place, transforming the water from saturated liquid state to feed water at high pressure).

The steam microturbine has also been incorporated into hybrid cogeneration, trigeneration and combined steam-gas power systems [12].

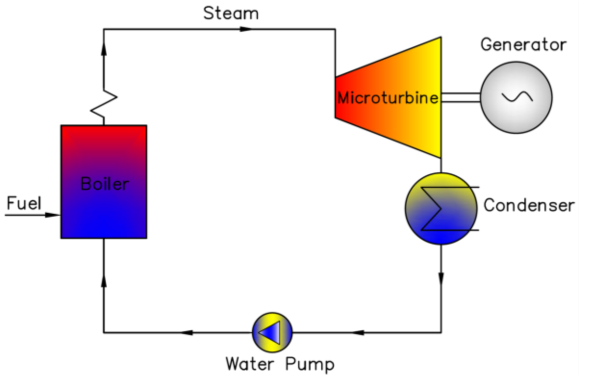

Fig. 2. Diagram of a steam microturbine cycle.

An example of a steam microturbine set is shown in Fig. 3 [13]. The Steam Turbine Generator (STG) system consists of a high-speed steam microturbine with an axial inlet and radial outlet with a high internal efficiency of 80%, a planetary gearbox reducing the speed in a ratio of 7.78:1 and a generator with efficiency above 95%. The efficiency depends on the parameters of the inlet steam. It has been demonstrated that the turbine set has the capacity to generate 275 kW of electrical power [14]. The centrifugal microturbine used in this solution allows large enthalpy drops to be realised with good efficiency at low mass flow rates.

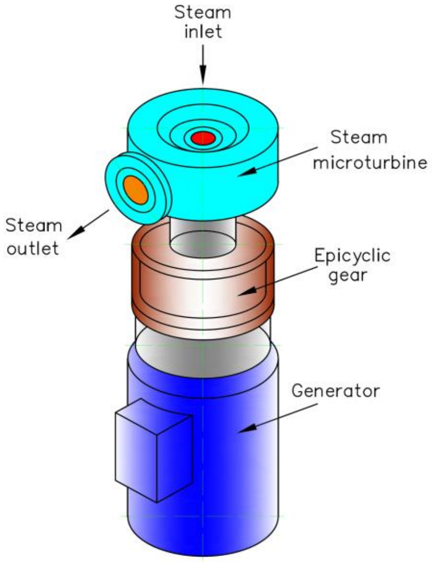

Fig. 3. Steam microturbine model STG.

In 2004, a prototype of a gas-powered domestic SteamCell unit for combined heat and power generation based on a steam unit was presented (Fig. 4) with an efficiency of 25%. The system has been demonstrated to deliver a range of electricity outputs between 0.5 kW and 4.6 kW, in conjunction with heat outputs ranging from 2 kW to 25 kW. In this particular instance, the conventional Rankine cycle is augmented by the incorporation of an additional domestic water heater [15].

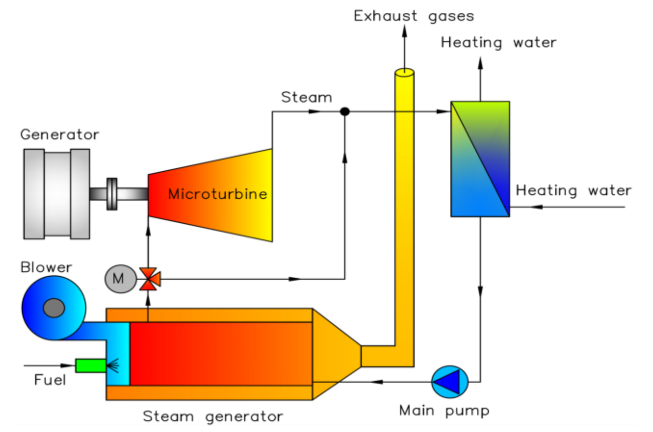

Fig. 4. Functional diagram of the SteamCell system.

The paper [16] presents a two-stream flow centripetal microturbine. The unit's maximum electrical power output is 50 kW at 12 000 rpm. The rotor is supported by rolling bearings. In experimental tests for an inlet steam pressure of 0.6 MPa, temperature of 159°C and mass flow rate of 0.21 kg/s, 30.37 kW of electrical power was obtained.

Another example of a steam turbine test rig is the system that was installed at the Maine Maritime Academy[17]. The facility has two steam turbine units. One is a single-stage Curtis turbine, and the other is a multi-stage axial turbine. Operation parameters: outlet pressure of 800 kPa, outlet temperature of 289°C, boiler inlet water temperature of 63°C, condenser pressure of 20 kPa, turbine outlet temperature of 110°C (Curtis stage) and 60.1°C (multi-stage turbine), rotational speed of 3 600 rpm, electric power of 8.21 kW (Curtis stage) and 13.32 kW (multi-stage turbine), with overall circuit efficiency of 11.4% (Curtis stage) and 18.55% (multi-stage turbine). There are some disadvantages to both solutions. The Curtis turbine stage is less efficient, and the multistage turbine is more complicated.

The New England Steam Turbine Corporation, on the other hand, makes NESTCO N17 H single-stage steam turbine units. These have a power output of 1260 hp (≈940 kW), an inlet steam temperature of 440°C, a pressure of 49 bar and a speed of 6 300 rpm. This is also a Curtis turbine stage device. The company also offers a vertical-flow version of the NESTCO N17 V microturbine. Both devices are used to drive pumps [18].

Another intriguing steam microturbine solution is a counter-rotation turbine with two separate rotors, without a stator between them, rotating in opposite directions, driving two separate high-speed permanent magnet generators (see Fig. 5). Figure 5a presents a microturbine set, while Fig. 5b shows a partially decomposed device with visible separate rotor blade cascades. It is a device that uses the summation of velocity vectors resulting from the modification of the Ljungström turbine. The microturbine has been demonstrated to facilitate a power output of approximately 1,5 kW at an inlet steam pressure of around 5 bar, a temperature of approximately 220°C, and outlet parameters of 10 kPa and 40°C. These conditions are maintained while the microturbine operates at a rotational speed of 30 000 rpm and a mass flow rate of 5 g/s. This approach has been patented [19] and has undergone theoretical testing and analysis. The feasibility of a compact design that is capable of effective electricity production was demonstrated [20,21].

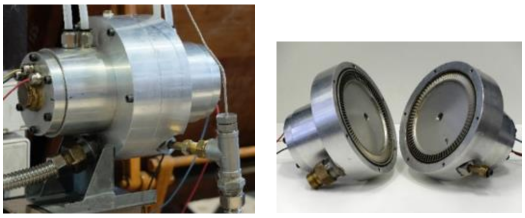
a) b)

Fig. 5. View of a steam microturbine with two generators (a) and both counter-rotating rotors in separate housings (b).

For example, in Russian developments led by the Don Technologies consortium, single-stage, two-flow active centripetal steam microturbines have been applied, operating in the range of 30–50 kW electric power and up to 600 kW thermal power. Their design enables independent regulation of electricity and heat generation, which distinguishes them from gas turbine and piston units. Experimental investigations, however, revealed the need for further optimisation of blade profiles and reduction of efficiency losses during wet steam operation [22].

In studies on cogeneration systems, integrating gas and steam microturbines with ORC loops and solar collectors has been emphasised. Advanced concepts couple a microturbine with a parabolic dish collector and a Brayton cycle, while waste heat recovery is performed through dual-stage ORC modules. Such configurations significantly improve exergy efficiency and reduce fuel consumption, achieving overall efficiencies exceeding 70% [23].

Although steam microturbines were not the primary focus in research on building-integrated nanogrid systems, they are often discussed in the broader context of decentralised trigeneration. Integration of microturbines with thermal energy storage highlights their potential use in Net Zero Energy Buildings (NZEBs), where they can complement renewable sources and support local heating and cooling demands [24].

Another promising direction is the application of microturbines in mobile and transport energy systems. Research on sustainable tramway power supply has demonstrated the feasibility of integrating microturbines with biomass gasifiers. In such configurations, microturbines act as stabilising units for the entire energy system, working in conjunction with energy storage and renewable sources, thereby enhancing energy autonomy and reducing CO_2 emissions [25].

Utilising the microturbine configuration presented in Fig. 5, the authors have proposed a solution for a steam micro-turbine that operates in an emission-free mode. This solution involves the combustion of hydrogen in an oxygen, resulting in the generation of steam as the working medium. The concept of such an installation is illustrated in Fig. 6, while the test stand is presented in Fig. 7. The proposed solution is straightforward and analogous to the Rankine system. The hydrogen burner generates high-temperature steam. The process of steam generation at a lower temperature, permissible for the turbine, is achieved by the supply of water to the burner. Steam expands in the turbine and is then condensed in a water-cooled condenser. The work of the turbine is used to produce electricity in the generator.

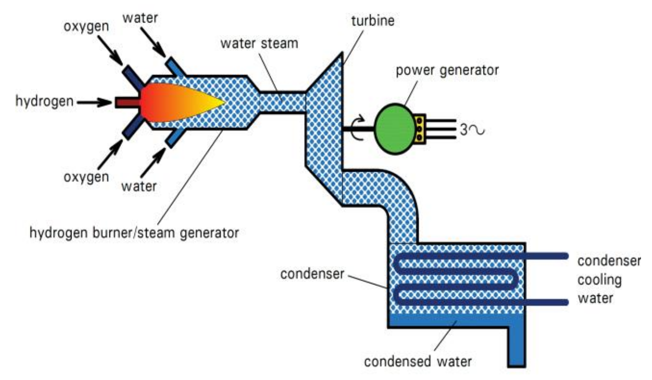

Fig. 6. Concept of operation of a hydrogen microturbine.

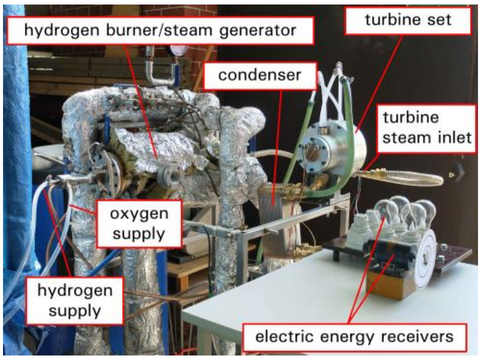

Fig. 7. View of the hydrogen microturbine test stand.

In addition to the commercial versions, laboratory-scale stations are also available. The steam parameters at the boiler outlet are a pressure of 827 kPa and a temperature of 250°C, and the resulting electrical power is approximately 15 W [26]. These are student stands designed to present the idea of the Rankine cycle.

In this chapter, the authors have conducted a review of extant design solutions for microturbines with steam as the working medium. Although few examples of steam-based microturbines have been cited, their development is ongoing. Steam microturbines have very low steam flow rates and high enthalpy drops, so special designs must be used to achieve good efficiency. A range of adaptations have been derived from high-power steam turbine solutions, including multi-stage axial micro-turbines, micro-turbines with Curtis stage, centripetal turbines, and turbines with contra-rotating rotors. Each of these has its own advantages and disadvantages, and ongoing development is focused on enhancing efficiency, durability, and reliability. However, recent trends in micro turbine development appear to be shifting towards the utilisation of working media other than water. These are ORC cycles, which will be discussed in more detail in the next chapter.

3. Microturbines in ORC cycles

The fundamental operating principle of ORC technology was first established in 1826 by Howard. He used ether as the working medium. It was not until more than a century later that D'Amelio constructed an ORC power plant in 1936, equipped with a single-stage impulse turbine and monochloroethane (C_2H_5Cl) as the working medium, heated by solar energy. Subsequently, during the 1960s, research into potential working fluids was initiated, which led to the identification of the advantages of chlorofluorocarbons (CFC) use and the establishment of the ORC cycle with regeneration. This cycle continues to be utilised extensively in the present day. This development subsequently prompted the conception of multiple prototypes by ORMAT in 1964 and Turboden in 1970. These enterprises have since emerged as the foremost entities within the ORC market [27].

The initial ORC systems, which were in operation between 1960 and 1980, are summarised in Table 1.

Table 1. First ORC systems built between 1960 and 1980.

Year	Power, kW	Working fluid	Temperature, °C	Pressure, bar	Number of systems	Country
1961	347	R11	-	-	1	USA
1966	190	R11	120	12,5	1	Japan
1967	750	R12	-	-	1	USSR
1968	3800	R11	121	12,8	1	Japan
1969	475	R11	116	11,6	1	Japan
1972	108	Fluorinol 85	288	48,3	1	USA
1974	500	R11	123	13,3	1	Japan
1975	600	Toluen	274	22	1	USA
1977	500	R113	90	12,4	1	Japan
1977	34	Fluorinol 50	321	55,2	1	USA
1978–1982	600	Toluen	251–274	16–22	5	USA
1979	200	Toluen	-	-	1	USA
1979	40	Tetrachloroethylen	110	0,7	1	Italy
1979	500	R11	88	6,2	1	USA
1979	21	R114	92	-	1	Germany
1979	100	Toluen	320	-	1	Germany
1979	170	Toluen	323	-	1	Germany
1979	500	R114	85	-	1	Germany
1979	30	R11	160	13	1	Germany
1980	45	C_8F_{16}	280	11,6	1	Italy
1980–1983	50–600	R114	-	-	22	Israel
1981	14000	Fluorinol 85	260	34	1	Japan
1981–1984	1000–1500	R113	130	7,9	3	USA
1982	130	R11	-	24	1	Germany
1982	500	R114	105	15,3	1	Italy
1982	5000	R114	75	8,1	1	USA
1983	1000	Fluorinol 85	330	50	1	France
1983	3280	R11	90	6,7	1	Japan
1984	100	Dichlorobenzen	173	0,9	1	Italy
1984	100	C_8H_{10}	130	0,8	1	Italy
1984	100	R114	170	22	1	Finland

The assembly of these power plants was primarily undertaken in the USA, Japan, Germany, Israel and Italy, with capacities ranging from a few tens of kilowatts to several megawatts. A solution with a capacity of up to 1 MW can be designated as a microturbine unit. At that time, the following refrigerants were typically utilised: R11, R12, R113, R114 and Fluorinol [7,28].

We can see from the table that the temperatures used in those years were quite low. They did not exceed 330°C. On the other hand, the pressures were already above 55 bar. It is generally accepted that steam power plants above 350°C have higher efficiencies than those using organic media [29]. At lower temperatures, thermodynamic cycles using organic fluids can achieve a higher level of efficiency than those using steam [30]. The construction of this type of power plant was later somewhat abandoned, but the last two decades have seen a rapid development of ORC systems and associated microturbine technology.

The ORC is similar to the cycle of a conventional steam turbine, except that the medium that drives the turbine is a high molecular weight organic fluid. The selected working fluids allow efficient use of low temperature heat sources to generate electricity over a wide power range (from a few kW up to 1 MW per unit). The organic working fluid is vaporised in the evaporator, then it expands in the turbine and is then condensed using cooling water in a heat exchanger (alternatively, ambient air can be used for cooling). The condensed medium is then pumped back to the evaporator, and the thermodynamic cycle is closed. Heating and cooling sources are not in direct contact with the working fluid or the turbine. For high temperature applications, e.g. combined heat and power biomass-powered plants, high temperature thermal oil is used as a heat carrier and a regenerator is added to further improve the cycle performance. The main technical advantages of ORC plants are as follows:

- relatively high cycle efficiency for a low value of upper cycle temperature,
- high turbine efficiency (up to 85%),
- no erosion of blades, due to the absence of moisture,
- long life time,
- no operator is required.

The system also has practical advantages, such as simple start-stop operation, quiet operation, minimum maintenance requirements, and good part load performance. Typical applications are:

- power plants with low temperature geothermal fluids, up to 1 MW electrical power per unit,
- biomass fueled plants,
- heat recovery applications (in the range of 400 to 1500 kW electrical power),
- solar systems application [31].

Many companies have developed and implemented their own technologies in recent years, e.g. radial flow turbines, axial microturbines, direct evaporation turbine units, centripetal radial flow microturbines or screw expanders [27,28]. By the end of 2016, 1754 ORC turbine units with a total installed capacity of more than 2.7 GW had been built, according to the study [27].

Often the main source of energy in ORC power plants is waste heat from various energy, industrial, agricultural or even domestic processes [32,33]. The utilisation of this particular type of heat facilitates enhanced energy efficiency by means of its recovery and reuse, as opposed to its dissipation into the environment. To illustrate, in industrial facilities such as steel mills, cement plants and chemical plants, waste heat is frequently a by-product of technological processes [34,35]. Numerous examples in the extant literature illustrate the utilisation of waste heat from internal combustion engines [36] as well as from gas turbines [37] as a source of thermal energy for ORC systems. The implementation of these solutions has the potential to enhance the overall energy efficiency of these units, which, in practical terms, is evidenced by a reduction in energy losses and an increase in efficiency by several percentage points.

In addition to waste heat, geothermal energy is a frequently analysed and utilised energy source for ORC systems [38]. Geothermal heat sources, including hot springs and geothermal boreholes, are a stable and renewable energy source that can power ORC power plants throughout the year, irrespective of weather conditions. Another area of interest is the use of solar energy [39], which, when utilising suitable solar collector technology, can be efficiently converted to thermal energy to power the ORC cycle. In coastal or island regions, examples are also emerging of the use of ocean thermal energy, known as Ocean Thermal Energy Conversion (OTEC) energy, as a heat source for ORC power plants [40]. This type of solution is based on the temperature difference between the warmer surface of the ocean and the cooler layers of the deep sea, making it possible to generate electricity in a renewable and environmentally friendly manner. The above-mentioned heat sources vary considerably in temperature from around 30°C to 200°C, which has a significant impact on the selection of working medium and, consequently, the design of the microturbine.

The working fluids utilised in ORC power plants are required to adhere to a multitude of criteria, which poses a significant challenge in the design of such systems. Operational safety is paramount, necessitating the use of a working fluid that exhibits minimal toxicity and environmental impact. In practice, substances with high greenhouse gas potential (GWP) and high ozone depletion potential (ODP) are typically excluded or used only in exceptional cases. The environmental impact of a given substance is also associated with its capacity for biodegradation and the emission of volatile organic compounds (VOCs). In addition to the environmental aspects, the working fluid should be inexpensive and readily available on the market. The cost of the working fluid has a direct impact on the cost-effectiveness of the overall project, particularly in the case of larger installations, where the quantity of fluid required is substantial. Another important requirement is its chemical stability, both thermal and material. It is imperative that the working medium does not react chemically with the components of the flow system (e.g. heat exchangers, turbines or piping), as this could lead to their corrosion or degradation and, consequently, result in the premature failure of the plant. In practice, it is often challenging to identify a working medium that fulfils all these requirements while preserving optimal thermodynamic properties. Consequently, designers are compelled to make compromises, which may entail the implementation of more sophisticated and costly safety technologies, such as leak detection systems or fire protection systems, particularly in the context of flammable media, including saturated hydrocarbons (methane, propane) and unsaturated hydrocarbons (ethane, ethylene). It is therefore evident that the selection of the operating medium constitutes a significant engineering challenge in the design of ORC systems, given the extensive range of potential substances that can be utilised.

The extant literature comprises analyses of diverse groups of compounds, including saturated hydrocarbons (e.g. n-pentane), unsaturated hydrocarbons (e.g. propylene), cyclic hydrocarbons (e.g. cyclohexane), heterocyclic hydrocarbons (e.g. furfural), aromatic hydrocarbons (e.g. toluene), as well as synthetic refrigerants (R134a, R1234yf), alcohols (ethanol, methanol), siloxanes (e.g. MM, MD2M) and other compounds [41]. A number of studies have been conducted on the selection of suitable operating agents for ORC systems, as it is crucial for process efficiency and stability. A range of studies have been conducted that consider both synthetic refrigerants and natural organic compounds with a view to determining whether they can meet the requirements of specific applications. The most commonly used working refrigerants include compounds such as R245fa, R123, n-butane, n-pentane and R1234yf [41]. These refrigerants possess relatively low boiling points, rendering them efficacious in ORC systems with low to medium heat source temperatures.

Ethanol, as an example of alcohol, is also used as a working fluid in ORC systems due to its thermodynamic properties and relatively low toxicity [40]. Other refrigerants, such as R134a, R152a, R236fa, R245fa, or mixtures such as R404a and SES36, have also been extensively studied in the context of ORC engine applications [37]. Many of these compounds have low ozone depletion potential (ODP) and moderate global warming potential (GWP), making them more environmentally friendly [42,43].

In the context of high-temperature ORC systems, compounds with higher boiling points, such as toluene, siloxanes (e.g. MDM, MM, MD2M), are often preferred [44], which show stability in higher temperature ranges. Furthermore, agents such as ammonia, cyclohexane or acetone are of interest in this context [45], which, due to their chemical and thermodynamic properties, can be used under more demanding conditions, e.g. using waste heat from higher temperature processes.

In the case of some ORC systems, mixtures of operating media are also considered. These mixtures may provide enhanced thermodynamic properties, but their composition and characteristics are often not commercially available and, in many cases, are protected by patents. Therefore, the selection of a suitable working medium should prioritise cycle efficiency and maximise the use of the available heat source, which directly affects the energy efficiency of the overall system.

A fundamental difference between ORC cycles and conventional Rankine cycles lies in the temperature of the working medium at the turbine inlet. This results from the specific properties of the organic fluids employed, such as isopentane, R245fa, or siloxanes. These fluids have a lower evaporation temperature than water, enabling the efficient utilisation of low- and medium-temperature heat sources. Consequently, conventional ORC power plants typically achieve efficiencies in the range of 10−12%, while modified ORC systems can reach efficiencies of up to 15−20% [46]. Such modifications may include an increase in the maximum temperature or a change in the structure of the entire plant. Increasing the temperature of the working medium at the turbine inlet leads to a higher temperature difference over the cycle and, consequently, an increase in thermodynamic efficiency [47]. This is achieved by using stronger materials in heat exchangers and turbines, allowing for safe operation at higher temperatures. Another method of increasing efficiency is to modify the plant structure. The incorporation of an additional cycle is an illustrative example of the concept, as it results in the establishment of a cascade system. In such a system, the waste heat from the first cycle is utilised as a heat source for the second cycle, which results in a substantial increase in the overall efficiency of the plant [48].

In addition, the implementation of an auxiliary heater has been demonstrated to enhance the temperature of the working medium prior to its expansion within the turbine, thus leading to an enhancement in process efficiency [49].

As in conventional steam turbine systems, the efficiency of ORC cycles can also be increased by using an interstage superheater. Interstage superheating entails heating the medium after partial expansion in the turbine, which enhances the efficiency of subsequent expansion [50]. Moreover, the utilisation of regenerators facilitates the recovery of heat from the working medium following expansion. This process elevates the temperature of the medium prior to its entry into the evaporator, thereby diminishing the heat demand [51,52].

Another modification that has the potential to enhance efficiency is the implementation of a parallel evaporator. This apparatus facilitates the concurrent utilisation of diverse heat sources, each with distinct parameters. Consequently, it enables the optimised alignment of the cycle's properties with the available resources, thereby ensuring enhanced efficiency [53].

In addition to structural changes, efficiency improvements can also be achieved by optimising the operation of individual power plant components such as turbines, compressors, boilers, pumps and electrical generators. The optimisation of turbines and compressors through the utilisation of contemporary materials and precision machining technologies has been demonstrated to reduce mechanical losses and enhance efficiency. Improvements to heat exchangers, such as boilers and evaporators, can increase the efficiency of heat transfer. Moreover, modern electric generators with higher efficiency allow for better conversion of mechanical energy into electricity.

Nevertheless, despite these advances, a significant disparity in efficiency persists between ORC systems and conventional steam or gas cycles. Consequently, there is an ongoing focus on research endeavours aimed at enhancing the efficiency of ORC power plants. A pivotal advancement is the augmentation of working fluid parameters, including temperature and pressure. New working fluids with higher thermal stability can enable operation at higher temperatures, which would significantly increase cycle efficiency. Concepts such as Kalina cycles and supercritical ORCs represent promising research directions, as they offer the potential to achieve higher efficiencies by better matching the properties of the working fluid with the available heat sources [54,55].

The development of ORC microturbine design focuses both on enhancing flow efficiency and minimising losses, as well as ensuring operational reliability. Of particular importance are sealing solutions aimed at reducing working fluid leakage. In addition to conventional labyrinth seals, honeycomb-type seals have been investigated, which effectively reduce leakage flows but require advanced manufacturing technology and may introduce additional frictional losses [56]. In parallel, experimental studies of microturbogenerators have demonstrated the existence of optimal heat source power and generator load values at which maximum electrical output can be achieved [57].

Another crucial direction of development is the implementation of advanced diagnostic and condition monitoring systems. Fibre Bragg Grating (FBG) optical sensors enable leakage detection and temperature monitoring of critical microturbine components [58], while artificial intelligence algorithms, such as Bayesian-optimised Long Short-Term Memory (LSTM) networks, allow rapid identification of sensor malfunctions, thereby improving the safety and reliability of ORC systems [59].

As previously stated, the implementation of supercritical parameters has been demonstrated to enhance the efficiency of ORC cycles. However, it has been demonstrated that replacing adiabatic expansion with isothermal expansion can lead to an enhancement in efficiency of up to ten percentage points (see Fig. 8) [47,60].

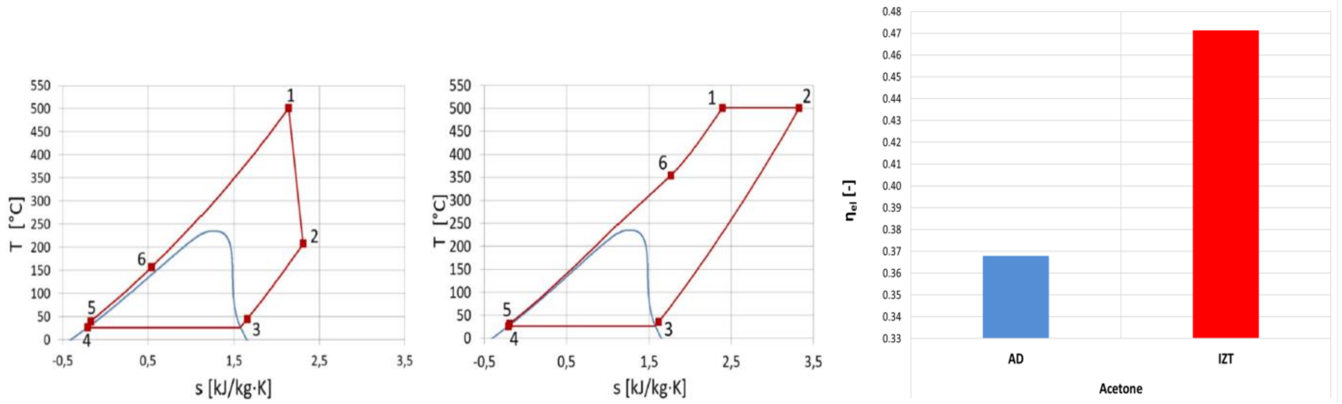

a) b) c)

Fig. 8. Thermodynamic cycle of the ORC power plant with acetone as a working medium: (a) adiabatic expansion in the turbine, (b) isothermal expansion in the turbine, (c) comparison of electrical efficiency (AD – adiabatic expansion, IZT - isothermal expansion).

Moreover, endeavours are currently being undertaken to engineer more robust materials for heat exchangers and turbines that have the capacity to function at elevated pressures. This development has the potential to enhance efficiency.

This section of the paper provides a comprehensive overview of the current state of ORC technology. It places particular emphasis on the operating medium, temperature and pressure levels, as well as the specifics of each application, which are primarily influenced by the heat source. The investigation identified the type of working medium and the turbine as two key aspects of ORC technology. A comprehensive literature review has identified numerous studies addressing working fluids, underscoring their various limitations. The emphasis placed on design solutions by designers and constructors is notable for its simplicity, with axial or radial single-stage turbines being of particular interest. These turbines are characterised by their relatively high efficiency, durability and cost-effectiveness. However, it should be noted here that each case should be treated individually in the design of an ORC micro-turbine, depending on the operating parameters, heat source, intended use and other technological aspects. The primary technological characteristics of ORC solutions were enumerated, and a comparison with the conventional steam cycle demonstrated that ORC systems were more appropriate for low-power (microturbines) and low-temperature applications. The subsequent chapter will address gas microturbines, which are also undergoing development.

4. Gas microturbines

Various configurations of gas microturbine systems have been documented in the existing literature. In the majority of cases, two distinct microturbine power plant schemes are employed: an open cycle scheme (Fig. 9a) and a closed cycle scheme (Fig. 9b). The majority of systems incorporate a recuperator, the function of which is to recover a portion of the exhaust heat. This heat is then utilised to preheat the combustion air (see Figs. 9c and 9d). As demonstrated in Fig. 9c, the air is compressed in the compression section, subsequently mixed with fuel, and then burned to generate power for the turbine section [61].

Gas microturbines are typically fuelled with natural gas, with a generation capacity ranging from 25 kW to 500 kW of electricity. The rotational speed of these engines is notably high, ranging from 50 000 rpm to 120 000 rpm, and occasionally exceeding 100 000 rpm. Their thermal efficiency, ranging from 20% to 30% without regeneration, is considered acceptable. However, with regeneration, the efficiency can be further enhanced. The provision of a diverse energy source within a specific region is facilitated by this mechanism. Gas microturbines are advantageous due to their compact size and relatively low investment cost. Furthermore, the emission levels exhibited during operation are minimal. It is evident that they serve to minimise the ecological impact of substantial transmission and distribution systems. In the contemporary business environment, a significant number of companies are engaged in extensive research and development initiatives related to the construction of gas microturbines. The primary objective of these endeavours is to enhance the efficiency, reliability and durability of these devices, while concurrently reducing their overall cost. The primary objective of these activities is to enhance the effective efficiency, whilst concomitantly reducing NO_x emissions, extending the time between successive overhauls beyond 45 000 hours, and minimising investment costs to below 500 USD/kW. Another issue that must be addressed is the necessity for greater flexibility with regard to the type of fuel utilised. This would entail the use of different fuels for the same turbine, with a particular emphasis on the use of biofuel.

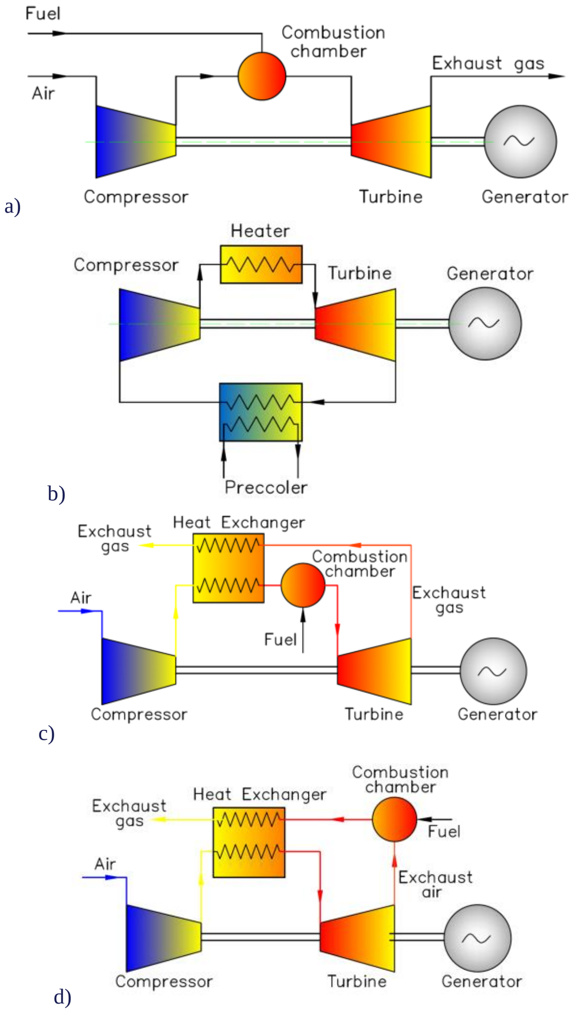

Fig. 9. Open cycle (a) and closed cycle (b) gas microturbine plant. Single shaft open cycle gas microturbines with a heat exchanger and a classical (c) or external (d) combustion chamber.

The majority of manufacturers are adopting a single-shaft design, whereby the compressor, turbine, and permanent-magnet generator are mounted on a single shaft supported by lubrication-free air bearings. These turbines are capable of operating at speeds of up to 120 000 rpm and are powered by natural gas, gasoline, diesel, and alcohol. The dual shaft design incorporates a power turbine and gear for mechanical drive applications and operates up to a speed of 40 000 rpm. The compact and lightweight design of microturbines renders them a viable option for a wide range of light commercial and industrial applications [62].

In industrial practice, gas microturbines (GMTs) are increasingly employed as prime movers in combined heat and power (CHP) systems, simultaneously generating electricity and heat with overall efficiencies of 80–90%. Their advantages include fuel flexibility—from natural gas to biogas—and very low exhaust emissions. Feasibility studies, such as those conducted for industrial laundries, confirm the high economic viability of GMT-based installations as well as significant primary energy savings [63].

As previously stated, a salient benefit of gas microturbines is their capacity to operate on a range of fuels e.g. natural gas, biogas, sewage gas, waste gas, stack gas, gas produced as products of carbon gasification or pyrolysis processes, biofuel, diesel fuel, gasoline, heating oil, methanol, ethanol, propane, hydrogen, etc. Microturbines produce thermal output at a temperature range between 200°C to 350°C, suitable for supplying various thermal needs. Their life time is estimated in the range of 40 000 to 80 000 hours. To date, these units have exhibited adequate reliability. However, not enough time has passed for them to be included in commercial services. As a result, providing data on their entire lifetime is currently unfeasible. Microturbine sets can be connected in parallel to support larger loads and improve power reliability. Reducing the output power of microturbines leads to lower mass flow and combustion temperature; consequently, the efficiency at part load may drop below the design value. Single-shaft gas microturbines with air bearings do not require lubricating oil or water, resulting in lower maintenance costs compared to conventional gas turbines. Microturbines that use lubricating oil do not need frequent oil changes because the oil is kept separate from the combustion products [64].

A distributed power generation system covers a variety of generating technologies, and in addition to microturbines, it includes fuel cells, wind turbines, photovoltaic cells, Stirling engines and internal combustion engines. The main advantages of a distributed power generation system are reducing transmission losses, distributing costs, ensuring higher reliability (especially in smaller systems), and potentially achieving greater overall efficiency by utilising waste heat for cogeneration. While the potential market for microturbines remains uncertain, propane-fueled microturbines offer significant advantages. Propane is often the preferred fuel in several situations, such as when natural gas is not available, when propane is more affordable than natural gas, or when a backup fuel source is needed for greater reliability, especially in conjunction with natural gas or diesel [65,66].

Modern gas microturbines are expected to demonstrate a set of advanced features, including reduced emission levels achieved through water or steam injection as well as dry low-emission combustion technologies [67], along with high fuel flexibility enabled by new combustion and fuel systems supported by advanced coatings [68]. Their operation should also ensure improved reliability and availability through extended component lifetimes, intelligent control, and condition monitoring systems, while maintaining higher overall efficiency and enhanced efficiencies of individual components resulting from tighter tolerances and advanced aerodynamic designs. Furthermore, progress is associated with higher firing temperatures, approaching the limits of material effectiveness [69], and the introduction of novel technological solutions such as recuperated cycles (Fig. 9c, [69]), intercooled recuperated cycles [70], integration with high-temperature fuel cells (solid oxide or molten carbonate), power plants equipped with Heat Recovery Steam Generators (HRSG) [71,72], wet cycles [6,70], combined heat and power systems, and photovoltaic integration [73]. At the same time, further developments are expected to reduce costs, increase power density through higher firing temperatures and innovative component designs based on advanced materials such as ceramics [74], and enable more compact turbomachinery with lower component costs resulting from more highly loaded elements.

The advanced cycle is a regenerative Closed Brayton Cycle (CBC) as presented in a paper [73]. The working fluid is a mixture of helium and xenon. The main components of the cycle are: the receiver, which has to collect solar energy, to store it in a phase-change eutectic salt ($LiF–CaF_2$) and to transfer it to the working fluid, the cooler, which refrigerates the working fluid and ejects the low temperature heat into space via the radiator device; the radial turbomachinery, consisting of the compressor, expander and electrical generator, all assembled on a single rotating shaft, and the recuperator, which recovers the exhaust heat from the expander outlet and transfers it to the compressed air.

Another example is the DynaJet 2.6 portable gas turbine generator, which has a rated output of 2.6 kVA and is shown in Fig. 10.

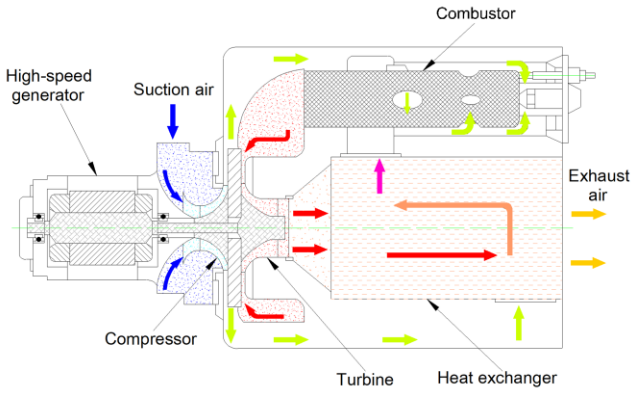

Fig. 10. Schematic diagram of DynaJet 2.6.

The unit is powered by a single-shaft regenerative gas turbine engine. It features a permanent magnet system for the generator, which requires effective cooling to ensure optimal performance at high speeds. The rated rotational speed is 100 000 rpm, and the rated power output is 100 V / 2,6 kVA. The device can operate at a frequency of either 50 Hz or 60 Hz, with the option to switch between these settings. It uses kerosene as fuel, with a consumption rate of less than 4.5 litres per hour at the rated output. The generator operates reliably within a temperature range of 20°C to 50°C. Its dimensions are 825 mm (length), 420 mm (width), and 455 mm (height). Small gas turbines with a power rating of 100 kW or less are attractive not only as distributed power generation systems or for mobile power supply, but also as the core of a combined heat and power system due to the excellent quality of the exhaust gas [75].

Another type of gas turbine is the wave rotor system (Fig. 11). Wave rotors do not use mechanical components such as pistons or blade cascades to compress the fluid. Instead, the pressure increase is achieved by generating compression waves in appropriately designed geometries. It has been proven that, for the same inlet and outlet conditions, wave rotors can significantly enhance performance. The essential feature of wave rotors is an array of channels arranged around the axis of a cylindrical drum. The drum rotates between two end plates, each with several ports or manifolds that control the fluid flow through the channels [76].

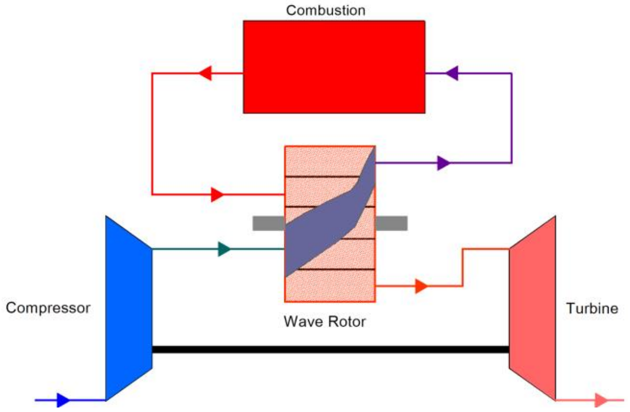

Fig. 11. Schematic diagram of a gas turbine topped by a four-port wave rotor.

The next example is a single-stage axial microturbine. It has been developed with a rotor diameter of 10 mm, see Fig. 12. The turbine is made from stainless steel using die-sinking electro-discharge machining. It has been tested for speeds up to 160 000 rpm and generates a maximum mechanical power of 28 W with an efficiency of 18% [77,78].

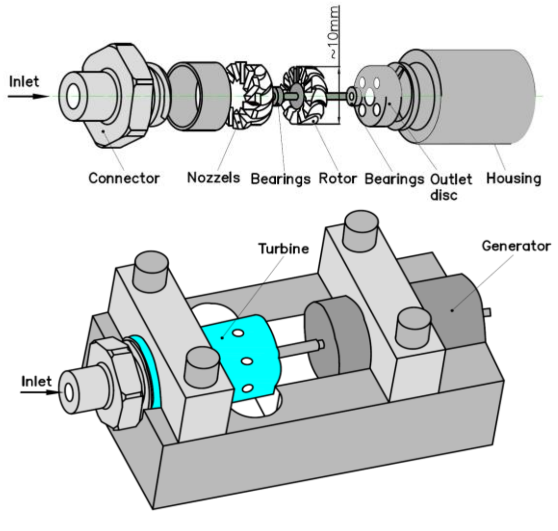

Fig. 12. Single-stage axial microturbine.

In contrast, a groundbreaking solution for a gas microturbine with isothermal expansion can be found in the paper [79] (see Fig. 13). In the proposed solution, the working medium, after isothermal expansion in the nozzles, is transferred to a guide system that provides the correct flow angle to the rotor blades. The rotor of the turbine is shown in Fig. 13a, the compressor in Fig. 13b, and the whole stand is illustrated in Fig. 13c.


a) b) c)

Fig. 13. Isothermal microturbine rotor (a), casing (b) and test rig (c).

The experimental rig consists of the combustion chamber, turbine, compressor, electric generator and regenerator. A large number of tests have been carried out on the operation with various changes and modifications. The test rig is equipped with sensors that measure the temperature and pressure of the working fluid at characteristic points of the unit (at the inlet and outlet of each component), the air flow rate, the rotor speed and the parameters of the electricity generated. The nominal power of the turbine was approximately 5.3 kW, and the rotational speed was 27 000 rpm. It is likely that there will be commercial offers for this type of microturbine set in the near future, as it is the solution with the highest achievable efficiency.

Gas turbines and turbojets are widely used in aviation. Micro jet turbines, on the other hand, have been used in modelling for many years. In these systems, they are small in size and the main parameters are: thrust of several hundred Newtons, temperatures behind the combustion chamber reaching up to 700°C, high revolutions exceeding 100 000 rpm. Table 2 shows examples of micro jet turbines and the operating parameters [80–83].

Microturbines are also used in air-conditioning systems in aircraft – Air Cycle Machine (ACM). ACM systems are the cooling units in the on-board atmosphere control system used in airtight aircraft cabins. Typically, aircraft have two or three ACM

Table 2. Parameters of exemplary airborne microturbines.

No.	Name	Thrust	Temperature, °C	Mass, kg	Diameter, mm	Length, mm	Mass flow, kg/s	Rotational speed, rpm	Compression
1	AMT Olympus	230 N	-	2.475	130	267	0.45	108000	4
2	KH-66	75 N	-	0.93	112	230	0.23	115000	2.2
3	Wren MW54	54 N	-	0.8	87	150	0.18	160000	2.3
4	JF-50 Bee Titanium	63 N	700	0.8	110	170	0.2	180000	2.3
5	JF-160 Rhino	35 lbs	650	1.5	110	300	0.52	116000	-
6	JF-120 SuperEagle	30 lbs	700	1.35	110	300	0.34	128000	2.37
7	Merlin JG-100	27.5 lbs	640	1.25	108	230	0.139	126000	2.37
8	Merlin KJ-66	92 N	590	-	108	230	0.154	128000	1.56
9	Merlin 160G	160 N	550–680	1.45	111	300	0.38	116000	3.2
10	GTM-70	80 N	600	1.2	115	300	-	120000	-
11	FD3 Schreckling	30 N	~700	0.75	-	-	0.16	-	1.5
12	Kamps	50 N	~650	1.14	-	-	0.166	-	2
13	T250P JPX	59 N	~740	1.55	-	-	0.177	-	2.15
14	JF-100 Falcon	22 lbs	650	1.4	98	300	0.27	122000	-
15	JF-50 Bee Tornado	25 N	565	0.4	58	132	0.2	200000	-

units. The cooling process uses air instead of freon in a gas cycle. There is no condensation or evaporation of the working medium in the cycle, the cooled air is used directly to cool the aircraft cabins. The microturbines in these systems run on gas bearings at speeds of 30 000−50 000 rpm [84].

Gas microturbines are increasingly recognised as a key component of modern energy systems, both in industrial applications and in specialised fields such as micro- and nanosatellites. Their design combines compact dimensions with the capability to operate in high-efficiency combined heat and power (CHP) systems as well as in applications requiring high precision and reliability. For space microengines, one of the fundamental design challenges is the modelling of flows in micronozzles and microchannels. The influence of the boundary layer, both laminar and turbulent, on velocity distribution and pressure losses is so significant that dedicated numerical and experimental models are required to design engines capable of delivering thrust in the order of milli-Newtons [85].

Small power turbines can also be found in various means of transport. Rolls-Royce manufactures turbines that have been used to power many small aircraft and helicopters for many years, such as the Bell helicopter. This turbine produces a power output of 533 kW. More than 29 000 units of this turbine have been installed since production began [86].

An older model of the Rolls-Royce 250 turbine was used to power Marine Turbine Technologies (MTT) motorbikes. Installing such a turbine allowed a top speed of around 400 km/h and acceleration from 0 to 320 km/h in around 15 seconds. The turbine produces 286 hp (≈213.4 kW) at 52 000 rpm [87].

Capstone, a company known primarily for its turbines for distributed heat and power generation, was awarded the contract in early April 2008 to manufacture 150 C30 turbines to power buses. The lightweight and robust buses, made mainly of aluminium, will be driven using the energy contained in the batteries; the turbine will only be used to recharge the batteries [88].

Volvo Aero, in turn, also developed a series of microturbines for use in cars, trucks and buses. Between 1988 and 1987, it developed a twin-shaft ceramic microturbine for cars of the KTT MK II/GT110 type with a power output of 115 kW. Later, it produced the new VT40 single-shaft microturbines for cars and the VT100 microturbines for trucks and buses [89].

Jaguar unveiled a prototype of the new Jaguar C-x75 car at the 2010 Paris Motor Show. It is a design that combines gas turbine engine technology with modern electric drive to create a hybrid car. The car has two gas microturbines with 97 hp (≈72.4 kW) each. These are used to drive the generators that charge the battery bank, which drives four electric motors with a total output of 800 hp (≈596.8 KW). The car is able to achieve acceleration in less than 14 s to 300 km/h. The range of this car on a full battery is 90 km, and with turbocharging 900 km can be driven on a full tank. The use of virtually any liquid fuel, gaseous fuel, biofuel, hydrogen, etc. opens a wide door to a new trend in motoring. The Jaguar C-X75 promised to be great, but never went into production [90].

Turbine drive of rotary tools is a relatively recent development and not widely used. In industry, microturbines can be found with powers from 1 to 5 kW, for driving precision tools. They are used as power sources in high-speed grinding spindles, drills, in measuring, control and research apparatus (gyroscopes, mirrors and rotating prisms of laser optical systems, high-speed camera drives, etc.), as expansion turbines in air-conditioning and refrigeration systems and as medical tools (dental and surgical drills). These microturbines operate at relatively low power and high frequencies, so their development has undoubtedly been influenced by the fact that they have mastered the problems of gas bearing to achieve very high frequencies (up to 30 000 Hz and even more). These microturbines are usually powered by compressed air with a pressure of 0.4 to 0.8 MPa and a temperature of about 20°C, drawn from [64].

Medical drills, especially dental drills, were introduced into practice because of the discomfort experienced by patients when preparing hard dental tissue with low-speed drills. The first compressed-air-driven turbine had rolling bearings. Since the mid-1960s, air-bearing drills with a maximum speed of approximately 500 000 rpm have been introduced. These drills are much quieter, and the drill bit is not stimulated to vibrate by the bearing balls. They also do not require oil lubrication and are very durable. Due to these advantages, numerous companies have started to introduce air bearing in the dental drills they manufacture [91,92].

Nowadays, many companies offer, for example, micro turbine tools for precision engraving work based on dental-type turbine cartridges. They offer a low power output of 30–60 W at speeds of up to 400 000 rpm. Thanks to this high speed, the “floating” effect of the cutter tip (torque effect) is minimised [93,94].

Turbine grinders and polishers are another example of the use of microturbines. A turbine grinder offers double the power compared to motorised angle grinders. They are about half the size and weight of motorised tools, offering comparable power. The turbine motor is more efficient than a conventional grinder motor. As a result, it takes less time to do the same amount of work. The overall air consumption is also lower during a specific task. The GTG21 turbine grinder reaches a maximum speed of 12 000 rpm with a power output of 2.1 kW and an air consumption of 30 l/s. The GTG40 turbine grinder, on the other hand, reaches a maximum speed of 8 500 rpm at 4.5 kW and air consumption of 60 l/s. The turbine motor used in these grinders does not need oil in the air for lubrication [95].

Another example of a turbine-driven machine (single-stage axial turbine) with special gas bearings for up to 100 000 rpm and a cutting capacity of up to 100 kW is the TurboTool™ cutting tool [96].

Another way in which microturbines are used are air motors with outputs ranging from 0,1 kW to 35 kW. They have found wide use in industry as a powerful and trouble-free drive motor. They are smoothly controllable over a very wide speed range and provide high starting torque. They can operate at pressures from 2 to 7 bar. The speed of such a motor varies between 2 500 and 7 600 revolutions per minute [97].

A typical microturbine consists of a shaft, on which a generator, a compressor and a turbine are mounted. The turbine shaft rotates at 50 000–100 000 rpm, which corresponds to electrical frequencies ~833–1667 Hz. This power has to be rectified and re-inverted to electrical energy at 50/60 Hz for interfacing with grid power. Rectifiers and inverters are usually very energy efficient but are highly nonlinear, which can negatively affect the system [98–101].

The microturbine control system represents a key problem for stable operation at different working conditions, ensuring a flexible usage of the machine. The experience gained in large-size turbine control systems can also be profitably exploited in the microturbine field, but the time scales of the phenomena are extremely reduced due to the small mechanical inertia of the shafts, which makes microturbines difficult systems to control [102].

Another important development area involves the integration of microturbines with microgrids and hybrid systems. This requires advanced solutions for protection, synchronisation, and control, including adaptive algorithms and diagnostic systems supported by artificial intelligence [103]. In parallel, intensive research is being carried out on the utilisation of alternative fuels, with hydrogen emerging as a particularly promising clean energy carrier for cogeneration and trigeneration systems [104]. These advancements highlight the potential of gas microturbines as a flexible and low-emission technology supporting the transition towards decentralised and sustainable energy systems of the future.

During the last years, we have observed an increasing interest in small nuclear power stations in different countries around the world [105]. It concerns the construction of so-called minireactors (or microreaktors), which are foreseen for energy supplying for houses or military uses. An example is a 200 kW microreactor built in Japan by Japan Atomic Energy Research Institute, which is cooled with liquid sodium. The most interesting thing is that the fuel should be changed every 10 years [106].

The literature analysis of micro gas turbines carried out in this chapter showed that there has been a tremendous development of this technology in the last two decades, and a large variety of proposed designs have emerged. This is due to the very different applications of this type of device. Designers' approaches are focused on improving efficiency, durability, reliability and, of course, low price. The next chapter presents a completely different type of microturbine design solution, namely the adhesion microturbine pioneered by the eminent inventor Nikola Tesla. Devices of this type have been classified in a separate chapter because they can operate as steam microturbines, including those for organic refrigerant vapours, and as gas microturbines.

5. Tesla microturbines

The first adhesion turbine, also known as the Tesla turbine, was designed, built and patented [107] by prominent inventor Nikola Tesla in 1913 (Fig. 14). It was an innovative type of bladeless turbine that operated on a completely different principle to traditional blade turbines.

The operating principle of this type of turbine is based on the phenomena of adhesion and friction, which primarily occur within the boundary layer of fluid between two closely spaced rotating discs. The fluid moves in a spiral pattern through the narrow gap between the discs, travelling from the outer diameter towards the inner diameter. As it flows, the fluid transfers a portion of its kinetic energy to the discs, causing them to rotate. The turbine is powered by one or more inlet nozzles positioned at the outer edge of the discs, directing the working fluid into the gap. The fluid then exits through openings located near the central shaft of the turbine. The distance between the turbine discs is typically very small and is determined by the thickness of the boundary layer.

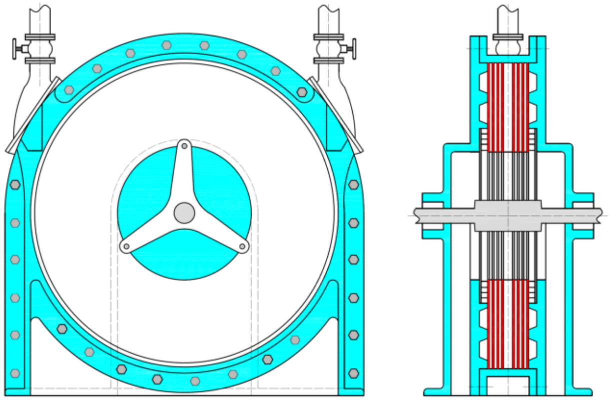

Fig. 14. A view of the Tesla turbine.

Tests conducted by Tesla on real adhesive turbines demonstrated that, as the diameter of the discs increased (and with it the power output, reaching up to 150 kW), structural damage could occur due to material deformation. It is important to note that during the time these experiments were performed, the technology for manufacturing and processing materials capable of withstanding high temperatures and high rotational speeds was limited. Despite the promise of his innovative approach, these material constraints hindered further progress. Tesla's financial situation had deteriorated significantly, and without sufficient resources, he was unable to continue developing and refining the turbine. Ultimately, the combination of material limitations and the absence of financial backing forced Tesla to abandon the project [108,109]. Although he had successfully patented the design and demonstrated its potential in laboratory tests, the adhesive turbine never reached commercial viability in Tesla's lifetime. Nevertheless, his work laid the foundation for future research into bladeless turbines and remains a source of inspiration for engineers and scientists exploring alternative methods of fluid dynamics and energy conversion.

For many years, Tesla’s innovative turbine design was largely overlooked, as the scientific community and industry favoured more conventional technologies like traditional bladed turbines and reciprocating engines. However, by the mid-20th century, there was a renewed interest in alternative turbine designs as researchers sought more efficient and simpler mechanical solutions for energy conversion. It was not until the 1950s that scientists began to revisit Tesla’s ideas, recognising the potential advantages of his bladeless turbine concept, particularly its simplified construction and reduced number of moving parts. One of the pioneers in this research was Armstrong, who in 1952 built his own turbine model. The device was steam-powered and based on the Rankine cycle. Armstrong introduced an innovation by using discs of varying thickness, which increased the rotor's strength and reduced fluid turbulence. Thanks to these modifications, an efficiency of a few per cent was achieved at speeds between 4 000 and 6 000 revolutions per minute [110].

In 1965, Warren Rice, building on Tesla's design, constructed six models that he tested using air as the working fluid. The efficiencies he achieved ranged from 36% to 41%. Using the research results and mathematical analysis, he developed a design relationship between the disc radius and the spacing between them, which allowed the turbines to achieve maximum efficiency at different flow rates. In his conclusions, he noted that Tesla's turbine could be suitable for low-power applications, particularly in situations where low production costs are crucial or where the properties of the working fluid make the use of conventional turbines impractical [111].

In 1966, Beans developed a turbine powered by compressed air. He tested his system for various values of angular velocity, inlet pressure and disc spacing, obtaining efficiencies ranging from 7% to 25% [112]. Although the efficiency values were significantly lower compared to those achieved by Warren Rice, Beans' work provided valuable information on the effects of various operating parameters on turbine performance. By varying the angular velocity, Beans was able to determine the optimum operating speeds for different configurations, highlighting the importance of precise speed control to increase efficiency [113,114].

The reported experimental efficiency of Tesla microturbines in the literature varies considerably, for example:

- 32% efficiency for a turbine with a power output of approximately 3 kW and a rotor speed of 15 000 rpm [115],
- 23% efficiency for a turbine with a power output of approximately 1.5 kW and a rotor speed of 12 000 rpm [116],
- 21% efficiency for a turbine with a power output of approximately 50 W and a rotor speed of 1 000 rpm [33],
- 49% efficiency for a turbine with a power output of approximately 1.56 kW and a rotor speed of 12 000 rpm [112].

For example, the numerical calculations resulted in an efficiency of about 50% obtained for an 11-stage turbine with an output power of about 2 kW at a rotor speed of 18 000 rpm [117].

Tesla's turbine continues to attract significant interest, as evidenced by numerous publications analysing the turbine both theoretically and practically. As demonstrated by the work of Thomazoni et al. [118], the number of publications related to Tesla's turbine has increased significantly in the 21st century. Of these, approximately 36% are analytical studies, 31% are analyses using CFD, 31% are experimental studies, and the remaining 2% are review papers. For example, in the works of Guha and Smiley [119] and Sengupta and Guha [120], similar to Beans, Tesla's turbine was tested by varying selected design parameters. The best configuration solution generated 140 W with an efficiency of about 25%. Modifications to the inlet nozzles were also investigated, which reduced pressure losses and improved efficiency by about 1 percentage point.

In 2015, Krishnan [121], in his qualification work, presented a series of guidelines for the design and construction of Tesla microturbines. The work contains a wealth of valuable data, analyses, and results of experimental studies related to Tesla's turbine and its potential applications. For example, the author determined the minimum radius-to-disc spacing ratio as 20.

Theoretical works employing CFD consider various aspects of designing Tesla-type turbine devices [122]. The efficiency of a Tesla turbine is influenced by both the working fluid parameters (pressure, temperature, inlet velocity) and its kinematics at the inlet and outlet, as well as geometric parameters (distance between rotor discs, diameter, thickness, and number of discs, roughness and micro-topography of their surfaces), rotor rotational speed, and mass flow rate. In the case of mass flow rate, there is a direct influence, namely, the greater the flow, the greater the output power [123]. Similarly, for the initial pressure, analyses have shown that an increase in pressure before the turbine increases efficiency [124]. For example, an increase in pressure by about 1 bar results in an increase in efficiency of about 5% [118].

Regarding the influence of temperature on the efficiency and power of a Tesla turbine, researchers' findings are divided. Publication [125] states that both power and efficiency increase with increasing inlet temperature, while publication [126] demonstrates the ambiguity of the influence of increasing temperature on output power. As in other works, including this one, there are no clear statements regarding the effect of the number and shape of inlet nozzles on turbine efficiency and power, and research in this area is still being developed [127].

In most published cases, the rotational speeds of Tesla turbine rotors are lower than those of bladed turbines [118]. Analyses can be found that define the output power and efficiency of a Tesla turbine as a non-linear function of rotational speed, approximately a second-order polynomial, for a fixed geometry and inlet conditions [128].

The outer diameter of the rotor affects both efficiency and output power. Most studies indicate an increase in turbine output power with an increase in the outer diameter of the rotor. According to some authors, there is an optimal value of the ratio of the outer to inner diameter of the rotor that maximises efficiency [129].

In the case of discs in a Tesla turbine, there is also no consensus among authors. Some argue that there is an optimal number of discs and their thickness that gives the maximum efficiency [130]. Other authors show that the fewer discs, the higher the efficiency [129], while still others argue that efficiency increases with the number of discs [131].

It is quite common to believe that bladed turbines are unrivalled compared to Tesla-type turbines in the range of higher powers, but at very low powers, one can expect a certain advantage of bladeless adhesive turbines [132].

For example, an analytical model incorporating wall roughness through the equivalent sand grain approach was proposed by Rusin et al. [133]. The model modifies dynamic viscosity in the governing equations, allowing the impact of roughness on velocity profiles and turbine efficiency to be assessed. Their results indicate that a surface roughness height of 10^{-5} m can noticeably improve both power output and isentropic efficiency.

In a complementary approach, Pahlavanzadeh et al. [134] introduced a porous layer model (PLM) for directly simulating roughness effects in the gap between rotating disks. This method eliminates the need for equivalent sand grain parameters and was validated against experimental data from minichannel flows. The study demonstrated that increasing surface roughness enhances the interaction between the working fluid and the rotor, thereby influencing overall turbine efficiency.

Similarly, there is no clear consensus on the influence of the number and shape of inlet nozzles on turbine performance. Research in this area is still ongoing [135].

Also worth noting is the growing interest in integrating Tesla turbines with low-temperature heat recovery technologies. A recent study by Teng et al. [136] presents a comprehensive experimental investigation of a Tesla microturbine integrated into an ORC system for low-grade heat recovery (90−130°C). The authors developed a prototype that achieved a maximum output power of 31.76 W and an isentropic efficiency of up to 62.28%, examining the effects of parameters such as heat source temperature, pump speed, and electrical load on system performance. The results highlight the potential of Tesla turbines as efficient and compact solutions for small-scale distributed energy systems and industrial waste heat recovery.

The concept of turbomachinery miniaturisation typically refers to the design of devices with reduced power output, intended to meet the demands of distributed, portable, or microscale systems. These scaled-down machines are used in applications such as portable electronics, IoT sensors, or microenergy systems. Energy micro-generators rely on piezoelectric, electromagnetic, electrostatic, or triboelectric transduction principles, effectively harvesting energy from low-frequency vibrations or human motion. Their power output is inherently limited and tailored to match their miniature form factor [138].

Huynh et al. [137] introduce a pioneering hybrid energy-harvesting system that combines a triboelectric nanogenerator (TENG) and an electromagnetic generator (EMG), both driven by a Tesla turbine. The optimised system achieves peak outputs of 312.5 V / 82 mA (TENG) and 4.2 V / 3.3 mA (EMG), with the hybrid configuration delivering 332 V / 3.5 mA. As demonstrated in the study, the device shows strong potential for use in wearable and low-power portable applications for biomechanical energy harvesting, as illustrated by practical demonstrations such as LED illumination and wireless sensor operation.

The miniaturisation of energy-conversion turbomachinery remains a significant challenge due to the nonlinear scaling of aerodynamic and mechanical phenomena. When reducing the physical size of rotating machines such as Tesla turbines, micro gas turbines, or centrifugal compressors, researchers must address issues including increased viscous effect and reduced flow uniformity. It is well documented that aerodynamic efficiency decreases at low Reynolds numbers due to boundary layer thickening and the dominant influence of viscosity [139].

Based on a literature review and the authors' own experience, a Tesla microturbine was built within a single enclosed hermetic housing (Fig. 15). The concept is based on a novel solution in which the magnets are placed in the rotating disc of the Tesla turbine. The stationary housing, on the other hand, houses the poles where the electric current is induced. The diameter of the disc is 140 mm, the clearance between the moving and stationary disc is approximately 1 mm, and the inlet nozzle is set at an angle of 12° [140,141].

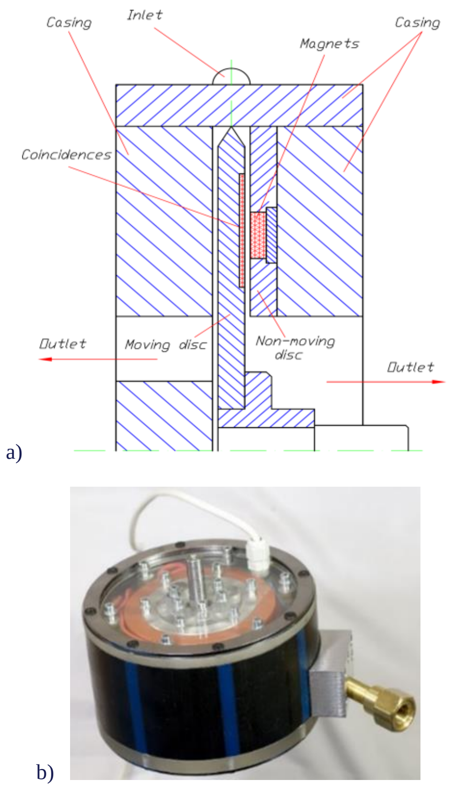

Fig. 15. An overview drawing of the Tesla micro-turbine-generator concept (a); view of the complete disc turbogenerator (b).

The conducted literature analysis has shown that despite the passage of over 100 years since Tesla's invention, work on its development is still ongoing and is certainly not complete. The next supplementary chapter presents examples of steam and gas microturbines made using MEMS technology.

6. Microturbines in MEMS technology

Micro-Electro-Mechanical Systems (MEMS) are miniaturised devices that integrate mechanical and electrical components on a single chip. These systems are fabricated using techniques derived from semiconductor manufacturing, such as photolithography, etching and deposition processes. This technology makes it possible to create devices that typically range in size from a few micrometres to a few millimetres. MEMS devices are extremely small, enabling the creation of compact systems with high functionality. They combine mechanical, electrical, thermal and sometimes optical components into a single system. MEMS devices are designed with nanometre precision and offer exceptional performance in precision applications [142].

Examples of steam microturbines made with MEMS technology are encountered in the literature [143,144]. More on MEMS can be found in publications [145–147], among others. An example of a steam microturbine, implementing the Rankine circuit, made with MEMS technology is presented in Fig. 16.

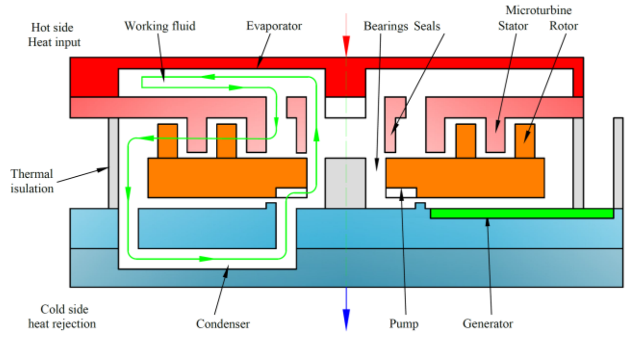

Fig. 16. Cross-section of a steam microturbine power plant on a chip.

The microturbine unit drives a micropump and a power generator and produces electricity with an efficiency of approximately 11%. The basic parameters of the microturbine unit are: steam pressures (inlet/outlet): 0,6/0,18 MPa, steam temperatures (inlet/outlet): 400/316°C, turbine diameters (inlet/outlet): 360/760 mm, blade height: 20−50 mm, steam mass flow rate: 24 mg/s, rotational speed: ~1 000 000 rpm, and the electrical power achieved 5 W.

MEMS technology has been effectively applied to micro gas turbines, resulting in the development of devices with dimensions measured in millimetres, power outputs ranging from 10 to 500 W, and compression ratios between 2:1 and 4:1. These microturbines have been developed alongside semiconductor technology and require exceptional precision during their manufacturing. Their power concentration factor of 33 kWh/kg is more than 20 times higher than that of lithium batteries, which have a density of 1.4 kWh/kg [148]. Microturbines represent a notable application of MEMS technology [149]. One specific example of a gas microturbine built using MEMS technology is the wafer genset, illustrated in Fig. 17.

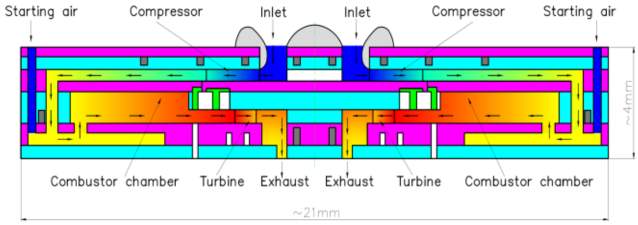

Fig. 17. General view of a wafer microturbine.

This device features a compressor with a diameter of 4 mm and a microturbine with a diameter of 21 mm, while the blade length measures 200 μm. The compressor achieves a tip velocity of 500 meters per second at a rotational speed of 1 million revolutions per minute, with an airflow rate of 0,3 milligrams per second. The blade angle, denoted as α_1, varies between 15° and 20°. The temperature after the combustion chamber reaches 1600 K, and the power density of the combustor chamber is 3 GW/m^3, significantly surpassing the typical value of approximately 2 GW/m^3 for classical turbines. The radial clearance is around 2 μm, and the cost ranges from 1 000 to 5 000 USD per kilowatt [150]. These parameters underline the remarkable capabilities and efficiency of MEMS-based micro gas turbines.

The economic impact of these devices will be dependent on the performance levels and the manufacturing costs, both of which have yet to be proven. It is certainly possible, however, that MEMS gas turbines may one day be competitive with conventional machines in a cost per installed kilowatt. Even at much higher costs, they will be very useful as compact power sources for portable electronics, equipment, and small vehicles [148]. Figure 18 presents the concept of MEMS gas microturbine engine packaged as a standard military battery. The other advantages of miniaturisation is shortening the time needed for acquiring the information on system behaviour, as well as decreasing the amount of required materials and energy for the manufacturing process.

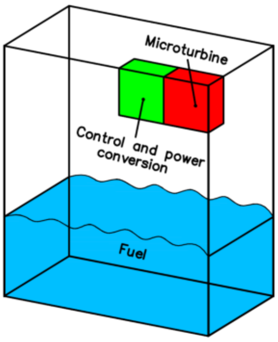

Fig. 18. Concept of MEMS gas microturbine engine packaged as a standard military battery.

Work on this type of device is also being developed, and it seems that in the future it could be used as an autonomous energy source for electronic equipment or small vehicles.

7. Summary

Modern power generation is increasingly focused on moving away from centralised power generation towards distributed systems. Microturbines, whether steam, gas or ORC, are the answer to the growing demand for local, flexible and renewable energy sources. They are a key component of prosumer micro-installations, cogeneration systems and small-scale energy networks (microgrids). Microturbines are extremely diverse in design, power range and application. They can be:

- steam turbines ranging from a dozen watts to hundreds of kilowatts,
- gas-fired microturbines with or without heat recovery,
- turbines in ORC systems to recover waste heat,
- Tesla bladeless turbines, simplified in design,
- MEMS turbines, which function as miniature energy sources, e.g. for portable electronics.

This differentiation allows the solution to be tailored to the specific application, from powering a laptop to recovering heat from a cement plant to driving a turbocharger or micro-generator.

These devices allow energy to be produced close to the point of consumption, minimising transmission losses and increasing supply reliability. Steam and gas microturbine design issues began to develop at the beginning of this century. Technological solutions, although using well-established knowledge of high-power turbines, are at an early stage of development. This requires the integration of knowledge from a number of disciplines, such as:

- thermodynamics (optimisation of thermal cycles),
- fluid mechanics (design of flow systems),
- strength of materials (use of ceramics, aluminium alloys, composites),
- mechatronics and electronics (control systems, energy conversion and storage),
- microengineering (manufacture of MEMS turbines).

The advances concern not only the turbine itself, but entire energy systems including generators, heat exchangers, bearings, gearboxes and cooling systems. Microturbines are part of the green energy transition because they can be:

- powered by biomass, biogas, hydrogen, alcohol, synthesis gas,
- used for waste heat recovery (in ORC, cogeneration, trigeneration),
- coupled to fuel cells or solar collectors,
- used in zero-emission projects (e.g. hydrogen-oxygen combustion).

They are thus part of the drive to decarbonise energy and improve energy efficiency in various sectors of the economy.

Despite tremendous progress, microturbine development still faces a number of technical barriers, including:

- difficulties in miniaturisation and high temperature resistant materials,
- dynamic stability problems at very high speeds (up to 1 million rpm in MEMS),
- challenges in lubrication and cooling (e.g. oil-free bearings),
- complications in designing very efficient, small heat exchangers,
- the need for precision control systems and power electronics (e.g. for high-frequency generators).

Key research directions in the coming years will be:

- increasing efficiency to > 40%,
- lowering the investment cost below 500 USD/kW,
- development of multi-fuel and zero-emission drives,
- integrated hybrid systems (e.g. microturbine + photovoltaics (PV) + energy storage),
- implementation of advanced materials (ceramics, superalloys).

Microturbines are increasingly used in means of transport (cars, motorbikes, buses, drones, aircraft) as:

- power sources,
- energy recovery systems (e.g. turbochargers),
- direct drives (in hybrids or research models).

In industry, they are used for:

- powering high-speed instruments (e.g. dental turbines),
- powering mobile diagnostic equipment,
- air conditioning and refrigeration (e.g. in aviation).

This shows that microturbines not only produce energy but also increase the efficiency of other technical systems.

The review of existing steam and gas microturbine designs carried out in this article does not provide clear answers as to what direction their development will take. According to the authors, the observed trends in the development of these devices allow the conclusion that they will move towards the construction of more efficient, reliable, and sustainable microturbines, both steam and gas. Analyses have also shown that there is now also a very strong emphasis on emissions, so the development of these devices will also move towards the use of low- or zero-emission fuels, such as hydrogen.

References

[1] Aquaro, D., & Pieve, M. (2007). High temperature heat exchangers for power plants: Performance of advanced metallic recuperators. *Applied Thermal Engineering*, 27(2), 389−400. doi: 10.1016/j.applthermaleng.2006.07.030

[2] Soares, C. (2007). *Microturbines* (1st ed.). Butterworth- Heinemann; Oxford, United Kingdom.

[3] Kolanowski, B.F. (2004). *Guide to Microturbines* (1st ed.). Marcel Dekker, New York, United States.

[4] Epstein, A.H., Senturia, S.D., Al-Midani, O., Anathasuresh, G., Ayon, A., Breuer, K., Chen, K-S., Ehrich, F.E., Esteve, E., Frechette, L., Gauba, G., Ghodssi, R., Groshenry, C., Jacobson, S., Kerrebrock, J.L., Lang, J.H., Lin, C-C., London, A., Lopata, J., Mehra, A., Mur, M.J.O., Nagle, S., Orr, D.J., Piekos, E., Schmidt, M.A., Shirley, G., Spearing, S.M., Tan, C.S., Tzeng, Y-S., & Waitz, I.A. (1997). *Micro-Heat Engines, Gas Turbines, and Rocket Engines - the MIT Microengine Project*. American Institute of Aeronautics and Astronautics Inc., AIAA97-1773.

[5] Epstein, A.H., Senturia, S.D., Anathasuresh, G., Ayon, A., Breuer, K., Chen, K-S., Ehrich, F.E., Gauba, G., Ghodssi, R., Groshenry, C., Jacobson, S., Lang, J.H., Lin, C-C., Mehra, A., Mur, M.J.O., Nagle, S., Orr, D.J., Piekos, E., Schmidt, M.A., Shirley, G., Spearing, S.M., Tan, C.S., Tzeng, Y-S., & Waitz, I.A. (1997). Power MEMS and Microengines. *IEEE Transducers'97 Conference*, 19 June, Chicago, United States.

[6] Kosowski, K. (2001). *Steam and Gas Turbines with the Examples of Alstom Technology*. Alstom: Saint-Quen, France.

[7] Beith, R. (2011). *Small and micro combined heat and power CHP systems*. Woodhead Publishing Limited, Sawston, Cambridge, United Kingdom.

[8] Gailfuß, M. (2003). Private meets Public—Small Scale CHP; Technological Developments, *Workshop BHKW-Infozentrum Rastatt*, 9 Sept., Berlin, Germany.

[9] Pujari, V., Vartabedian, A., Collins, B., & Garrett, J. (2005). Optimization of High Temperature Silicon Nitride for Microturbine Applications. *Proceedings of the 29 th International Conference on Advanced Ceramics and Composites*, January 23−28, Cocoa Beach, Florida, United States.

[10] Breuer, K.S. (2000). *MEMS Sensors for Aerodynamic Measurements - the Good, the Bad and the Ugly*. American Institute of Aeronautics and Astronautics Inc., AIAA00-0251.

[11] Bonnie, S. (2004). Overview of Microturbines Powered by Steam. *Colorado Wind and Distributed Energy Conference Bio-Energy Corporation*, 14 May, Colorado, United States.

[12] Colombo, L.P.M., Armanasco, F., & Perego, O. (2007). Experimentation on a Cogenerative System Based on a Microturbine. *Applied Thermal Engineering*, 27, 705−711. doi: 10.1016/j.applthermaleng.2006.10.005

[13] Kiciński, J., &·Żywica, G. (2014). *Steam Microturbines in Distributed Cogeneration*. Springer Cham Heidelberg New York Dordrecht London, Springer International Publishing Switzerland.

[14] Valencia, H.D. (2005). *Vertical Steam Turbine Generators: Opening a New Market for Energy Recovery Industrial Water Chillers*. Carrier Corporation, Syracuse, New York.

[15] Riggi, A.L. (2014). Mississippi Cooling, Heating, and Power (micro-CHP) and Bio-fuel Center. *Technical report*, United States Department of Energy. doi: 10.2172/1178540

[16] Efimov, N.N., Papin, V.V., & Bezuglov R.V. (2016). Micro Energy Complex Based on Wet-SteamTurbine. *Procedia Engineering*, 150, 324–329. doi: 10.1016/j.proeng.2016.07.022

[17] Sarnacki, W.P., Kimball, R., & Fleck, B. (2007). Development of a Combined Cycle Gas Turbine/Steam plant for Training Marine and Power Engineers. *Proceedings of ASME Turbo Expo 2007 Power and Land, Sea and Air*, 14−17 May, Montreal, Canada.

[18] *Electronic document, home page*. http://www.nestco1.com/ index.htm [accessed 27 Dec. 2011].

[19] Post, J. (2012). *Microturbine System and Method for Generating Electricity*, European Patent, EP 2 203 629 B1.

[20] Peng, N., Wang, E., Wang, W., Lu, J., & Li, M. (2024). Aerodynamic analysis of a 1.5 kW two-stage counter-rotating partial-admission impulse turbine for small-scale power system with a high expansion pressure ratio. *Case Studies in Thermal Engineering*, 53, 103824. doi: 10.1016/j.csite.2023.103824

[21] Paulides, J.J.H., Post, E., Post, J, Encica, L., & Lomonova, E.A. (2015). Green Turbine: A High Speed Double Turbine for Sustainable Energy Harvesting from Waste Heat. *10th International Conference on Ecological Vehicles and Renewable Energies (EVER)*, 31 March – 2 April, Monte-Carlo, Monaco. doi: 10.1109/EVER.2015.7112926

[22] Efimov, N.N., Parshukov, V.I., Oshchepkov, A.S., Ryzhkov, A.V., Rusakevich, I.V., & Blokhin E.E. (2023). Steam plant based on high-speed active microturbine with valve-inductor generator as part of power engineering complex for processing of CURRENT and power plant for hydrogen production, *International Journal of Hydrogen Energy*, 48, 18557–18566. doi: 10.1016/j.ijhydene.2023.01.368.

[23] Mirzaei, M.R., Kasaeian, A., Motlagh, M.S., & Fereidoni, S. (2024). Thermo-economic analysis of an integrated combined heating, cooling, and power unit with dish collector and organic Rankine cycle. *Energy*, 296, 131089. doi: 10.1016/j.energy.2024.131089

[24] Kalair, A.R., Seyedmahmoudian, M., Stojcevski, A., Mekhilef, S., Abas, N., & Koh, K. (2023). Thermal comfort analysis of a trombe wall integrated multi-energy nanogrid building. *Journal of Building Engineering*, 78, 107623. doi: 10.1016/j.jobe.2023.107623

[25] Cano, A., Arévalo, P., Benavides, D., & Jurado, F. (2021). Sustainable tramway, techno-economic analysis and environmental effects in an urban public transport. A comparative study. *Sustainable Energy, Grids and Networks*, 26, 100462. doi: 10.1016/j.segan.2021.100462

[26] *Creating Educational Laboratory Equipment For Tomorrow's Engineer „MiniLab Gas Turbine Power System"*, http://www.turbinetechnologies.com/steam.html [accessed 26 Jan. 2008].

[27] Tartière, T., & Astolfi, M.A. (2017). World Overview of the Organic Rankine Cycle Market. *Energy Procedia*, 129, 2–9. doi: 10.1016/j.egypro.2017.09.159

[28] Quoilin, S., Broek, M., Declaye, S., Dewallef, P., & Lemort, V. (2013). Techno-economic survey of Organic Rankine Cycle (ORC) systems. *Renewable and Sustainable Energy Reviews*, 22, 168–186. doi: 10.1016/j.rser.2013.01.028

[29] Mikielewicz, D., & Mikielewicz, J. (2008). Cogenerative micro power plants − A new direction for development of power engineering? *Archives of Thermodynamics*, 29, 109–132.

[30] Mikielewicz, J., & Mikielewicz, D. (2009). Comparative study of selected fluids for use in supercritical Organic Rankine Cycles. *Archives of Thermodynamics*, 30, 3–15.

[31] Simader, G.R., Krawinkler, R., & Trnka, G. (2006). Micro CHP systems: state-of-the-art. *Final Report, Deliverable 8 (D8) of Green Lodges Project (EIE/04/252/S07.38608)*, Austrian Energy Agency, Vienna, Austria.

[32] Quoilin, S., Declaye, S., Tchanche, B.F., & Lemort, V. (2011). Thermo-economic optimization of waste heat recovery Organic Rankine Cycles. *Applied Thermal Engineering*, 31, 2885−2893. doi: 10.1016/j.applthermaleng.2011.05.014

[33] Lecompte, S., Huisseune, H., Van den Broek, M., Vanslambrouck, B., & DePaepe, M. (2015). Review of organic Rankine cycle (ORC) architectures for waste heat recovery. *Renewable and Sustainable Energy Reviews*, 47, 448–461, doi: 10.1016/j.rser.2015.03.089

[34] Zhao, Y., Liu, G., Li, L., Yang, Q., Tang, B., & Liu, Y. (2019). Expansion devices for organic Rankine cycle (ORC) using in low temperature heat recovery: A review. *Energy Conversion and Management*, 199, 111944. doi: 10.1016/j.enconman.2019.111944

[35] Kermani, M., Wallerand, A.S., Kantor, I.D., & Maréchal, F. (2018). Generic superstructure synthesis of organic Rankine cycles for waste heat recovery in industrial processes. *Applied Energy*, 212, 1203–1225. doi: 10.1016/j.apenergy.2017.12.094

[36] Da Silva, J.A.M., Seifert, V., de Morais, V.O.B., Tsolakis, A., Herreros, J., & Torres, E. (2018). Exergy evaluation and ORC use as an alternative for efficiency improvement in a CI-engine power plant. *Sustainable Energy Technologies and Assessments*, 30, 216–223. doi: 10.1016/j.seta.2018.10.007.

[37] Li, T., Meng, N., Liu, J., Zhu, J., & Kong, X. (2019). Thermodynamic and economic evaluation of the organic Rankine cycle(ORC) and two-stage series organic Rankine cycle (TSORC) for flue gas heat recovery. *Energy Conversion and Management*, 183, 816–829. doi: 10.1016/j.enconman.2018.12.094

[38] Altun, A.F., & Kilic, M. (2020). Thermodynamic performance evaluation of a geothermal ORC power plant. *Renewable Energy*, 148, 261-274. doi: 10.1016/j.renene.2019.12.034

[39] Tartiere, T., & Astolfi, M. (2017). A World Overview of the Organic Rankine Cycle Market. *Energy Procedia*, 129, 2−9. doi: 10.1016/j.egypro.2017.09.159

[40] Piwowarski, M. (2013). Design analysis of ORC microturbines making use of thermal energy of oceans. *Polish Maritime Research*, 20(2), 48−60. doi: 10.2478/pomr-2013-0016

[41] Quoilin, S., & Lemort, V. (2009). Technological and Economical Survey of Organic Rankine Cycle Systems. *Proceedings of the 5-th European Conference Economics and Management of Energy in Industry*, 14−17 April, Vilamoura, Portugal.

[42] Kosowski, K., Piwowarski, M., Stepien, R., & Włodarski, W. (2018). Design and investigations of the ethanol microturbine. *Archives of Thermodynamic*, 39, 41–54. doi: 10.1515/aoter-2018-0011

[43] Landelle, A., Tauveron, N., Haberschill, P., Revellin, R., & Colasson, S. (2017). Organic Rankine cycle design and performance comparison based on experimental database. *Applied Energy*, 204, 1172–1187.

[44] Colonna, P., Nannan, N.R., Guardone, A., & Lemmon E.W. (2006). Multiparameter equations of state for selected siloxanes. *Fluid Phase Equilibria*, 244(2), 193–211. doi: 10.1016/j.fluid.2006.04.015

[45] Tchanche, B.F., Lambrinos, Gr.. Frangoudakis, A., & Papadakis, G. (2011). Low-grade heat conversion into power using organic Rankine cycles – A review of various applications. *Renewable*

and Sustainable Energy Reviews, 15(8), 3963–3979. doi: 10.1016/j.rser.2011.07.024

[46] Stępniak, D., & Piwowarski, M. (2014). Analyzing selection of low-temperature medium for cogeneration micro power plant. *Polish Journal of Environmental Studies*, 23, 1417–1421.

[47] Kosowski, K., & Piwowarski, M. (2020). Subcritical Thermodynamic Cycles with Organic Medium and Isothermal Expansion. *Energies*, 13, 4340. doi: 10.3390/en13174340

[48] Vescovo, R., & Spagnoli, E. (2017). High Temperature ORC Systems. *Energy Procedia*, 129, 82−89. doi: 10.1016/j.egypro.2017.09.160

[49] Piwowarski, M., & Kosowski, K. (2020). Advanced Turbine Cycles with Organic Media. *Energies*, 13, 1327. doi: 10.3390/en13061327

[50] Braimakis, K., & Karellas, S. (2018). Energetic optimization of regenerative Organic Rankine Cycle (ORC) configurations. *Energy Conversion and Management*, 159, 353–370. doi: 10.1016/j.enconman.2017.12.093

[51] Abam, F.I., Ekwe, E.B., Effiom, S.O., Ndukwu, M.C., Briggs, T.A., & Kadurumba, C.H. (2018). Optimum exergetic performance parameters and thermo-sustainability indicators of low-temperature modified organic Rankine cycles (ORCs). *Sustainable Energy Technologies and Assessments*, 30, 91–104. doi: 10.1016/j.seta.2018.09.001

[52] Imran, M., Park, B.S., Kim, H.J., Lee, D.H., Usman, M., & Heo, M. (2014). Thermo-economic optimization of Regenerative Organic Rankine Cycle for waste heat recovery applications. *Energy Conversion and Management*, 87, 107−118. doi: 10.1016/j.enconman.2014.06.091

[53] Li, T., Zhu, J., Hu, K., Kang, Z., & Zhang, W. (2014). Implementation of PDORC (parallel double-evaporator organic Rankine cycle) to enhance power output in oilfield. *Energy*, 68, 680−687. doi: 10.1016/j.energy.2014.03.007

[54] Vetter, Ch., Wiemer, H.-J., & Kuhn, D. (2013). Comparison of sub- and supercritical Organic Rankine Cycles for power generation from low-temperature/low-enthalpy geothermal wells, considering specific net power output and efficiency. *Applied Thermal Engineering*, 51, 871−879. doi: 10.1016/j.applthermaleng.2012.10.042

[55] Xia, X.X., Qi W.Z., Hua, H.Y., & Jun, Z.N. (2018). A novel comprehensive evaluation methodology of organic Rankine cycle for parameters design and working fluid selection. *Applied Thermal Engineering*, 143, 283–292. doi: 10.1016/j.applthermaleng.2018.07.061

[56] Zaniewski, D., Klimaszewski, P., Klonowicz, P., Lampart, P., Witanowski, Ł., Jędrzejewski, Ł., Suchocki, T., & Antczak, Ł. (2021). Performance of the honeycomb type sealings in organic vapour microturbines. *Energy*, 226, 120242. doi: 10.1016/j.energy.2021.120242

[57] Kaczmarczyk, T.Z., & Żywica, G. (2024). Experimental study of the effect of load and rotational speed on the electrical power of a high-speed ORC microturbogenerator. *Applied Thermal Engineering*, 238, 122012. doi: 10.1016/j.applthermaleng.2023.122012

[58] Mieloszyk, M., Majewska, K., Żywica, G., Kaczmarczyk, T.Z., Jurek, M., & Ostachowicz, W. (2020). Fibre Bragg grating sensors as a measurement tool for an organic Rankine cycle microturbogenerator. *Measurement*, 157, 107666. doi: 10.1016/j.measurement.2020.107666

[59] Zuo, Q., Liu, P., Meng, W., Zeng, X., Li, H., Wang, H., Tian, H., & Shu, G. (2025). Bayesian optimized LSTM-based sensor fault diagnosis of organic Rankine cycle system. *Energy and AI*, 21, 100519. doi: 10.1016/j.egyai.2025.100519

[60] Piwowarski, M., Kosowski, K., & Richert, M. (2023). Organic Supercritical Thermodynamic Cycles with Isothermal Turbine. *Energies*, 16, 4745. doi: 10.3390/en16124745

[61] Cohen, H., Rogers, G.F.C., & Saravanamuttoo, H.I.H. (1987). *Gas Turbine Theory* (3 rd ed.), Longman Scientific & Technical.

[62] Kesseli, J., Sullivan, S., Swarden, M., Duffy, S.F., Baker, E.H., Ferber, M., & Jounkouski, J. (2003). Advancements in the IR PowerWorks Employing a Ceramic Turbine Rotor, *International Gas Turbine Institute, IGTI Microturbine Session*, June 16, 2003.

[63] Konecna, E., Masa, V., Miklas, V., Slovak, R., Jordening, A., & Blaha, V. (2023). Gas microturbine as a main source of energy for industrial laundry – feasibility study, *Energy*, 267, 126630. doi: 10.1016/j.energy.2023.126630

[64] Kazimierski, Z., & Krysiński, J. (1981). *Gas bearing and microturbine drives*. WNT Warszawa (in Polish).

[65] Boyce, M.P. *Gas Turbine Engineering Handbook* (2nd ed.), Gulf Professional Publishing, An Imprint of Butterworth-Heinemann, Boston, Oxford, Auckland, Johannesburg, Melbourne, New Delhi.

[66] Logan, E. Jr., & Ro, R. (2003). *Handbook of Turbomachinery* 2nd ed.), Arizona State University, Marcel Dekker Inc. New York, Basel.

[67] McDonald, C.F. (2003). Recuperator considerations for future higher efficiency microturbines. *Applied Thermal Engineering*, 23(12), 1463–1487. doi: 10.1016/S1359-4311(03)00083-8.

[68] *Advanced Catalytic Reactors and Systems for the Energy Sector. Clean Power Solutions for the 21st Century*. (2004). http://www.precision-combustion.com/products.html, Precision Combustion, INC. Company Capabilities [accessed 4 Nov. 2024].

[69] Haught, D. (2004). Final ATS Annual Program Review Meeting. *Clean Energy for 21 st Century*, December 4− 6, Alexandria, VA.

[70] Horlock, J.H. (2003). *Advanced Gas Turbine Cycles* (1st ed.). An imprint of Elsevier Science, Amsterdam, Boston, Heidelberg, London, New York, Oxford, Paris, San Dego, San Francisco, Singapore, Sydney, Tokyo.

[71] Brown, M. (2004). An Introduction to Gas Turbines & Microturbines for DE Applications. *World Energy Technologies Summit*, 10–11 February.

[72] Spentzas, S., Chimack, M., & Worek, W. (2006). Optimization of a Cogeneration System in the Automotive Industry. *SAE 2006 World Congress & Exhibition. SAE Technical Paper 2006-01-0831*. doi: 10.4271/2006-01-0831

[73] *Microturbine Systems Big Energy Savings in a Small Package PowerWorks*. (2005). Ingersoll-Rand Energy Systems.

[74] Kang, S., Johnston, J.P., Arima, T., Matsunaga, M., Tsuru, H., & Printz, F.B. (2004). Microscale Radial-Flow Compressor Impeller Made of Silicon Nitride: Manufacturing and Performance. *Transactions of the ASME, Journal of Engineering for Gas Turbines and Power*, 126, 358−365. doi: 10.1115/1.1739246

[75] Kumakura, H., Maekawa, H., & Murakami, K. (2004). Development of Portable Gas Turbine Generator "Dynajet 2.6". *IHI Engineering Review*, 37(3), 113−114.

[76] Akbari, P., Nalim, R., & Müller, N. (2006). Performance Enhancement of Microturbine Engines Topped with Wave Rotors. *Transactions of the ASME, Journal of Engineering for Gas Turbines and Power*, 128, 190−202. doi: 10.1115/1.1924484

[77] Peirs, J., Reynaerts, D., & Verplaetsen, F. (2003) Development of an axial microturbine for a portable gas turbine generator. *Journal of Micromechanics and Microengineering*, 13, S190. doi: 10.1088/0960-1317/13/4/328

[78] Peirs, J., Reynaerts, D., & Verplaetsen, F. (2004). A microturbine for electric power generation. *Sensors and Actuators A: Physical*, 113(1), 86−93. doi: 10.1016/j.sna.2004.01.003

[79] Kosowski, K., Piwowarski, M., Richert, M., Stępień, R., & Włodarski, W. (2024). Isothermal turbines New challenges. Numerical and experimental investigations into isothermal expansion in turbine power plants. *Energy Conversion and Manage*ment, 315, 118772. doi: 10.1016/j.enconman.2024.118772

[80] Kamps, T. (2005). *Model Jet Engines* (3rd ed.). Traplet Publication Ltd., North Las Vegas, NV, U.S.A.

[81] Rowbotham, R. (2005). *Merlin 160 G Instruction Manual-Version 1.1.2005*. Cami del Pollastre, 108358, Arenys de Munt, Barcelona, Spain.

[82] http://www.jetmodel.webpark. pl/silniki.html [accessed 27 Dec. 2011] (in Polish).

[83] http://www.artesjet.com/products.htm [accessed 27 Dec. 2011].

[84] http://www.mt-online.com/component/content/article/67-may/538-balance-and-vibration-test-solutions-for-air-cycle-machines.html [accessed 27 Dec. 2011].

[85] Boryaev, A.A. (2021). Boundary layer calculation in gas flows in micronozzles. *International Journal of Non-Linear Mechanics*, 137, 103831. doi: 10.1016/j.ijnonlinmec.2021.103831

[86] http://www.fh1100.com/250.html [accessed 28 Dec. 2011].

[87] http://www.marineturbine.com/motorcycles.asp [accessed 28 Dec. 2011].

[88] http://www.capstoneturbine.com [accessed 28 Dec. 2011].

[89] Gabrielsson, R. (2005). Microturbines Volvo Aero Corporation. *Personal communication*, 117.

[90] https://moto.pl/MotoPL/7,88389,27944219,jaguar-c-x75-z-spectre-nigdy-nie-wszedl-do-produkcji-jednak.html [accessed 4 Nov. 2024] (in Polish).

[91] http://stoma.abc24.pl/default.asp?kat=12968&pro=63806 [accessed 28 Dec. 2011].

[92] http://www.elmedes.pl/index.php?m=2&subview=82&id=46, [accessed 28 Dec. 2011].

[93] http://atmo.com.pl/portal/product/450/szlifierka-bezolejowa-wysokoobrotowa-biax-85-tys [accessed 28 Dec. 2011] (in Polish).

[94] http://atmo.hrba.flexopartner.net/portal/product/ 451/szlifierka-bezolejowa-wysokoobrotowa-biax-100-tys [accessed 28 Dec. 2011] (in Polish).

[95] http://www.narzedzia-pneumatyka.info/pl/szlifierki/ [accessed 28 Dec. 2011] (in Polish).

[96] http://pergatory.mit.edu/perg/awards/TURBOTOO.html [accessed 29 Dec. 2011].

[97] http://www.pressura.com/demag/motoren/katalog/silniki4.pdf [accessed 29 Dec. 2011] (in Polish).

[98] Kirawanich, P., & O'Connell, R.M. (2003). Potential Harmonic Impact of Microturbines on a Commercial Power Distribution System. *Institute of Electrical and Electronics Engineers (IEEE)*, 1118−1123.

[99] *Environmental Technology Verification Report*. *Ingersoll-Rand Energy Systems IR PowerWorksTM 70 kW Microturbine System*. (2003). SRI/USEPA-GHG-VR-21. Greenhouse Gas Technology Center, Southern Research Institute, U.S. Environmental Protection Agency, New York State Energy Research and Development Authority, USA.

[100] Staunton, R.H., & Ozpineci, B. (2003). *Microturbine Power Conversion Technology Review*. Report ORNL/TM-2003/74. April 8, OAK Ridge National Laboratory, Oak Ridge, Tennessee 37831, USA.

[101] Walsh, P.P., & Fletcher, P. (2004). Gas Turbine Performance (2nd ed.). Blackwell Science Ltd, Oxford, UK. doi: 10.1002/9780470774533

[102] Traverso, A., Calzolari, F., & Massardo, A. (2005). Transient Analysis of and Control System for Advanced Cycles Based on Micro Gas Turbine Technology. *Journal of Engineering for Gas Turbines and Power*, 127, 340−347. doi: 10.1115/1.1839918

[103] Kumar, K., Kumar, P., & Kar, S. (2024). A review of microgrid protection for addressing challenges and solutions. *Renewable Energy Focus*, 49, 100572. doi: 10.1016/j.ref.2024.100572

[104] Kamran, M., & Turzyński, M. (2024). Exploring hydrogen energy systems: A comprehensive review of technologies, applications, prevailing trends, and associated challenges. *Journal of Energy Storage*, 96, 112601. doi: 10.1016/j.est.2024.112601

[105] Schock, R.N., Brown, N.W., & Smith, C.F. (2001). Nuclear Power, Small Nuclear Technology, and the Role of Technical Innovation. *Conference: New Energy Technologies: A Policy Framework for Micro-Nuclear Technology*, 9 Mar., Houston, USA.

[106] Jezierski, G. (2005). Increased interest in small nuclear power plants, *Energia Gigawat*, 12 (in Polish).

[107] Tesla, N. (1913). *Turbine*, Patent No. 1,061,206. United States Patent Office, N.Y., May 6.

[108] Cairnes, W.M.J. (2001). *The Tesla Disc Turbine*. Camden Miniature Steam Services, USA.

[109] Ladino, A.F.R. (2004). *Numerical simulation of the flow field in a friction-type turbine (Tesla turbine)*. Diploma Thesis, Vienna University of Technology, Austria.

[110] Armstrong, J.H. (1952). *An Investigation of the Performance of a Modified Tesla Turbine*. A Thesis Presented to the Faculty of the Division of Graduate Studies, Georgia Institute of Technology, USA.

[111] Rice, W. (1965). An Analytical and Experimental Investigation of Multiple-Disk Turbines. *Journal of Engineering for Gas Turbines and Power, Transaction of the ASME*, 87(1), 29−36, doi: 10.1115/1.3678134

[112] Davydov, A.B., & Sherstyuk, A.N. (1980). Experimental Research on a Disc Microturbine. *Russian Engineering Journal*, 60(8), 19–22.

[113] Beans, W.E. (1966). Investigation Into the Performance Characteristics of a Friction Turbine, *Journal of Spacecraft and Rockets*, 3(1), 131−134. doi: 10.2514/3.28398

[114] North, R.C. (1969). *An Investigation of the Tesla Turbine*. Thesis, University of Maryland.

[115] Gruber, E.L. (1960). *An Investigation of a Turbine with a Multiple Disc Rotor*. Thesis, Arizona State University, Tempe, Arizona, 1960.

[116] Rice, W. (1991). Tesla Turbomachinery. *Conference Proceedings of the IV International Tesla Symposium*, Serbian Academy of Sciences and Arts, 22−25 Sept. Belgrade, Yugoslavia.

[117] Schmidt, D.D. (2002). Final Report Biomass Boundary Layer Turbine Power. *Energy Innovations Small Grant*, EISG Final Report, Appendix A FAR 00-06.

[118] Thomazoni, A.L.R., Ermel, C., Schneider, P.S., Vieira, L.W., Hunt, J.D., Ferreira, S.B., Rech, Ch., & Gouvea, V.S. (2022). Influence of operational parameters on the performance of Tesla turbines: Experimental investigation of a small-scale turbine. *Energy*, 261, 125159. doi: 10.1016/j.energy.2022.125159

[119] Guha, A., & Smiley, B. (2010). Experiment and analysis for an improved design of the inlet and nozzle in Tesla disc turbines. *Proceedings of the Institution of Mechanical Engineers, Part A: Journal of Power and Energy*, 224, 261–277. doi: 10.1243/09576509 JPE818

[120] Sengupta, S., & Guha, A. (2012). A theory of Tesla disc turbines. *Proceedings of the Institution of Mechanical Engineers, Part A: Journal of Power and Energy*, 226(5), 650–663. doi: 10.1177/0957650912446402

[121] Krishnan, V.(2015). *Design and Fabrication of cm-scale Tesla Turbines*. PhD dissertation, University of California, June 1, Berkeley, USA.

[122] Alonso, D.H., & Silva, E.C.N. (2022). Topology optimization applied to the design of Tesla-type turbine devices. *Applied Mathematical Modelling*, 103, 764–791. doi: 10.1016/j.apm.2021.11.007

[123] Li, R., Wang, H., Yao, E., Li, M., & Nan, W. (2017). Experimental study on bladeless turbine using incompressible working medium. *Advances in Mechanical Engineering*, 9(1). doi: 10.1177/1687814016686935.

[124] Qi, W., Deng, Q., Feng, Z., & Yuan, Q. (2016). Influence of disc spacing distance on the aerodynamic performance and flow field of Tesla turbines. *Conference: ASME Turbo Expo 2016: Turbomachinery Technical Conference and Exposition*, June 13−17, Seoul, South Korea. doi: 10.1115/GT2016-57971

[125] Manfrida, G., Pacini, L., & Talluri, L. (2018). An upgraded Tesla turbine concept for ORC applications. *Energy*, 158, 33–40. doi: 10.1016/j. energy.2018.05.181

[126] Deng, Q., Qi, W., & Feng, Z. (2013). Improvement of a theoretical analysis method for tesla turbines. *ASME Turbo Expo 2013: Turbine Technical Conference and Exposition*, June 3−7, San Antonio, Texas, USA. doi: 10.1115/gt2013-95425

[127] Kamran, M.A., & Manzoor, S. (2020). Effect of nozzle angle, turbine inlets and mass flow rate on the performance of a bladeless turbine. *Proceeding of the Institution of Mechanical Engineering, Part A: Journal of Power and Energy*, 234(8), 1101–1107. doi: 10.1177/0957650919893539

[128] Klingl, S., Lecheler, S., & Pfitzner, M. (2019). Experimental, numerical and theoretical investigations of Tesla turbines. *E3S Web of Conferences*, 113, 03003doi: 10.1051/e3 sconf/201911303003

[129] Talluri, L., Fiaschi, D., Neri, G., & Ciappi, L. (2018). Design and optimization of a Tesla turbine for ORC applications. *Applied Energy*, 226, 300−319. doi: 10.1016/j. apenergy.2018.05.057

[130] Pfenniger, A., Vogel, R., Koch, V.M., & Jonsson, M. (2014). Performance analysis of a miniature turbine generator for intracorporeal energy harvesting. *Artificial Organs*, 38(5), E68−E81. doi: 10.1111/aor.12279

[131] Shaw, D., Liu, F.T., & Yu, J.J. (2013). Experiment of a tesla engine for wind energy capture. *Applied Mechanics and Materials*, 284–287, 1051–1056. doi: 10.4028/www.scientific.net/AMM.284-287.1051

[132] Lampart, P., Kosowski, K., Piwowarski, M., & Jędrzejewski, Ł. (2009). Design analysis of Tesla microturbine operating on a low-boiling medium. *Polish Maritime Research*, S1, 28−33. doi: 10.2478/v10012-008-0041-5

[133] Rusin, K., Wróblewski, W., Malekshah, E.H., Pahlavanzadeh, M., & Rulik, S. (2024). Extended analytical model of tesla turbine with advanced modelling of velocity profile in minichannel between corotating disks with consideration of surface roughness. *Energy*, 307, 132775. doi: 10.1016/j.energy.2024.132775.

[134] Pahlavanzadeh, M., Rusin, K., Wróblewski, W., & Rulik, S. (2025). Roughness effects on flow in Tesla turbine with parametric adjustment of porous layer model. *Physics of Fluids*, 37(1), 015139. doi:10.1063/5.0247548

[135] Pahlavanzadeh, M., Rusin, K., Wróblewski, W. (2025). Evaluation of nozzle configuration impact on flow structures and performance in Tesla turbine, International Journal of Heat and Mass Transfer 243, 126900, https://doi.org/10.1016/j.ijheatmasstransfer.2025.126900

[136] Teng, S., Li, L., Yan, C., An, D., Zhao, Y., & Xi, H. (2025). Multi-parameter experimental study of a tesla turbine applied to an Organic Rankine Cycle system for low-grade heat utilisation. *Energy Conversion and Management*, 333, 119824. doi: 10.1016/j.enconman.2025.119824

[137] Huynh, N.D., Lin, Z.-H., & Choi, D. (2021). Dynamic balanced hybridization of TENG and EMG via Tesla turbine for effectively harvesting broadband mechanical pressure. *Nano Energy*, 85, 105983. doi: 10.1016/j.nanoen.2021.105983

[138] Kiziroglou, M.E., & Yeatman, E.M. (2021). Micromechanics for energy generation. *Journal of Micromechanics and Microengineering*, 31(11), 114003. doi: 10.1088/1361-6439/ac2a52

[139] Li, C., Guo, Z., Guo, H., Bao, X., & Zhou, L. (2022). Influences of main design parameters on the aerodynamic performance of a micro-radial in flow turbine. *AIP Advances*, 12(10), 105012. doi: 10.1063/5.0090173

[140] Kosowski, K., Blekiewicz, T., Piwowarski, M., Stępień, R., Włodarski, W., Mikielewicz, J., & Kiciński, J. (2013). *Disc turbine generator with armature winding in the rotor, especially for small power plants, including hydroelectric and wind power plants*. Polish Patent PL 223125 B1 (in Polish).

[141] Kosowski, K., Blekiewicz, T., Piwowarski, M., Stępień, R., Włodarski, W., Mikielewicz, J., & Kiciński, J. (2013). *Disc turbine generator with magnetic elements in the rotor, especially for small power plants, including hydroelectric and wind power plants*. Polish Patent PL 223126 B1 (in Polish).

[142] Gad-el-Hak, M. (2006). *MEMS Introduction and Fundamentals* (2nd ed.). Taylor&Francis Group, Boca Raton, London, New York.

[143] Fréchette, L.G., Lee, C., Arslan, S.; Liu, & Y-Ch. (2003). Design of a microfabricated Rankine cycle steam turbine for power generation. *Proceedings of IMECE'03 ASME International Mechanical Engineering Congress & Exposition*, IMECE2003-42082, November 16−21, Washington, USA. doi: 10.1115/IMECE2003-42082

[144] Fréchette, L.G., Lee, C., & Arslan, S. (2004). Development of a MEMS-Based Rankine Cycle Steam Turbine for Power Generation. *4 th Workshop on Micro and Nano Technology for Power Generation & Energy Conversion Applications* (*Power MEMS'04*), (pp. 92–95), November 28−30, Kyoto, Japan.

[145] Cui, L., & Brisson, J.G. (2005). Modeling of MEMS-Type Ranking Cycle Machines. *Journal of Engineering for Gas Turbines and Power*, 127, 683−692.

[146] Maluf, N. (2000). *An Introduction of Microelectromechanical Systems Engineering*. Artech House, Inc., Boston, London.

[147] Varadan, V.K., Vinoy, K.J., & Gopalakrishnan, S. (2006). *Smart Material Systems and MEMS: Design and Development Methodologies*. John Wiley & Sons Ltd, England.

[148] Epstein, A.H. (2003). Millimeter-Scale, MEMS Gas Turbine Engines. Proceedings of ASME Turbo Expo 2003, GT-2003-38866, Power for Land, Sea, and Air Atlanta, June 16−19, Georgia, USA.

[149] Sullivan, S., Zhang, X., Ayón, A.A., & Brisson, J.G. (2001). Demonstration of a Microscale Heat Exchanger for a Silicon Micro Gas Turbine Engine. *11th International Conference on Solid-State Sensors and Actuators*, June 10–14, Munich, Germany.

[150] Müller, N., & Fréchette, L.G. (2002). Performance Analysis of Brayton and Rankine Cycle Microsystems for Portable Power Generation. *Proceedings of IMECE2002 ASME International Mechanical Engineering Congress & Exposition*, IMECE2002-39628., 513−522, November 17−22, New Orleans, Louisiana, USA. doi: 10.1115/IMECE2002-39628

Co-published by
Institute of Fluid-Flow Machinery
Polish Academy of Sciences
Committee on Thermodynamics and Combustion
Polish Academy of Sciences

http://www.imp.gda.pl/archives-of-thermodynamics/

ARCHIVES
OF THERMODYNAMICS

Measurements of electrical capacitance in the flow of reservoir fluid with gas bubbles

Remigiusz Ornowski[a,b*], Stanisław Żwan[a]

[a]TERCJA Measuring and Computer Systems, Dywizjonu 303 5B/24, 80-462 Gdańsk, Poland
[b]Institute of Fluid Flow Machinery, Polish Academy of Sciences, ul. Fiszera 14, 80-231 Gdańsk, Poland
*Corresponding author email: rornowski@imp.gda.pl

Received: 18.08.2025; revised: 01.09.2025; accepted: 11.09.2025

Abstract

The paper discusses tests of an electric capacitance sensor designed and built to measure gas fraction in a reservoir fluid flow. These tests were conducted under conditions typical for oil field testing and productivity monitoring. In such an application, the electrical permittivity of the liquid and gas components is of the same order of magnitude, which poses a significant challenge in capacitance metering of the phase content. The studied two-electrode capacitance sensor is a novel design. It uses a commercial, high-resolution ΔΣ capacitance-to-digital converter. The sensor was experimentally tested on the flow of reservoir fluid (from Lubiatów-Międzychód-Grotów field in Poland) heated to 40–50°C to reproduce field conditions during actual gas and oil extraction. The gas fraction in the reservoir fluid was generated by the injection of air or methane bubbles. Fluid velocities during the testing ranged from 1 to 3.1 m/s, and the void fraction reached 4.4%. After calibration, the examined capacitance sensor was able to detect a void fraction as low as 1%. The measured capacitance differences due to gas content were dependent on the spatial distribution of voids in the inter-electrode space. This effect was confirmed by photographs of the flow patterns and numerical simulations of the electric field distributions.

Keywords: Capacitance sensor; Reservoir fluid; Oil-gas flow; Oil and gas extraction; ΔΣ capacitance-to-digital converter;

Vol. 46(2025), No. 3, 39–49; doi: 10.24425/ather.2025.154922

Cite this manuscript as: Ornowski, R., & Żwan, S. (2025). Measurements of electrical capacitance in the flow of reservoir fluid with gas bubbles. *Archives of Thermodynamics*, 46(3), 39–49.

1. Introduction

Electrical capacitance measurement has a wide range of applications, both in industry and laboratory practice. In particular, it enables the measurement of the void fraction, i.e. the gas content in a liquid. Measuring gas content, both quantitatively and qualitatively, is crucial in many technological processes. One of the most important potential applications is two-phase liquid-gas flows, which are common, for example, in the refrigeration industry [1,2]. Detecting the presence of liquid at the steam turbine inlets is equally important. In the drilling industry, void fraction measurement is used during the drilling process to determine the amount of drilling fluid flowing from the well. This is a crucial parameter for blowout prevention. Using void fraction measurement during oil field sampling provides additional information about separator performance, which positively affects the control of operating parameters and separator efficiency. In the later stages of the oil field development, void fraction measurements are important for determining the phase composition of the reservoir fluid during well testing and productivity monitoring.

The most common method for measuring the phase composition of the reservoir fluid involves using a separator to measure each phase separately. This method is expensive and requires ongoing maintenance by qualified personnel. Due to the

Nomenclature

C – capacitance, F
$\mathbf{E}$ – electric field vector, V/m
$\mathbf{n}$ – unit normal vector
S – surface area, m^2
U – electric potential, V
V – voltage, V

Greek symbols
ε – absolute permittivity, F/m
ε_r – relative permittivity, –
ε_0 – vacuum permittivity, $\varepsilon_0 = 8.8541878188(14)\times10^{-12}$ F/m
φ – void fraction, –

Abbreviations and Acronyms
CDC – capacitance-to-digital converter
LMG – Lubiatów-Międzychód-Grotów

separator size, it also requires considerable space, which can be problematic on offshore drilling platforms. Due to the high inertia of the separator, this method has low time resolution but offers high measurement accuracy for quasi-steady flows. Therefore, implementing a system that allows for direct and continuous measurement of the void fraction without prior separation offers many advantages [3]. In this context, non-invasive and continuous capacitance measurement can be applied [4,5].

Over the years, many capacitance sensor designs based on analogue electronic circuits have been described in the literature. Salehi et al. [6], for instance, investigated a capacitance sensor aimed at measurements in oil–gas two-phase flow. The focus was on finding the optimal exciting frequency of the voltage applied to the electrodes. Based on the sensor impedance modelling and static experiments representing annular flow (with a void in the core) were made. They found that a frequency of 0.8–1.0 MHz gives the best sensitivity for the oil-gas medium. Continuing their research, Salehi et al. [7] investigated the performance of different electrode configurations for oil–gas flows in bubbly, plug, stratified and slug regimes. They concluded that an interlocking electrode arrangement (termed TRFLC) or a concave shape is best for identifying flow regimes. For measuring gas fraction, a helical shape is preferable. Ahmed and Ismail [8] also reviewed the performance of capacitance sensors with different electrode shapes.

In addition to previous studies, a system with a capacitance sensor specifically designed to measure water content in crude oil was constructed by Aslam and Tang [9]. Its electronics operated based on capacitance to phase angle conversion [10,11] and achieved a resolution of ±50 ppm of water content during laboratory tests on crude oil samples. A new design of the capacitance sensor also dedicated to oil-water flows was proposed by Demori et al. [12]. It was tested on an experimental setup with controlled two-phase annular and slug flows in a horizontal tube for oil fractions ranging from 20% to 65%.

Similarly, capacitance sensors with two concave, two helical, or double ring electrodes were experimentally investigated by dos Reis and da Silva Cunha [13] in water–air horizontal flow. Their study covered the full range of void fractions, from 0% to 100%. Their measurements showed that the highest sensitivity was observed for the concave electrodes, while the lowest for the double ring ones. However, measurements with concave electrodes were most dependent on the air–water flow patterns, and the double ring was least affected in this respect. The characteristics of the helical electrodes were similar to those of the double ring.

The problem of calibration of capacitance sensor was studied, among others, by Abou-Arkoub et al. [14]. They postulated that simple capacitance-sensing techniques can be used for online validation of multiphase flow meters. It was demonstrated that capacitance measurement combined with statistical and fuzzy-logic-type methods can provide the basis for a simple and robust validation of multiphase flow meters' performance by identifying the carrier, dispersed phase and flow structures. Furthermore, the proposed system could be retrofitted to existing multiphase flow meters.

Recent research has explored the use of digital signal processing in capacitance sensor electronics. For example, Wu et al. [15] used digital control in their combined conductance and capacitance sensor designed to measure water holdup in oil–water flow. Maurya and Parasuraman [16] built two- and four-electrode sensors for micro-droplet detection, which were based on the AD7150 capacitance-to-digital converter and were intended for use in drug delivery systems. Their sensor was mounted on an 8 mm outer diameter tube. It had a high sensitivity of 0.7409 fF/µL with repeatability of ±0.032%. Dos Santos et al. [5] developed an oil and gas pipeline monitoring system with a fast capacitance sensor designed for operation in hazardous areas. The sensor operated based on a resonant circuit with a 40 MHz reference oscillator with a frequency tolerance of ±100 ppm/K. The frequency output was digitised with a 15-bit resolution. Data was transmitted in real time to a microcomputer for analysis. The system achieved absolute uncertainty for a gas fraction content of 1.41% in slug flow.

The research presented below aimed to experimentally verify a two-electrode capacitance sensor using a commercially available high-resolution ΔΣ capacitance-to-digital converter (CDC).

The examined system is intended to be developed for use in real-time reservoir fluid characterisation, supporting well testing and productivity monitoring in the oil (petroleum) and gas industry. In this application, the electrical permittivity of liquid and gas components can be of the same order of magnitude, which constitutes a significant difficulty in capacitance metering of the phase content. Despite this, laboratory tests clearly demonstrate that the ΔΣ CDC enables the accurate detection of even small amounts of gas in reservoir fluid, successfully overcoming this difficulty. This finding highlights the capability and sensitivity of the system. Moreover, the measurements were carried out using the fluid at a temperature of 40–55°C, which is typical for oil and gas field production.

2. Materials and methods

The electrical capacitance in the pipe flow of reservoir fluid with gas bubbles was investigated experimentally using a capacitance sensor of our design and construction. The measurements were made on a custom-built laboratory test stand with a horizontal test section.

2.1. Experimental setup

The test stand used during the present research is schematically shown in Fig. 1.

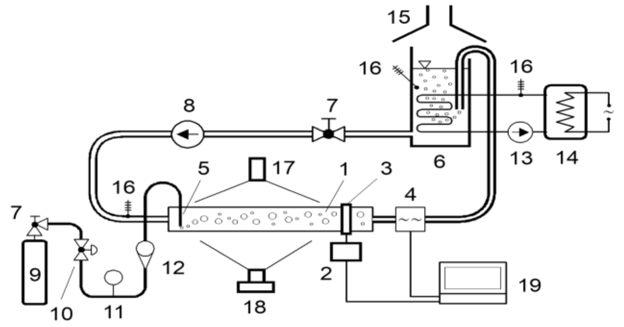

Fig. 1. Experimental setup: 1 – test section, 2 – capacitance sensor, 3 – measuring electrodes, 4 – ultrasonic flow meter, 5 – gas injection, 6 – degasser (flash tank), 7 – cut-off valve, 8 – reservoir fluid circulation pump, 9 – compressed gas cylinder (air or methane), 10 – gas flow control valve, 11 – gas pressure gauge, 12 – rotameter, 13 – heating water circulation pump, 14 – water heater, 15 – gas extraction chimney, 16 – temperature sensor, 17 – electronic flash, 18 – digital still camera, 19 – data acquisition.

It essentially consists of a loop in which the reservoir fluid circulates, including the test section 1 made of a horizontal, transparent polycarbonate tube with an internal diameter of 45 mm and a length of 400 mm. The electrodes 3 of the capacitance sensor 2 were precisely wrapped around the outer surface of this tube at a position near the downstream end. Upstream, a clean segment was used to observe and photograph gas bubbles injected by the needle 5, which was mounted at the beginning of the test section. Downstream of the test section, a polyamide tube segment served as the mounting point for the ultrasonic flow meter 4, with the instrument secured directly onto this segment. The rest of the loop was made of a rubber hose with an internal diameter of 50 mm. Between the flow meter and the circulating pump was the degasser 6, an open tank with a coil used for heating the fluid to the required temperature. The heating medium was water, which circulated between the degasser 6 and the electric boiler 14 via the pump 13. Gases (especially methane) separated from the reservoir fluid were removed from the laboratory through the extraction chimney 15. Downstream of the degasser tank 6, the cut-off valve 7 was installed. It was closed when the circulation pump 8 was turned off. Gas injected into the reservoir fluid was drawn from cylinder 9. The valve 10 adjusted its pressure to achieve the required flow rate. These parameters were monitored using the manometer 11 and the rotameter 12. To control the temperature, sensors 16 were placed at three specific locations: upstream of the test section, within the degasser and in the heating water loop. The flow pattern upstream of the capacitance sensor was photographed using the still camera 18, which was synchronised with the electronic flash 17. The readings from the capacitance sensor 2 and the ultrasonic flow meter 4, both fixed at their described positions, were recorded on-line and processed by laptop computer 19.

Main pump 8 of the centrifugal type was driven by a 2.2 kW electric motor. While the normal rotating speed of this pump was 1450 rpm, it was reduced by an inverter to achieve the required flow rate of the reservoir fluid. To determine this value, the flow velocity was measured with a Flexim Flexus F608 portable ultrasonic meter with an accuracy of ±0.005 m/s. The rotameter 12 (Brooks Instruments Sho-Rate glass tube) used to control gas flow had an accuracy of ±5%. The temperature was measured with industrial PT100 sensors with an accuracy of ±0.5°C.

2.2. Capacitance sensor

The capacitance sensor used in this research was developed in-house based on the AD7746 microchip, an integrated ΔΣ capacitance-to-digital converter from Analog Devices [17]. The converter can measure capacitances up to 21 pF with an accuracy of up to 4 fF ($4 \cdot 10^{-15}$ F), a resolution of 4 aF ($4 \cdot 10^{-18}$ F), and a frequency of up to 90 Hz, depending on the configuration. It operates based on a ΔΣ modulator with a maximum resolution of 24 bits and a square-wave excitation signal with a frequency of 32 kHz.

The measurement system was monitored by software running on a PC, see Fig. 2.

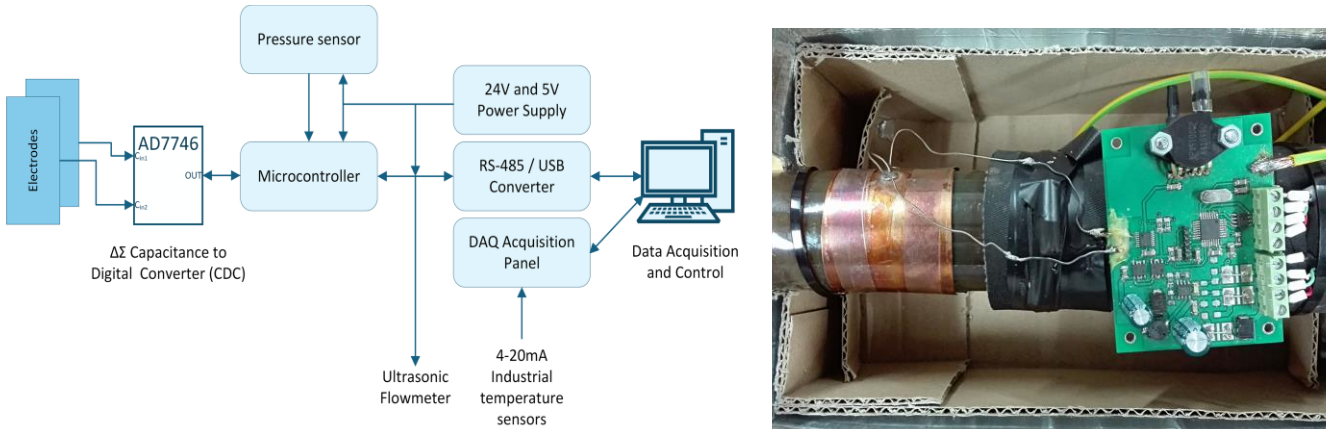

a) b)

Fig. 2. Capacitance sensor with ΔΣ CDC: a) block diagram of the sensor components; b) photograph of the sensor board end electrodes mounted in the test section.

The RS-485 interface allowed for configuration and readout of the AD 7746, as well as readings from the ultrasonic flowmeter. Additionally, the DAQ panel connected to the Ethernet interface enabled readings from the temperature sensors. All read data was saved to a file every second.

2.3. Material properties

The relative permittivity of the materials used in the present study is listed in Table 1. The reservoir fluid came from the Lubiatów-Międzychód-Grotów (LMG) gas and oil field in western Poland. The air and methane were of industrial grade and were drawn from pressurised cylinders. The test section was made of a polycarbonate tube with inner and outer diameters of 45 mm and 50 mm.

Table 1. Relative permittivity.

Material	**Relative permittivity ε_r (-)**
Reservoir fluid	2.5
Air	1.00054
Methane	1.00081
Polycarbonate	2.9

The permittivity of the reservoir fluid was measured by the authors using the air capacitor method. It should be noted that it is only 2.5 times larger than that of the gases.

2.4. Test procedure

Measurements were performed at a constant flow rate and temperature. Capacitance values were sampled at a rate of 1 Hz. Each individual measurement for a specified flow parameter lasted 2 minutes, and the average capacitance during this time interval was recorded for further analysis. For each specified value of liquid flow rate, the liquid-only capacitance was first recorded. Next, two-phase flow capacitance measurements were taken for six values of injected gas flow rate. Before each series of measurements, the reservoir fluid temperature was stabilised at the desired level with an accuracy of ±2°C or better. Flash tank in the flow circuit ensured that the injected gas was removed and did not circulate in the test loop, its content did not increase during the two-minute data acquisition. Several photographs of the flow structure were also taken.

2.5. Supplementary numerical simulations

To gain insight into the phenomena occurring in the inter-electrode space of the capacitive sensor, numerical simulations were performed using the finite element method implemented in the FlexPDE 5 software [18,19]. The electrodes form a capacitor in which the distribution of the electric field in static conditions can be described by the Laplace equation [20]:

$$\nabla \cdot (-\varepsilon \, \nabla U) = 0, \tag{1}$$

where U denotes electric potential and $\varepsilon = \varepsilon_0 \varepsilon_r$ is absolute permittivity. Equation (1) was solved numerically in a cylindrical domain comprising a segment of the polycarbonate tube with two sensor electrodes, as shown in Fig. 3. The value of U at one of the electrodes was set to 0 and at the other to U_e = 0.625 V. The boundary condition on the outer surface of the solution domain was imposed in the form:

$$\nabla U \cdot \mathbf{n} = 0, \tag{2}$$

where $\mathbf{n}$ is a unit vector normal to this surface.

The condition (2) means that the electric field vector:

$$\mathbf{E} = -\nabla U, \tag{3}$$

is perpendicular to the outer surface of the domain, and the electrical charge induced on this surface is zero.

When the solution of Eq. (1) is known, the capacitance C can be calculated from the integral:

$$C = \frac{1}{V_e} \iint_S \varepsilon (\mathbf{E} \cdot \mathbf{n}) dS, \tag{4}$$

where S is a surface enclosing the excited electrode at the potential U_e, and $V_e = U_e$ is the voltage between electrodes.

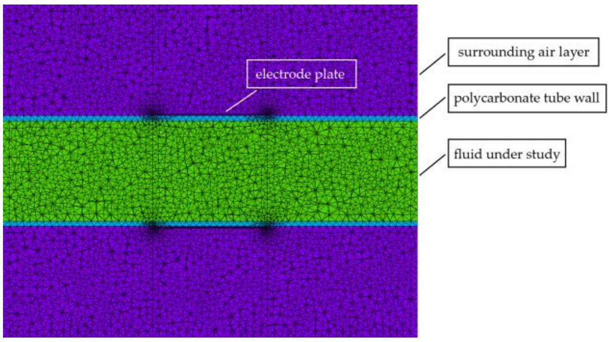

Fig. 3. Axial cross-section through the computational mesh (949 802 cells in total).

Details of the computational mesh are shown in Fig. 3. It forms a cylinder with a diameter of 150 mm and a length of 180 mm, which means that a 50 mm thick air layer was added around the outer walls of the polycarbonate tube and the electrode plates. The 50 mm wide plates were placed halfway along the tube. The mesh cells were generated automatically, but their size could be controlled. Mesh independence tests confirmed that meshes with approximately 1 million cells produced solutions with sufficient accuracy. Capacitance calculated for a fully filled tube with 1 million cells differs by around 0.1% from capacitance calculated with a minimum possible 300 thousand cells, and differs by around 0.01% from capacitance calculated with 2 million cells.

3. Results

The experiments began by assessing how the angular position and width of the electrode gap affected the capacitance readings. Next, with the electrodes set in their final configuration, tests were performed to evaluate the effect of liquid temperature. These measurements were done over a preselected range of fluid temperature, velocity and air void fraction. A similar set of experiments was later performed using methane instead of air. Finally, tests on the long-term stability and repeatability of the sensor concluded the study.

3.1. Effect of electrodes gap position and width

The performance of the capacitance sensor was investigated using three sets of electrodes with different gap widths: 3 mm, 26 mm and 40 mm, corresponding to 1/60, 1/6 and 1/4 of the pipe circumference, respectively. The width of each electrode was 50 mm. The effect of both gap size and angular position was investigated in the following sequence. First, the gaps were placed on the sides of the pipe, in the horizontal plane (0°). Next, the electrodes were rotated so that the centre of the gap was at a 45° angle. Finally, the gaps were placed at the top and bottom of the pipe, i.e. at a 90° angle. These gap positions and sizes are illustrated in Fig. 4.

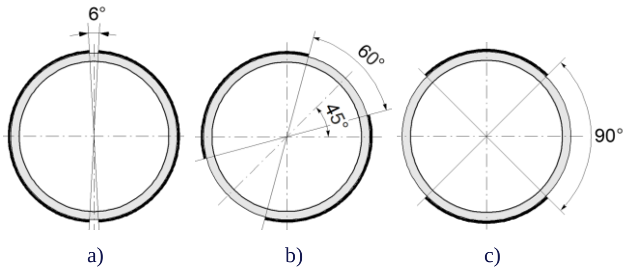

Fig. 4. Tested electrodes differing in gap angular position and width (note: each electrode size was tested at the three angular positions illustrated): a) large electrode at 90° angle (gap width 3 mm), b) medium electrode at 45° angle (gap width 26 mm), c) small electrode at 0° angle (gap width 40 mm)

Simultaneously with the measurement of electrical capacitance, photographs of the flow structure were taken on the pipe section upstream of the capacitance sensor.

During each test run, the flow rate was maintained at 5.8, 9.8, 13.9 or 17.8 m^3/h, corresponding to flow velocities in the test section ranging from 1 to 3.1 m/s. For each flow rate value, the air content in the reservoir fluid was increased stepwise from 0 to 4.2 L/min, which resulted in a maximum void fraction φ ranging from 1.4% in the fastest flow to 4.4% in the slowest one.

A single test series uses one electrode configuration and includes 28 individual measurements (4 liquid flow rates times 7 gas fraction values). For each test series, capacitance measured with only the reservoir fluid flowing (no gas added, void fraction equal to 0) served as the reference value, and was subtracted from the subsequent capacitances measured in two-phase gas-liquid flow. The resulting capacitance differences are shown in Figs. 5–7 for the three electrode sizes investigated, i.e. large, medium and small electrodes with the gaps of 3 mm, 26 mm and 40 mm, respectively. The fluid temperature during the tests ranged from 45°C to 55°C, with the variation of no more than ±2°C during a single measurement series.

The average capacitances measured for each electrode size and angular position are shown in Fig. 8 for liquid-only flow. The average value was calculated from 4 measurements corresponding to the number of flow rates tested. The standard deviation for these averages ranges from 0.001 pF to 0.004 pF, except for the large electrode at the 0° position, for which it is 0.008 pF.

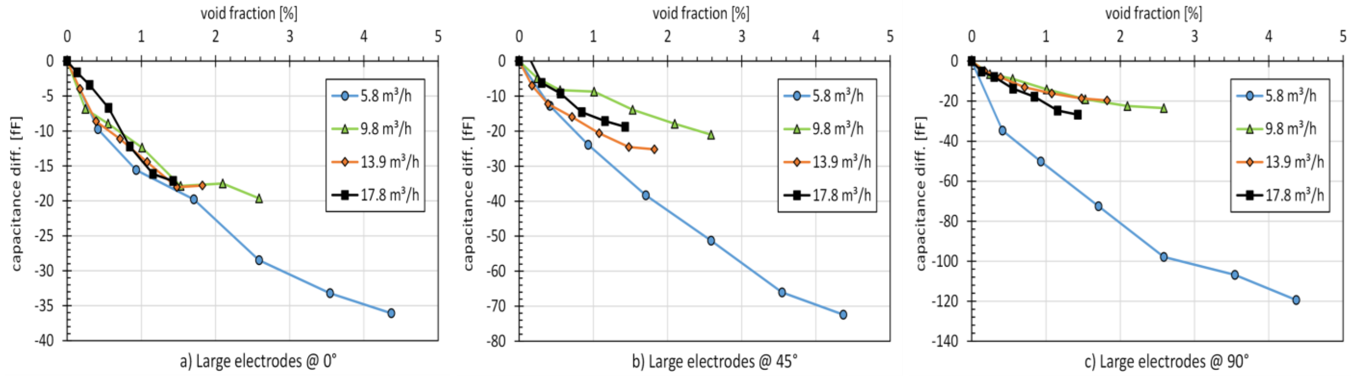

a) Large electrodes @ 0° b) Large electrodes @ 45° c) Large electrodes @ 90°

Fig. 5. Capacitance difference (in fF) measured for large electrodes (gap width 3 mm) in three gap angular positions.

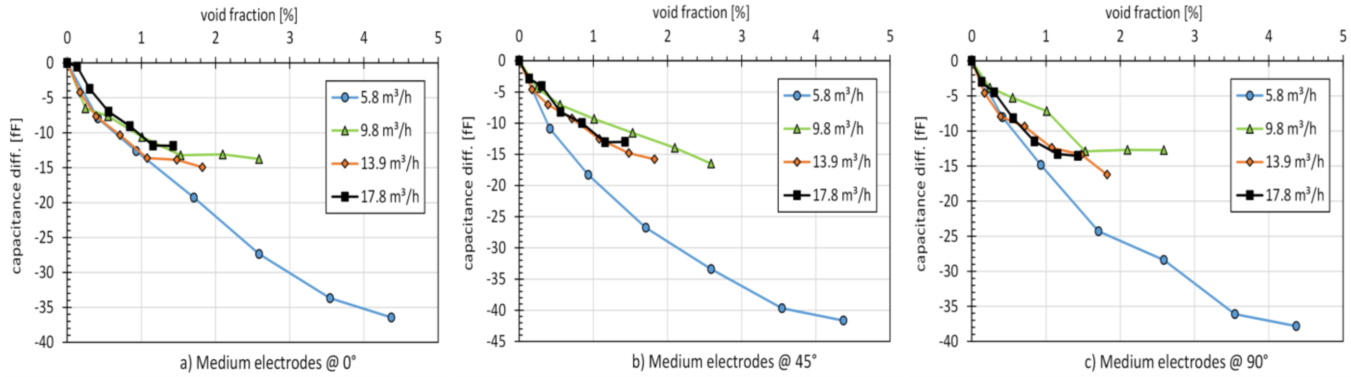

a) Medium electrodes @ 0° b) Medium electrodes @ 45° c) Medium electrodes @ 90°

Fig. 6. Capacitance difference (in fF) measured for medium electrodes (gap width 26 mm) in three gap angular positions.

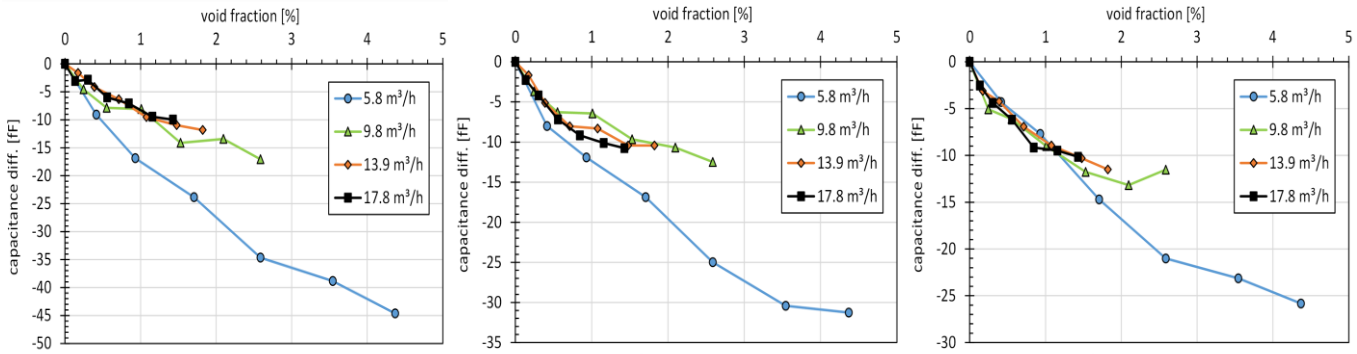

a) Small electrodes @ 0°

b) Small electrodes @ 45°

c) Small electrodes @ 90°

Fig. 7. Capacitance difference (in fF) measured for small electrodes (gap width 40 mm) in three gap angular positions.

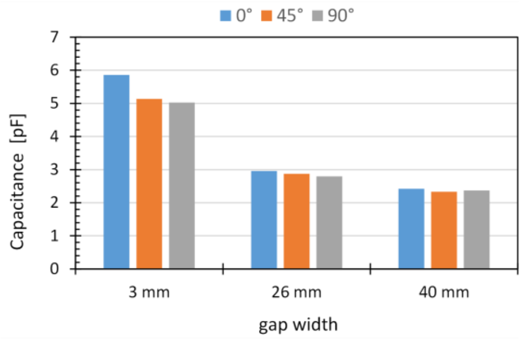

Fig. 8. Average capacitance measured for each configuration of the electrodes and liquid-only flow.

3.2. Effect of reservoir fluid temperature

The effect of fluid temperature on the capacitance sensor operation was checked using the largest electrodes with a 3 mm gap positioned at a 90° angle. For each measurement series, the temperature was constant and the set value was selected from 23°C to 50°C. For each temperature, the air content in the fluid was increased stepwise from 0 to 4.2%.

The test results for varying flow temperature are shown in Fig. 9, illustrating how the capacitance difference changes with air fraction. For each temperature tested, this relationship was measured sequentially for three liquid flow rates: 5.8, 9.8 and 13.9 m^3/h. As before, the capacitance difference was calculated using the value of liquid-only flow as a reference.

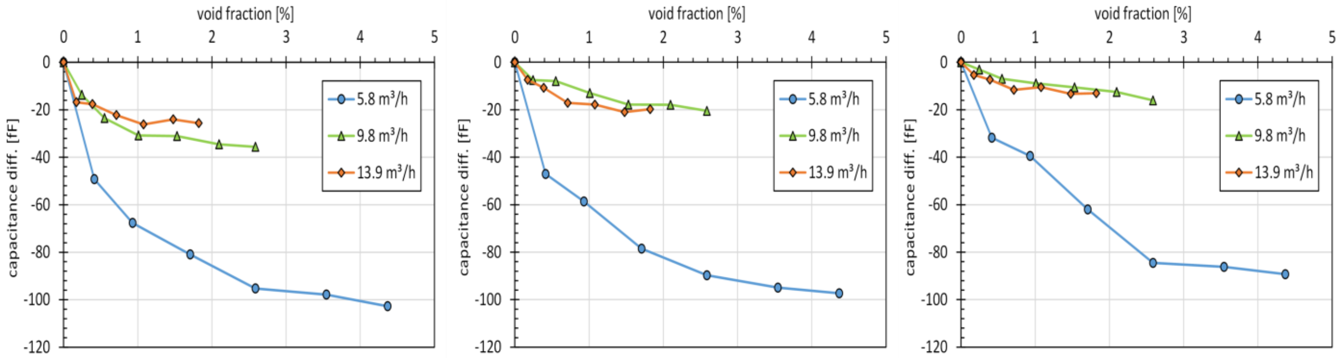

a) Large electrodes @ 90°, T = 23 °C

b) Large electrodes @ 90°, T = 30 °C

c) Large electrodes @ 90°, T = 35 °C

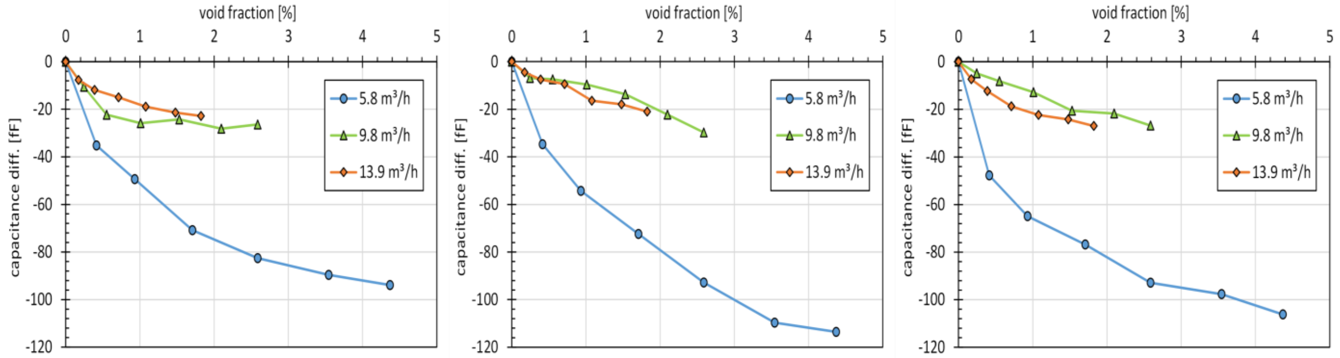

d) Large electrodes @ 90°, T = 40 °C

e) Large electrodes @ 90°, T = 45 °C

f) Large electrodes @ 90°, T = 50 °C

Fig. 9. Capacitance difference measured for large electrodes (gap width 3 mm at 90° angle) for selected reservoir fluid temperature values between 23°C and 50°C.

3.3. Test with methane

The tests with methane injection were carried out for fluid temperatures of 45°C and 50°C. Figure 10 shows the test results for methane. The format is the same as for the measurements with air injection. The capacitance difference relative to the value of liquid-only flow was calculated for three liquid flow rates of 5.8, 9.8, and 13.9 m^3/h. The volume flow rate of methane covers the same range as for the air case.

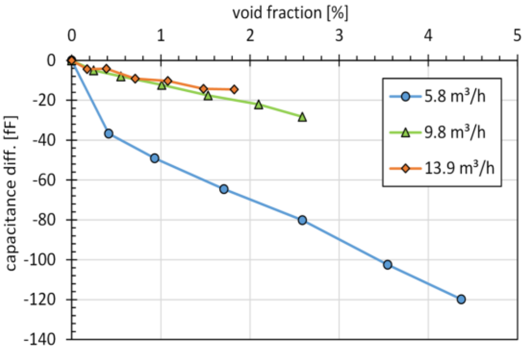

a) Large electrodes @ 90°, T = 45 °C

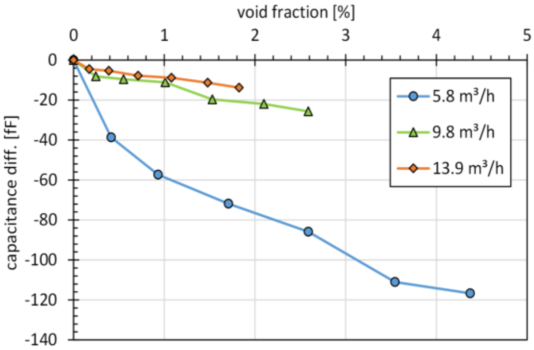

b) Large electrodes @ 90°, T = 50 °C

Fig. 10. Capacitance difference measured for large electrodes (gap width 3 mm at 90° angle) for methane injected into the reservoir fluid at temperature 45°C and 50°C.

3.4. Sensor repeatability tests

Continuous measurements of capacitance were taken under steady flow conditions to assess the stability of the sensor readings.

One of the stability tests examined the effect of reservoir fluid temperature on capacitance during a liquid-only flow, as shown in Fig. 11a. Continuous measurements were recorded for approximately 2 hours at 45°C. The temperature was then increased to 50°C, and recording continued for another 2 hours. The next day, the test at 50°C was repeated. All recorded capacitance values were within ±15 fF of the value recorded at the beginning of the measurement session on day one. Another stability test involved a gas injection period, as shown in Fig. 11b. The purpose of gas injection was to check whether the sensor readings returned to their initial level after the gas injection ended. It turned out that the capacitance in the second period of liquid-only flow was close to the initial level, although lower on average by about 4 fF.

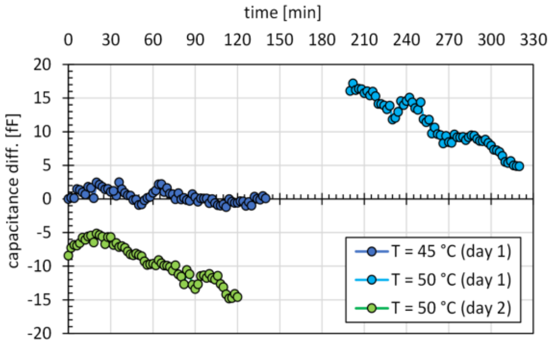

a) Large electrodes @ 90°, φ = 0

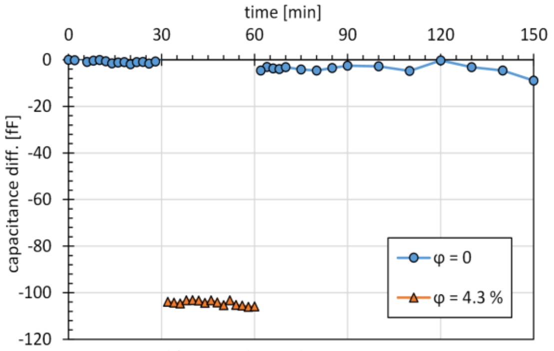

b) Large electrodes @ 90°, T = 50 °C

Fig. 11. Capacitance stability tests: a) repeatability of liquid-only capacitance, b) return of the sensor readings after a period of gas injection.

3.5. Flow structure photographs

Photographs of gas bubbles in the tube segment between the gas injection point and capacitance sensor were taken for each individual capacitance measurement. Figures 12 and 13 show example images that are typical for the used values of gas flow rate.

φ = 0.4%

φ = 1.7%

φ = 4.4%

Fig. 12. Backlit photographs of flow patterns. Gas bubbles emerged from the needle outlet located at the bottom of the test tube, on the left. The capacitance sensor was located downstream (on the right), just outside the image. Liquid flow rate – 5.8 m^3/h, temperature – 52°C, void fraction φ = 0.4%, 1.7% or 4.4%.

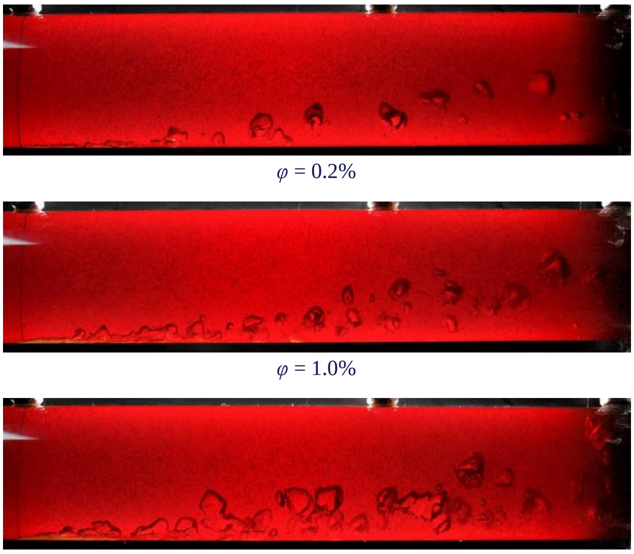

φ = 0.2%

φ = 1.0%

φ = 2.6%

Fig. 13. Backlit photographs of flow patterns. Gas bubbles emerged from the needle outlet located at the bottom of the test tube, on the left. The capacitance sensor was located downstream (on the right), just outside the image. Liquid flow rate – 9.8 m^3/h, temperature – 51°C, void fraction φ = 0.2%, 1.0% or 2.6%.

The photographs show the flow inside the polycarbonate tube viewed from the side, illuminated by light from the flash coming from behind the tube (backlight). Under this illumination, the colour of the reservoir fluid appeared red. The camera and flash were positioned in the horizontal plane. The gas was injected in the upstream part of the photographed segment, on the left in the images. The injection needle outlet was located near the bottom part of the tube inner wall, so the gas bubbles originate in the lower part of the images and move to the right, rising and expanding.

4. Discussion

The experiments discussed here aimed at reproducing reservoir fluid flow conditions similar to those found in a production well. Therefore, the temperature was elevated to 40–50°C in most tests. Due to limitations encountered (only one injection needle could be used), the maximum gas fraction in the flow did not exceed 4.4%. Nevertheless, the presence of gas was reliably detected by the capacitance sensor.

Most experiments have shown that capacitance differences due to increasing void fraction were greater at the lowest flow rate (5.8 m^3/h) than at higher rates. This difference decreased as the gap between the sensor electrodes increased, and was also more pronounced when the gaps were arranged vertically at the top and bottom of the test tube wall (position angle 90°, Fig. 4a). Similar trends appear in tests using methane instead of air.

Numerical simulations and photographs of actual flow explain the above-described effects. It turns out that the capacitance in the inter-electrode space depends not only on the amount of gas in the liquid, but also on its spatial distribution. As can be seen in Fig. 14, gas voids concentrating near the gap between the electrodes cause the largest decrease in capacitance.

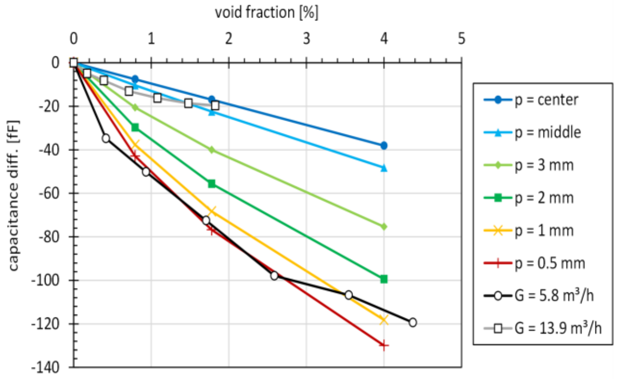

a) Large electrodes and 90°

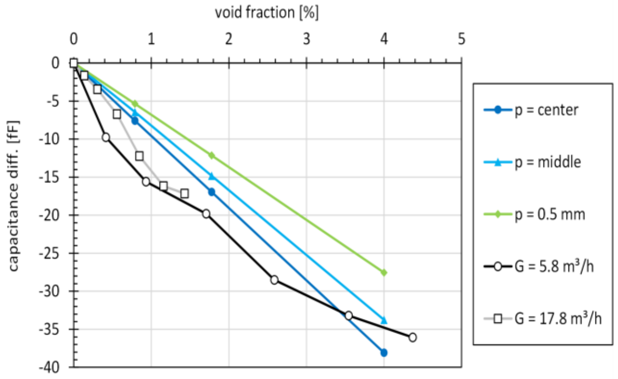

b) Large electrodes and 0°

Fig. 14. Comparison of measurements with numerical simulations of capacitance changes depending on the void fraction and the void position “p” relative to the electrode plates. The effect of the void position is different when it approaches (a) the gap between the electrodes or (b) their centre.

The same amount of gas, when concentrated near the centre of the flow tube cross-section has a much smaller effect, as seen in Fig. 14a. The same can be said for gas concentration near the centre of the electrode plate, Fig. 14b. Comparison of the measurements with simulations leads to the hypothesis that for the lowest flow rate (and velocity), the injected gas created a bubble train that concentrated near the top of the tube wall, where the electrode gap at a 90° angular position was also located. For higher velocities and flow rates, the simulation results suggest that the gas bubbles concentrated and flowed along the centre of the tube. This is confirmed by the images of the flow patterns shown in Figs. 12 and 13. With this assumption about gas phase position in the tube cross-section, quantitative agreement is achieved between the measured and calculated capacitance difference values, Fig. 14a. Similarly, good agreement is also observed when the angular position of the gap was 0°, Fig. 14b. In this electrode configuration, bubbles flowing near the top of the tube cross-section approached the middle of the electrode plate and did not cause as large a capacitance drop as that near the gap. In summary, the concentration of gas voids in different areas of the tube cross-section causes different changes in electrical capacitance. Other researchers have reported this effect as well [7,8,21].

The calculated distributions of electric potential in the inter-electrode space, shown in Figs. 15 and 16, provide more details on the influence of the location of gas voids. To explain these details, Figure 15 illustrates the potential distributions when the flow tube is completely filled with the reservoir fluid. The appearance of gas voids causes a disturbance of this potential, which affects the capacitance. Examples of potential distributions with voids representing gas bubble trains at a void fraction of 4% are shown in Fig. 16 (with the detailed views of parts of Figs. 16c and 16d presented in Fig. 17). The capacitance differences resulting from introduction of the voids can be found in Fig. 14 (position p = center, middle or 0.5 mm).

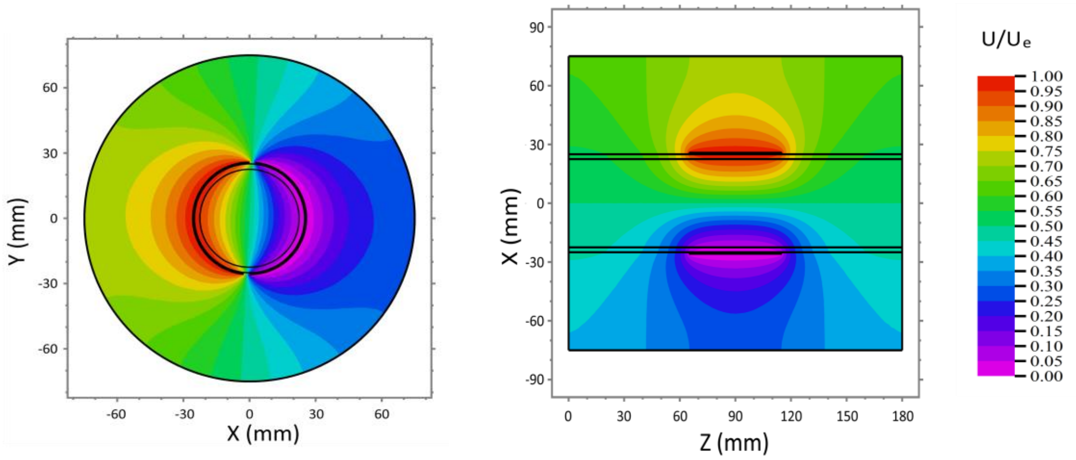

a) b)

Fig. 15. Electric potential distributions in the inter-electrode space filled with reservoir fluid: a) transverse section in the middle of the electrodes, b) axial section.

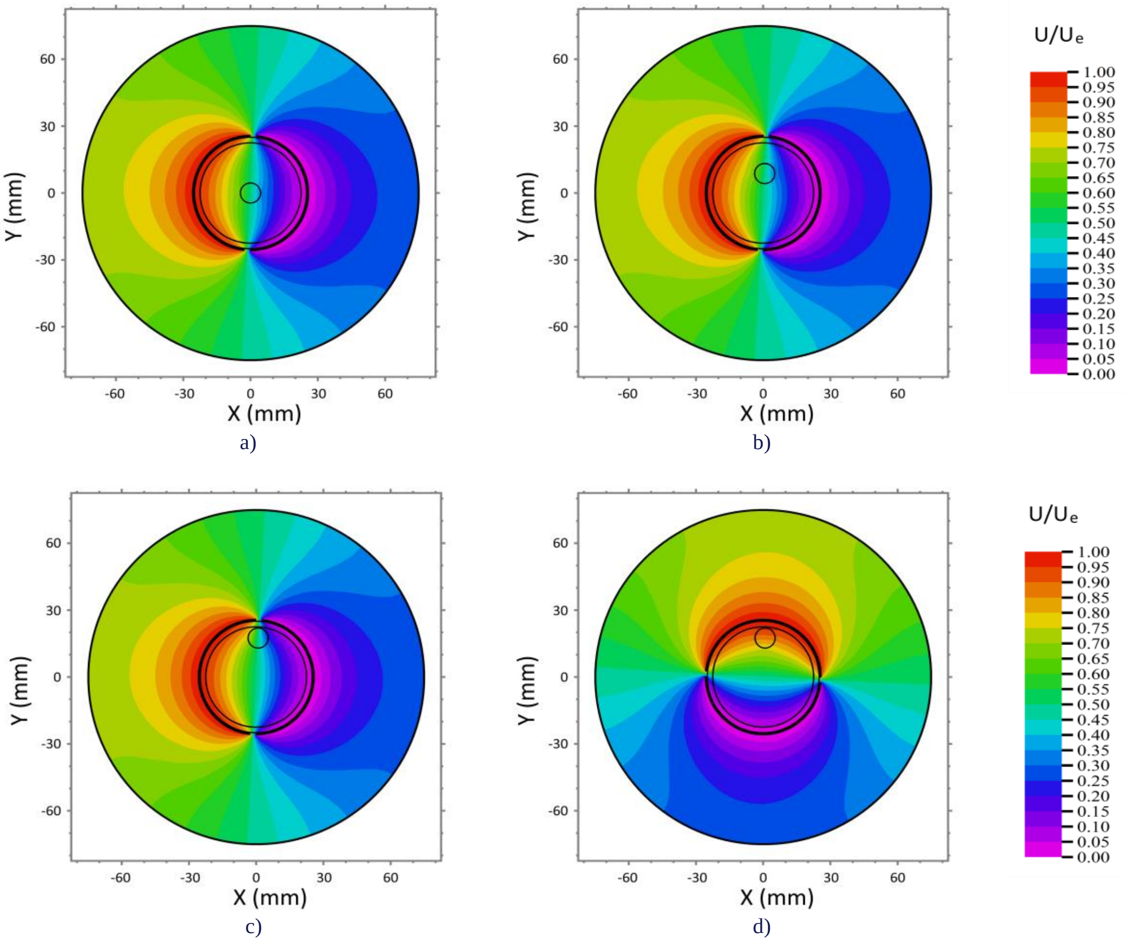

a) b) c) d)

Fig. 16. Electric potential distributions in inter-electrode space for simulated two-phase flow with a 4% void fraction: a) gas phase concentrated in the tube centre, b) gas phase in the “middle” position shifted towards the gap, c) gas phase in the position 0.5 mm from the gap, d) gas phase in the position 0.5 mm from the plate centre.

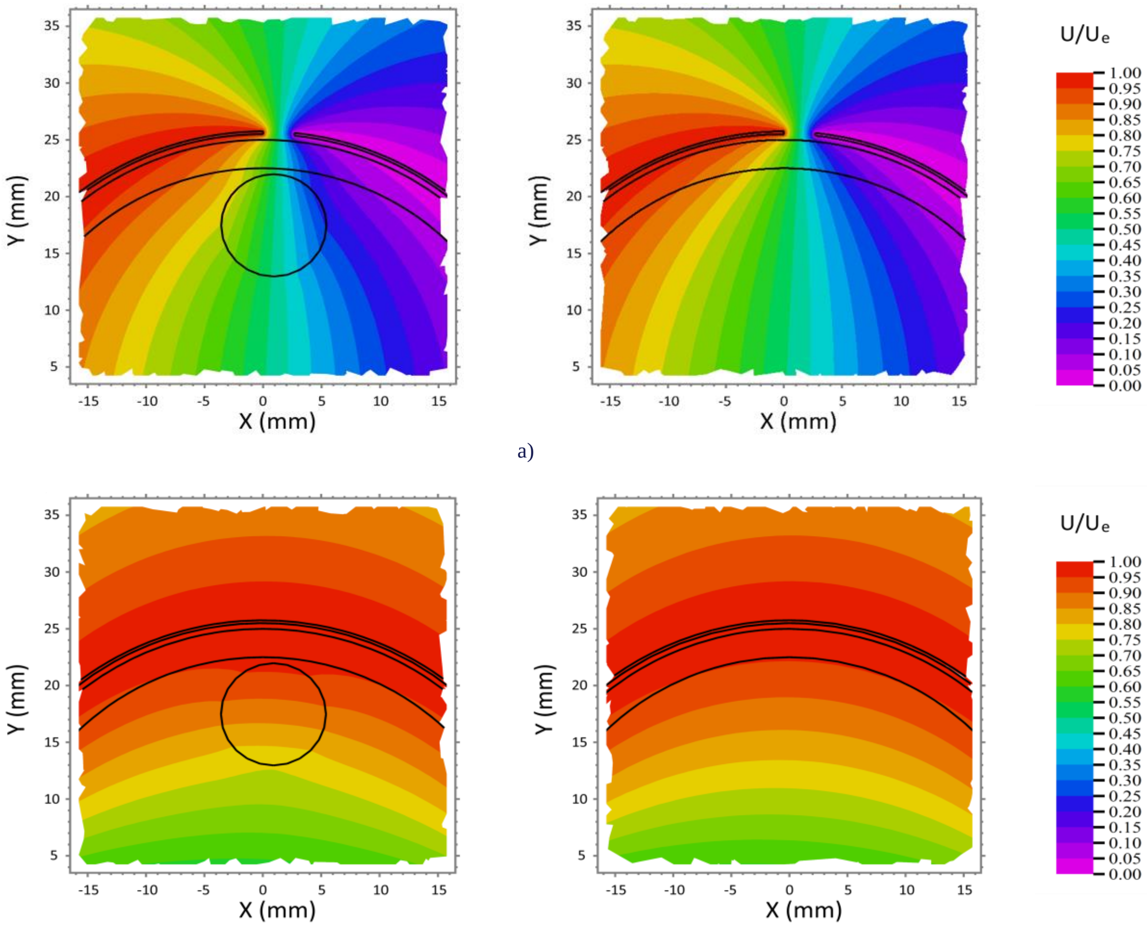

a)

b)

Fig. 17. Detail view of electric potential distributions near the simulated gas void with a 4% void fraction: a) gas phase in the position 0.5 mm from the gap, b) gas phase in the position 0.5 mm from the plate centre. Details at left are parts of Fig. 16c and 16d. Undisturbed liquid-only potentials are also shown at right for comparison.

The dependence of the measured capacitance difference on the electrode gaps angular position is weakest for large electrodes at 0° (when the gaps are located on the sides of the tube, Fig. 4c) or the gap itself is large, as in the tests with small electrodes (Fig. 7). However, as the gap increases (and therefore the plate becomes smaller), the measured capacitances decrease, as shown in Fig. 8. As a result, accurately measuring gas content becomes difficult due to the decrease in the signal-to-noise ratio. For example, the capacitance measured in liquid-only flow at temperatures of 45°C and 50°C averaged 5.23 ±0.05 pF, which is close to the value of 5.11 pF calculated from numerical simulations. The capacitance of gas-only flow, determined from the simulation, is 3.99 pF. Therefore, the full range of the sensor readings would be 1.12 pF.

The permittivity of the reservoir fluid varies with temperature [22], as verified in the tests described in Section 3.2. These measurements, however, did not demonstrate a clear relationship between capacitance and temperature. This is probably due to the fact that the change in the electrical capacity of the reservoir fluid in the tested temperature range from 23°C to 50°C was smaller than the measurement uncertainty of the sensor.

When methane instead of air filled the voids in the reservoir fluid, there were no significant changes in the measured capacitance difference. This conclusion can be supported by comparing the results in Fig. 5c or Fig. 9e,f and Fig. 10, where data for large electrodes with the gap at a 90° angle and flow temperatures of 45°C and 50°C are presented. In all these cases, the largest measured capacitance difference reached 120 fF for a flow rate of 5.8 m^3/h and a void fraction of 4.4%. At higher flow rates, this difference was much lower and amounted to approximately 30 fF at most.

For most liquid-only measurements, repeatability of 5 fF or better was achieved. Only for some tests of the reservoir fluid at 50°C, the repeatability was worse, reaching 15 fF. This means that the tested meter can measure with satisfactory accuracy the gas content above about 1% at low flow rates (corresponding to a velocity of about 1 m/s) and gas content above 2% at higher flow rates. Improving repeatability is only possible through periodic calibration of the device.

5. Conclusions

The experimental research described above concerned capacitance measurements of two-phase liquid-gas flow under conditions encountered during well testing and productivity monitoring in the oil and gas industry. Therefore, the liquid fraction used was actual reservoir fluid at elevated temperatures of 40–50°C.

To further increase the realism of the research, methane was intentionally used as the gas phase in some measurements to better simulate real-world conditions relevant to the study.

The following general conclusions can be drawn after analysing the experimental results discussed above:

- The commercial ΔΣ CDC can reliably detect small changes in capacitance, but quantitative measurements of small gas fractions require calibration of the sensor at the beginning of the measurement session.
- The measured capacitance value depends on both the gas fraction and the spatial distribution of voids in the reservoir fluid.
- Voids concentrated near the electrode gaps have the most significant impact on the capacitance drop in the inter-electrode space.

The capacitance sensor used in this research can be easily developed into a multi-electrode version that allows the reconstruction of the two-phase flow patterns.

Acknowledgements

This research was supported by the (Polish) National Centre for Research and Development (NCBR) under the Smart Growth Operational Program, grant number POIR.01.01.01-00-0780/15-00

References

[1] Kim, M., Komeda, K., Jeong, J., Oinuma, M., Sato, T., & Saito, K. (2022). Optimizing calibration for a capacitance-based void fraction sensor with asymmetric electrodes under horizontal flow in a smoothed circular macro-tube. *Sensors*, 22, 3511. doi: 10.3390/s22093511

[2] Qian, H., & Hrnjak, P. (2020). Mass measurement based calibration of a capacitive sensor to measure void fraction for R134a in smooth tubes. *International Journal of Refrigeration*, 110, 168−177. doi: 10.1016/j.ijrefrig.2019.10.019

[3] Hansen, L.S., Pedersen, S., & Durdevic, P. (2019). Multi-phase flow metering in offshore oil and gas transportation pipelines: trends and perspectives. *Sensors*, 19, 2184. doi: 10.3390/s19092184

[4] Okoro, E.E., Rachael, J.E., Sanni, S.E., & Emetere, M.E. (2021). Liquid holdup measurement in crude oil transportation using capacitance sensors and electrical capacitance tomography: concept review. *IOP Conference Series: Earth and Environmental Science*, 655, 012037, *4th International Conference on Science and Sustainable Development* (*ICSSD 2020*), *"Advances in Sciences and Technology for Sustainable Development"*, 3−5 August, Ota, Nigeria. doi: 10.1088/1755-1315/655/1/012037

[5] dos Santos, N.E., Reginaldo, N.S., Longo, J.N., da Fonseca Jr, R., Conte, M.G., Morales, R.E.M., & da Silva, M.J. (2024). Advancing oil and gas pipeline monitoring with fast phase fraction sensor. *Measurement Science and Technology*, 35, 125302. doi: 10.1088/1361-6501/ad73f5

[6] Salehi, S.M., Karimi, H., & Dastranj, A.K. (2017). A capacitance sensor for gas/oil two-phase flow measurement: exciting frequency analysis and static experiment. *IEEE Sensors Journal*, 17, 679–686. doi: 10.1109/JSEN.2016.2637399

[7] Salehi, S.M., Karimi, H., Moosavi, R., & Dastranj, A.K. (2017). Different configurations of capacitance sensor for gas/oil two phase flow measurement: An experimental and numerical study. *Experimental Thermal and Fluid Science*, 82, 349–358. doi: 10.1016/j.expthermflusci.2016.11.027

[8] Ahmed, W.H., & Ismail, B.I. (2008). Innovative techniques for two-phase flow measurements. *Recent Patents on Electrical Engineering*, 1, 1–13. doi: 10.2174/1874476110801010001

[9] Aslam, M.Z., & Tang, T.B. (2014). A high resolution capacitive sensing system for the measurement of water content in crude oil. *Sensors*, 14, 11351–11361. doi: 10.3390/s140711351

[10] Wolffenbuttel, R.F., & Regtien, P.P.L. (1987). Capacitance-to-phase angle conversion for the detection of extremely small capacities. *IEEE Transactions on Instrumentation and Measurement*, IM-36(4), 868–872. doi: 10.1109/TIM.1987.6312572

[11] Jaworek, A., & Krupa, A. (2010). Phase-shift detection for capacitance sensor measuring void fraction in two-phase flow. *Sensors and Actuators A*, 160, 78–86. doi: 10.1016/j.sna.2010.04.003

[12] Demori, M., Ferrari, V., Strazza, D., & Poesio P. (2010). A capacitive sensor system for the analysis of two-phase flows of oil and conductive water. *Sensors and Actuators* A, 163, 172–179. doi: 10.1016/j.sna.2010.08.018

[13] dos Reis, E., & da Silva Cunha, D. (2014). Experimental study on different configurations of capacitive sensors for measuring the volumetric concentration in two-phase flows. *Flow Measurement and Instrumentation*, 37, 127–134. doi: 10.1016/j.flowmeasinst.2014.04.001

[14] Abou-Arkoub, A., Thorn, R., & Bousbaine, A. (2010). Online validation of multiphase flowmeters using simple capacitance sensors. *IEEE Transactions on Instrumentation and Measurement*, 59(10), 2671–2682. doi: 10.1109/TIM.2010.2045554

[15] Wu, H., Tan, Ch., Dong, X., & Dong, F. (2015). Design of a Conductance and Capacitance Combination Sensor for water holdup measurement in oil–water two-phase flow, *Flow Measurement and Instrumentation*, 46, 218–229. doi: 10.1016/j.flowmeasinst.2015.06.026

[16] Maurya, O.P., & Parasuraman, S. (2024). Semi-cylindrical and cylindrical cross-capacitive sensors for micro-droplet detection. *Sensors and Actuators A*, 377, 115747. doi: 10.1016/j.sna.2024.115747

[17] *AD7746: 24-bit, 2 Channel Capacitance to Digital Converter*. Data sheet. https://www.analog.com/en/products/ad7746.html [accessed 23 July 2025].

[18] *FlexPDE – Multiphysics Software for Partial Differential Equations*. https://www.pdesolutions.com [accessed on 23 July 2025].

[19] Backstorm, G. (2004). *Fields of Physics by Finite Element Analysis: Electricity, Magnetism, and Heat in 2D and 3D. Using FlexPDE® Version 5*. GB Publishing, Malmö, Sweden.

[20] Guru, B., & Hiziroğlu, H.R. (2004). *Electromagnetic Field Theory Fundamentals* (2nd ed.). Cambridge University Press, Cambridge, UK.

[21] Tollefsen, J, & Hammer, E.A. (1998). Capacitance sensor design for reducing errors in phase concentration measurements. *Flow Measurement and Instrumentation*, 9, 25–32. doi: 10.1016/S0955-5986(98)00006-5

[22] Alvarez, J.O., Jacobi, D., Althaus, S., & Elias, S. (2012). Dielectric characterization of geochemical properties of liquid hydrocarbons 25°C to 125°C. *Fuel*, 288, 119679. doi: 10.1016/j.fuel.2020.119679

Co-published by
Institute of Fluid-Flow Machinery
Polish Academy of Sciences
Committee on Thermodynamics and Combustion
Polish Academy of Sciences

http://www.imp.gda.pl/archives-of-thermodynamics/

ARCHIVES
OF THERMODYNAMICS

Heat Transfer Analysis of a Longitudinal Fin Attached to a Beta-Type Stirling Engine

Ishita Rai*, Rajeev Kumar

Birla Institute of Technology, Mesra 835215, India
*Corresponding author email: phdme10006.21@bitmesra.ac.in

Received: 01.01.2025; revised: 31.05.2025; accepted: 26.07.2025

Abstract

Our proposed model is a highly non-linear parabolic heat transfer equation for the longitudinal fin with an insulated fin tip, temperature dependent thermal conductivity, and internal heat generation in the transient condition. The research comprises several components, namely, a discussion of the longitudinal fin heat transfer model, its solution, the validation of the numerical scheme and solution analysis, and finally, the influence of fin attachment on the system. Mathematical formulations were developed to represent identified fin parameters. This enables us to investigate further their variation patterns, therefore making future modelling easy as well as providing a better understanding of their applicability in developing energy storage systems.

Keywords: Stirling engine; Longitudinal fin; FERK (4,5) scheme; Heat transfer; Thermoelectric generator

Vol. 46(2025), No. 3, 51–60; doi: 10.24425/ather.2025.156578

Cite this manuscript as: Rai, I., & Kumar, R. (2026). Heat Transfer Analysis of a Longitudinal Fin Attached to a Beta – Type Stirling Engine. *Archives of Thermodynamics*, 46(3), 51–60.

1. Introduction

Stirling engines were developed in 1816 by Rev. Robert Stirling. They work in a closed regenerative cycle in which a working fluid is externally heated. The cyclic compression and expansion of fluid is utilised by the piston to produce power. As a result of its multi-fuel functionality, it has a wide range of applications, Yang et al. [1]. Based on the location of the piston and cylinder configuration, these engines are classified into three types: Alpha, Beta and Gamma type Stirling Engines. Other classifications include free-piston Stirling engines, double-acting Stirling engines, thermal lag Stirling engines, multi-cylinder liquid-piston Stirling engines, pulse tube Stirling engines, and thermoacoustic Stirling engines, etc. [2]. Stirling engines have been designed in a wide range from large marine engines to the nanoscale [3,4]. Its applications are prophesied from outer space to the human heart [3,5].

It has been found that although the Stirling cycle claims to have an efficiency on the same scale as the Carnot cycle, its practical application does not have that high efficiency. Simultaneous heating and cooling come as the biggest challenge, in maintaining the desired temperature difference.

The first analytical model for the Stirling engine was developed by Schmidt in 1871 [6]. Building on this, researchers like Finkelstein et al. [7], Walker [8], and Kirkley [9] explored optimal phase angles and swept volume ratios for alpha, beta, and gamma types of Stirling engines and refrigerators. In their findings, it appears that the β-type Stirling engine produces the high-

Nomenclature

A_c – cross-sectional area of fin, m^2
A_m – dimensionless amplitude of base temperature
c – specific heat of fin material, J/(kg·K)
Fo – Fourier number
f – frequency related to engine operating speed
G – internal heat generation coefficient or generation number
h – Newton's cooling constant, W/(m^2·K)
$k(T)$– thermal conductivity, W/(m·K)
L – length of the fin, m
N – thermogeometric fin parameter
P – fin perimeter, m
q – internal heat generation, W/m^2
Re – Reynolds number,
T – temperature, K
t – time, s
x – space co-ordinate, m

Greek symbols

ε – internal heat generation parameter, 1/K
θ – local fin temperature
X – coordinate space
ε_G – associate coefficient of internal heat generation
ρ – density of fin material, kg/m^3
ω – periodicity, s^{-1}
Ω – non-dimensional periodicity
Φ – phase shift

Subscripts and Superscripts

b – base
∞ – ambient
m – mean

Abbreviations and Acronyms

FERK – finite element Runge-Kutta
ERS – energy recovery systems
TEG – thermoelectric generator

est indicated work, while the gamma-type yielded the lowest. Further studies confirmed that β-types are more efficient than alpha or gamma types under similar conditions [10].

In addition to thermodynamic models, a three-dimensional CFD approach can be used to analyse the Stirling engine. Mahkamov [11] conducted a CFD simulation for a solar powered Striling engine, while Hung and Cheng [12] used CFD methods to predict flow, pressure, and thermal fields in a piston-cylinder assembly. Although CFD methods provide detailed information, they are more time-consuming and computationally intensive than thermodynamic models [13].

The performance of the Stirling engine depends on the temperature difference between the hot and cold regions. Once the engine starts to work, the heated working fluid is forced to expand and moves towards the colder region. This exchange of working fluid between the cold region and hot region, if remains unchecked, will generate a uniform temperature profile throughout the cylinder and will seize the engine operation. Fins are attached to perform this task efficiently. Kumaravelu et al. [14] studied the Stirling engine performance without and with different fin configuration models. They found that engine efficiency without fin attachment is 10.26%; with circular fins attached, its efficiency is 14.41%, with pin fins attached, its efficiency is 16.64%, and when rectangular fins are attached, its efficiency is 19.03%. They concluded that rectangular fins are more efficient due to their larger surface area. Since fin properties and geometry vary, mathematical studies are needed to assess their impact on cooling efficiency. In Stirling engines, since there are no valves or ports for induction or exhaust, energy is transferred through cylinder walls or heat exchangers. Thus, fins play a crucial role in indirect heat rejection to the surroundings. Numerous studies have modelled heat transfer in fins [14−18].

Energy recovery systems (ERS) such as a thermoelectric generator (TEG) work on the principle of the Seebeck effect. When combined with Stirling engines, TEG provides an opportunity to convert waste heat into additional electric power. It has been found by Faraj et. al. [19] that attaching fins to a 40×40 cm^2 flat plate TEG system generates 3.8 W of electrical power in combination with solar radiation of 2000 W/m^2 and reduces one ton of carbon dioxide emission yearly. Energy recovery systems are strategies used to recover system energy that would otherwise be squandered. In recent years, ERS has been regarded as a cost-effective choice for increasing efficiency, and as a result, the potential advantages of those systems are being fully utilised [20]. Ideally, when applying ERS, energy must be utilised continuously, and the efficiency gain must be significant in all conditions. Waste energy from the Stirling engine can be harvested in developing ERS utilising the fins attached to its colder section. For a waste heat recovery system for power generation, in a lower temperature range, Chen et al. [21] suggested adding fins within a range of 0–27 items, which significantly enhances heat transport and the performance of thermoelectric modules (TEMs). At Re = 10 and 100, a perfect number of fins is 21, whereas it is 27 at Re =1000. At Re =1000, the highest overall power generated is 0.411 W, and the average efficiency of conversion is 0.95%. When compared to TEMs without fins, these figures represent 105.5% and 43.94% enhancements, respectively.

1.1. Present contribution

Our proposed model is a highly non-linear parabolic heat transfer equation for the longitudinal fin with an insulated fin tip, temperature dependent thermal conductivity and internal heat generation. It is a realistic model of the longitudinal fin compared to the existing model. This type of model is for the first time used in the transient and highly non-linear conditions in the fin material. FERK(4,5) scheme is used for the solution of our non-linear parabolic heat transfer equation. The research comprises six components. The first component is to discuss longitudinal fin heat transfer modelling. The second section contains a system description; the third section concentrates on solving the problem. In the fourth section, the validation analysis of the numerical scheme has been presented. The fifth section discusses the influence of parameters on the system. The sixth section is devoted to final conclusions.

A key gap identified in the available research literature is the absence of transient heat transfer modelling of a fin attached to the cold region of a β-type Stirling engine. The given model represents a realistic situation as:

1. the mathematical formulation was developed to represent identified fin parameters; this enables us to investigate further their variation patterns, therefore making future modelling easy as well as providing a better understanding of their applicability in developing energy storage systems;
2. the model provides a mathematical backup to the study of heat transfer through the fin.

2. System description

We consider a system consisting of a β-type Stirling heat engine operating between a heat source and a heat sink at the temperatures T_H and T_L, respectively (Fig. 1). Near the wall area, hydrodynamically non-slip walls satisfying the temperature continuity and heat flux continuity at both sides of the wall are applied to accurately simulate the thermo-hydraulic output [14]. The cold region includes longitudinal fins (Fig. 2).

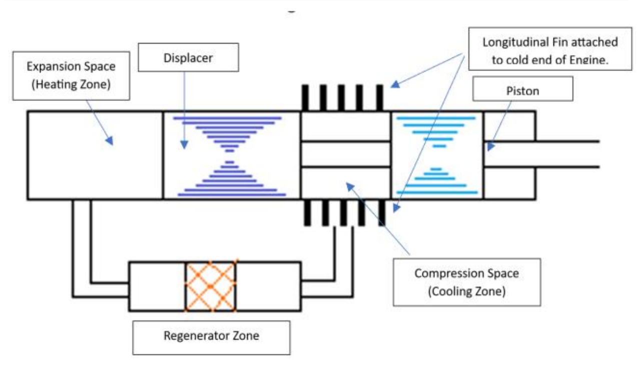

Fig. 1. Fin attachment to “cold region” of β-type Stirling engine.

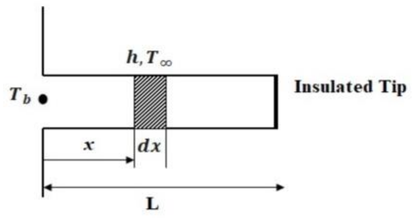

Fig. 2. Schematic geometry of the longitudinal fin.

For boundary conditions, a conjugated heat transfer was assumed for the fin fluid/solid wall [14]. The temperature at the base of the longitudinal fin varies cyclically due to cyclic changes in the temperature of the working gas, within the cylinder. The area of the cross-section of the fin is A_c, thickness b, length L, and perimeter P. Width is dominated by length, i.e. $b/L \ll 1$. The amount of heat dissipated from the tip can be discounted to be zero as the tip area is negligible in comparison to the total fin area [22,23]. When heat is generated inside the fin by utilising an external energy source, an opportunity for dynamic thermal management, hybrid thermal circuit and energy recovery is observed. The internal heat generation term, q, has been added in the analysis to cover such scenarios. The physical properties of the longitudinal fin and system assumptions are considered as follows:

1. A transient state is assumed.
2. The fin material has a temperature dependent thermal conductivity.
3. The density of longitudinal fin material is ρ, and the specific heat is c.
4. Fin is assumed to have a uniform cross-sectional area.
5. Conduction is assumed to be in one dimension.
6. We assume a constant convective heat transfer coefficient h. The convection is assumed to happen at the fin surface exposed to the surrounding only.
7. A local fin temperature-dependent internal heat generation is denoted by q.
8. Temperature variation at the fin base is assumed to be a function of engine dynamic characteristic, phase angle Φ.

2.1. Mathematical Formulation

Under the above assumptions, the differential equations governing heat transfer in the longitudinal fin come out as [23−25]:

$$\rho c \frac{\partial T}{\partial t} = \frac{\partial}{\partial x}\left\{k(T)\frac{\partial T}{\partial x}\right\} - \frac{hP}{A_c}(T - T_\infty) + q(T), \qquad (1)$$

where:

$$q(T) = q_\infty\{1 + \varepsilon(T - T_\infty)\},$$

$$k(T) = k_\infty\{1 + \alpha(T - T_\infty)\}.$$

The initial conditions are assumed as:

$$T(x, o) = T_\infty, \qquad (2)$$

and the temperature at the base of the longitudinal fin is given by [24−27]:

$$T(0, t) = T_{b,m} + A_m\left(T_{b,m} - T_\infty\right)\cos(\omega t + \Phi), \qquad (3)$$

where $T_{b,m}$ is the mean base temperature of the cold side during the cycle. A_m is the dimensionless amplitude of the base temperature and $\omega = 2\pi f t$, where frequency f is directly related to the engine operating speed. Time in seconds is represented by t. $\Phi \in [0, 2\pi]$ represents the phase shift, covering the one complete cycle of the cosine wave.

In the actual phenomenon, the temperature profile decreases with respect to x, see Fig. 2. We consider the insulated tip [22,23] in our assumption, so at $x = L$, we use the condition:

$$\frac{\partial T}{\partial x}(L, t) = 0. \qquad (4)$$

By introducing non-dimensional variables and similarity criteria as follows:

$$\theta = \frac{T - T_\infty}{T_{b,m} - T_\infty}, \quad X = \frac{x}{L}, \quad \mathrm{Fo} = \frac{k_\infty t}{\rho c L^2}, \quad N^2 = \frac{hPL^2}{k_\infty A_c}, \quad \Omega = \frac{\rho c L^2 \omega}{k_\infty} \qquad (5)$$

$$G = \frac{q_\infty A_c}{hP(T_{b,m} - T_\infty)}, \quad \varepsilon_G = \varepsilon\left(T_{b,m} - T_\infty\right), \quad \beta = \alpha\left(T_{b,m} - T_\infty\right),$$

the system of Eqs. (1)–(4), in a non-dimensional form reduces to:

$$\frac{\partial\theta(X,\mathrm{Fo})}{\partial\mathrm{Fo}} = (1+\beta\theta)\frac{\partial^2\theta(X,\mathrm{Fo})}{\partial X^2} + \beta\left(\frac{\partial\theta}{\partial X}\right)^2$$

$$-N^2(1-G\varepsilon_G)\theta(X,\mathrm{Fo}) + N^2G, \tag{6}$$

$$\theta(X,0) = 0, \tag{7}$$

$$\theta(0,\mathrm{Fo}) = 1 + A_m\cos(\varOmega\mathrm{Fo}+\varPhi), \tag{8}$$

$$\frac{\partial\theta(1,\mathrm{Fo})}{\partial X} = 0. \tag{9}$$

3. Solution of the problem

The hybrid numerical scheme combining two techniques has been developed. The first one is discretization in space coordinates, and the other one is the Runge-Kutta (4,5) scheme. We discretised the space coordinate [0, 1] into n+1 equal size subintervals of length h. Using finite differences, the boundary value problem (Eqs. (6)–(9)) reduces to an initial value problem of the system of first-order non-linear ordinary differential equations, as follows:

$$\frac{\mathrm{d}\theta_1}{\mathrm{dF_o}} = -\left[\frac{2}{h^2} + N^2(1-\varepsilon_G G)\right]\theta_1 + \frac{\theta_2}{h^2} + \frac{\beta}{h^2}\left(-2\theta_1^2 + \theta_1\theta_2 + \frac{1}{4}\theta_2^2\right) + \frac{\beta}{h^2}\left(\theta_1 - \frac{1}{2}\theta_2\right)(1 + A_m\cos(\varOmega\mathrm{Fo}+\varPhi)) +$$
$$+\frac{(1+A_m\cos(\varOmega\mathrm{Fo}+\varPhi))}{h^2} + \frac{\beta}{4h^2}(1+A_m\cos(\varOmega\mathrm{Fo}+\varPhi))^2 + N^2G, \tag{10}$$

$$\frac{d\theta_i}{d\mathrm{Fo}} = \frac{\theta_{i-1}}{h^2} - \left[\frac{2}{h^2} + N^2(1-\varepsilon_G G)\right]\theta_i + \frac{\theta_{i+1}}{h^2} + \frac{\beta}{h^2}(\theta_i\theta_{i+1} - 2\theta_i^2 + \theta_i\theta_{i-1}) + \frac{\beta}{4h^2}(\theta_{i+1}^2 - 2\theta_{i+1}\theta_{i-1} + \theta_{i-1}^2) + N^2G,$$
$$i = 2,\dots,n-1, \tag{11}$$

$$\frac{d\theta_n}{d\mathrm{Fo}} = \frac{\theta_{n-1}}{h^2} - \left[\frac{2}{h^2} + N^2(1-\varepsilon_G G)\right]\theta_n + \frac{\beta}{h^2}\left[-2\theta_n^2 + \theta_n\theta_{n-1}\right] + \frac{\beta}{4h^2}\theta_{n-1}^2 + N^2G + \frac{1}{h^2}\left[1 + \beta\theta_n - \frac{\alpha}{2}\theta_{n-1}\right]\theta_{n+1} + \frac{\beta}{4h^2}\theta_{n+1}^2, \tag{12}$$

under the initial condition:

$$\theta_i(0) = 0. \tag{13}$$

To calculate the tip temperature of the fin, using a three-point formula, we write:

$$\theta_{n+1} = \frac{1}{21}(13\theta_n + 17\theta_{n-1} - 9\theta_{n-2}). \tag{14}$$

The highly non-linear system of first-order non-linear ordinary differential equations (10)−(12) under the initial condition (13) is solved using the Runge-Kutta (4,5) technique. For all computational work, MATLAB-R2024 software is utilised.

3.1. Exact solution

For the validation of the proposed numerical scheme of the problem, an analytical solution is required. When we assume the associated coefficient of thermal conductivity β =0, and the boundary condition at the base of the fin as constant in Eqs. (6) and (8), then the proposed model of heat transfer is changed into the following form:

$$\frac{\partial\theta(X,\mathrm{Fo})}{\partial\mathrm{Fo}} = \frac{\partial^2\theta(X,\mathrm{Fo})}{\partial X^2} - N^2(1-G\varepsilon_G)\theta(X,\mathrm{Fo}) + N^2G, \tag{15}$$

$$\theta(X,0) = 0, \tag{16}$$

$$\theta(0,\mathrm{Fo}) = 1, \tag{17}$$

$$\frac{\partial\theta(1,\mathrm{Fo})}{\partial X} = 0. \tag{18}$$

Applying the Laplace transform technique, the exact solution of the system of Eqs. (15)–(18) comes out as follows:

$$\theta(X,\mathrm{Fo}) = \frac{\cosh\left(\sqrt{N^2(1-G\varepsilon_G})(X-1)\right)}{\cosh\left(\sqrt{N^2(1-G\varepsilon_G}\right)} + \sum_{n=1}^{\infty}\frac{(-1)^{n+1}e^{s_n\mathrm{Fo}}(2n-1)\pi\cos(2n-1)\frac{\pi}{2}(X-1))}{s_n} - \frac{G\cosh\left(\sqrt{N^2(1-G\varepsilon_G)}(X-1)\right)}{(1-G\varepsilon_G)\cosh(\sqrt{N^2(1-G\varepsilon_G)}} + \frac{G\,e^{-N^2(1-G\varepsilon_G)\mathrm{Fo}}}{(1-G\varepsilon_G)} +$$
$$\sum_{n=1}^{\infty}\frac{(-1)^{n+1}4N^2Ge^{s_n\mathrm{Fo}}\cos\left((2n-1)\frac{\pi}{2}(X-1)\right)}{s_n(2n-1)\pi} + \frac{G\left(1-e^{-N^2(1-G\varepsilon_G)\mathrm{Fo}}\right)}{(1-G\varepsilon_G)}, \tag{19}$$

where: $s_n = -(2\pi-1)^2\left(\frac{\pi^2}{4}\right) - N^2(1-G\varepsilon_G);\ n \in N.$

4. Numerical simulation and analysis

In the proposed work, the temperature in the longitudinal fin is studied under the Neumann boundary condition. We consider a temperature dependent thermal conductivity and internal heat generation term, which are functions of local temperature. The FERK (4,5) scheme is applied for the solution of this non-linear parabolic equation to calculate the temperature in the longitudinal fin. The obtained solution is presented in the form of two- and three-dimensional figures. Only the parameters whose values differ from the reference values have been indicated. The selected reference values of dimensionless parameters used to calculate the non-dimensional temperature profile in the longitudinal fin in the finite domain are given in Table 1.

Table 1. The selected reference value of dimensionless parameters.

Parameter	Symbol	Numerical value	Reference
Associated coefficient of thermal conductivity	β	0.2	[28]
Fin parameter	N	1	[28]
Internal heat generation coefficient	G	0.2	[1]
Associated coefficient of internal heat generation	ε_G	0.2	[1]
Dimensionless amplitude of the base temperature	A_m	0	[18]
Dimensionless periodicity	$\varOmega$	0	[18]

4.1. Validation of proposed numerical scheme

The FERK (4,5) scheme has been used to obtain a numerical solution of the highly non-linear parabolic equation of heat transfer in the longitudinal fin. By unifying the two techniques, we achieve a greater accuracy with a negligible local error [29,30]. Figure 3 shows a comparative analysis between the FERK (4,5) scheme and the exact analytical solution obtained using the Laplace transform technique. It is found that the developed FERK (4,5) scheme is in excellent agreement with the exact solution. By analysing Fig. 3, we observe a good accuracy with minimum computational complexity, highlighting the advantage of the proposed method [28].

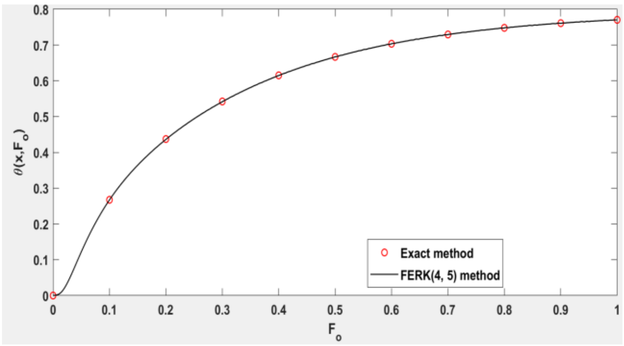

Fig. 3. Comparison between the exact method and FERK (4,5) method.

5. Results and discussion

We discuss the effects of several non-dimensional parameters, affecting heat transfer analysis in the longitudinal fin.

5.1. Effect of Ω and A_m at $\Phi = 0, \pi/2, \pi$

In order to include cyclic temperature variation in the cold wall side, we have introduced three parameters, namely, A_m, dimensionless amplitude of base temperature, Ω, non-dimensional periodicity, and Φ, representing the phase shift, which are included in Eq. (8) [18].

Here A_m represents thermal inertia, reflecting temperature fluctuations, in reference to the mean temperature difference in the cold cylinder wall. In other words, by using A_m in the model, the intensity of thermal oscillations can be quantified. From previous studies [31,32], it was evident that a suitable value of A_m for stable heat transfer in Stirling engines lies between 0.1 and 0.3. Higher values beyond 0.7–1.0 provide a non-ideal behaviour with a thermal lag leading to lower efficiency. Very high values of A_m may cause entropy generation, reducing the network output of the engine. It is evident from Fig. 4 that the non-dimensional temperature increases with the non-dimensional space coordinate as A_m increases, for $\Phi = 0$; the non-dimensional temperature decreases with the non-dimensional space coordinate as A_m increases, for $\Phi = \pi$, and remains constant for $\Phi = \pi/2$. A similar result is obtained by Singh et al. [18] for $\Phi = 0$, as they have studied for $\Phi = 0$, only. Real Stirling engines have thermal inertia: there is a delay between heating the wall and gas temperature rising. Φ can model this delay, accounting for thermal diffusion time. ωt tracks the cyclical evolution of the engine over time. It helps predict when in time the system reaches peak or trough temperatures for optimal heat exchange.

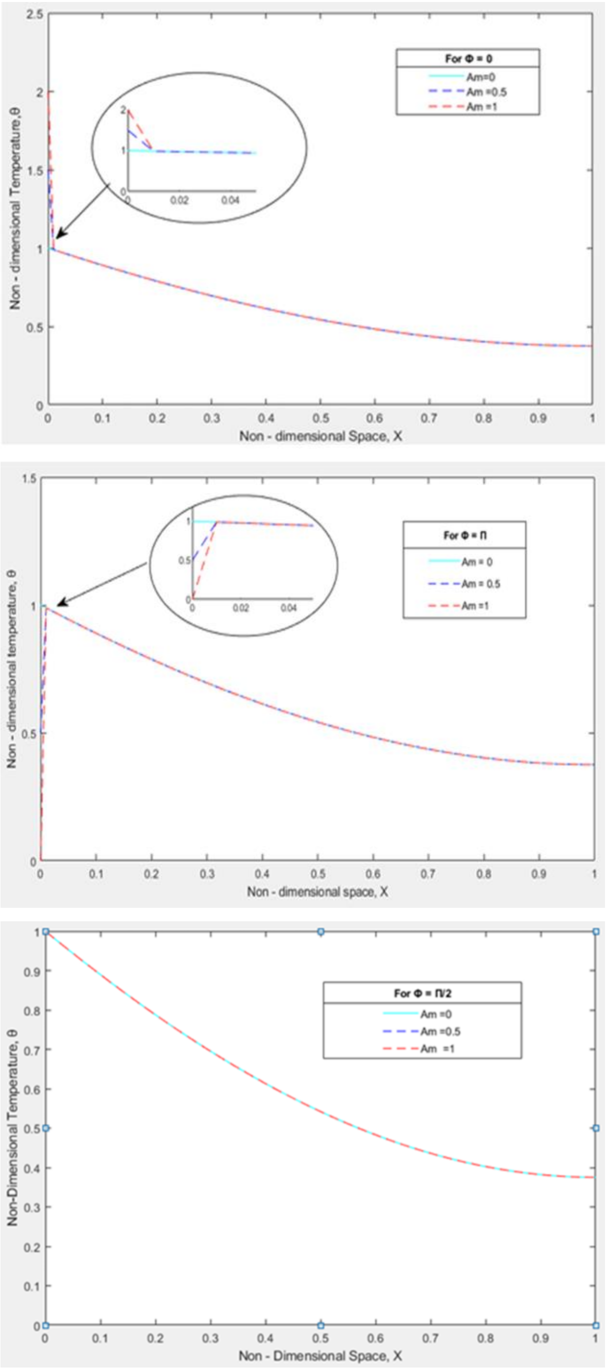

Fig. 4. Variation in dimensionless amplitude of base temperature A_m for fixed values of $\alpha = 1$, $G = 0.2$, $\Omega = 0$, $N = 1$, $\varepsilon_G = 0.2$, Fo = 0.3.

Figure 5 shows the variation of non-dimensional temperature with respect to non-dimensional space coordinates for different values of Ω. It is evident from these figures that θ is the maximum for $\Omega = 0$, and the lowest for $\Omega = 10$, while it lies in between for $\Omega = 100$ when $\Phi = 0$. For $\Phi = \pi$, the non-dimensional temperature θ with respect to non-dimensional space coordinate is the highest when $\Omega = 10$, and the lowest when $\Omega = 0$, and in between for $\Omega = 100$. Further, the non-dimensional temperature, θ, is the highest for $\Omega = 100$ and the lowest for $\Omega = 0$, but in between when $\Omega = 10$, for $\Phi = \pi/2$. A similar result is obtained by Singh et al. [18] for $\Phi = 0$.

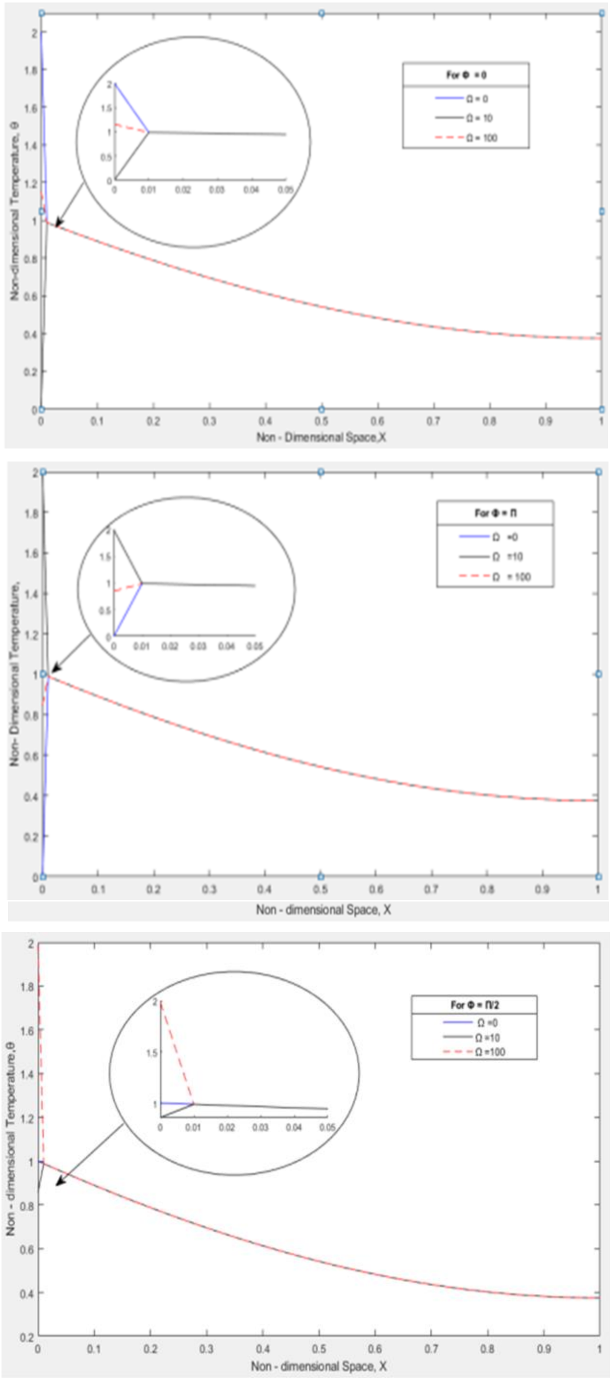

Fig. 5. Variation in non-dimensional periodicity, Ω, for fixed values of $\alpha = 1$, $G = 0.2$, $A_m = 1$, $N = 1$, $\varepsilon_G = 0.2$, Fo = 0.3.

5.2. Effect of Fo and *X*

In Figure 6, we analyse the behaviour of temperature distribution in the longitudinal fin with respect to non-dimensional time, Fo, and non-dimensional space coordinate X. This figure has two components – Figs. 6(a) and 6(b). Figure 6(a) demonstrates the variation of non-dimensional temperature with Fo for different values of X, when $\beta = G = \varepsilon_G = 0.2$ and $N = 1$. We observe from this figure that the non-dimensional temperature increases with Fo but decreases as X increases. Figure 6(b) presents the variation of non-dimensional temperature vs. X for varying Fo, for the same values of fin parameters. It shows that the tip temperature increases as Fo grows, and decreases with time.

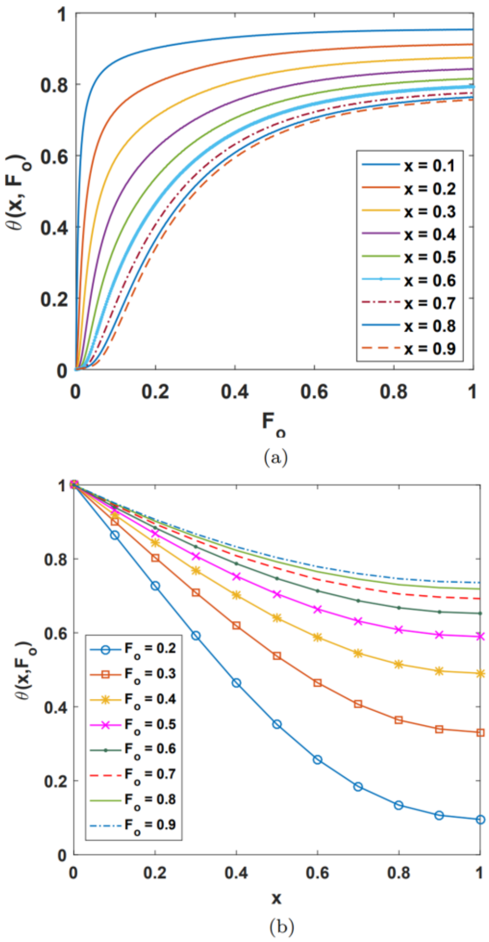

(a)

(b)

Fig. 6. Temperature distribution in fin vs.: (a) dimensionless time coordinate (F_o), (b) dimensionless space coordinate (x) when $\beta = 0.2$, $N = 1$, $G = 0.2$, and $\varepsilon_G = 0.2$.

5.3. Effect of *β*

Figure 7 shows the effect of β in two- and three-dimensional coordinate space. It is observed that as β increases, the temperature in the fin increases with Fo and X. This confirms the improved fin conductivity and a more uniform temperature distribution in the fin.

5.4. Effect of *N*

Figure 8 demonstrates the effect of fin parameter N in two- and three-dimensional coordinate systems. We draw Fig. 8(a) as non-dimensional temperature vs. non-dimensional time, Fo, and Fig. 8(b) as non-dimensional temperature vs. non-dimensional space coordinate. It is observed that the temperature in the longitudinal fin increases along Fo and X as the values of N decrease. The fin parameter N increases as convective heat transfer coefficient h, fin perimeter p, and fin length L increase, while the conductivity of fin material, k, and its cross-sectional area A_c decrease. Therefore, it can be concluded that a higher value of N promotes convection, resulting in a better cooling effect.

Thus, a long thin fin will have a prominent temperature difference between both ends. Therefore, it can be concluded that, as *N* increases, the conductivity pattern deteriorates. In other words, a lower *N* number denotes thick and short fins, whereas a higher value of *N* shows a better cooling effect.

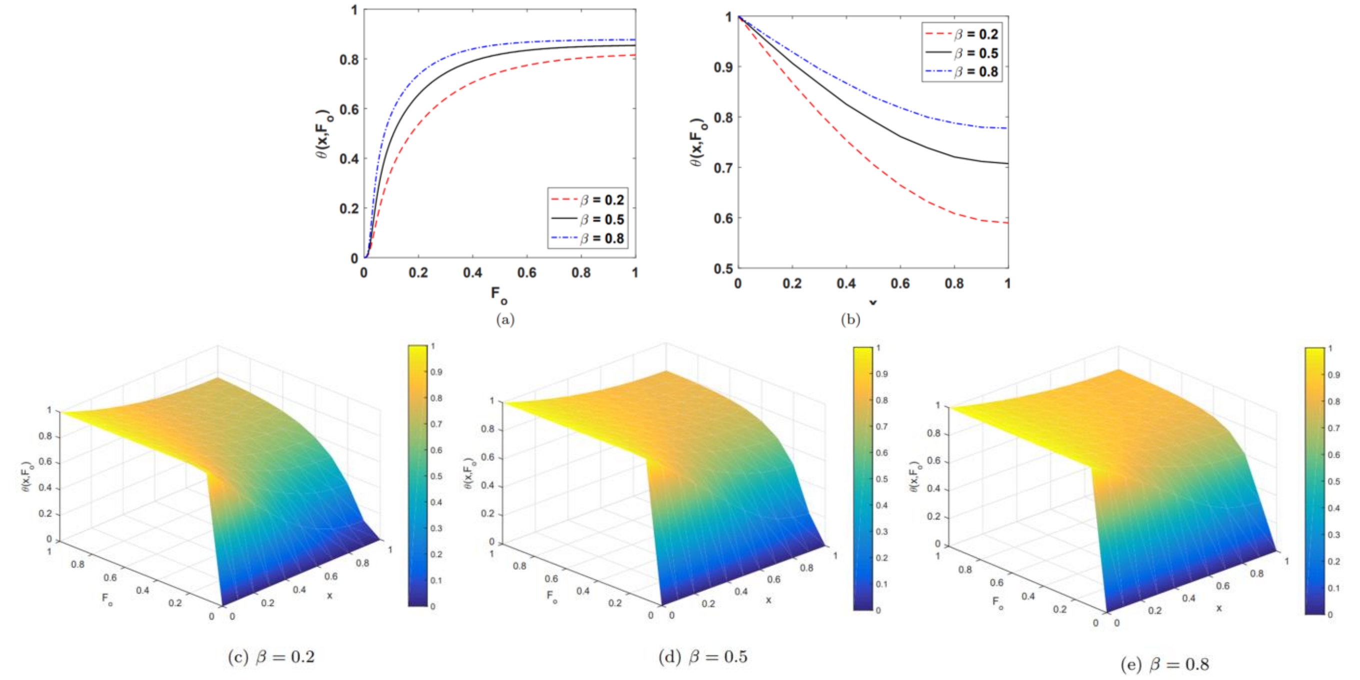

(a)

(b)

(c) $\beta = 0.2$

(d) $\beta = 0.5$

(e) $\beta = 0.8$

Fig. 7. Temperature distribution in fin vs.: (a) dimensionless time coordinate (F_o), when β =0.2, 0.5, 0.8 and X = 0.5; (b) dimensionless space coordinate (X), when β = 0.2, 0.5, 0.8 and Fo =0.5; (c) Fo and X, when β = 0.2; (d) Fo and X, when β = 0.5; (e) Fo and X, when β =0.8 for fixed numerical values of β = 0.2, N =1, G = 0.2, and ε_G = 0.2.

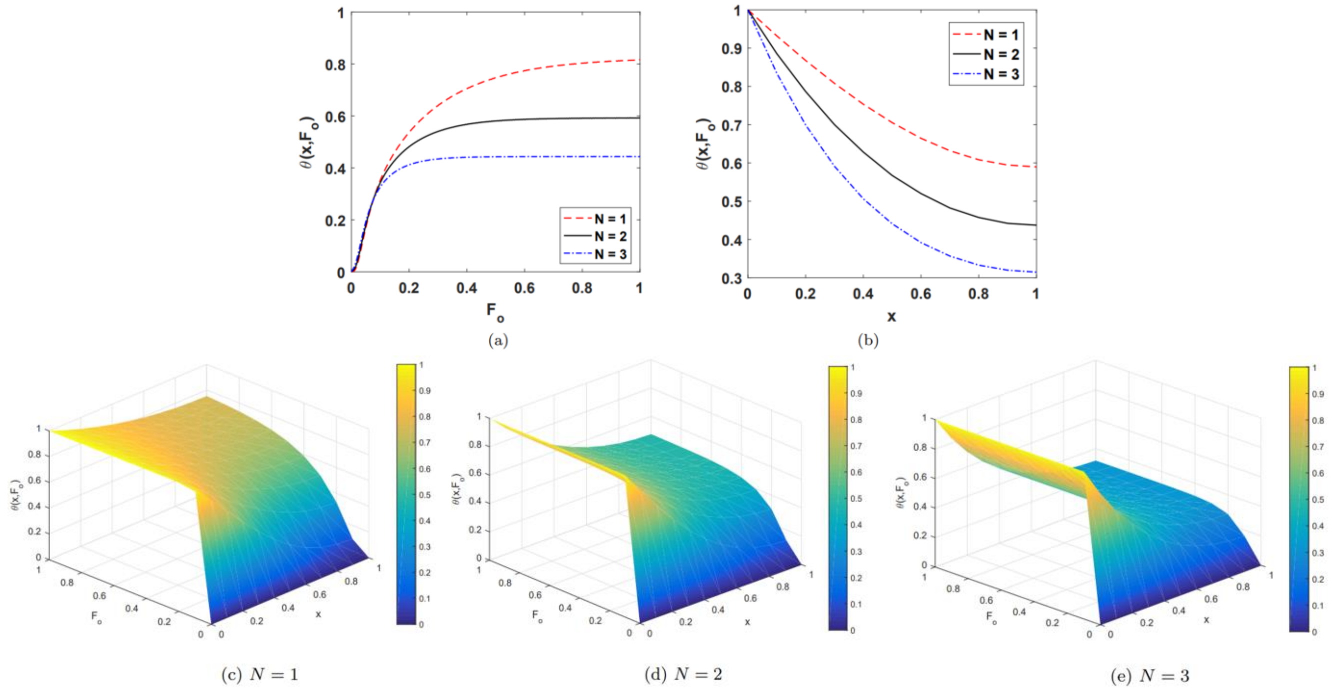

(a)

(b)

(c) $N = 1$

(d) $N = 2$

(e) $N = 3$

Fig. 8. Temperature distribution in fin vs.: (a) dimensionless time coordinate (F_o), when β =0.2, 0.5, 0.8 and X = 0.5; (b) dimensionless space coordinate (X), when β = 0.2, 0.5, 0.8 and Fo =0.5; (c) Fo and X, when β = 0.2; (d) Fo and X, when β = 0.5; (e) Fo and X, when β =0.8 for fixed numerical values of β = 0.2, N =1, G = 0.2, and ε_G = 0.2.

5.5. Effect of *G*

The effect of the internal heat generation coefficient in two- and three-dimensional coordinate systems is shown in Fig. 9. We draw Fig. 9(a) for the non-dimensional temperature vs. non-dimensional time coordinate, and Fig. 9(b) for the non-dimensional temperature vs. non-dimensional space coordinate. The temperature in the longitudinal fin increases along Fo and *X*, with an increase in G. This can be achieved by fin geometry where the cross-sectional area A_c has a smaller value and the perimeter p of the fin is large. This again supports a long fin for better cooling performance.

5.6. Effect of ε_G

Internal heat generation represents the amount of heat generated internally in the fin by consistent heating of the cooling section in the Stirling engine. Figure 10 depicts the effect of the associated coefficient of internal heat generation ε_G in two- and three-dimensional coordinate systems. We draw Fig. 10(a) for the non-dimensional temperature vs. non-dimensional space coordinate. The temperature in the longitudinal fin increases along both Fo and X as the values ε_G increase.

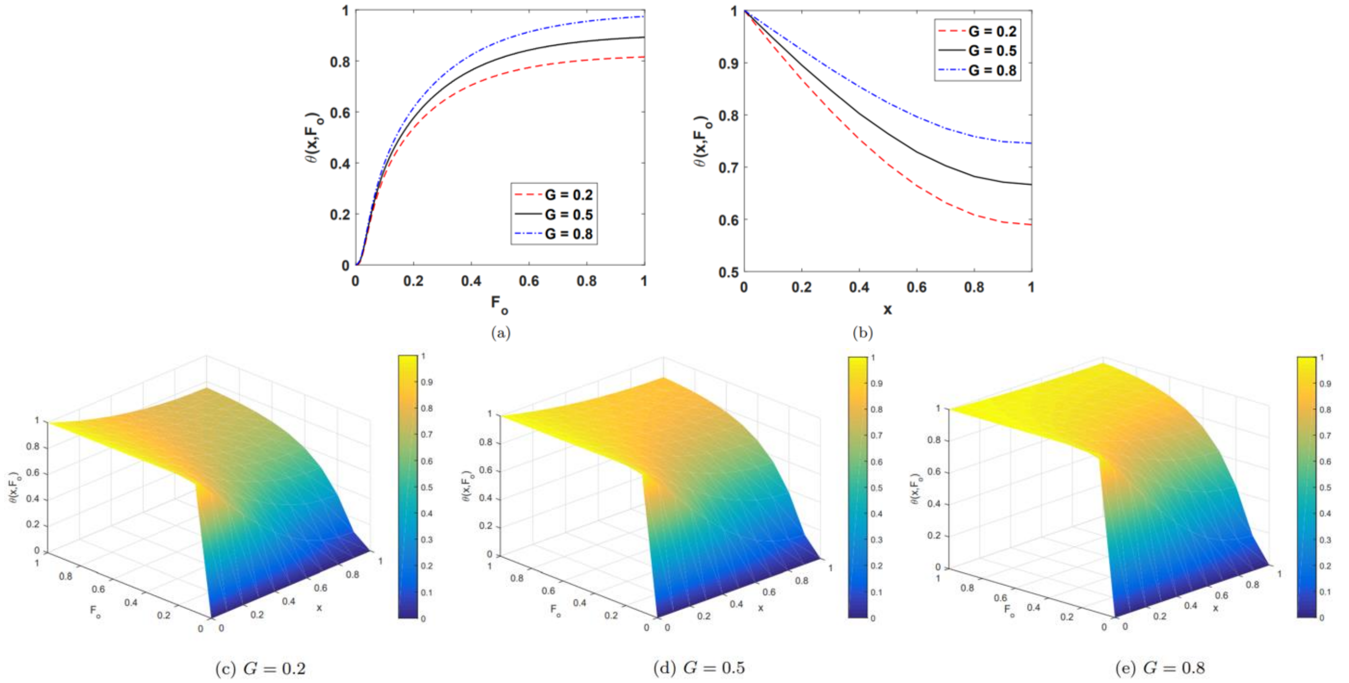

(c) $G = 0.2$ (d) $G = 0.5$ (e) $G = 0.8$

Fig. 9. Plot the temperature distribution in fin vs.: (a) dimensionless time coordinate (Fo), when $G = 0.2, 0.5, 0.8$; (b) dimensionless space coordinate (x), when $G = 0.2, 0.5, 0.8$; (c) Fo and x, when $G = 0.2$; (d) Fo and x, when $G = 0.5$; (e) Fo and x, when $G = 0.8$ for fixed numerical values of $\beta = 0.2$, $N = 1$ and $\varepsilon_G = 0.2$.

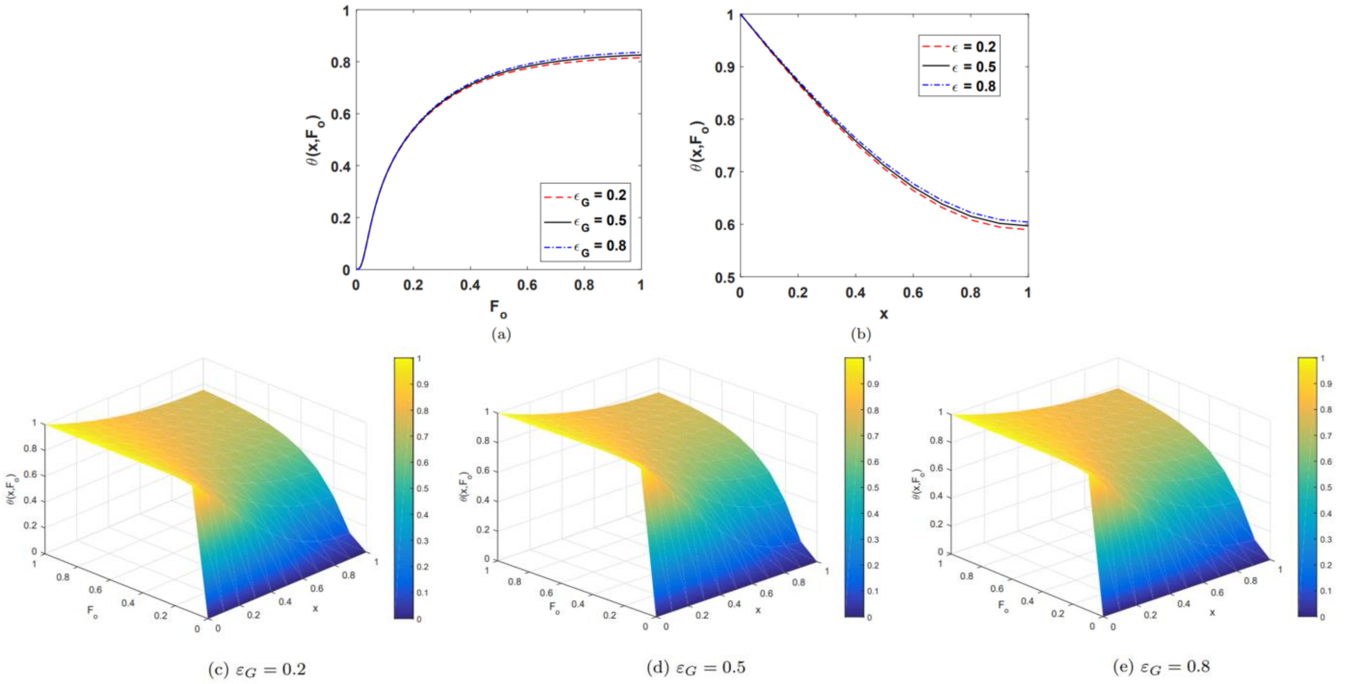

(c) $\varepsilon_G = 0.2$ (d) $\varepsilon_G = 0.5$ (e) $\varepsilon_G = 0.8$

Fig. 10. Plot of the temperature distribution in fin vs.: (a) dimensionless time coordinate (Fo),when $\varepsilon_G = 0.2, 0.5 , 0.8$; (b) dimensionless space coordinate (X), when $\varepsilon_G = 0.2, 0.5, 0.8$; (c) Fo and X, when $\varepsilon_G = 0.2$, (d) Fo and X, when $\varepsilon_G = 0.5$; (e) Fo and X, when $\varepsilon_G = 0.8$ for fixed numerical values of β= 0.2, N =1 and $G = 0.2$.

6. Conclusions

The goal of this study is to provide validation of the FERK (4,5) method and use this technique for evaluation of the thermal profile in a longitudinal fin attached to a cooler region of a β-type Stirling engine. The wasted heat through the fin is proposed to be utilised by an ERS in generating electricity. The obtained results were analysed for the variability of thermal conductivity and internal heat generation with temperature, thermogeometric fin parameters, and generation number. The important findings are summarised as follows:

1. FERK (4,5) method is justified with exact results in a specific case, and good accuracy is observed.
2. A_m and Ω do not significantly affect temperature distribution in the non-dimensional space over a wide range. For different values of A_m, graphs representing the non-dimensional temperature distribution in non-dimensional space quickly overlap.
3. A suitable value of phase angle Φ was shown by various researchers to be in the range of 60°−80°; As a function of cosine, the range in which Φ varies is from −1 to 1. It has been observed that by varying Φ, a delay can be introduced in the temperature curve for different values of A_m and Ω. The variation only affects the boundary condition at the base of the fin, and the nature of the curve soon follows similar trends for different values.
4. The temperature profile in the longitudinal fin increases along Fo and X both as the value of β increases. A higher value of β represents conduction as a prominent phenomenon, resulting in a uniform temperature profile in the fin.
5. The temperature profile in the longitudinal fin decreases when the fin parameter N increases, i.e. the temperature profile is inversely proportional to N. For fast cooling, we require a higher value of the N parameter.
6. An increase in the value of G will result in an increase in ambient heat generation as well as internal heat generation. This will elevate the fin temperature.
7. ε_G increases as the internal heat generation parameter ε increases. This will reduce the heat flux through the fin. As a result, the temperature of the fin will increase, providing an opportunity for hybrid energy system utilisation.

The above study concludes that thermodynamic parameters of the fin, temperature dependent conductivity of fin material, generation number G, and coefficient of internal heat generation play a significant role in releasing internally generated heat of machines into the environment. This research may be expanded to create a mathematical framework combining thermoelectric production in plate fins using simulation to calculate a low-temperature waste energy harvesting system to produce electricity. The developed system will consist of several thermoelectric modules (TEMs) attached to the cooling zone of the Stirling engine, which will provide an opportunity for waste heat utilisation in combination with the Stirling engine power. As a result, the system will incorporate a waste energy channel, a cooling zone, and thermoelectric modules. TEM is placed amid the cooling fins and the waste heat pipes. The temperature differential between the thermoelectric materials hot and cold surfaces will be utilised to transform wasted energy into electrical energy [32,33]. The heat transfer rate provides the researchers with sufficient opportunity to generate electricity utilising ERS. This model can be utilised to design the cold section of the Stirling engine to maintain the desired temperature difference for proper operation.

References

[1] Yang, H.S., Cheng, C.H., & Ali, M.A. (2011). Performance and operating modes of a thermal-lag Stirling engine with a flywheel. *Applied Thermal Engineering,* 205, 118061. doi 10.1016/j.applthermaleng.2022.118061

[2] Kitaya, K., & Isobe, M. (2022). Molecular Dynamics Study of a nano-scale Beta-Type Stirling Engine. *Journal of Pysics: Conference Series*, 2207, 012006. doi: 10.1088/1742-6596/2207/1/012006

[3] McKellar, S. (2016). Atomic hearts: A decade of US government-sponsored development. *Physics Today,* 69(5), 38−44.

[4] Hirata, K., & Kawada, M. (2005). Discussion of Marine Stirling Engine Systems. *Proceedings of the 7th International Symposium on Marine Engineering*, (pp. 1−5), October 24−28, Tokyo, Japan.

[5] Martini, W.R. (1983). *Stirling Engine Design Manual*. 2nd ed. NASA-CR-168088, Martini Engineering, Washington, USA.

[6] Schmidt, G. (1871). Theorie der geschlossenen calorischen maschine. Journal Zeitschrift des Österreichischen Ingenieur- und Architekten-Vereins, p. 79.

[7] Finkelstein, T., Walker, G., & Joschi, J. (1970). Design optimization of Stirling cycle cryogenic cooling engines, *Cryogenic Engineering Conference,* Paper K4, Boulder, Colorado, USA.

[8] Walker, G. (1962). An optimization of the principle design parameters of Stirling-cycle-machines. *Journal of Mechanical Engineering Science*, 4(3). doi: 10.1243/JMES_JOUR_1962_004_032_02

[9] Kirkley, D.W. (1965). A thermodynamic analysis of the Stirling cycle and a comparision with experiment. International Automotive Engineering Congress, Detroit, USA.

[10] Yang, H.S., Ali, M.A., Ravi Teja, K.V., & Yen, Y.F. (2022). Parametric study and design optimization of a kW-class beta-type Stirling engine. *Applied Thermal Engineering,* 215, 119010, doi: 10.1016/j.applthermaleng.2022.119010

[11] Mahkamov, K. (2006). An Axisymmetric Computational Fluid Dynamics Approach to the Analysis of the Working Process of a Solar Stirling Engine. *Journal of Solar Energy Engineering*, 128(1), 45−53, doi: 10.1115/1.2148979

[12] Hung, K.S., & Cheng, C.H. (2010). Numerical Prediction of Flow and Thermal Fields in a Reciprocating Piston-Cylinder Assembly. *Numerical Heat Transfer Part A: Application,* 38(4), 397−421, doi: 10.1080/104077800750022539

[13] Cheng, Ch.H., & Yang, H.S.. (2012). Optimisation of geometrical parameter for Stirling engine based on theoretical Analysis. *Applied Energy,* 92, 395−405, doi: 10.1016/j.apenergy.2011.11.046

[14] Kumaravelu, T., Saadon, S., & Talib, A.R.A. (2021). Heat transfer enhancement of a Stirling engine by using fins attachment in an energy recovery system. *Energy,* 239, 121881, doi: 10.1016/j.energy.2021.121881

[15] Singh, S., Kumar, D., & Rai, K.N. (2013). Wavelet collocation solution for convective radiative continuously moving fin temperature-dependent thermal conductivity. *International Journal of Engineering Advanced Technology*, 2(4), 6−10.

[16] Singh, S., Kumar, D., & Rai, K.N. (2014). Convective - radiative fin with temperature depnedent thermal conductivity, heat transfer coefficient and wavelength dependent surface emissivity.

Propulsion and Power Research, 3(4), 207−221, doi: 10.1016/j.jppr.2014.11.003

[17] Sigh, S., Kumar, D., & Rai, K.N. (2015). Wavelength collocation solution of non-linear Fin problem with temperrature-dependent thermal conductivity and heat transfer coefficient. *International Journal of Nonlinear Analysis and Applications*, 6(1), 105−118. doi: 10.22075/ijnaa.2015.222

[18] Sigh, S., Kumar, D., & Rai, K.N. (2018). Analytical solution of Fourier and non-Fourier heat transfer in longitudinal fin with internal heat generation and periodic boundary condition. *International Journal of Thermal Sciences*, 125, 166−175. doi: 10.1016/j.ijthermalsci.2017.11.029

[19] Faraj, A., Jaber, H., Chahine, K., Faraj, J., Ramadan, M., El Hage, H.E., & Khaled, M. (2020). New Concept of Power Generation Using TEGs: Thermal Modeling, Parametric Analysis and Case Study. *Entropy*, 22(5), 503. doi: 10.3390/e22050503

[20] Buenaventura, G., & Azzopardi, B. (2015). Energy recovery system for retrofitting in internal combustion engine vehicles: A review of techniques. *Renewable and Sustainable Energy Review*, 41, 955−964. doi: 10.1016/j.rser.2014.08.083

[21] Chen, W.H., Chiou, Y.B., Chein, R.Y., Uan, J.Y., & Wang, X.D. (2022). Power generation of thermoelectric generator with plate fins for recovering low-temperature waste heat. *Applied Energy*, 306, 118012. doi: 10.1016/j.apenergy.2021.118012

[22] Ma, J., Sun, Y., & Li, B. (2017). Simulation of combined conductive, convective and radiative heat transfer in moving irregular porous fins by spectral element method. *International Journal of Thermal Sciences*, 118, 475−487. doi: 10.1016/j.ijthermalsci.2017.05.008

[23] Kundu, B., & Lee, K.S. (2013). A Non-Fourier analysis for transmitting heat in fins with internal heat generation. *International Journal of Heat and Mass Transfer*, 64, 1153−1162. doi: 10.1016/j.ijheatmasstransfer.2013.05.057

[24] Aziz, A., & Na, T.Y. (1981). Perturbation analysis for periodic heat transfer in radiating fins. *Wärme- und Stoffübertragung*, 15, 245–253. doi: 10.1007/BF01003645

[25] Ahmadikia, H., & Rismanian, M. (2011). Analytical solution of non-Fourier heat conduction problem on a fin under periodic boundary conditions. *Journal of Mechanical Science and Technology*, 25(11), 2919−2926. doi: 10.1007/s12206-011-0720-5

[26] Aziz, A., & Na, T.Y. (1981). Periodic heat transfer in fins with variable thermal parameters. *International Journal of Heat and Mass Transfer*, 24(8), 1397-1404, doi: 10.1016/0017-9310(81)90189-7

[27] Reader, G.T., & Hooper, C. (1983). *Stirling Engines*. Cambridge: University Press.

[28] Sharma, S.K., & Kumar, D. (2020). A study on Non-Linear DPL Model for Describing Heat Transfer in Skin Tissue during Hyperthermia Treatment. *Entropy*, 22, 481. doi: 10.3390/e22040481

[29] Strikwerda, J.C. (1989). *Finite Difference Schemes and Partial Differential Equations*. Chapman Hall New York.

[30] Bogachki, P., & Shampine, L.F. (1996). An Efficient Runge-Kutta (4,5) Pair. *Computers & Mathematics with Application*, 36(2), 15−28. doi: 10.1016/0898-1221(96)00141-1

[31] Kuosa, M., Saari, K., Kankkunen, A., & Tveit, T.-M. (2012). Oscillating flow in a Stirling engine heat exchanger. *Applied Thermal Engineering*, 45/46, 15−23. doi: 10.1016/j.applthermaleng.2012.03.023

[32] Araoz, J.A., Cardozo, E., Salomon, M., Alejo, L., & Fransson, T.H. (2015). Development and validation of a thermodynamic model for the performance analysis of a gamma Stirling engine prototype. *Applied Thermal Engineering*. 83, 16−30. doi: 10.1016/j.applthermaleng.2015.03.006

[33] Gibson, L., Wilman, E., & Laurance, W. (2017). How green is 'green energy'? *Trends in Ecology & Evolution*, 32(12), 922−935. doi: 10.1016/j.tree.2017.09.007

Co-published by
Institute of Fluid-Flow Machinery
Polish Academy of Sciences
Committee on Thermodynamics and Combustion
Polish Academy of Sciences

http://www.imp.gda.pl/archives-of-thermodynamics/

ARCHIVES OF THERMODYNAMICS

Sensitivity Analysis of Magnetohydrodynamic Mixed Convective Trapezoidal Heat Exchanger Containing Hybrid Nanofluid: Numerical and Statistical Approach

Saiful Islam[a], Goni Molla[b], Badhan Neogi[a], Muhammad Faiaz[a],
B.M. Jewel Rana[c], Md. Mamun Molla[d,e*]
[a]Department of Mathematics, Gopalganj Science and Technology University, Gopalganj 8100, Bangladesh
[b]Department of Applied Physics, Electronics & Communication Engineering, Gopalganj Science and Technology University, Gopalganj 8100, Bangladesh
[c]Department of Quantitative Sciences (Mathematics), International University of Business Agriculture and Technology, Dhaka 1230, Bangladesh
[d]Department of Mathematics & Physics, North South University, Dhaka 1229, Bangladesh
[e]Center for Applied and Computational Sciences (CACS), North South University, Dhaka 1229, Bangladesh
[*]Corresponding author email: mamun.molla@northsouth.edu

Received: 02.09.2024; revised: 02.05.2025; accepted: 05.05.2025

Abstract

The consequences of magnetohydrodynamic mixed convection in a trapezoidal heat exchanger are investigated through numerical analysis. Due to the extensive applications of both mono and hybrid nanofluids in manufacturing and thermal engineering, the Ag-MgO-H_2O hybrid nanofluid is selected as the working material for the entire domain. Additionally, a horizontal magnetic field is applied to the cavity. The finite element method is involved to solve the corresponding mathematical equations. The physical implications of the results are examined over a range of Reynolds numbers ($10 \leq \mathrm{Re} \leq 200$), Hartmann numbers ($0 \leq \mathrm{Ha} \leq 100$), and nanoparticle volume fractions ($0 \leq \phi \leq 0.08$) using streamlines, isotherms, and line graphs. The impact of key factors on the response function is illustrated using the response surface methodology with 2D and 3D visualizations. Sensitivity rates are analysed by developing a best-fit correlation. It is concluded that the thermal enhancement of the hybrid nanofluid is achieved up to 11.4% by incorporating hybrid nanoparticles, and due to the upsurge of the Reynolds number. Conversely, the influence of the magnetic field leads to a decline in this rate to 10.02%. The use of Ag-MgO-H_2O hybrid nanofluid improves the heat transfer efficiency of water by 6.62%. Finally, the results of this study may offer valuable insights for designing an efficient mixed convective mechanical device.

Keywords: Hybrid nanofluid; Mixed convection; Heat exchanger; Response surface methodology; Sensitivity analysis

Vol. 46(2025), No. 3, 61–76; doi: 10.24425/ather.2025.156579

Cite this manuscript as: Islam, S., Molla, G., Neogi, B., Faiaz, M., Rana, B.M.J., & Molla, M.M. (2025). Sensitivity Analysis of Magnetohydrodynamic Mixed Convective Trapezoidal Heat Exchanger Containing Hybrid Nanofluid: Numerical and Statistical Approach. *Archives of Thermodynamics*, 46(3), 61−76.

1. Introduction

Current researchers are also captivated by mixed convective heat transfer involving fluid movement in enclosed spaces, where the combination of forced and natural convection results in mixed convection. This phenomenon has gained increasing attention in metalworking and metallurgical sciences due to its substantial influence on the heat transfer of electrically conductive fluids. The investigation, understanding, and prediction of fluid flow dynamics have been of great interest. Leonardo da Vinci was the first to observe and document fluid flow phenomena in the early fifteenth century, sparking a substantial amount of research in fluid mechanics. Mixed convective heat transfer in various enclosures is a crucial topic in engineering sectors because of its extensive applications in heat exchangers, nuclear reactors, drying technologies, solar panels, building in-

Nomenclature

c_p – specific heat at constant pressure, J/(kg·K)
Ha – Hartman number
Nu – Nusselt number
p – pressure, kPa
P – dimensionless pressure
Pr –Prandtl number
Re – Reynolds number
Ri – Richardson number
T – temperature, K
u, v – dimensional velocity, m/s
U, V – dimensionless velocity

Greek symbols

α – thermal diffusivity, m^2/s^2
β – coefficient of thermal expansion, K^{-1}
θ – dimensionless temperature
μ – dynamic viscosity, kg/(m·s)
ν – kinematic viscosity, m^2/s
ρ – density, kg/m^3
σ – electric conductivity, $\Omega^{-1}\cdot m^{-1}$
ϕ – particle concentration
ψ – stream function
Ω – vorticity vector

Subscripts and Superscripts

HS – hot surface
hnf – hybrid nanofluid

Abbreviations and Acronyms

FEM – finite element method
RSM – response surface methodology

sulation, lubrication technologies, and chemical industries. Among the most studied areas are mixed convective flows in enclosed spaces, aiming for a quantitative understanding and expanding their practical applications [1−5]. Nanofluids, which consist of nanoparticles with diameters less than 100 nm, enhance the thermodynamic properties and thermal efficiency of base fluids even at low concentrations when properly dispersed and stabilised [6−10]. Numerous researchers have explored methods to improve heat transfer and cooling effects by considering various geometries and configurations of different nanofluids [11−15]. In the context of a variety of engineering and industrial applications for nanofluids, it is essential to significantly modify the attributes of mono nanofluids significantly to enhance their thermophysical and rheological properties. To meet these needs, a new type of fluids known as hybrid nanofluids (HNFs) were developed. These fluids allow for the proper combination of two or more nanoparticles within a single base fluid. Essentially, composite or hybrid nanofluids are a novel category of nanofluids created by mixing metal oxide, metal particles, or both into a primary fluid. Significant research has already been conducted on hybrid nanofluids. For instance, Kaushik et al. [16] conducted both numerical and experimental studies to compare the flow behaviour between CuO-ZnO-H_2O and the base fluid in a small channel. They concluded that due to the addition of solid nanoparticles, the outcomes improved up to 18−21%. Hussain et al. [17] used numerical methods to study an open enclosure with a square adiabatic barrier, using Al_2O_3-Cu-H_2O hybrid nanofluid. Their findings indicated that the rate of heat transfer was enriched by increasing the Richardson number, Reynolds number, and nanoparticle size. Zaboli et al. [18] reported that hybrid nanofluids could enhance heat exchange in solar systems, including trough collectors. Mahalakshmi [19] conducted a numerical study on a lid-driven mixed convection with heat sources containing hybrid nanofluids. The study concluded that the Ag-CuO-water hybrid nanofluid transfers heat more efficiently compared to Ag-MgO-water and Ag-TiO_2-water. Mandal et al. [20] numerically explored the effects of several geometric factors on a porous W-shaped cavity experie-ncing mixed convection with a Cu-Al_2O_3-H_2O hybrid nanofluid. They found that increasing the bottom undulation amplitude improved thermal energy transmission despite the reduced fluid volume. Anee et al. [21] applied the Lattice Boltzmann method (LBM) to examine the heat transfer behaviour of hybrid nanofluid in an enclosed shape with multiple heaters, revealing that the size of the nanoparticles and the Hartmann number (Ha) significantly affected heat transfer. Thumma et al. [22] studied the heat transfer phenomena of a magnetised hybrid nanofluid (Cu-Ag-H_2O) in a radiative flow across a rotating disc, taking into account the Hall current and heat source. Their investigation showed that the Hall current parameter not only regulates cross-radial velocity and energy but also increases radial motion. The hybrid nanofluid exhibited superior heat transfer performance compared to a single fluid with respect to thermal radiation and ESHS coefficients.

The study of the influence of magnetic forces on electrically conducting fluids is known as magnetohydrodynamics (MHD). MHD encompasses mechanisms such as the Earth's magnetic field, nuclear fusion, cooling of fission reactors, X-ray radiation, and solar wind cooling. Various researchers have examined MHD heat transfer in different enclosures over time due to these practical applications [23−27]. Owing to its numerous uses, MHD mixed convection involving various geometries, temperatures, and boundary conditions has garnered significant attention in scientific research. For instance, Tayebi et al. [28] explored heat transfer behaviour of a hybrid nanofluid in a square cavity including a wavy cylinder. Gibanov et al. [29] investigated MHD of ferrofluid in a chamber with moving upper edges and a porous layer. Mebarek-Oudina et al. [30] studied the magnetohydrodynamic transport of a hybrid nanofluid within a porous chamber, finding that the upsurge of magnetic field intensity inhibits the convective heat transfer rate. Selimefendigil and Chamkha [31] completed a numerical study on MHD flow in a square cavity with a partial triangular porous layer, filled with Ag-MgO-water hybrid nanofluid. They observed that increasing the porosity of the container significantly boosts heat transfer, while the presence of a magnetic field substantially decreases it. Ma et al. [32] statistically examined the MHD effects using a Shamse Knot-shaped cavity filled with Ag-TiO_2-water hybrid nanofluid, discovering that MHD influences heat transfer and that increases in the Rayleigh number (Ra) and cavity side length (D) enhance heat transport. Munawar et al. [33] numerically studied MHD mixed convection using Ag-MgO-water in an inclined cavity with a circular heater. They determined that increasing the Hartmann number (Ha) reduces the average Nusselt number (Nu_{av}), and greater heat transfer rates were achieved by using central heaters with smaller radii for free convection and larger radii for forced convection. Mourad et al. [34] explored the impact of MHD on a hybrid nanofluid within a wavy cavity using the finite element method (FEM). Their findings indicated that Nu_{av} increases with the Darcy number (Da) and Ra but decreases with Ha.

An apparatus that moves heat from an energy source to a working fluid is called a heat exchanger. It is utilised in systems that heat and cool, where the fluids may be near one another or kept apart by a solid barrier to avoid direct contact. Heat exchangers are essential in different applications, such as ventilation, freezing, sewage treatment, chemical and pharmaceutical plants, power plants, natural gas processing, and space heating [35−39]. Chen et al. [40] developed a heat exchanger model to explore the relationship between fin pitches and tube diameters in a fin-tube heat exchanger, using both numerical and experimental methods to solve it. Lee et al. [41] created a 3D model of unsteady free convection for a circular fin-tube heat exchanger. Additionally, Pakalka et al. [42] developed a theoretical and experimental framework for a heat exchanger based on fin-tube design.

The review of publications mentioned above makes it evident that the MHD mixed convective heat exchanger is a subject of great attraction to investigators on account of its creative uses across a wide range of engineering sectors. While numerous studies have been conducted on a variety of cavities to examine mixed convective fluid with MHD and heat transfer mechanisms, some recent studies have focused on schematic cavities that can hold a wide variety of nanoparticles [43−46]. Similarly, comparatively little research was done on heat exchangers to construct a fast heat transmission structure [47−49]. Yet, in the current research, a sensitivity analysis of a trapezoidal heat exchanger that contains an Ag-MgO-H_2O hybrid nanofluid using RSM is performed after integrating these two phenomena, heat exchanger and mixed convection. Moreover, in rela life aplications, there are numerous trapezoildal-shaped industrial architecture where mono or hybrid nanofluids are used for distinct purposes. To the greatest of the writer's understanding, no investigation has been done on this topic yet. The FEM is a popular computational technique that is used to simulate the governing formulas [50, 51]. Another reason to implement the RSM is to investigate the geometric and statistical impact of involved parameters with a best-fitted correlation with Nu_{av} and involved parameters. Investigating the heat transfer mechanisms for this hybrid nanofluid-based mixed convective trapezoidal heat exchanger mathematically and statistically using FEM and RSM is the primary goal of this study.

2. Physical description and mathematical model

Using water (H_2O) as the primary fluid, a schematic-shaped cavity is examined numerically as a fluid region containing Ag and MgO nanoparticles. This fluid is an incompressible, steady and Newtonian fluid that takes magnetic field impacts into ac-count. The height and length of this schematic-shaped cavity, which is mass and heat isolated, are H and L, accordingly. With a lid motion of u, the top horizontal wall is moving. On the right and left sides, accordingly, two cylinder pipes with a $0.1L$ radius can be utilized as a heater and cooler. Figure 1 shows the ar-rangement of this fluid framework with a schematic-shaped heat exchanger. It is proposed that the left cylindrical pipe indicates a cool surface T_c while the right pipe indicates a hot surface T_h.

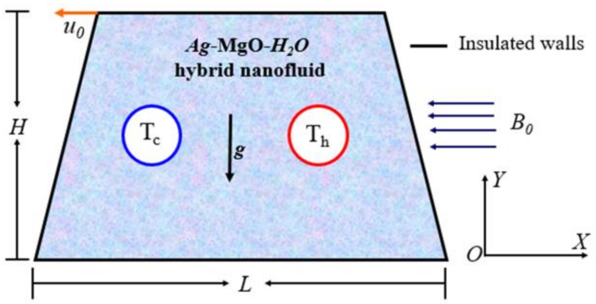

Fig. 1. Schematic diagram of the proposed model.

The outer boundaries of the fluid area are totally intact and adiabatic. Additionally, the gravitational acceleration g works in the exact reverse position of the Y-dimension. Further, the frame is enveloped by a B_0 form of Ag-MgO magnetic field that is constant and flows from right to left. The nearby medium is considered non-slip because of the assumed equality of size and nanoparticles. In this situation, Table 1 lists the thermophysical properties of the considered nanofluid.

Table 1. Characteristics of nanoparticles and base fluid [52].

Nanoparticle and base fluid	**c_p, J·kg^{-1}·K^{-1}**	**ρ, kg·m^{-3}**	**κ, W·m^{-1}·K^{-1}**	**β, K^{-1}**	**σ, S·m^{-1}**	**μ, kg·m^{-1}·s^{-1}**
Ag	235	10500	429	5.4×10^{-5}	8.1×10^{-4}	-
MgO	879	3970	30	3.36×10^{-5}	8×10^{-4}	-
H_2O	4179	997.1	0.613	21×10^{-5}	5.5×10^{-6}	8.91×10^{-4}

Some assumptions served as the foundation for this study and the creation of the model. The following assumptions were considered:

(i) this hybrid nanofluid has a two-dimensional laminar, incompressible flow,
(ii) magnetohydrodynamic mixed convection is considered,
(iii) the governing equations are simulated using the Galerkin weighted residual finite element method,
(iv) the flow problem is considered under the Boussinesq approximation.

To see the entire fluid flow area, a two-dimensional (2D) Cartesian structure is set up, with the left sidewall marked by the Y-axis and the bottom wall by the X-axis. The basic governing equations to make a mathematical form for this mixed convective two dimensional model using hybrid nanofluid are the continuity, momentum, and energy equations as follows:

$$\frac{\partial u}{\partial x}+\frac{\partial v}{\partial y}=0, \tag{1}$$

$$\rho_{hnf}\left(\frac{\partial u}{\partial x}+\frac{\partial u}{\partial y}\right)=-\frac{\partial p}{\partial x}+\mu_{hnf}\left(\frac{\partial^2 u}{\partial x^2}+\frac{\partial^2 u}{\partial y^2}\right)+F, \qquad (2a)$$

$$\rho_{hnf}\left(\frac{\partial v}{\partial x}+\frac{\partial v}{\partial y}\right)=-\frac{\partial p}{\partial y}+\mu_{hnf}\left(\frac{\partial^2 v}{\partial x^2}+\frac{\partial^2 v}{\partial y^2}\right)+F, \qquad (2b)$$

$$\frac{\partial T}{\partial x}+\frac{\partial T}{\partial y}=\frac{k_{hnf}}{(\rho c_p)_{hnf}}\left(\frac{\partial^2 T}{\partial x^2}+\frac{\partial^2 T}{\partial y^2}\right). \qquad (3)$$

Here, in the u-momentum equation, there is no external effect; as a result, Eq. (2a) does not include any additional body force (F=0); Eq. (2b) adds $F=g(\rho\beta)_{hnf}(T-T_c)-\mu_{hnf}{B_0}^2 v$ because of an outside magnetic field and gravitational force. Also, the dimensionless initial and boundary conditions are:

$$\left.\begin{array}{lll}\text{At right circular surface:} & T=T_h, & u=v=0\\ \text{At left circular surface:} & T=T_c, & u=v=0\\ \text{Rest of the walls:} & \dfrac{\partial T}{\partial n}=0, & u=v=0\end{array}\right\}. \qquad (4)$$

Additionally, Table 2 explains the correlations of hybrid nanofluids which have been taken into account between base fluid (H_2O) and nanoparticles (Ag and MgO). Here, n is the orthogonal unit vector on the XY-plane. To put it practically, base fluid and nanoparticles are needed to obtain the properties of nanofluid. The correlations that are taken into consideration between primary fluid (H_2O) and nanoparticles (Ag and MgO) are explained in this part of the paper. The characteristics of nanofluid are truly dependent upon the primary fluid and nanomaterials. In order to estimate the characteristics of nanofluids, correlations gathered in Table 2 are used.

Table 2. Used correlations of hybrid nanofluid [53].

Properties	**Applied Correlations**
Concentration of nanoparticles	$\phi=\phi_{Ag}+\phi_{MgO}$
Density of nanofluid	$\rho_{hnf}=(1-\phi)\rho_{bf}+\phi\rho_{sp}$ where: $\phi\rho_{sp}=\phi_{\mathrm{Ag}}\phi\rho_{\mathrm{Ag}}+\phi_{\mathrm{MgO}}\rho_{\mathrm{MgO}}$
Specific heat capacity	$(\rho c_p)_{hnf}=(1-\phi)(\rho c_p)_{bf}+\phi(\rho c_p)_{sp}$ where: $\phi(\rho c_p)_{sp}=\phi_{\mathrm{Ag}}(\rho c_p)_{\mathrm{Ag}}+\phi_{\mathrm{MgO}}(\rho c_p)_{\mathrm{MgO}}$
Thermal conductivity	$\kappa_{hnf}=\kappa_{bf}\left\{\dfrac{\kappa_{sp}+2\kappa_{bf}-2\phi(\kappa_{bf}-\kappa_{sp})}{\kappa_{sp}+2\kappa_{bf}+\phi(\kappa_{bf}-\kappa_{sp})}\right\}$ where: $\phi\kappa_{sp}=\phi_{\mathrm{Ag}}\kappa_{\mathrm{Ag}}+\phi_{\mathrm{MgO}}\kappa_{\mathrm{MgO}}$
Thermal diffusivity	$\alpha_{hnf}=\dfrac{k_{hnf}}{(\rho c_p)_{hnf}}$
Dynamic viscosity	$\mu_{hnf}=\mu_{hnf}(1+2.5\phi+6.2\phi^2)$
Thermal expansion coefficient	$(\rho\beta)_{hnf}=(1-\phi)(\rho\beta)_{bf}+\phi(\rho\beta)_{sp}$ where: $\phi(\rho\beta)_{sp}=\phi_{\mathrm{Ag}}(\rho\beta)_{\mathrm{Ag}}+\phi_{\mathrm{MgO}}(\rho\beta)_{\mathrm{MgO}}$
Electrical conductivity	$\sigma_{hnf}=\sigma_{bf}\left[1+\dfrac{3\phi\left(\frac{\sigma_{sp}}{\sigma_{bf}}-1\right)}{\left(\frac{\sigma_{sp}}{\sigma_{bf}}+2\right)-\phi\left(\frac{\sigma_{sp}}{\sigma_{bf}}-1\right)}\right]$ where: $\phi\sigma_{sp}=\phi_{\mathrm{Ag}}\sigma_{\mathrm{Ag}}+\phi_{\mathrm{MgO}}\sigma_{\mathrm{MgO}}$

By incorporating the dimensionless quantities in Eq. (5) into Eqs. (1−3), the subsequent dimensionless governing equations (6−9) are generated:

$$X=\frac{x}{L},\quad Y=\frac{y}{L},\quad U=\frac{u}{u_0},\quad V=\frac{v}{u_0},\quad P=\frac{p}{\rho_{nf}{u_0}^2}\quad\text{and}\quad\theta=\frac{T-T_c}{T_h-T_c}. \qquad (5)$$

The adjusted set of dimensionless equations is as follows:

$$\frac{\partial U}{\partial X}+\frac{\partial V}{\partial Y}=0, \qquad (6)$$

$$U\frac{\partial U}{\partial X}+V\frac{\partial U}{\partial Y}=-\frac{\partial P}{\partial X}+\left(\frac{\upsilon_{hnf}}{\upsilon_{bf}}\right)\frac{1}{\mathrm{Re}}(\nabla^2 U), \qquad (7)$$

$$U\frac{\partial V}{\partial X}+V\frac{\partial V}{\partial Y}=-\frac{\partial P}{\partial Y}+\left(\frac{\upsilon_{hnf}}{\upsilon_{bf}}\right)\frac{1}{\mathrm{Re}}(\nabla^2 U)+ +\frac{(\rho\beta)_{hnf}}{\rho_{hnf}\beta_{bf}}\mathrm{Ri}\,\theta-\left(\frac{\rho_{bf}\sigma_{hnf}}{\rho_{hnf}\mu_{bf}}\right)\frac{\mathrm{Ha}^2}{\mathrm{Re}}V, \qquad (8)$$

$$U\frac{\partial \theta}{\partial X}+V\frac{\partial \theta}{\partial Y}=\left(\frac{\alpha_{hnf}}{\alpha_{bf}}\right)\frac{1}{\mathrm{Re\,Pr}}(\nabla^2\theta), \qquad (9)$$

where $\mathrm{Re}=\frac{u_0 L}{\mu_{bf}}$, $\mathrm{Pr}=\frac{\upsilon_{bf}}{\alpha_{bf}}$ and $\mathrm{Ha}=\frac{LB_0\sqrt{\sigma_{bf}}}{\sqrt{\mu_{bf}}}$ represent the Reynolds number, Prandtl number and Hartmann number, respectively. Also, again, $\frac{\mathrm{Gr}}{\mathrm{Re}^2}=\mathrm{Ri}$ is known as the Richardson number, where $\mathrm{Gr}=\frac{g\beta_{bf}(T_h-T_c)L^3}{{\upsilon_{bf}}^2}$ is the Grashoff number. Additionally, the reduced boundary conditions are:

$$\left.\begin{array}{lll}\text{At right circular surface:} & \theta=1, & U=V=0\\ \text{At left circular surface:} & \theta=0, & U=V=0\\ \text{Rest of the walls:} & \dfrac{\partial \theta}{\partial N}=0, & U=V=0\end{array}\right\}. \qquad (10)$$

Furthermore, from the heated left circular surface, the average Nusselt number ($\mathrm{Nu}_{\mathrm{av}}$), which is employed to quantify the rate of heat transfer, is obtained by employing:

$$Nu_{av}=-\left(\frac{k_{hnf}}{k_{bf}}\right)\int_S\frac{\partial\theta}{\partial N}ds, \qquad (11)$$

where S stands for the surface that is heated, and N is the perpendicular unit vector on the XY-plane. Moreover, ψ signifies the stream function that is associated by $U=\frac{\partial\psi}{\partial X}$ and $V=\frac{\partial\psi}{\partial Y}$.

Furthermore, $\frac{\partial^2\psi}{\partial X^2}+\frac{\partial^2\psi}{\partial Y^2}=-\left(\frac{\partial V}{\partial X}-\frac{\partial U}{\partial Y}\right)=-\Omega$, where Ω expresses the vorticity vector, and U, V stand for the velocity vector along the X and Y axis, respectively.

3. Numerical methodology

3.1. Solution technique

The dimension-free governing expressions (6) to (9) are mathematically solved utilising the Galerkin weighted residual finite element method (FEM) with boundary settings (10). The entire region is distributed into separate triangular elements, requiring six nodes and accounting for quadratic interpolation functions, in order to monitor the thermal performance and fluid motion. Furthermore, the linear interpolation approach is used to calculate the gradient of pressure. Moreover, the participation of interpolation functions roughly represents the dependent variables of each element as local element coordinates. These equations can be simulated by using the Newton-Raphson iteration method by MATLAB, which generates a set of global nonlinear algebraic equations. In this process, the convergence condition is defined as follows: $\left|\Gamma^{m+1}-\Gamma^{m}\right| < 10^{-5}$, where m+1 and m stand for two successive repetitions, and $\Gamma(U, V, \theta)$ stands for the iterative value. The complete set of FEM was detailed in [54,55]. The whole flowchart of this computation process is shown in Fig. 2.

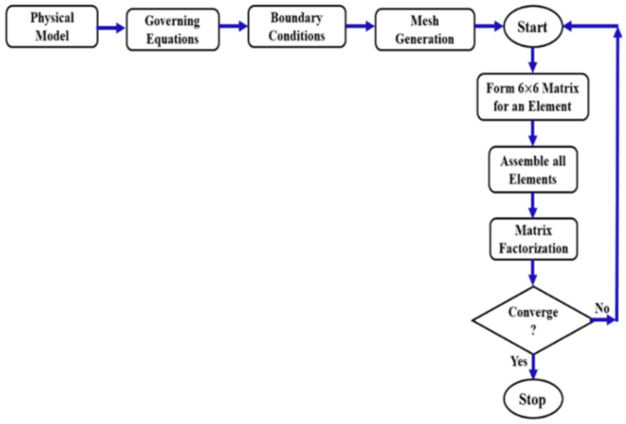

Fig. 2. A complete flow chart of the computational procedure.

This finite element scheme can have the optimal number of elements by taking the following factors into account, which can be determined via a grid sensitivity evaluation. Ri = 1, Ha = 20, Pr = 6.8377, Re = 100, $\phi_{\mathrm{Ag}} = 0.02$ and $\phi_{\mathrm{MgO}} = 0.02$ are the magnitudes. Again, the magnitude of $\mathrm{Nu}_{\mathrm{av}}$ is designated in order to continue this independence test for meshing. For applying FEM, the entire geometry is subdivided into five distinct triangular elements. These are 2369, 3400, 9570, 27305, and 35665. The computed results of $\mathrm{Nu}_{\mathrm{av}}$ using FEM for different numbers of triangle members are demonstrated in Table 3 and Fig. 3.

Table 3. Grid independence analysis for the present study.

Elements	**2369**	**3400**	**9570**	**27305**	**35665**
$\mathrm{Nu}_{\mathrm{av}}$	10.975	11.046	11.207	11.277	11.276

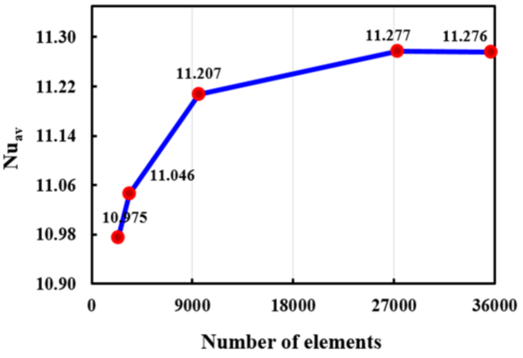

Fig. 3. Grid test by using $\mathrm{Nu}_{\mathrm{av}}$ and number of elements.

Though for the first three meshing types, the differences are clearly noticeable, it is clear that the magnitude of $\mathrm{Nu}_{\mathrm{av}}$ for 27305 triangular elements is nearly identical to the cases ensuing a greater number of elements. As a result, 27305 triangular elements are selected for discretisation and solving this proposed heat exchanger model.

3.2. Code validation

The purpose of this section is to validate the findings of this study by comparing streamlines and isotherms with those obtained from a lid-driven mixed convective investigation conducted by Sivakumar et al. [56]. To ensure accuracy, the results of Sivakumar's proposed mixed convective heat exchanger model are compared with the present outcomes. The simulation was performed with parameters Re = 100, Pr = 0.71, and Ri = 0.01, within a partially heated square cavity on the left wall, with the right wall maintained at a relatively low temperature and a moving lid on the upper wall. Additionally, we have replicated the work of Sivakumar et al. [56] in this study and compared the streamlines and isotherms (as shown in Fig. 4).

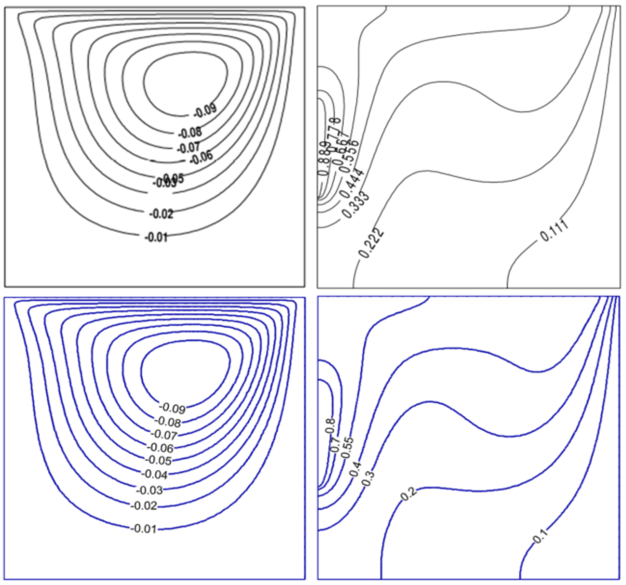

Fig. 4. Comparison of results of Sivakumar et al. [56] (top row) with the current study (bottom row): streamlines (left), isotherms (right).

The top two figures are from Sivakumar's research, while the bottom two are from the current study. The present results closely match the streamline and isotherm patterns, reinforcing our confidence in the accuracy of this mixed convective analysis in near cavities, as it demonstrates strong consistency with the current numerical analysis.

4. Results and discussion

This section explores the effects of physical variables with an engineering focus on trapezoidal mixed convective flow of hybrid nanofluid, including the influence of a magnetic field. The results obtained within this cavity are presented through velocity profiles, streamlines, isotherms, and 2D and 3D response surfaces. The study involves a hybrid nanofluid composed of Ag, MgO, and H_2O, with spherical solid nanoparticles confined within a trapezoidal chamber. Key parameters such as the Reynolds number (Re), nanoparticle volume fraction (ϕ), Richardson number (Ri), and Hartmann number (Ha) are analysed to show their impact on the heat exchanger model, as in Figs. 5−18. Additionally, the average Nusselt number (Nu_{av}) is used to evaluate the performance of the heat exchanger for water, mono-nanofluid, and hybrid nanofluid. For this analysis, standard values for the above-mentioned key parameters are Ri = 1, Ha = 20, Pr = 6.8377, Re = 100, $\phi_{Ag} = 0.02$ and $\phi_{MgO} = 0.02$.

4.1. Influence of Reynolds number

Figures 5−6 illustrate how the contours of streamlines and isotherms change with varying Reynolds numbers (Re).

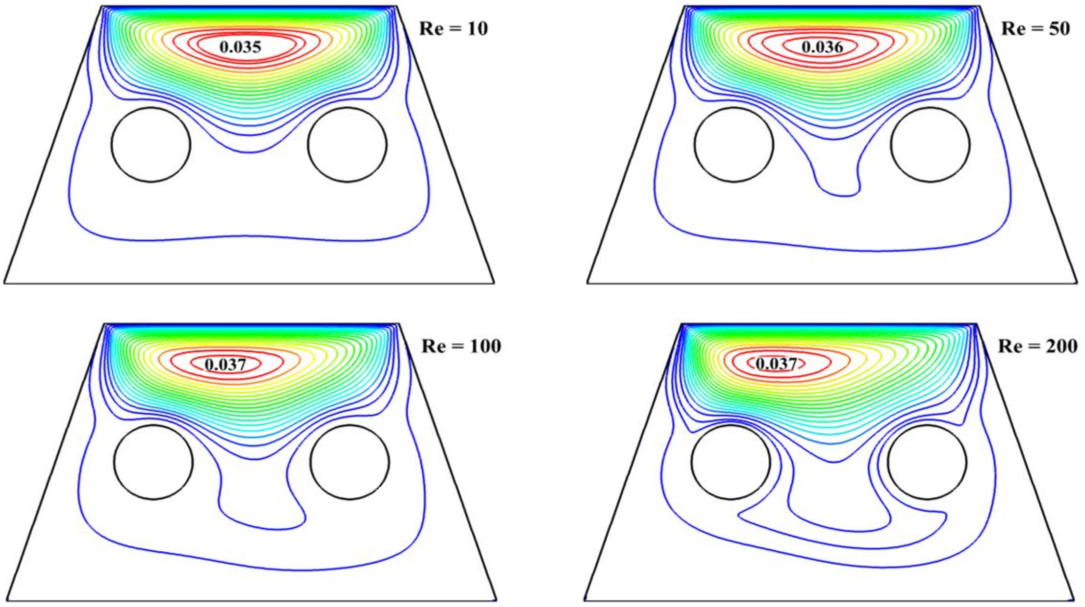

Fig. 5. Effect of Re on streamlines.

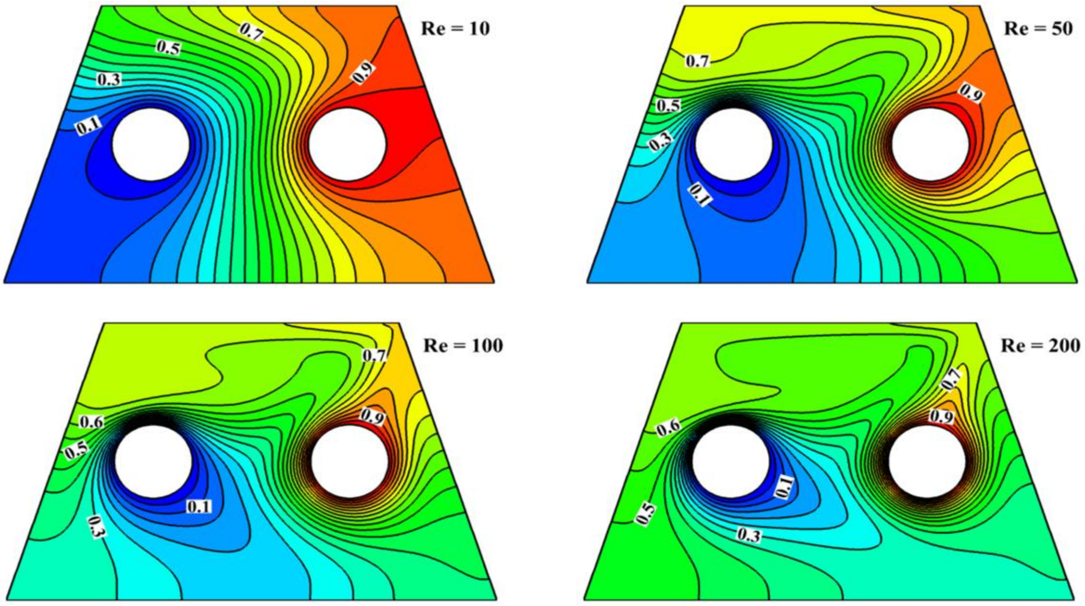

Fig. 6. Effect of Re on isotherms.

Figure 5 uses streamline contours to demonstrate how Re (10−200) may be controlled for a fluid velocity field when the other parameters are Ri = 1, Ha = 20, Pr = 6.8377 and $\phi_{Ag} = 0.02$, $\phi_{MgO} = 0.02$. By contrasting the effects of viscous forces and inertia, Re provides insight into the pattern of fluid motion under various circumstances. The streamline concentration and flow circulation are uniformly circulating throughout the uppermost part of the wall when Re =10. Physically, this is caused by the combined effects of shear force and buoyant force, both of which are controlled at low Re. After that, the streamline vortex and lid velocity both noticeably alter as the Re spikes from 50 to 100. Higher Re values physically result in increased fluid inertia, which raises the flow circulation and magnitude with streamlines concentration. Furthermore, the strengthening of Re signifies the lid velocity of the trapezoidal cavity's top wall; fluid flow follows the lid velocity along the upper wall from the right to the left. The fluid's movement over the upper surface, from right to left, is growing as Re rises. This movement reaches its peak when Re = 200. This is because the velocity of the top lid increases with increasing Re, and as a result, forced convection becomes more prominent than sheer force and buoyant force. It is evident that the entire domain experiences an increase in fluid velocity along a line (0.5, 0) to (0.5, 0.6) as Re develops, which can be seen in Fig. 7.

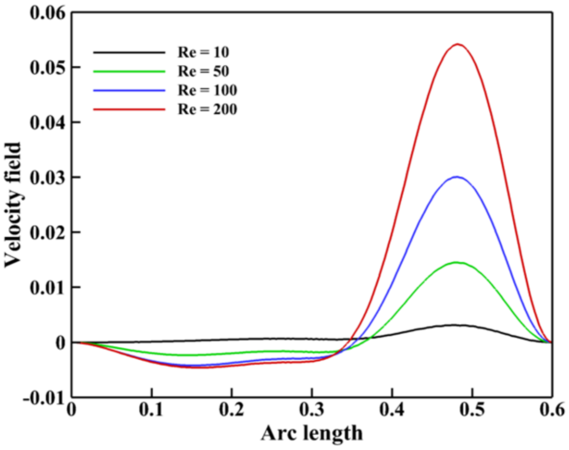

Fig. 7. Velocity profile for Re.

Moreover, Fig. 6 shows how Re affects the interior isotherms of the cavity. Natural convection is dominant in fluid flow when Re =10. As a result, from the right hot cylinder to the left cooler one, the isotherm lines change uniformly. Force convection occurred, as evidenced by the rising value of Re (50), brought about by the upper wall's rising lid velocity. As can be seen, the red contour lines in the isothermal patterns indicate how fluid movement carries heat from the heated surface to the colder surface. Consequently, there is a 97.07% intensification of heat transmission rate compared to that before. It is apparent, therefore, that when Re rises, the isotherm contour lines distort.

4.2. Influence of Richardson number

The relative significance of forced convection caused by a lid vs. thermal natural convection forces is measured by the Richardson number (Ri) where Ri = Gr/Re^2. Here, Figs. 8 and 9 are applied to explain the effect of fluid flow and heat transmission using streamlines and isotherms at various Ri values when Re = 100, Ha = 20, Pr = 6.8377, and $\phi_{\mathrm{Ag}} = 0.02$, $\phi_{\mathrm{MgO}} = 0.02$. In this investigation, the parameter that has the largest influence on describing the mixed convection is Ri. It is evident from Fig. 8 that the fluid flow pattern is also affected by changes in Ri. Firstly, when Ri = 0.1, a forced convection is evident, with the streamlines moving more along the enclosure's upper wall and to the left. Furthermore, the bulk motion inside the cavity is circulating as a result of the top moving lid's motion, which is caused by the dominance of inertial forces over buoyancy forces. Furthermore, when the forces of buoyancy and inertia are balanced (for Ri = 1), examine the mixed convection mode.

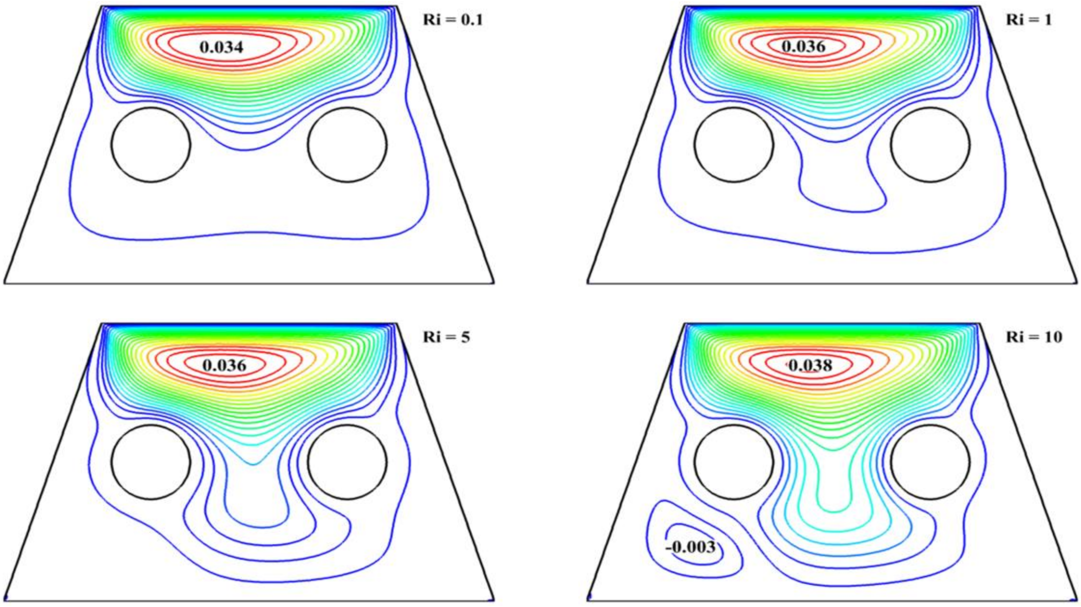

Fig. 8. Effect of Ri on streamlines.

Consequently, the top lid wall experiences a movement effect from the core vortex. Moreover, the streamlines' vortex widens as the value of Ri rises. According to the physical explanation, an escalation of Ri signifies the predominance of natural convection, which reduces shear stress. This created shear stress provides hurdles for fluid motion. The fluid velocity decreases as the value of Ri rises from 1 to 5, indicating that natural convection is now more significant in this condition.

As a result, the streamlines are shifted somewhat towards the lid wall. A clockwise rotating vortex can be noticed in the cavity's lower left corner at the highest value of Ri = 10. Also, Fig. 9 illustrates how isotherms are impacted by Ri in the entire trapezoidal cavity. A significant reduction of heat transmission is designated by Nu_{av} of 10.549 at Ri = 0.1. The heat transfer rate rises 6.9% over the lower value prior to the expansion of Ri from 0.1 to 1. Moreover, for Ri = 1, the mixed convection occurs in the entire cavity and at that time Nu_{av} is 11.277. An additional 15.46% enhancement in heat transmission may be seen by increasing Ri from 1 to 5. This analysis shows an increase in Nu_{av} with the enlargement of Ri values. And, there is an 11.16% increase in Nu_{av} as Ri increases from 5 to 10.

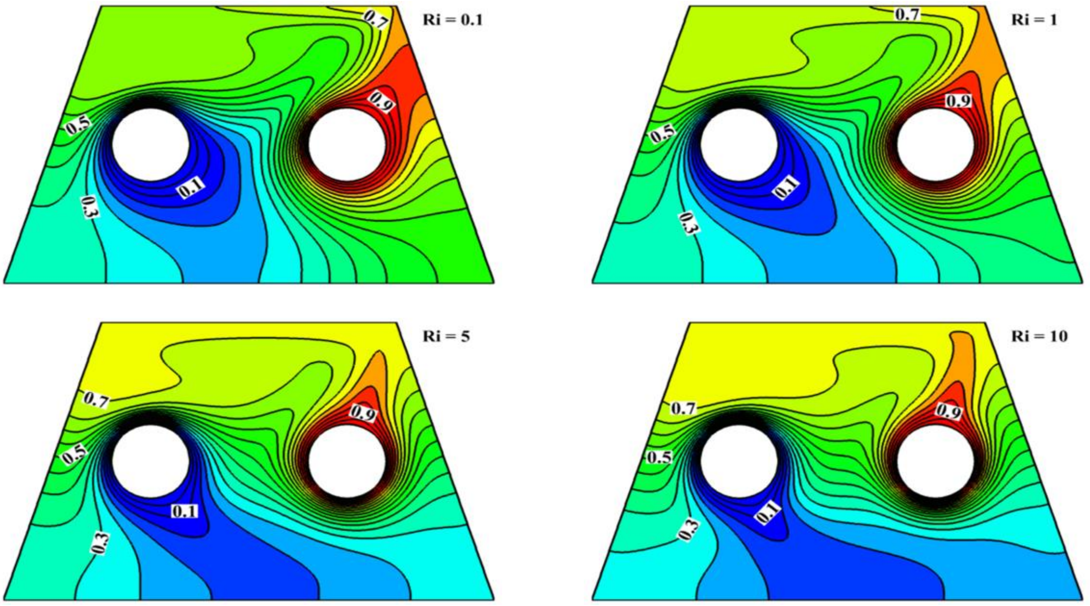

Fig. 9. Effect of Ri on isotherms.

4.3. Influence of Hartmann number

The streamline and isotherm contours in Figs. 10 and 11 demonstrate the consequences of Hartmann number (Ha) on fluid velocity and thermal transportation, keeping Ri = 1, Re = 100, Pr = 6.8377, $\phi_{Ag} = 0.02$ and $\phi_{MgO} = 0.02$. In reality, Ha illustrates how the magnetic force influenced this trapezoidal heat exchanger.

From Fig. 10, the streamline's concentrations are significantly denser without the existence of an external magnetic field (Ha = 0). It appears that the flow pattern is consistent across the hollows. However, as the magnitude of fluid vorticity inside the insertion becomes slow, the flow circulation becomes slightly blocked following the intensification of the magnetic field (Ha = 20).

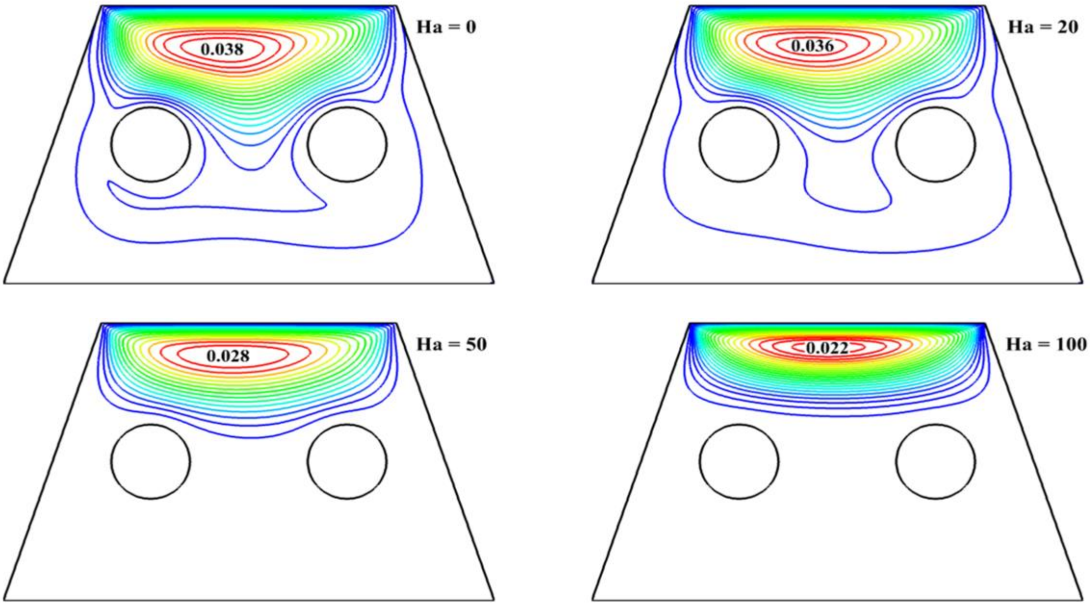

Fig. 10. Effect of Ha on streamlines.

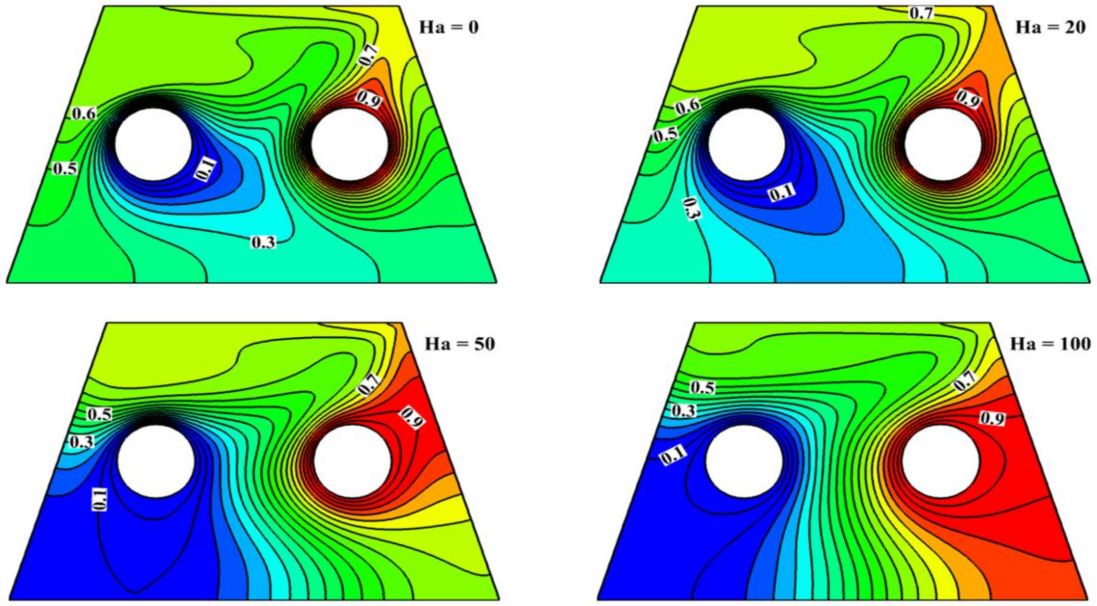

Fig. 11. Effect of Ha on isotherms.

It is evident that, in comparison to greater magnetic field effects (Ha = 20, 50, 100), lower magnetic fields (Ha = 0) boost flow behaviour. After increasing the value of Ha from 20 to 50 and from 50 to 100, there is a perceptible effect on the flow circulation. Because of the magnetic force effect, there is an active resistive force inside the enclosure known as the Lorentz force, which has the potential to slow down the mobility of the nanofluid. Precisely, the isotherm lines have a consistent shape in the vertical direction as the convection type of heat transmission progressively gives way to the conduction mode. This physical phenomenon causes the fluid flow to diminish more in the direction of the top lid surface. More importantly, the velocity profile falls with increasing Ha, as Fig. 12 illustrates the velocity profile of Ha. Furthermore, for greater Ha values (Ha = 20, 50, 100), the isothermal lines in Fig. 11 show that the variation of isothermal lines is rather mild (not significant).

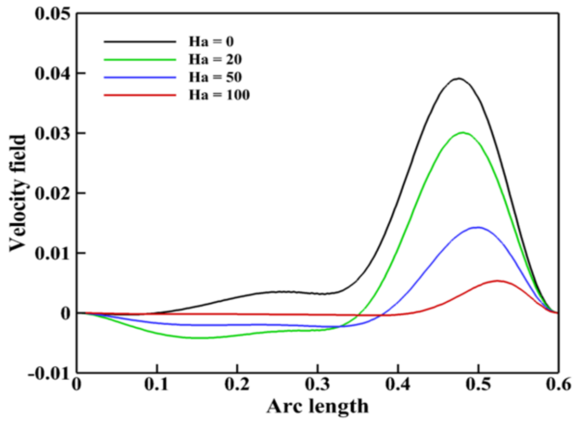

Fig. 12. Velocity profile for Ha.

When there is no active magnetic field, convectional heat transfer (Nu_{av}) occurs at a high rate. This indicates that due to the addition of magnetic field, the fluid flow meets impedance. When the value of Ha is enforced from 0 to 20, there is a 7.85% decrease in heat transfer. After the value reached 50, there was a significant decline in heat transfer, around 33.04%. Also, this decreased rate is 31.43% at the maximum magnetic impact value (Ha = 100). The investigation shows that the rate of heat transmission declines at 58.7% from the lowest active magnetic field to the greatest active magnetic field.

4.4. Importance of nanofluids

This section uses Figs. 13 and 14 to expound the nature of heat transfer and fluid motion on the present model for different magnitudes of the ϕ. Since the velocity profile is therefore controlled by the inherent characteristics of the base fluid, such as density and viscosity, the fluid is a pure base fluid devoid of nanoparticles ($\phi = 0$). The introduction of a modest percentage of nanoparticles ($\phi = 0.02$) really starts to affect the fluid dyna-mics and causes resistance to the particles' mobility in this fluid area. The fluid's inertia force is increased by the cavity's total mass of the fluid. The fluid velocity is significantly reduced as a result of the significant rise in viscosity, which increases flow resistance. An additional factor is that the solution becomes more viscous when more nanoparticles are added. From Fig. 13, it is evident that when ϕ rises, the fluid velocity along the line (0.5, 0) to (0.5, 0.6) decreases significantly. Conversely, the heat transfer rate (Nu_{av}) is rising due to intensification of ϕ, as seen in Fig. 14. The parameters of the base fluid alone dictate Nu_{av}, which is 10.648 in the absence of nanoparticles ($\phi = 0$), as shown by this line graph. Nanoparticle addition begins to marginally increase the heat transfer rate to 3% (10.968) at modest ϕ =0.02. Because of the nanoparticles' increased thermal conductivity, and therefore improved heat transmission within the fluid, there has been an improvement. By increasing the mass of the nanoparticles in the fluid up to 0.04, Nu_{av} is increased by 2.82%. On top of that, compared to $\phi = 0$, Nu_{av} is greatly increased by 11.4% when ϕ is raised by 8% ($\phi = 0.08$).

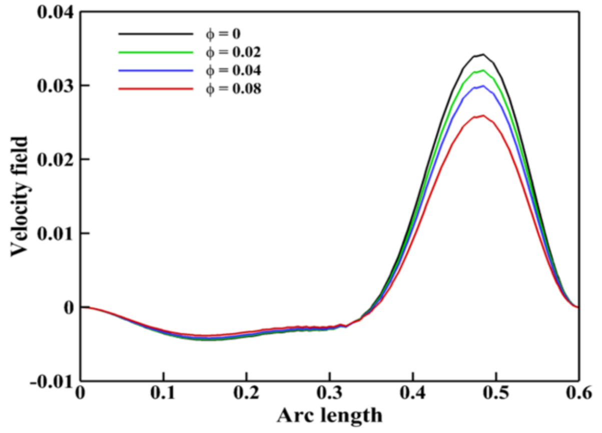

Fig. 13. Velocity profile of ϕ.

Superior heat transfer rates arise from the fluid's increased thermal conductivity, which is further enhanced by the high concentration of nanoparticles. Moreover, let's take a look at the significance of accumulation of solid nanoparticles in water more closely (Fig. 14). Here, utilising the properties of Re and Ha, Nu_{av} is used to clarify and illustrate the rate of heat transfer for several fluid types. For pure fluid (H_2O), MgO-H_2O nanofluid, Ag-H_2O nanofluid and Ag-MgO-H_2O hybrid nanofluid, Fig. 14(a) shows that Nu_{av} grows monotonically with the increasing Re. Without the existence of any nanoparticles in water, Nu_{av} is equal to 10.53 by taking all other parameters in a standard form. When $\phi_{MgO} = 0.02$ and $\phi_{Ag} = 0$, adding MgO nanoparticles quickly improves Nu_{av} (10.885) relative to the pure base fluid, which becomes 3.37% greater than that of the base fluid. A similar tendency can be found while adding Ag nanoparticles ($\phi_{MgO} = 0$ and $\phi_{Ag} = 0.02$), which increases the Nu_{av} value relative to the pure base fluid by 3.5% (10.908). But both solid nanoparticles ($\phi_{MgO} = 0.02$ and $\phi_{Ag} = 0.02$) increased Nu_{av} significantly, which is 11.277. This time, the improvement rate is 7.09%. In addition, Fig. 14(b) illustrates how adding mono or hybrid nanoparticles enhances Nu_{av} for distinct values of Ha. The findings indicate that the Ag-MgO-H_2O hybrid nanofluid has a larger Nu_{av} than Ag-H_2O nanofluids, yet for all fluid combinations, the rate of Nu_{av} decreases as the Ha factor rises. This indicates that because of the hybrid nanofluid's exceptional thermal properties, the Ag-MgO-H_2O hybrid nanofluid performs better in terms of heat transport than either MgO-H_2O or Ag-H_2O nanofluid. This is the primary reason for utilising hybrid nanofluid as opposed to the base fluid or nanofluid containing a particular nanoparticle.

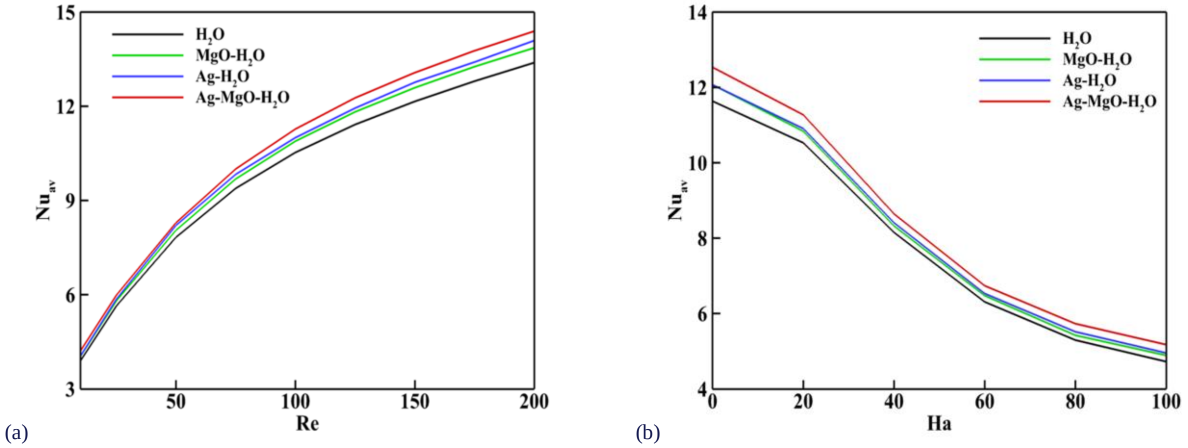

(a) (b)

Fig. 14. Deviation of Nu_{av} for base fluid and nanofluid using (a) Re and (b) Ha.

4.5. Response surface methodology

A well-known statistical analytic technique that explains how the included parameters (Re, ϕ and Ha) impact the response function (Nu_{av}) for this fluid model is called the response surface methodology, or RSM, as described by [57]. This is a useful method for simulating multivariate scenarios in which the input components simultaneously influence the responses that generate interest. Generally, the second-order model produces an acceptable approximation of the response, even in cases where alternative RSM models exist. As per certain accounts, the quadratic RSM model is:

$$y = s_0 + \sum_{i=1}^{3} s_i x_i + \sum_{i=1}^{3} s_{ij} x_i x_j + \sum_{i=1}^{3} s_{ii}\, {x_i}^2. \qquad (12)$$

Here, y is the response function, s_0, s_i, s_{ij} and s_{ii} are the corresponding terms' coefficients. Here, Nu_{av} is considered the response faction (y), while the significant parameters Re, Ha and the ϕ function are input parameters. Finding the response function that most closely matches the interaction between independent parts is the primary goal. Here, a second-order RSM model based on central composite design (CCD) is used [58]. This model has 20 runs in total for 3 independent factors: 6 centres, 8 cubes, and 6 axial points per factor. The coded level for CCD-based RSM is shown in Table 4. In addition, Table 5 expresses the real values, response function values, and 20 runs of coded values. The results of this statistical investigation of this model utilising RSM are also displayed in Table 6. The greatest number of autonomous terms is what we refer to as degrees of freedom, or DOF. Moreover, a significant piece of evidence from this analysis is p-value, which reflects the probability that the null hypothesis is accurate for a definite statistical technique. When the p-value is low, it indicates that the null hypothesis is rejected, which indicates that the model is significant. Typically, this is less than 5%.

Table 4. Original and coded levels for CCD-based RSM.

Factors	**Coded & original level**		
	Lowest value (-1)	Mid value (0)	Lowest value (-1)
Re	10	105	200
φ	0	0.04	0.08
Ha	0	50	100

Table 5. Magnitude of the response function for distinct cases.

Run	**Coded values**			**Real values**			**Response**
	Re	ϕ	Ha	Re	ϕ	Ha	Nu$_{av}$
1	1	0	0	200	0.04	50	10.569
2	-1	-1	1	10	0	100	3.1986
3	1	1	-1	200	0.08	0	16.28
4	0	0	1	105	0.04	100	5.2279
5	0	1	0	105	0.08	50	8.1926
6	0	0	0	105	0.04	50	7.7234
7	1	-1	1	200	0	100	6.0078
8	-1	1	-1	10	0.08	0	4.8334
9	0	0	0	105	0.04	50	7.7234
10	0	0	0	105	0.04	0	12.722
11	1	1	1	200	0.08	100	6.8295
12	-1	0	0	10	0.04	50	3.8024
13	0	0	0	105	0.04	50	7.7234
14	0	-1	0	105	0	50	7.2798
15	1	-1	-1	200	0	0	14.227
16	0	0	0	105	0.04	50	7.7234
17	-1	1	1	10	0.08	100	3.9276
18	-1	0	1	10	0.04	100	7.7234
19	-1	-1	-1	10	0	0	4.2158
20	0	0	1	105	0.04	100	7.7234

Table 6. Analysis of variance for Nu$_{av}$.

Source	**DOF**	**F-value**	***p*-value**	**Comment**
Model	9	38.18	< 0.0001	Significant
Re	1	210.44	< 0.0001	
φ	1	69.67	0.019	
Ha	1	9.65	< 0.0001	
Re^2	1	7.59	0.0273	
φ^2	1	0.0059	0.3358	
Ha^2	1	0.0317	0.0302	
Re·φ	1	37.64	0.3743	
Re·Ha	1	0.3335	< 0.0001	
φ·Ha	1	0.5012	0.511	
Lack-of-Fit	5	-	-	Insignificant

Here, **R^2 = 98.53%**, **Adjusted R^2 = 97.21%**

The model's statistical analysis and the procedures for testing indicate that the R^2 value (97.85%) for Nu$_{av}$ is superior, indicating that this model is apposite for calculating the response function Nu$_{av}$, despite having a lower adjusted R^2 value (95.92%). Another crucial statistic that must be exceptionally small for a model to be deemed suitable is lack-of-fit. In order to investigate the relation between Nu$_{av}$ and the factors Re, Ha and ϕ, a general RSM model is developed as indicated below:

$$y = s_0 + s_1\mathrm{Re} + s_2\phi + s_3\mathrm{Ha} + s_{12}\mathrm{Re}\cdot\phi + s_{13}\mathrm{Re}\cdot\mathrm{Ha} + s_{23}\phi\cdot\mathrm{Ha} + s_{11}\mathrm{Re}^2 + s_{22}\phi^2 + s_{33}\mathrm{Ha}^2, \qquad (13)$$

where s_0, s_1, s_2, s_3, s_{12}, s_{13}, s_{23}, s_{11}, s_{22} and s_{33} are taken as the coefficients of the regression line concerning Re, Ha and ϕ. Furthermore, Nu$_{av}$'s anticipated coefficients of Eq. (13) are provided in Table 7 and are calculated as coded units.

Table 7. Coefficients of the regression equation with corresponding *p*-values based on RSM.

Coefficients	S_0	S_1	S_2	S_3	S_{11}
Values	7.87	3.39	0.5134	−2.71	−0.905
***p*-values**	-	<0.0001	0.019	<0.0001	0.0273
Coefficients	S_{22}	S_{33}	S_{12}	S_{13}	S_{23}
Values	−0.3545	0.8842	0.1910	−1.97	−0.14
***p*-values**	**0.3358**	0.0302	**0.3743**	< 0.0001	**0.511**

A suitable regression equation has only been developed utilising the significant model terms with lower p-values, owing to their importance. On the contrary, the terms that are not essential have been neglected (bold emphasised). Therefore, the terms ϕ^2, Re·ϕ and ϕ·Ha have no influence whatsoever on Nu$_{av}$'s regression equation (13). Consequently, the subsequent mathematical correlation can be applied to relate Nu$_{av}$ with the parameters Re, ϕ and Ha:

$$\mathrm{Nu}_{av} = 7.87 + 3.39\mathrm{Re} + 0.5134\phi - 2.71\mathrm{Ha} - 0.905\mathrm{Re}^2 + 0.8842\mathrm{Ha}^2 - 1.97\mathrm{Re}\cdot\mathrm{Ha}. \qquad (14)$$

4.6. Response surface analysis

With a view to analysing the influence of independent components on the response function, in this segment, Figs. 15−17 provide 2D and 3D contour plots regarding the response surface developed using RSM (Nu$_{av}$). Figure 15(a) demonstrates Nu$_{av}$'s reaction to Re and ϕ. This 2D contour map clearly illustrates that the response function rises with both Re and ϕ. For example, the rate of heat transmission proliferations increases by about 103.1% when the value of Re goes up from 10 (coded value 1) to 105 (coded value 0). At this point, Nu$_{av}$ grows by around 36.84% when the magnitude of Re is raised from 105 (coded value 0) to 200 (coded value 1). At the greatest magnitude of Re and ϕ (coded value 1), the fluctuating rate of Nu$_{av}$ is maximal, as seen in the 2D contours in Fig. 15(a). Moreover, Fig. 15(b) displays a 3D surface plot of the effects of Re and ϕ on Nu$_{av}$. Moreover, several 2D and 3D graphical representations are also shown in Fig. 16(a) to show how Re and Ha influence Nu$_{av}$ in this hybrid nanofluid model. Furthermore, although ϕ remains constant, a rise in Ha diminishes the rate of Nu$_{av}$. Additionally, Fig. 16(b) displays a 3D surface depiction of Re and Ha's effects on Nu$_{av}$. Likewise, Fig. 17 illustrates Nu$_{av}$'s impact from Ha and ϕ. Here, the altering rate of Nu$_{av}$ is advanced by increasing the size of ϕ while decreasing the magnetic field. Nu$_{av}$'s fluctuating rate is lower than it was in the prior two cases, though.

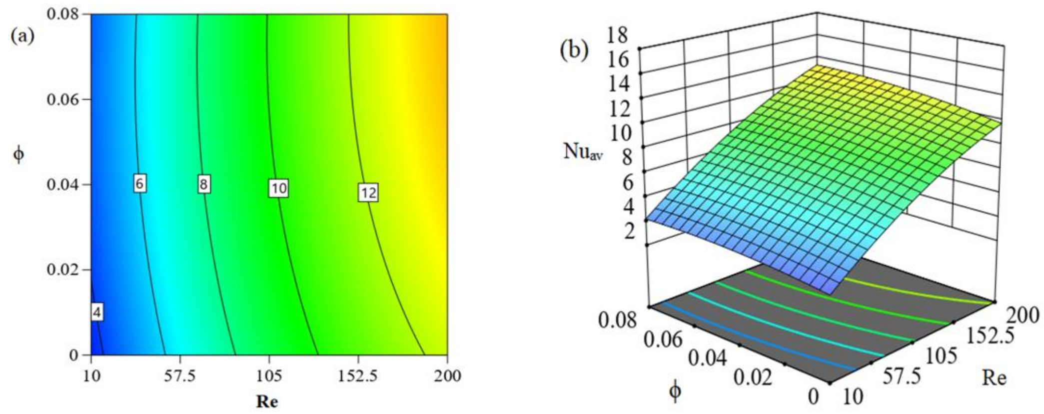

Fig. 15. Effect of Re and ϕ on Nu$_{av}$: (a) 2D sight; (b) 3D sight.

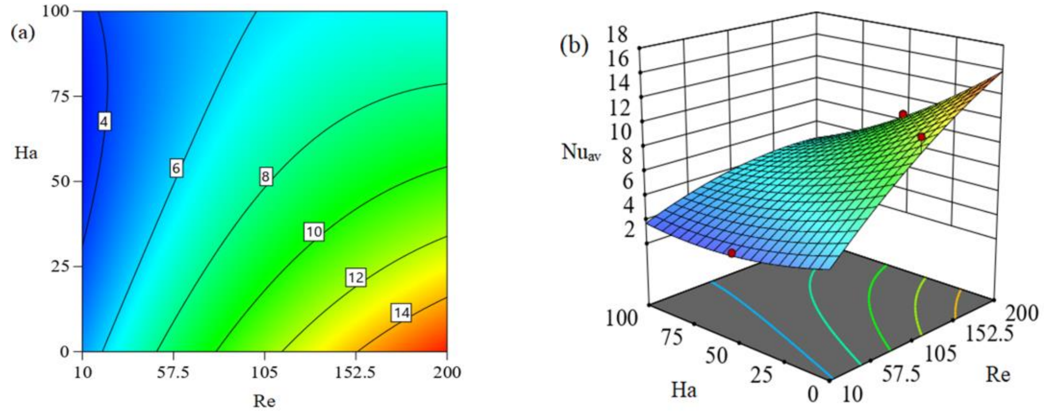

Fig. 16. Effect on Nu$_{av}$ for Re and Ha: (a) 2D sight; (b) 3D sight.

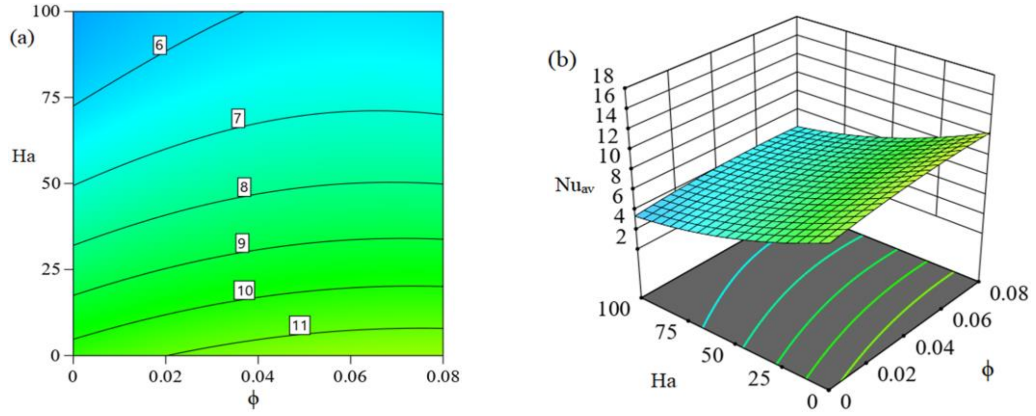

Fig. 17. Effect on Nu$_{av}$ for ϕ and Ha: (a) 2D sight; (b) 3D sight.

4.7. Sensitivity analysis of parameters

Sensitivity analysis, a process for the determination of how input uncertainty affects the model's response, is crucial to numerical simulation. By doing a "sensitivity analysis", it is possible to determine the extent to which the model's parameter distresses the generated variables [59]. Using the results of the sensitivity analysis, the important variables can be ranked in order of influence to determine which parameter is the most beneficial. By differentiating (partially) the response function with respect to autonomous factors (Re, ϕ and Ha), one can analytically evaluate the sensitivity of the output. Consequently, the following computation is made for Nu$_{av}$ with respect to the input parameters as in Eq. (14):

$$\frac{\partial \mathrm{Nu}_{av}}{\partial \mathrm{Re}} = 3.39 - 1.81\mathrm{Re} - 1.97\mathrm{Ha}, \tag{15}$$

$$\frac{\partial \mathrm{Nu}_{av}}{\partial \phi} = 0.5134, \tag{16}$$

$$\frac{\partial \mathrm{Nu}_{av}}{\partial \mathrm{Ha}} = -2.71 + 1.7684\mathrm{Ha} - 1.97\mathrm{Re}. \tag{17}$$

Eqs. (15) to (17) can now be used to calculate the rate of sensitivity of Nu_{av} to Re, ϕ and Ha. Table 8 presents the findings.

Table 8. Sensitivity analysis for Nu_{av}.

Re	**φ**	**Ha**	$\frac{\partial \mathrm{Nu}_{av}}{\partial \mathrm{Re}}$	$\frac{\partial \mathrm{Nu}_{av}}{\partial \phi}$	$\frac{\partial \mathrm{Nu}_{av}}{\partial \mathrm{Ha}}$
−1	0	−1	7.17	0.5134	−0.226
		0	5.2	0.5134	−0.74
0		−1	5.36	0.5134	−4.478
		0	3.39	0.5134	−2.71
1		−1	3.55	0.5134	−6.448
		0	1.58	0.5134	−4.68
−1	1	−1	7.17	0.5134	−0.226
		0	5.2	0.5134	−.74
0		−1	5.36	0.5134	−4.478
		0	3.39	0.5134	−2.71
1		−1	3.55	0.5134	−6.448
		0	1.58	0.5134	−4.68

The values obtained by applying this model are as follows: Ha at −1 and 0 (0 and 50), ϕ at 0 and 1 (0.04 and 0.08), and Re at −1, 0 and 1 (10, 105 and 200). Furthermore, it's critical to remember that a positive sensitivity indicates that the input factors are intensifying this response. This demonstrates how the Re and ϕ stimulate Nu_{av} in a positive way. Conversely, a negative sensitivity signifies the exact opposite trend, where raising input factors causes the response to drop. This signal suggests that the input factor Ha has a negative effect on Nu_{av}. Moreover, Fig. 18 illustrates negative sensitivity with respect to Nu_{av} by the flipped bar and positive sensitivity with respect to Nu_{av} by the upright bar. The sensitivity level is also displayed along the entire length of the bar.

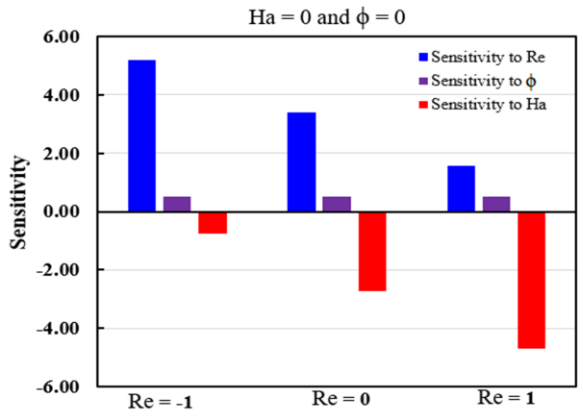

Fig. 18. Rate of sensitivity of Nu_{av} for independent factors at Ha = 0 and ϕ = 0.

6. Conclusions

This study focuses on the interaction between heat transport processes and the effects of magnetic fields, examining the behaviour of mixed convective heat fluxes in a confined cavity using a hybrid ($Ag\text{-}MgO\text{-}H_2O$) nanofluid. A numerical solution is developed using the Galerkin finite element method to capture the complex behaviour. The key findings are outlined below:

- Sensitivity analysis of the response function is performed using RSM to gain a comprehensive understanding of the heat transportation mechanism.
- The impact of the hybrid nanofluid on streamlines, isotherms, and Nu_{av} is investigated.
- Surface plots in two and three dimensions provide a clear visual representation of the heat transmission process for significant components involved.
- The hybrid nanofluid (Ag-MgO-H2O) shows superior thermal properties, resulting in better heat transfer performance than the base fluid or mono nanofluid, with heat transfer improvements of 3.37% and 7.09%, respectively.
- The Hartmann number (Ha) has a negative impact on the velocity profile.
- Sensitivity analysis results show that Reynolds number (Re) and nanoparticle volume fraction (ϕ) positively influence heat transfer from hot surfaces, while Ha has a negative impact on it.

This study can be extended in the future for non-Newtonian fluids and temperature-dependent thermophysical properties with a three-dimensional approach.

Acknowledgements

This research received funding BSMRSTU-RC-24-024, 2023–2024, from Bangabandhu Sheikh Mujibur Rahman Science and Technology University, Gopalganj 8100, Bangladesh.

References

[1] Cha, C.K., & Jaluria, Y. (1984). Recirculating mixed convection flow for energy extraction. *International Journal of Heat and Mass Transfer*, 27(10), 1801−1812. doi: 10.1016/0017-9310(84)90162-5

[2] Sadeghi, H.M., Babayan, M., & Chamkha, A. (2020). Investigation of using multi-layer PCMs in the tubular heat exchanger with periodic heat transfer boundary condition. *International Journal of Heat and Mass Transfer*, 147, 118970. doi: 10.1016/j.ijheatmasstransfer.2019.118970

[3] Qureshi, M.A., Hussain, S., & Sadiq, M.A. (2021). Numerical simulations of MHD mixed convection of hybrid nanofluid flow in a horizontal channel with cavity: Impact on heat transfer and hydrodynamic forces. *Case Studies in Thermal Engineering*, 27, 101321. doi: 10.1016/j.csite.2021.101321

[4] Islam, S., Islam, M.M., Rana, B.M.J., Islam, M.S., Reza-E-Rabbi, S., Hossain, M.S., & Rahman, M.M. (2023). Numerical investigation with sensitivity study of MHD mixed convective hexagonal heat exchanger using $TiO_2\text{–}H_2O$ nanofluid. *Results in Engineering*, 18, 101136. doi: 10.1016/j.rineng.2023.101136

[5] Mahalakshmi, T. (2023). A numerical analysis on MHD mixed convective hybrid nanofluid flow inside enclosure with heat

sources. *Journal of Nanofluids*, 12(4), 942−954. doi: 10.1166/jon.2023.1975

[6] Choi, S.U., & Eastman, J.A. (1995). *Enhancing thermal conductivity of fluids with nanoparticles* (No. ANL/MSD/CP-84938; CONF-951135-29). Argonne National Lab. (ANL), Argonne, IL (United States).

[7] Nadeem, S., Abbas, N., & Malik, M.Y. (2020). Inspection of hybrid based nanofluid flow over a curved surface. *Computer methods and programs in biomedicine*, 189, 105193. doi: 10.1016/j.cmpb.2019.105193

[8] Habiba, U., Hudha, M.N., Neogi, B., Islam, S., & Rahman, M.M. (2025). Numerical exploration on n-decane nanofluid based MHD mixed convection in a lid driven cavity: impact of magnetic field and thermal radiation. *International Journal of Thermofluids*, 27, 101209. doi.org/10.1016/j.ijft.2025.101209

[9] Kaushik, S., Singh Mahar, V., Singh, S., Kshetri, R., Kumar, B., Singh Mehta, J., & Kumar, A. (2024). Comparative experimental analysis of fluid flow in a concentric tube exchanger having semi hollow cylindrical macro inserts with nanofluid and base fluid. *Archives of Thermodynamics*, 45(2). doi: 10.24425/ather.2024.150866

[10] Islam, S., Siddiki, M.N.A.A., & Islam, M.S. (2024). Numerical simulation and sensitivity analysis using RSM on natural convective heat exchanger containing hybrid nanofluids. *Mathematical Problems in Engineering*, 2024(1), 2834556. doi: 10.1155/2024/2834556

[11] Dogonchi, A.S., Chamkha, A.J., & Ganji, D.D. (2019). A numerical investigation of magneto-hydrodynamic natural convection of Cu–water nanofluid in a wavy cavity using CVFEM. *Journal of Thermal Analysis and Calorimetry*, 135(4), 2599−2611. doi: 10.1007/s10973-018-7339-z

[12] Siddiki, M.N.A.A., Islam, S., Ahmmed, M.U., & Molla, M.M. (2024). Numerical simulation of a non-Newtonian nanofluid on mixed convection in a rectangular enclosure with two rotating cylinders. *International Journal of Ambient Energy*, 45(1), 2332525. doi: 10.1080/01430750.2024.2332525

[13] Hashemi-Tilehnoee, M., Dogonchi, A.S., Seyyedi, S.M., Chamkha, A.J., & Ganji, D.D. (2020). Magnetohydrodynamic natural convection and entropy generation analyses inside a nanofluid-filled incinerator-shaped porous cavity with wavy heater block. *Journal of Thermal Analysis and Calorimetry*, 141(5), 2033−2045. doi: 10.1007/s10973-019-09220-6

[14] Acharya, N., & Chamkha, A.J. (2022). On the magnetohydrodynamic Al2O3-water nanofluid flow through parallel fins enclosed inside a partially heated hexagonal cavity. *International Communications in Heat and Mass Transfer*, 132, 105885. doi: 10.1016/j.icheatmasstransfer.2022.105885

[15] Wang, D., & Hai, T. (2023). Effect of the length and thickness of three constant temperature baffles on the natural convection heat transfer of nanofluid flow inside an enclosure affected by a magnetic field. *Engineering Analysis with Boundary Elements*, 150, 70−83. doi: 10.1016/j.enganabound.2023.01.038

[16] Kaushik, S., Uniyal, V., Verma, A.K., Jha, A.K., Joshi, S., Makhloga, M., Pargai, P.S., Sharma, S.K., Kumar, R., & Pal, S. (2023). Comparative experimental and cfd analysis of fluid flow attributes in mini channel with hybrid CuO+ Zno+ H_2O nano fluid and (H2O) base fluid. *EVERGREEN Joint Journal of Novel Carbon Resource Sciences and Green Asia Strategy*, 10(1), 182−195. doi: 10.5109/6781069

[17] Hussain, S., Ahmed, S.E., & Akbar, T. (2017). Entropy generation analysis in MHD mixed convection of hybrid nanofluid in an open cavity with a horizontal channel containing an adiabatic obstacle. *International Journal of Heat and Mass Transfer*, 114, 1054−1066. doi: 10.1016/j.ijheatmasstransfer.2017.06.135

[18] Zaboli, M., Ajarostaghi, S.S.M., Saedodin, S., & Kiani, B. (2021). Hybrid nanofluid flow and heat transfer in a parabolic trough solar collector with inner helical axial fins as turbulator. *The European Physical Journal Plus*, 136(8), 841. doi: 10.1140/epjp/s13360-021-01807-z

[19] Mahalakshmi, T. (2023). A numerical analysis on MHD mixed convective hybrid nanofluid flow inside enclosure with heat sources. *Journal of Nanofluids*, 12(4), 942−954. doi: 10.1166/jon.2023.1975

[20] Mandal, D.K., Biswas, N., Manna, N.K., Gorla, R.S.R., & Chamkha, A.J. (2023). Hybrid nanofluid magnetohydrodynamic mixed convection in a novel W-shaped porous system. *International Journal of Numerical Methods for Heat and Fluid Flow*, 33(2), 510−544. doi: 10.1108/HFF-03-2022-0163

[21] Anee, M.J., Hasan, M.F., Siddiqa, S., & Molla, M.M. (2024). MHD Natural Convection and Sensitivity Analysis of Ethylene Glycol Cu-Al_2O_3 Hybrid Nanofluids in a Chamber with Multiple Heaters: A Numerical Study of Lattice Boltzmann Method. *International Journal of Energy Research*, 2024(1), 5521610. doi: 10.1155/2024/5521610

[22] Thumma, T., Pyari, D.R., Ontela, S., Al-Mdallal, Q.M., & Jarad, F. (2023). Heat transfer analysis of magnetized Cu-Ag-H_2O hybrid nanofluid radiative flow over a spinning disk when the exponential heat source and Hall current are substantial: optimization and sensitivity analysis. *Case Studies in Thermal Engineering*, 50, 103448. doi: 10.1016/j.csite.2023.103448

[23] Sheikholeslami, M. (2019). New computational approach for exergy and entropy analysis of nanofluid under the impact of Lorentz force through a porous media. *Computer Methods in Applied Mechanics and Engineering*, 344, 319−333. doi: 10.1016/j.cma.2018.09.044

[24] Khatun, S., Kundu, R., Islam, S., Aktary, R., & Kumar, D. (2025). Sensitivity analysis on natural convective trapezoidal cavity containing hybrid nanofluid with magnetic effect: Numerical and statistical approach. *Heliyon*, 11(1). doi: 10.1016/j.heliyon.2024.e41508

[25] Ali, M.Y., Islam, S., Alim, M.A., Biplob, R.A., & Islam, M.Z. (2024). Numerical investigation of MHD mixed convection in an octagonal heat exchanger containing hybrid nanofluid. *Heliyon*, 10(17).doi: 10.1016/j.heliyon.2024.e37162

[26] Alahmadi, R.A., Raza, J., Mushtaq, T., Abdelmohsen, S.A., Gorji, M.R., & Hassan, A. M. (2023). Optimization of MHD flow of radiative micropolar nanofluid in a channel by RSM: sensitivity analysis. *Mathematics*, 11(4), 939. doi: 10.3390/math11040939

[27] Neogi, B., Islam, S., Faiaz, M., Rana, B.J., & Rahman, M.M. (2025). Numerical exploration and sensitivity analysis on MHD natural convective hexagonal enclosure using Ag-MgO-H_2O hybrid nanofluids. *International Journal of Ambient Energy*, 46(1), 2444369. doi: 10.1080/01430750.2024.2444369

[28] Tayebi, T., & Chamkha, A.J. (2020). Magnetohydrodynamic natural convection heat transfer of hybrid nanofluid in a square enclosure in the presence of a wavy circular conductive cylinder. *Journal of Thermal Science and Engineering Applications*, 12(3), 031009. doi: 10.1115/1.4044857

[29] Gibanov, N.S., Sheremet, M.A., Oztop, H.F., & Abu-Hamdeh, N. (2017). Effect of uniform inclined magnetic field on mixed convection in a lid-driven cavity having a horizontal porous layer saturated with a ferrofluid. *International Journal of Heat and Mass Transfer*, 114, 1086−1097. doi: 10.1016/j.ijheatmasstrans-fer.2017.07.001

[30] Mebarek-Oudina, F., Redouane, F., & Rajashekhar, C. (2020). Convection heat transfer of MgO-Ag/water magneto-hybrid nanoliquid flow into a special porous enclosure. *Algerian Journal*

of Renewable Energy and Sustainable Development, 2(2), 84−95. doi: 10.46657/ajresd.2020.2.2.1

[31] Selimefendigil, F., & Chamkha, A.J. (2021). MHD mixed convection of Ag–MgO/water nanofluid in a triangular shape partitioned lid-driven square cavity involving a porous compound. *Journal of Thermal Analysis and Calorimetry*, 143(2), 1467−1484. doi: 10.1007/s10973-020-09472-7

[32] Ma, Y., Rashidi, M.M., Mohebbi, R., & Yang, Z. (2021). Investigation of magnetohydrodynamics in Ag-TiO_2/water hybrid nanofluid in a Shamse knot shaped cavity. *International Journal of Numerical Methods for Heat and Fluid Flow*, 31(1), 251−272. doi: 10.1108/HFF-12-2019-0909

[33] Munawar, S., Saleem, N., Ahmad Khan, W., & Nasir, S. (2021). Mixed convection of hybrid nanofluid in an inclined enclosure with a circular center heater under inclined magnetic field. *Coatings*, 11(5), 506. doi: 10.3390/coatings11050506

[34] Mourad, A., Aissa, A., Mebarek-Oudina, F., Jamshed, W., Ahmed, W., Ali, H.M., & Rashad, A.M. (2021). Galerkin finite element analysis of thermal aspects of Fe_3O_4-MWCNT/water hybrid nanofluid filled in wavy enclosure with uniform magnetic field effect. *International Communications in Heat and Mass Transfer*, 126, 105461. doi: 10.1016/j.icheatmasstransfer.2021. 105461

[35] Kaushik, S., Singh, S., & Panwar, K. (2021). Comparative analysis of thermal and fluid flow behaviour of diverse nano fluid using Al_2O_3, ZnO, CuO nano materials in concentric spiral tube heat exchanger. *Materials Today: Proceedings*, 46, 6625−6630. doi: 10.1016/j.matpr.2022.10.117

[36] Zhang, Y., Hangi, M., Wang, X., & Rahbari, A. (2023). A comparative evaluation of double-pipe heat exchangers with enhanced mixing. *Applied Thermal Engineering*, 230, 120793. doi: 10.1016/j.applthermaleng.2023.120793

[37] Kaushik, S., Singh, S., & Panwar, K. (2023). Experimental study of fluid flow properties in spiral tube heat exchanger with varying insert shape over spiral tube profile. *Materials Today: Proceedings*, 80, 78−84. doi: 10.1016/j.matpr.2022.10.117

[38] Tian, G., Tian, C., Alizadeh, A.A., Shirani, N., Nasajpour-Esfahani, N., Shamsborhan, M., & Baghaei, S. (2023). Entropy analysis and mixed convection of nanofluid flow in a pillow plate heat exchanger in the presence of porous medium. *Alexandria Engineering Journal*, 82, 541−556. doi: 10.1016/j.aej.2023. 10.019

[39] Kaushik, S., Singh, S., Kanojia, N., Rawat, K., & Panwar, K. (2020, March). Comparative study for thermal and fluid flow peculiarities in cascading spiral inner tube heat exchanger with or without diverse inserts over spiral tube. In *IOP Conference Series: Materials Science and Engineering*, 802(1), 012009. doi: 10.1088/1757-899X/802/1/012009

[40] Chen, H.T., Lin, Y.S., Chen, P.C., & Chang, J.R. (2016). Numerical and experimental study of natural convection heat transfer characteristics for vertical plate fin and tube heat exchangers with various tube diameters. *International Journal of Heat and Mass Transfer*, 100, 320−331. doi: 10.1016/j. ijheatmasstransfer.2016. 04.039

[41] Lee, J.H., Shin, J.H., Chang, S.M., & Min, T. (2020). Numerical analysis on natural convection heat transfer in a single circular fin-tube heat exchanger (Part 1): numerical method. *Entropy*, 22(3), 363. doi: 10.3390/e22030363

[42] Pakalka, S., Valančius, K., & Streckienė, G. (2021). Experimental and theoretical investigation of the natural convection heat transfer coefficient in phase change material (PCM) based fin-and-tube heat exchanger. *Energies*, 14(3), 716. doi: 10.3390/ en14030716

[43] Haq, R.U., Soomro, F.A., Wang, X., & Tlili, I. (2020). Partially heated lid-driven flow in a hexagonal cavity with inner circular obstacle via FEM. *International Communications in Heat and Mass Transfer*, 117, 104732. doi: 10.1016/j.icheatmasstransfer. 2020.104732

[44] Toudja, N., Labsi, N., Benkahla, Y.K., Ouyahia, S.E., & Benzema, M. (2022). Thermosolutal mixed convection in a lid-driven irregular hexagon cavity filled with MWCNT-MgO (15–85%)/CMC non-Newtonian hybrid nanofluid. *Journal of Thermal Analysis and Calorimetry*, 147, 855–878. doi: 10.1007/s10973-020-10288-8

[45] Rehman, K.U., Malik, M.Y., Al-Mdallal, Q.M., & Al-Kouz, W. (2020). Heat transfer analysis on buoyantly convective non-Newtonian stream in a hexagonal enclosure rooted with T-Shaped flipper: hybrid meshed analysis. *Case Studies in Thermal Engineering*, 21, 100725. doi: 10.1016/j.csite.2020.100725

[46] Majeed, A.H., Mahmood, R., Shahzad, H., Pasha, A.A., Islam, N., & Rahman, M.M. (2022). Numerical simulation of thermal flows and entropy generation of magnetized hybrid nanomaterials filled in a hexagonal cavity. *Case Studies in Thermal Engineering*, 39, 102293. doi: 10.1016/j.csite.2022.102293

[47] Garoosi, F., Hoseininejad, F., & Rashidi, M.M. (2016). Numerical study of heat transfer performance of nanofluids in a heat exchanger. *Applied Thermal Engineering*, 105, 436−455. doi: 10.1016/j.applthermaleng.2016.03.015

[48] Goodarzi, M., D'Orazio, A., Keshavarzi, A., Mousavi, S., & Karimipour, A. (2018). Develop the nano scale method of lattice Boltzmann to predict the fluid flow and heat transfer of air in the inclined lid driven cavity with a large heat source inside, Two case studies: Pure natural convection & mixed convection. *Physica A: Statistical Mechanics and Its Applications*, 509, 210−233. doi: 10.1016/j.physa.2018.06.013

[49] Plant, R.D., & Saghir, M.Z. (2021). Numerical and experimental investigation of high concentration aqueous alumina nanofluids in a two and three channel heat exchanger. *International Journal of Thermofluids*, 9, 100055. doi: 10.1016/j.ijft.2020.100055

[50] Hirpho, M., & Ibrahim, W. (2022). Mixed convection heat transfer of a hybrid nanofluid in a trapezoidal prism with an adiabatic circular cylinder. *Mathematical Problems in Engineering*, 2022(1), 8170224. doi: 10.1155/2022/8170224

[51] Aktary, R., Islam, S., Ray, S.C., Khatun, S., Kundu, R., & Biswas, A. (2025). Thermal performance analysis of Cu-MgO-H2O hybrid nanofluid in a partially heated trapezoidal cavity: FEM, RSM and ANN approaches. *Thermal Advances*, 4, 100062. doi.org/10.1016/ j.thradv.2025.100062

[52] Chabani, I., Mebarek-Oudina, F., Vaidya, H., & Ismail, A.I. (2022). Numerical analysis of magnetic hybrid Nano-fluid natural convective flow in an adjusted porous trapezoidal enclosure. *Journal of Magnetism and Magnetic Materials*, 564, 170142. doi: 10.1016/j.jmmm.2022.170142

[53] Rostami, S., Aghakhani, S., Hajatzadeh Pordanjani, A., Afrand, M., Cheraghian, G., Oztop, H.F., & Shadloo, M.S. (2020). A review on the control parameters of natural convection in different shaped cavities with and without nanofluid. *Processes*, 8(9), 1011. doi: 10.3390/pr8091011

[54] Basak, T., Roy, S., & Thirumalesha, C. (2007). Finite element analysis of natural convection in a triangular enclosure: effects of various thermal boundary conditions. *Chemical Engineering Science*, 62(9), 2623−2640. doi: 10.1016/j.ces.2007.01.053

[55] Siddiki, M.N.A.A., Islam, S., Ahmmed, M.U., & Molla, M.M. (2024). Numerical simulation of a non-Newtonian nanofluid on mixed convection in a rectangular enclosure with two rotating cylinders. *International Journal of Ambient Energy*, 45(1), 2332525. doi: 10.1080/01430750.2024.2332525

[56] Sivakumar, V., Sivasankaran, S., Prakash, P., & Lee, J. (2010). Effect of heating location and size on mixed convection in lid-

driven cavities. *Computers & Mathematics with Applications*, 59(9), 3053−3065. doi: 10.1016/j.camwa.2010.02.025

[57] Montgomery, D.C. (2017). *Design and analysis of experiments*. (9th ed.) John Wiley & Sons.

[58] Box, G.E., & Wilson, K.B. (1992). On the experimental attainment of optimum conditions. In *Breakthroughs in statistics: methodology and distribution* (pp. 270−310). Springer New York. doi: 10.1007/978-1-4612-4380-9_23

[59] Campolongo, F., & Braddock, R. (1999). The use of graph theory in the sensitivity analysis of the model output: a second order screening method. *Reliability Engineering & System Safety*, 64(1), 1−12. doi: 10.1016/S0951-8320(98)00008-8

Co-published by
Institute of Fluid-Flow Machinery
Polish Academy of Sciences
Committee on Thermodynamics and Combustion
Polish Academy of Sciences

http://www.imp.gda.pl/archives-of-thermodynamics/

ARCHIVES OF THERMODYNAMICS

Numerical analysis of the Soret and Dufour effects on boundary layer flow past a curved stretching surface in porous media with thermal slip and variable magnetic field

Temjennaro Jamir[a*], Hemanta Konwar[b], Bendangwapang Tzudir[b]

[a]Phek Government College, Phek, Phek 797108, India
[b]Kohima Science College, Jotsoma, Kohima 797001, India
*Corresponding author email: temjennaro@kscj.ac.in

Received: 28.09.2024; revised: 21.05.2025; accepted: 27.05.2025

Abstract

This study presents a novel investigation into the boundary layer flow, heat, and mass transfer of a Newtonian, incompressible and electrically conducting viscous fluid flow past a permeable curved stretching surface embedded in porous media with Soret and Dufour effects subject to varying magnetic fields and thermal slip. The research uniquely combines these complex phenomena, addressing a significant gap in the literature. This configuration has potential applications in electronic cooling systems, polymer manufacturing and compact heat exchangers in various industries. The main objectives are to understand how various parameters influence fluid flow, heat and mass transfer behaviour to optimize the design for enhanced performance. To attain the numerical results the governing equations are transformed into to a set of nonlinear ordinary differential equations, which are then solved numerically by using MATLAB's built-in solver bvp4c. The parameters of engineering interest are tabulated and validated with previous results. The outcomes of the study suggest that the presence of a larger magnetic parameter, Dufour number, Joule parameter, thermal slip and curvature parameter contribute to reducing the cooling rate of the system by 2.73%, 10.53%, 12.39%, 9.29% and 6.28%, respectively. Also, the curvature of the surface can be enlarged from 5 to 10 to obtain 6.87% reduction in surface drag force.

Keywords: Curved stretching surface; Variable magnetic field; Soret; Dufour; Porous media

Vol. 46(2025), No. 3, 77–87; doi: 10.24425/ather.2025.156580

Cite this manuscript as: Jamir, T., Konwar, H., & Tzudir, B. (2025). Numerical analysis of the Soret and Dufour effects on boundary layer flow past a curved stretching surface in porous media with thermal slip and variable magnetic field. *Archives of Thermodynamics*, 46(3), 77–87.

1. Introduction

In boundary layer flow, heat and mass transfer across a curved stretching surface is an important topic among researchers due to its numerous applications in polymer production, metallurgy and chemical engineering. Designing and creating new machinery and equipment with a high rate of heating or cooling draws the curiosity of many engineers and scientists. In industries, the intended final products are mostly determined by the rate of cooling. Additionally, a magnetic field has the potential to change heat transfer properties by rearranging fluid concentration. Furthermore, the direction and intensity of the applied magnetic field can be used to alter the fluid's behaviour. In industry, pure crystal semiconductor growth may be regulated by varying the magnetic field. Variable magnetic fields have been used to cure peptic ulcers, as well as for medical diagnostic and therapeutic purposes. Thus, studying the interactions between flow, heat, and mass transfer across curved stretching surfaces provides insights into complex physical phenomena and facilitates the development of innovative technologies and solutions across a wide range of industries.

Sajid et al. [1] were the first to explore the viscous flow caused by a curved stretching surface, discovering that dimensionless curvature increases boundary layer thickness while decreasing skin friction coefficients. Abbas et al. [2] investigated viscous fluid flow

Nomenclature

a – stretching rate
B – strength of magnetic field, T
B_0 – constant magnetic field, T
C – species concentration, kg m^{-3}
c_p – specific heat at constant pressure, J kg^{-1} K^{-1}
C_{fs} – local skin friction coefficient
C_∞ – ambient fluid concentration, kg m^{-3}
C_w – surface concentration, kg m^{-3}
c_s – concentration susceptibility
Da – Darcy parameter, $= \frac{\nu}{k_p a}$
D_m – mass diffusion coefficient, m^2 s^{-1}
Du – Dufour number, $= \frac{D_m k_T (C_w - C_\infty)}{c_s c_p \nu (T_w - T_\infty)}$
Ec – Eckert number, $= \frac{u_w^2}{c_p (T_w - T_\infty)}$
f – dimensionless stream function
J – Joule heating parameter, $= M^2$PrEc
K – curvature parameter, $= R\sqrt{\frac{a}{\nu}}$
k – thermal conductivity, W m^{-1} K^{-1}
k_p – coefficient of permeability
k_T – ratio of thermal diffusion
L – thermal slip parameter, $= L_1\sqrt{\frac{a}{\nu}}$
L_1 – thermal slip constant
M – magnetic parameter, $\sqrt{\frac{\sigma B_0^2}{\rho a}}$
Nu$_s$ – local Nusselt number
P – dimensionless pressure
p – pressure, N m^{-2}
Pr – Prandtl number, $= \frac{\mu c_p}{k}$
R – radius of curved surface, m
Re$_s$ – local Reynolds number, $= \frac{u_w s}{\nu}$
r, s – curvilinear coordinates
Sc – Schmidt number, $= \frac{\nu}{D_m}$
Sh$_s$ – local Sherwood number
Sr – Soret number, $= \frac{D_m k_T (T_w - T_\infty)}{T_m \nu (C_w - C_\infty)}$
T – fluid temperature, K
T_∞ – ambient fluid temperature, K
T_w – surface temperature, K
T_m – mean fluid temperature, K
u, v – velocity components in r- and s- directions, m s^{-1}
$(\cdot)'$, $(\cdot)''$, $(\cdot)'''$ – differentiation with respect to variable η

Greek symbols

ν – kinematic viscosity of the fluid, m^2 s^{-1}
η – similarity variable
μ – dynamic viscosity
σ – electrical conductivity of the fluid, S m^{-1}
ρ – fluid density, kg m^{-3}
θ – dimensionless fluid temperature
ϕ – dimensionless fluid concentration
λ – suction/injection parameter

and heat transfer in the presence of a constant applied magnetic field over a curved stretched surface. Rosca and Pop [3] used mass suction to study the problem of unstable viscous flow across a curved stretching or shrinking surface and found that, in the case of a curved stretching surface, the pressure inside the boundary layer cannot be disregarded. Sanni et al. [4,5] studied the transfer of heat from a non-linear curved stretched surface in the absence and presence of a varying magnetic field. Hayat et al. [6] investigated the flow of viscous fluid across a nonlinear curved stretching surface under convective heat and mass circumstances. Saranya et al. [7] analysed bio-convective nanofluid flow over a curved surface employing the shifted Legendre collocation method, concluding that the concentration of motile bacteria significantly decreases with an increase in the curvature parameter. Abbas and Shatanawi [8] employed the bvp4c numerical technique to examine micropolar fluid on a curved surface. Majeed et al. [9] observed that the presence of a magnetic field reduces the heat transfer rate and shear stress in the analysis of bio-convective nanoparticle fluid flow across a stretched surface. Abbas et al. [10] examined cilia flow in a curved channel subjected to a radial magnetic field, revealing a substantial influence on the thermal characteristics of the system. Mahesha et al. [11] investigated nanofluid behaviour within an annular space formed by two concentric cylinders, indicating that quadratic resistance significantly affects both flow dynamics and heat transfer characteristics.

A medium with holes or blank spaces is said to be porous. Some examples of materials with pores include sand, wood, boulders, and soil. Porosity and permeability are two of a porous material's most crucial characteristics. Porosity is the quality of being porous, whereas permeability measures how easily gases, liquids, or certain compounds may transport through a material. Understanding porous media may help explain a lot of elements of transport processes. The porous material can regulate the heating or cooling process. Because of their importance in geophysics, petroleum technology, cooling of nuclear reactors, biochemical processes and other fields, transport mechanisms in porous media have received a lot of attention in recent years. Ahmed et al. [12] discussed boundary layer flow over a curved surface embedded in a porous medium and it was observed that increasing values of the porosity parameter decreases the fluid velocity. Using the homotopy analysis method, Riaz et al. [13] examined the motion of nanoparticles in a non-Darcy porous curved channel. Adeyemo et al. [14] emphasized understanding the impact of changing viscosity on nonlinear convective fluid flow in a porous medium. Sonam and Yadav [15] examined steady, laminar Casson fluid flow generated by a semi-infinite vertical plate, incorporating the effects of the Darcy-Forchheimer model and employing the bvp4c numerical method. Similarly, Jagadha et al. [16] developed a model for the steady flow of Jeffrey nanofluid over a nonlinearly stretching flat sheet of variable thickness, also governed by the Darcy-Forchheimer relation, using the Runge-Kutta numerical approach.

Due to its numerous applications, including the solidification of binary alloys, oil reservoirs, isotope separation, chemical reactors, and mixtures of gases, Soret and Dufour effects are significant fields of study in heat and mass transfer processes. Energy flux due to concentration gradient and mass flux due to temperature gradient in a medium are known as the Dufour and Soret effects, respectively. They are important mechanisms in transport phenomena and are often ignored because of their low order of magnitude. Imtiaz et al. [17] identified the impacts of Soret and Dufour in the flow of viscous fluid by a curved stretching surface. Magnetohydrodynamic (MHD) boundary layer mixed convection flow past an exponentially extending permeable sheet in porous media was presented by Konwar et al. [18] together with the Soret and Dufour effects. In another numerical investigation conducted by Jamir et al. [19], the significance of Soret and Dufour effects on the fluid flow system about a stretching sheet was presented. Soret and Dufour effects were found to impact the concentration and temperature profile for a system involving ferromagnetic hybrid nanofluid flow over a permeable surface [20].

In engineering and industries, the study of viscous dissipation is a crucial factor in understanding the energy balance within a system. The dissipation of mechanical energy into heat through viscous effects can have implications for the efficiency and heat generation in various processes, such as fluid transport in pipelines, blood flow in arteries, or any situation involving the flow of viscous fluids. Heat and mass transfer through a porous medium was discussed by Haile and Shankar [21] on MHD flow of nanofluids with the effects of viscous dissipation, thermal radiation and chemical reaction. A study conducted by Oladapo et al. [22], who reported that the presence of slip effect significantly influences the flow and heat transfer of the system, referred to the case of a non-Newtonian fluid for enhanced heat transfer devices. Sademaki [23] elucidated the impact of viscous dissipation on sustained heat transfer in chemically reactive MHD nanofluid flow, incorporating mass and heat diffusion characteristics within a vertical cone filled with a saturated porous medium. Another study indicated that the Soret and Dufour effects impact the heat transfer rate in the flow of viscoelastic fluid caused by a stretching surface with viscous dissipation [24].

In the above literature survey, it is evident that MHD flow over curved surfaces is of great interest to researchers and is applicable in various fields of engineering. Taking into account the significance of the flow on curved surface, the present problem aims to provide insight into the problem of boundary layer flow, heat, and mass transfer over a permeable curved stretching sheet in porous media with Soret and Dufour effects subject to variable magnetic fields and thermal slip, which has not been accounted for in any of the literature cited above. The study aims to analyse the outcomes as well as find answers to how these parameters may possibly contribute to improving or reducing the boundary layers of the system under consideration. The study also looks into the parameters of engineering interest, which will significantly contribute towards finding new innovations to enhance cooling rates in curved devices and equipment, such as cooling electronics, heat exchanger design, polymer manufacturing and metal forming.

2. Mathematical formulation

This issue pertains to examining the flow of a two-dimensional, steady, Newtonian, incompressible, and electrically conducting viscous fluid flow past a permeable curved stretching sheet curled in a circle of radius R and the sheet is being stretched in s-direction with a velocity $u = as$, where $a > 0$ (see Fig. 1). Also, a variable magnetic field of strength $B(r) = RB_0(R+r)^{-1}\hat{e_r}$ is applied in the radial direction of the curved sheet and takes a constant value, when $R \to \infty$, where $\hat{e_r}$ is the unit vector in the radial direction. Assuming the magnetic Reynolds number is negligible, the influence of the induced magnetic field can be disregarded. Additionally, the work presents thermal slip conditions at the surface-fluid interface. This enhancement enriches our analysis and enables a more detailed examination of fluid flow.

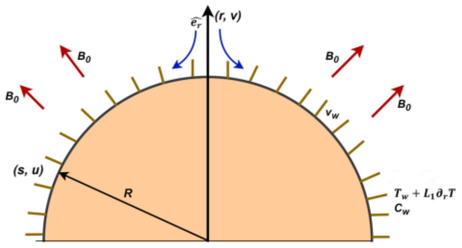

Fig. 1. Geometric configuration of the flow.

The present analysis includes a thorough array of assumptions, such as:

1. Integration of porous media effects, recognizing the impact of permeability on flow dynamics.
2. Assessment of suction-injection effects, essential for evaluating fluid transport phenomena.
3. Incorporation of viscous dissipation, Soret and Dufour effects to improve heat and mass transfer, particularly relevant to energy systems, augmentation of heat transfer, polymer processing, and advanced thermal management technologies.
4. Utilization of boundary layer approximation methods to analyse fluid flow near walls.
5. Consideration of thermal slip effect to reflect the realistic scenarios.

The flow in curvilinear coordinates is modelled by the governing equations, which are expressed as [5,7]:

$$\partial_r[(R+r)v] + R\partial_s u = 0, \tag{1}$$

$$\frac{u^2}{R+r} = \frac{1}{\rho}\partial_r p, \tag{2}$$

$$v\partial_r u + \left(\frac{Ru}{R+r}\right)\partial_s u + \frac{uv}{R+r} = -\frac{1}{\rho}\left(\frac{R}{R+r}\right)\partial_s p$$
$$+\nu\left[\partial_r^2 u + \left(\frac{1}{R+r}\right)\partial_r u - \frac{u}{(R+r)^2}\right] - \frac{\sigma B_0^2 R^2 u}{\rho(R+r)^2} - \frac{\nu u}{k_p}, \tag{3}$$

$$\left[v\partial_r T+\left(\frac{Ru}{R+r}\right)\partial_s T\right]=\frac{k}{\rho c_p}\left[\partial_r^2 T+\left(\frac{1}{R+r}\right)\partial_r T\right]+$$
$$+\frac{\mu}{\rho c_p}\left(\partial_r u-\frac{u}{R+r}\right)^2+\frac{D_m k_T}{c_s c_p}\left[\partial_r^2 C+\left(\frac{1}{R+r}\right)\partial_r C\right]+\frac{\sigma B_0^2 R^2 u^2}{\rho c_p (R+r)^2}, \quad (4)$$

$$v\partial_r C+\left(\frac{Ru}{R+r}\right)\partial_s C=D_m\left(\partial_r^2 C+\frac{1}{R+r}\partial_r C\right)+$$
$$+\frac{D_m k_T}{T_m}\left(\partial_r^2 T+\frac{1}{R+r}\partial_r T\right). \quad (5)$$

The appropriate boundary conditions are [8]:

$$u=u_w=as,\ v=-v_w,\ T=T_w+L_1\partial_r T,\ C=C_w \quad \text{at}\ r=0, \quad (6)$$

$$u\to 0,\ \partial_r u\to 0,\ T\to T_\infty,\ C\to C_\infty\ \text{as}\ r\to\infty, \quad (7)$$

where $v_w=\frac{Rv_0}{R+r}$ and v_0 is the initial value and variable velocity at the wall, respectively.

The following similarity transformations [1]:

$$u=asf'(\eta),\ v=\frac{-R}{R+r}\sqrt{av}\,f(\eta),\ \eta=\sqrt{a/v}\,r,$$
$$p=\rho a^2 s^2 P(\eta),\ \theta(\eta)=\frac{T-T_\infty}{T_w-T_\infty},\ \phi(\eta)=\frac{C-C_\infty}{C_w-C_\infty} \quad (8)$$

satisfy Eq. (1), and Eqs. (2) and Eq. (3) transform to:

$$P'=\frac{f'^2}{\eta+K}, \quad (9)$$

$$\frac{2K}{\eta+K}P=f'''+\frac{f''}{\eta+K}-\frac{f'}{(\eta+K)^2}-\frac{Kf'^2}{\eta+K}+\frac{Kff''}{\eta+K}+$$
$$+\frac{Kff'}{(\eta+K)^2}-\frac{M^2K^2f'}{(\eta+K)^2}-\mathrm{Da}f'. \quad (10)$$

Eliminating pressure P from Eqs. (9) and (10), the following dimensionless momentum equation is obtained:

$$f'^{v}+\frac{2f'''+K\left(ff'''-f'f''\right)}{\eta+K}-\frac{f''-K\left(ff''-f'^2\right)}{(\eta+K)^2}+\frac{f'-Kff'}{(\eta+K)^3}+$$
$$-\frac{M^2K^2}{(\eta+K)^2}\left[f''-\frac{f'}{(\eta+K)}\right]-\mathrm{Da}\left(f''+\frac{f'}{\eta+K}\right)=0. \quad (11)$$

Prime in this case represents derivatives with regard to the similarity variable η.

With the transformations (8), the energy and species concentration equations in dimensionless form become:

$$\theta''+\frac{\theta'}{\eta+K}+\frac{\mathrm{Pr}Kf\theta'}{\eta+K}+\mathrm{PrEc}\left(f''-\frac{f'}{\eta+K}\right)^2+$$
$$+\mathrm{PrDu}\left(\phi''+\frac{\phi'}{\eta+K}\right)+\frac{JK^2f'^2}{(\eta+K)^2}=0, \quad (12)$$

$$\phi''+\frac{\phi'}{\eta+K}+\frac{\mathrm{Sc}Kf\phi'}{\eta+K}+\mathrm{ScSr}\left(\theta''+\frac{\theta'}{\eta+K}\right)=0 \quad (13)$$

together with transformed boundary conditions:

$$f(\eta)=\lambda,\ f'(\eta)=1,\ \theta(\eta)=1+L\theta'(\eta),\ \phi(\eta)=1\ \text{at}\ \eta=0, \quad (14)$$

$$f'(\eta)\to 0,\ f''(\eta)\to 0,\ \theta(\eta)\to 0,\ \text{as}\ \eta\to\infty, \quad (15)$$

were suction is represented by $\lambda=\frac{v_0}{\sqrt{av}}>0$ and injection by $\lambda<0$ [18].

The skin friction coefficient $C_{fs}=\tau_{rs}/(\rho u_w^2)$, Nusselt number $\mathrm{Nu}_s=sq_w/\{k(T_w-T_\infty)\}$, and Sherwood number $\mathrm{Sh}_s=sq_m/\{D_m(C_w-C_\infty)\}$ are engineering characteristics that contribute significantly to understanding heat and mass transfer. Here, $\tau_{rs}=\mu\left(\partial_r u-\frac{u}{r+R}\right)_{r=0}$ is the wall shear stress, $q_w=-k(\partial_r T)_{r=0}$ is the wall heat flux and $q_m=-D_m(\partial_r C)_{r=0}$ represents the wall mass flux.

Upon using Eqs. (8), the following are determined:

– the skin friction coefficient:

$$\mathrm{Re}_s^{\frac{1}{2}}C_{fs}=f''(0)-\frac{f'(0)}{K}, \quad (16)$$

– the Nusselt number:

$$\mathrm{Re}_s^{-\frac{1}{2}}\mathrm{Nu}_s=-\theta'(0), \quad (17)$$

and the Sherwood number:

$$\mathrm{Re}_s^{-\frac{1}{2}}\mathrm{Sh}_s=-\phi'(0). \quad (18)$$

3. Numerical procedure

The bvp4c method (a finite difference method that provides C^1-continuous solution) [25] is utilized to derive the computational solution of Eqs. (11)−(13), subject to the limitations defined by Eqs. (14) and (15). Current flow difficulties include dimensionless ordinary differential equations that exhibit a particularly high nonlinear nature. The principal research objective is to precisely tackle challenges pertaining to non-linear flow phenomena. The bvp4c numerical approach within the MATLAB software is the most suitable for acquiring the quantitative solution of the present model [25]. It is important to supply three distinct categories of data: the first-order equations to be solved, the corresponding boundary conditions, and the first guess employed to ascertain the solution to the problem. The integration interval is defined from zero to five and from zero to ten, with a relative tolerance set at 10^{-7}. The mesh is automatically changed to enhance accuracy based on this tolerance.

We reformulate the provided equations for the bvp4c code as a system of first-order ordinary differential equations (ODEs):

$$f=y_1,\ f'=y_2,\ f''=y_3,\ f'''=y_4,$$
$$\theta=y_5,\ \theta'=y_6,\ \phi=y_7,\ \phi'=y_8. \quad (19)$$

By substituting Eqs. (19) into equations Eqs. (11)−(13), the resultant system of 1st-order ODE can be derived:

$$y_1'=y_2, \quad (20)$$

$$y_2'=y_3, \quad (21)$$

$$y_3'=y_4, \quad (22)$$

$$y_4'=-\frac{2y_4+K(y_1y_4-y_2y_3)}{\eta+K}+\frac{y_3-K\left(y_1y_3-{y_2}^2\right)}{(\eta+K)^2}-\frac{y_2-Ky_1y_2}{(\eta+K)^3}+$$
$$+\frac{M^2K^2}{(\eta+K)^2}\left(y_3-\frac{y_2}{\eta+K}\right)+\mathrm{Da}\left(y_3+\frac{y_2}{\eta+K}\right), \quad (23)$$

$$y_5'=y_6, \quad (24)$$

$$y_6' = \frac{1}{1-\mathrm{PrDuSrSc}}\left[-\frac{y_6}{\eta+K} - \frac{\mathrm{Pr}Ky_1y_6}{(\eta+K)} - \mathrm{PrEc}\left(y_3 - \frac{y_2}{(\eta+K)}\right)^2 + \right.$$
$$\left. - \frac{JK^2{y_2}^2}{(\eta+K)^2} - \mathrm{PrDu}\left(-\frac{K\mathrm{Sc}y_1y_8}{\eta+K} - \frac{\mathrm{ScSr}y_6}{\eta+K}\right)\right], \tag{25}$$

$$y_7' = y_8, \tag{26}$$

$$y_8' = -\frac{y_8}{\eta+K} - \frac{K\mathrm{Sc}y_1y_8}{\eta+K} - \mathrm{ScSr}\left\{\frac{1}{(1-\mathrm{PrDuSrSc})}\left[-\frac{y_6}{\eta+K} + \right.\right.$$
$$- \frac{\mathrm{Pr}Ky_1y_6}{\eta+K} - \mathrm{PrEc}\left(y_3 - \frac{y_2}{\eta+K}\right)^2 - \frac{JK^2{y_2}^2}{(\eta+K)^2} +$$
$$\left.\left. -\mathrm{PrDu}\left(-\frac{K\mathrm{Sc}y_1y_8}{\eta+K} - \frac{\mathrm{ScSr}y_6}{\eta+K}\right)\right] + \frac{y_6}{\eta+K}\right\} \tag{27}$$

with the transformed boundary conditions as follows:

$$y_1(0) - \lambda,\ y_2(0) - 1,\ y_5(0) - 1 - Ly_6(0), y_7(0) - 1, \tag{28}$$

$$y_2(\infty);\ y_3(\infty);\ y_5(\infty);\ y_7(\infty). \tag{29}$$

4. Validation of results

To validate the methodology used in this study, numerical values that have been obtained in the study have been compared to those obtained by Abbas et al. [2] and Sanni et al. [5], using the shooting method with the Runge-Kutta algorithm in MATLAB. This is shown in Table 1, which tabulates the values of the surface drag force and the heat transfer rate upon varying the curvature parameter and the magnetic parameter. The data recorded in Table 1 are seen to be in good convergence, which shows the accuracy of the present numerical scheme.

Table 1. Comparison of $-\mathrm{Re}_s^{\frac{1}{2}}C_{fs}$ and $\mathrm{Re}_s^{-\frac{1}{2}}\mathrm{Nu}_s$ for different values of K and M, when Pr = 0.7, Ec = 0.2, in absence of other parameters.

		Abbas et al. [2]		**Sanni et al. [5]**		**Present result**	
K	***M***	$-\mathrm{Re}_s^{\frac{1}{2}}C_{fs}$	$\mathrm{Re}_s^{-\frac{1}{2}}\mathrm{Nu}_{fs}$	$-\mathrm{Re}_s^{\frac{1}{2}}C_{fs}$	$\mathrm{Re}_s^{-\frac{1}{2}}\mathrm{Nu}_{fs}$	$-\mathrm{Re}_s^{\frac{1}{2}}C_{fs}$	$\mathrm{Re}_s^{-\frac{1}{2}}\mathrm{Nu}_{fs}$
5	**0.2**	1.22881	0.43268	1.20372	0.42418	1.20442	0.42716
10	**0.2**	1.12311	0.41896	1.10709	0.41132	1.10485	0.41137
20	**0.2**	1.07541	0.41094	1.06389	0.40365	1.06045	0.40009
50	**0.2**	1.04849	0.40571	1.03958	0.39864	1.02779	0.39370
100	**0.2**	1.03982	0.40390	1.03175	0.39691	1.02389	0.39113
200	**0.2**	1.03553	0.40298	1.02788	0.39604	1.02080	0.38981
10	**0.2**	1.12311	0.41896	1.10709	0.41132	1.11909	0.41137
10	**0.4**	1.18306	0.40717	1.16408	0.39975	1.17579	0.39754
10	**0.6**	1.27633	0.38927	1.25344	0.38190	1.26228	0.38109
10	**0.8**	1.39562	0.36727	1.36870	0.35953	1.37096	0.35223

5. Results and discussion

This paper examines the steady, two-dimensional boundary layer flow, heat and mass transfer, thermal slip, and variable magnetic field of a Newtonian, incompressible, viscous, and electrically conducting fluid past a permeable curved stretching surface in porous media. The distributions of fluid temperature, concentration, and velocity are represented graphically with the numerical findings, and the behaviour of different parameters is examined. Different parameter values are taken into consideration, with Prandtl number Pr = 0.7 taken for air and Schmidt number Sc = 0.6 taken for water vapour, K = 5, Da = 0.5, M = 0.2, J = 0.2, Ec = 0.2, Sr = 0.4, Du = 0.2, λ = 0.2, L = 0.2, unless stated otherwise.

Figures 2−7 illustrate the outcome of the curvature parameter (K) and the magnetic parameter (M) on the boundary layers of the fluid. It has been observed that $f'(\eta)$, $\theta(\eta)$, and $\phi(\eta)$ exhibit an increase as K becomes greater. As K grows, the surface shape transforms, hence modifying the fluid flow over it. Enhanced curvature results in elevated gradients within the velocity field owing to the more significant bending of the surface. This improves velocity distributions. The extended surface will improve the thermal and species dispersion of the fluid due to its significant capacity for fluid movement and contact with the surface. Consequently, the thickness of the thermal and concentration boundary layers will increase.

A reverse effect is noticed for the magnetic parameter. The resistive force known as the Lorentz force, produced due to the effect of the magnetic field on an electrically conducting fluid, suppresses the bulk motion of the fluid and, as a result, both the components of fluid velocity decrease. Moreover, because of the friction caused by this resistive force, more heat is generated, which eventually increases the temperature and concentration distribution in the flow. According to tabulated data in Table 3, upon increasing curvature of the surface (5 ≤ K ≤ 10) and magnetic field intensity (0.2 ≤ M ≤ 0.5), both the heat transfer rate and mass transfer rate reduce, by 6.28% and 2.73%, and by 7.3% and 1.15%, respectively. Thus, one can increase the cooling rate in conducting fluid flows by considering lesser curvature parameter and magnetic field. Moreover, for a larger curved surface, the

Table 2. Numerical values of $-\mathrm{Re}_s^{\frac{1}{2}}C_{fs}$ with Pr = 0.7, Ec = 0.2, Du = 0.2, J = 0.2, Sc = 0.6, Sr = 0.4 and L = 0.2.

K	***M***	**Da**	***λ***	$-\mathrm{Re}_s^{\frac{1}{2}}C_{fs}$
5	0.2	0.5	0.2	1.54627
10	0.2	0.5	0.2	1.44009
5	0.5	0.5	0.2	1.61541
5	0.2	0.7	0.2	1.62783
5	0.2	0.5	0.4	1.63839

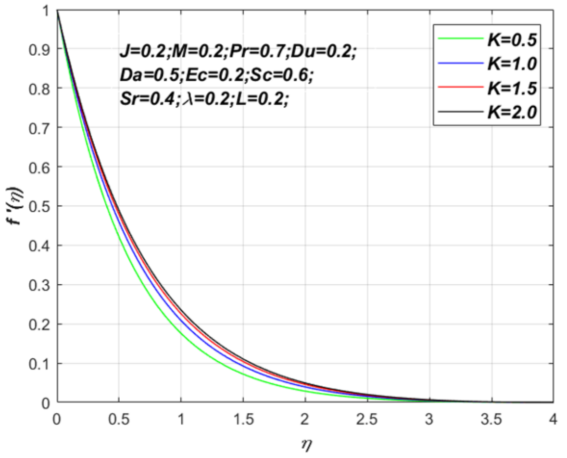

Fig. 2. Velocity distribution over varying *K*.

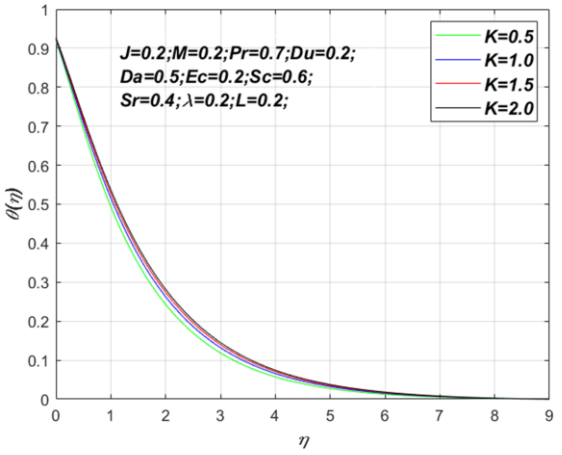

Fig. 3. Temperature distribution over varying *K*.

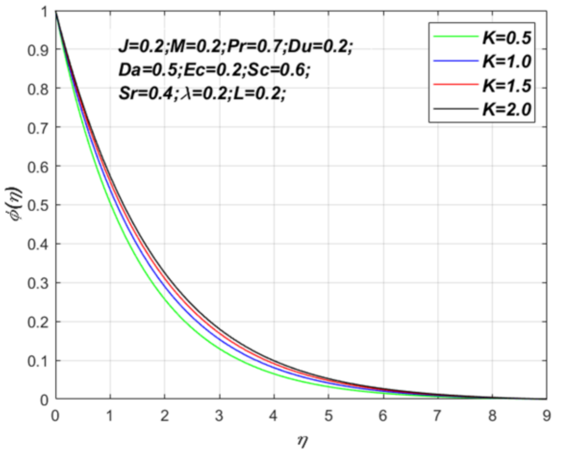

Fig. 4. Concentration distribution over varying *K*.

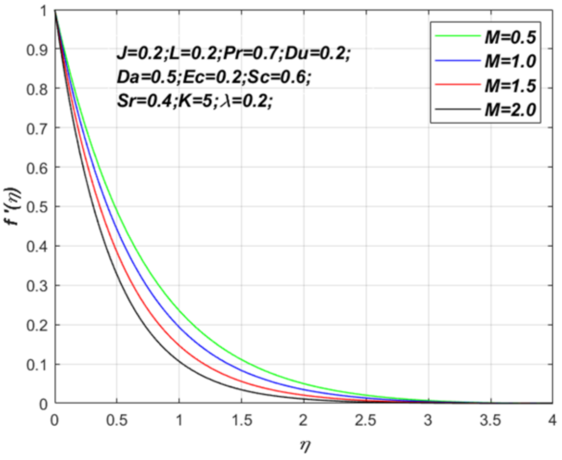

Fig. 5. Velocity distribution over varying *M*.

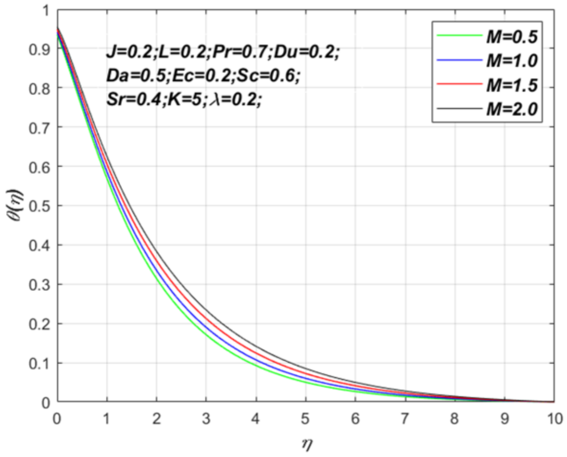

Fig. 6. Temperature distribution over varying *M*.

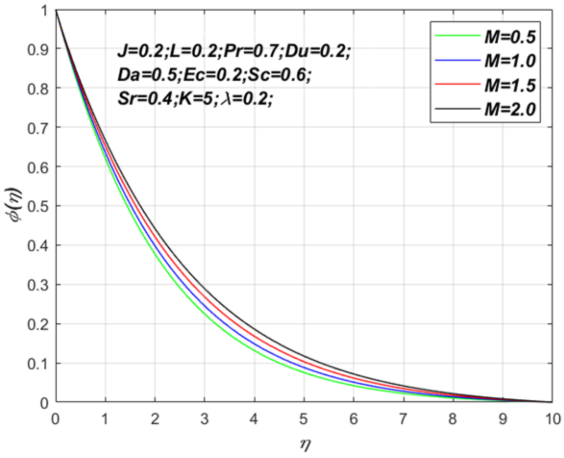

Fig. 7. Concentration distribution over varying *M*.

surface drag force decreases by about 6.87%, while as the magnetic field intensifies, the surface drag also improves by around 4.47% (see Table 2).

Figures 8−10 represent the effects of Darcy parameter (Da) on velocity component ($f'(\eta)$), temperature ($\theta(\eta)$) and concentration ($\phi(\eta)$) distributions. The porous medium physically exemplifies a type of external resistance that restricts fluid movement, resulting in a reduction of fluid velocity. It is established that an increase in Darcy number alters the permeability rate of the fluid through the porous medium, consequently diminishing the velocity distribution. However, the temperature of the fluid increases due to the rising values of Da. This is because increased porosity facilitates greater

Table 3. Numerical values of $\mathrm{Re}_s^{-\frac{1}{2}}\mathrm{Nu}_s$ and $\mathrm{Re}_s^{-\frac{1}{2}}\mathrm{Sh}_s$ when $\lambda = 0.2$.

K	M	Da	Pr	Ec	Du	J	Sc	Sr	L	$\mathrm{Re}_s^{-\frac{1}{2}}\mathrm{Nu}_{fs}$	$\mathrm{Re}_s^{-\frac{1}{2}}\mathrm{Sh}_{fs}$
5	0.2	0.5	0.7	0.2	0.2	0.2	0.6	0.4	0.2	0.33151	0.47911
10	0.2									0.31066	0.44414
5	0.5									0.32246	0.47359
	0.2	0.7								0.32085	0.47264
		0.5	1.38							0.46581	0.44967
			0.7	0.4						0.22965	0.50344
				0.2	0.4					0.29661	0.48721
					0.2	0.4				0.29044	0.48892
						0.2	0.94			0.31418	0.62965
							0.6	0.8		0.33513	0.44537
								0.4	0.4	0.30072	0.48362

fluid movement across the medium, hence enhancing convective heat transfer, which effectively transports heat and causes a temperature increase within the porous medium. Also, an increase in the concentration distribution is noted when the values of Da increase. This is due to the rate of permeability of the porous medium, which makes the thickness of the boundary layer continuously increasing (see Fig. 10). From Tables 2 and 3, it has been observed that surface drag increases by about 5.27%, while the heat and mass transfer rates both reduce by 3.22% and 1.35%, respectively, within 0.5 ≤ Da ≤0.7.

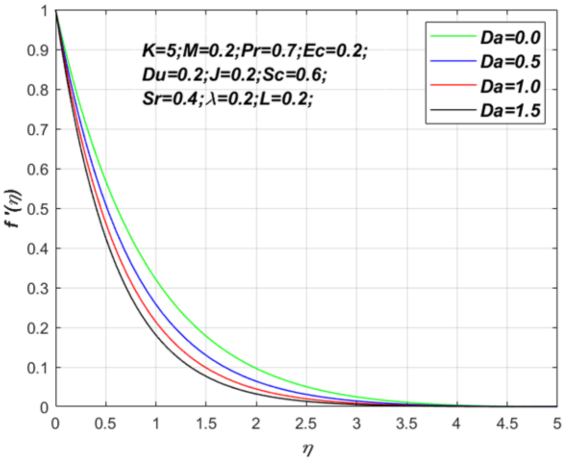

Fig. 8. Velocity distribution over varying Da.

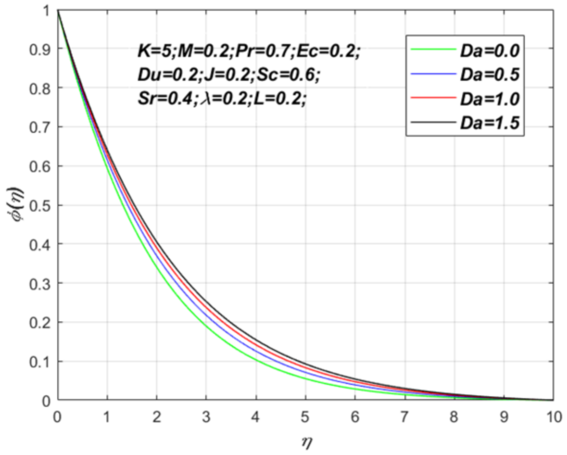

Fig. 10. Concentration distribution over varying Da.

Figures 11 and 12 depict the impact of the Prandtl number (Pr) on the temperature distribution $(\theta(\eta))$ and the concentration distribution $(\phi(\eta))$, correspondingly. The parametric values evaluated for Pr are 0.015, 0.7, 1.38 and 7.0, which correspond

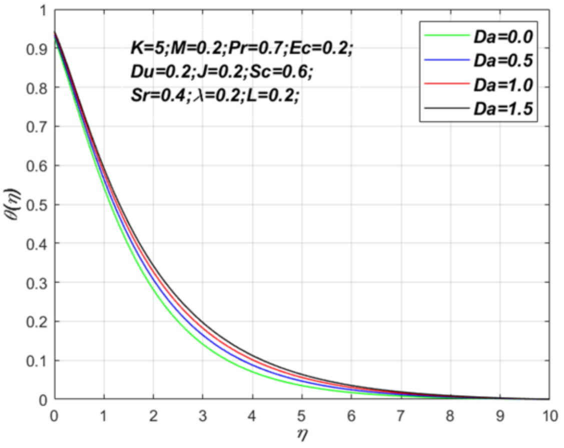

Fig. 9. Temperature distribution over varying Da.

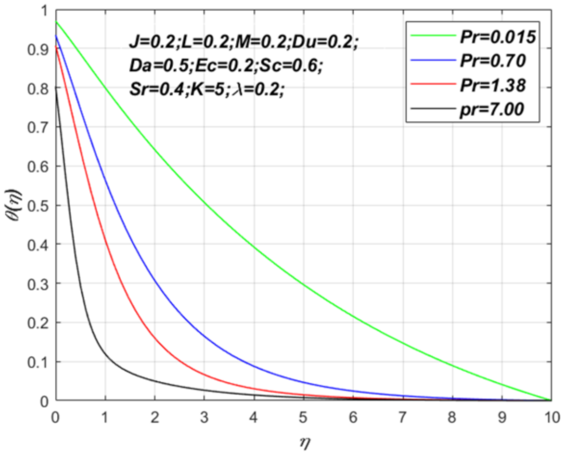

Fig. 11. Temperature distribution over varying Pr.

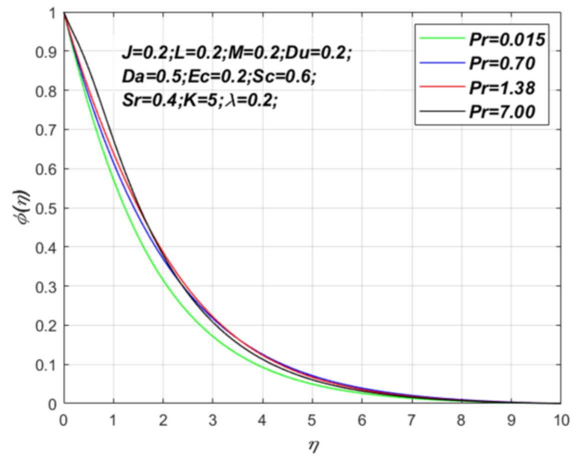

Fig. 12. Concentration distribution over varying Pr.

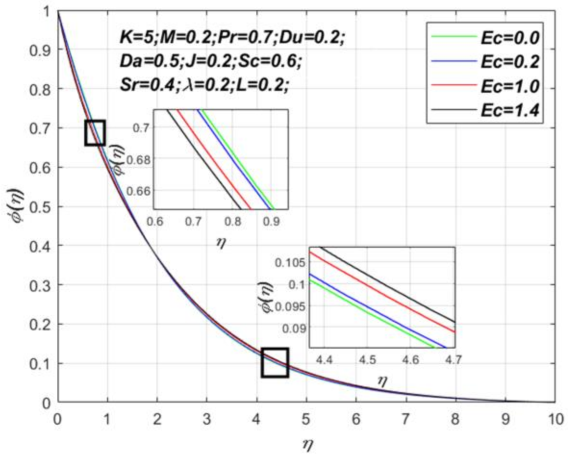

Fig. 14. Concentration distribution over varying Ec.

to liquid metal, air, ammonia, and water, respectively. The results indicate a significant decrease in temperature for large Prandtl numbers, resulting in the weakening of the thermal boundary layer. The concentration of fluid along the wall increases and falls away from the sheet when the value of η is greater than 2.3 for materials with high Pr values. Physically, a higher Pr value indicates a lower thermal diffusivity, which means that heat is dispersed more slowly from the surface, resulting in a drop in the temperature of the fluid. Table 3 demonstrates that when the values of Pr grow ($0.7 \leq \mathrm{Pr} \leq 1.38$), the heat transfer rate experiences a substantial increase of 40.51%; however, the mass transfer rate decreases by approximately 6.14%. Fluids with lower Prandtl numbers have stronger thermal conductivities, facilitating faster heat dissipation from the surface compared to fluids with higher Pr values. Prandtl number can therefore be used to increase the cooling rate in conducting fluid flows.

The outcome of the rising values of the Eckert number (Ec) on the temperature ($\theta(\eta)$) and concentration ($\phi(\eta)$) distributions is depicted in Figs. 13 and 14. It is known that temperature is considered the average of kinetic energy, while on the other hand, Ec exhibits a relation with kinetic energy. Thus, keeping these two conditions, it can be concluded that upon improving the energy dissipation, the kinetic energy increases, which in turn significantly improves the temperature distribution. It is also important to note that because of this factor, the concentration of the fluid near the vicinity of the surface declines, while upon entering the region $\eta > 1.9$, a reverse trend is noticed in the concentration distribution. Also, from Table 3, it can be concluded that Ec is an important parameter in the heat transport phenomenon and can be incorporated to significantly reduce, by 30.73%, the rate of cooling and enhance by 5.08% the mass transfer rate.

In Figs. 15 and 16, the influence of the Joule heating parameter (J) on the distributions of temperature and concentration is presented. Physically, as the Joule heating parameter enhances the impact of the energy dissipation, as well as the magnetic field, intensifies, thus the resulting Lorentz force aids in promoting the heating of the curved surface; also, due to inside friction of molecules, the mechanical energy, which gets converted to thermal energy aids in improving the temperature distribution significantly (mainly near the vicinity of the curved surface).

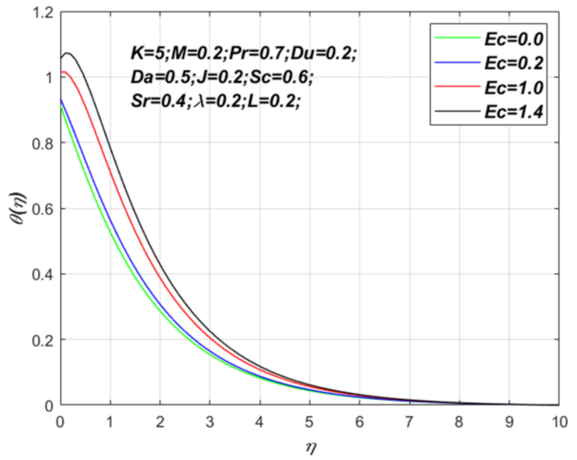

Fig. 13. Temperature distribution over varying Ec.

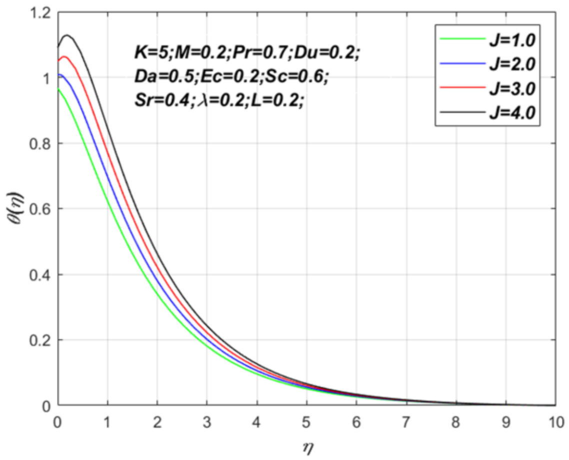

Fig. 15. Temperature distribution over varying J.

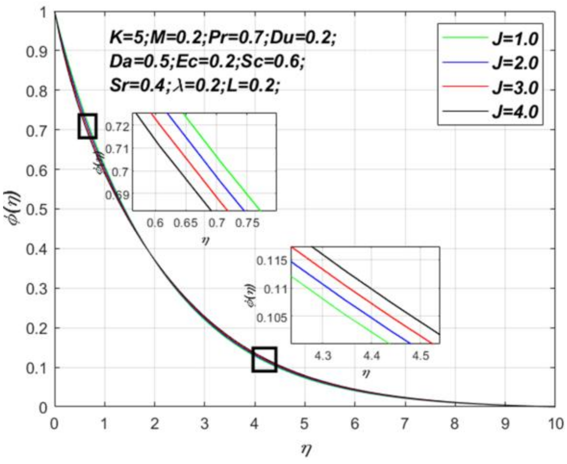

Fig. 16. Concentration distribution over varying *J*.

Because of these factors, although the concentration distribution is found to be declining near the vicinity of the surface in a region beyond $\eta > 1.9$, the species concentration distribution slowly rises. From Table 3, it can be concluded that improving J can significantly reduce, by 12.39%, the cooling rate and enhance by 2.05% the mass transfer rate.

The effects of Schmidt number (Sc) on concentration ($\phi(\eta)$) distribution of the fluid are shown in Fig. 17. Parametric values considered for Sc are 2.35, 1.32, 0.94, and 0.22 corresponding to naphthalene, ethanol, hydrogen sulphide, and helium, respectively. Data plotted show that as the Sc concentration increases, the fluid concentration within the boundary layer drops. The reason for this is that a greater value of Sc indicates a higher kinematic viscosity, which hinders the movement of mass and, consequently, results in a reduction of the fluid concentration. A significant hike in the mass transfer rate (by 31.42%) is also recorded in Table 3 for $0.6 \le \mathrm{Sc} \le 0.94$.

Figures 18 and 19 depict the effects of Dufour (Du) and Soret (Sr) on the temperature ($\theta(\eta)$) and species concentration ($\phi(\eta)$) distributions, respectively. It has been observed that an increase in the Dufour number causes a rise in the temperature of the fluid, while under the same influence, a varying outcome is observed on the concentration distribution. As reflected in Fig. 19, the concentration of species declines near the vicinity of the curved surface; however, beyond $\eta > 4.5$, the species concentration begins to rise. When the Dufour number is relatively elevated, thermal diffusion prevails over mass diffusion. This may lead to fluctuations in temperature gradients, which can subsequently generate buoyancy effects, altering the density distribution and perhaps affecting flow patterns through natural convection. The Dufour phenomenon results in a broader temperature distribution compared to its absence. From Figs. 18 and 19, it is also clear that Sr significantly improves species concentration, while reducing the temperature profile to a certain extent. The distribution of concentrations in the Soret phenomenon is influenced by the temperature gradient. In fact, higher Soret numbers cause more convective flow since they are linked to larger temperature gradients. The dispersion of the concentration rises as a result. Analysis from Table 3 shows that a higher $0.2 \le \mathrm{Du} \le 0.4$ aids in reducing the heat transfer rate significantly (by 10.53%), while enhancing the mass transfer rate (by 1.69%). On the contrary, higher $0.4 \le \mathrm{Sr} \le 0.8$ aids in enhancing the heat

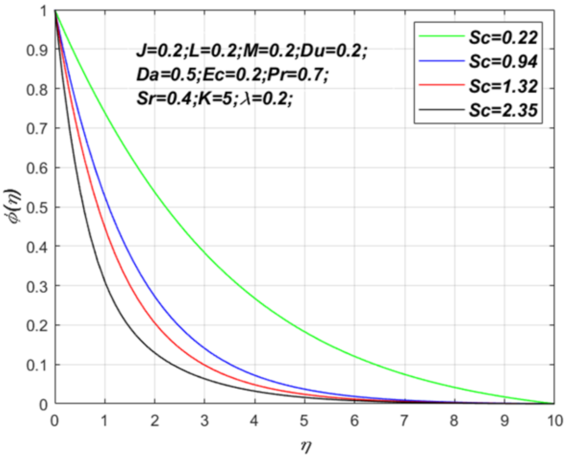

Fig. 17. Concentration distribution over varying Sc.

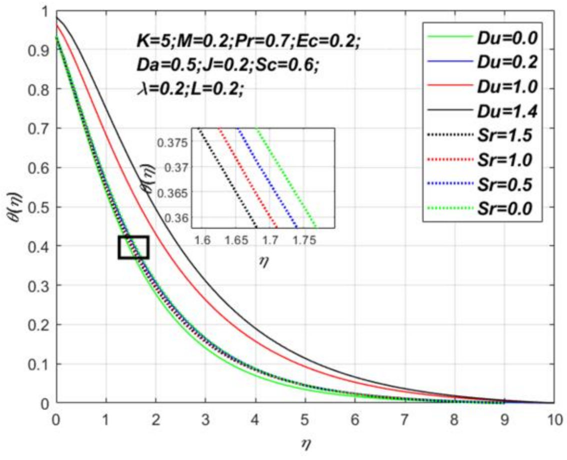

Fig. 18. Temperature distribution over varying Du and Sr.

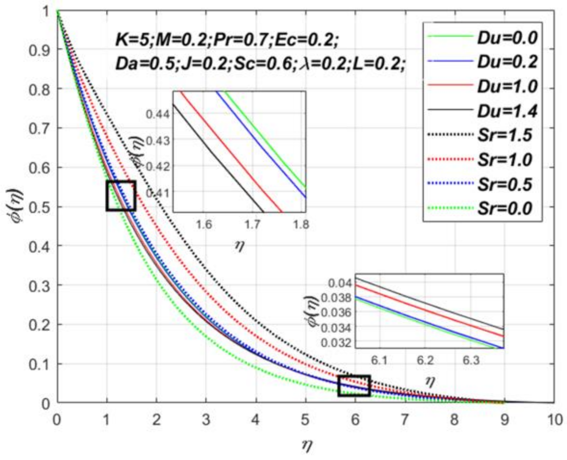

Fig. 19. Concentration distribution over varying Du and Sr.

transfer rate (by 1.09%) and significantly reduces the mass transfer rate (by 7.04%).

Figure 20 depicts the graphical data of the temperature ($\theta(\eta)$) distribution upon enhancing the thermal slip parameter (L). It is clear from Fig. 20 that increasing L results in a substantial decrease in the temperature distribution in the region closer to the curved wall. Physically, this decrease in surface temperature happens as a result of thermal slip, which facilitates heat transfer from the fluid surface to its interior. The temperature inside the thermal boundary layer drops as a result of the improved heat transfer brought on by thermal slip. The data presented in Table 3 indicates a notable decrease of around 9.29% in heat transfer rates for $0.2 \le L \le 0.4$.

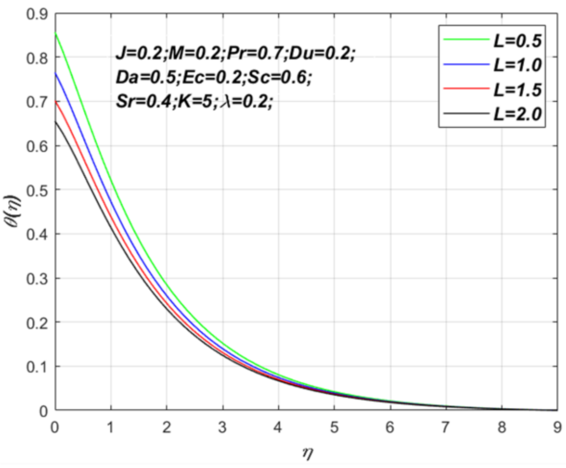

Fig. 20. Temperature distribution over varying L.

6. Conclusions

Based on the preceding discussions, the following conclusions can be drawn:

- Velocity of fluid increases for higher curvature parameter and decreases with increasing Darcy parameter and magnetic parameter.
- The curvature parameter, magnetic parameter and Darcy parameter can be increased for the reduction of the heat transfer rate (by around 6.28%, 2.73%, and 3.22%, respectively), as well as the mass transfer rates (by around 7.30%, 1.15%, and 1.35%, respectively).
- For large Prandtl numbers, there is a significant decrease in temperature. Therefore, the Prandtl number can be utilized to enhance the cooling rate (by around 40.51%) in the flow of conducting fluids.
- The Eckert number, Dufour number and the Joule heating parameter tend to reduce the species concentration in the vicinity of the curved region, while at a distance away from the surface, they also aid in gradually boosting the species concentration.
- The Soret number increases the concentration of the fluid. The heat transfer rate increases (by 1.09%), but the mass transfer rate decreases (by 7.04%) for larger values of the Soret number.
- The Dufour number significantly contributes towards raising the temperature of the fluid and aids in reducing the cooling rate by 10.53%.
- The mass transfer rate increases for higher values of the Dufour number (by 1.69%), the Schmidt number (by 31.42%), the Joule heating parameter (by 2.05%) and the Eckert number (by 5.08%).

The physics of flow on curved surfaces with variable magnetic field and heat slip can be employed in various physical domains, including industries, aeronautics, medicinal research, and engineering sciences.

Acknowledgements

The authors are grateful to the authority of the Directorate of Higher Education, Nagaland and Kohima Science College, Jotsoma, Nagaland for financial support to pursue this work.

References

[1] Sajid, M., Ali, N., Javed, T., & Abbas, Z. (2010). Stretching a curved surface in a viscous fluid. *Chinese Physics Letters*, 27(2), 024703. doi: 10.1088/0256-307X/27/2/024703

[2] Abbas, Z., Naveed, M., & Sajid, M. (2013). Heat transfer analysis for stretching flow over a curved surface with magnetic field. *Journal of Engineering Thermophysics*, 22(4), 337–345. doi: 10.1134/S1810232813040061

[3] Roşca, N.C., & Pop, I. (2015). Unsteady boundary layer flow over a permeable curved stretching/shrinking surface. *European Journal of Mechanics, B/Fluids*, 5161–67. doi: 10.1016/j.euromechflu.2015.01.001

[4] Sanni, K.M., Asghar, S., Jalil, M., & Okechi, N.F. (2017). Flow of viscous fluid along a nonlinearly stretching curved surface. *Results in Physics*, 7(12), 1–4. doi: 10.1016/ j.rinp.2016.11.058

[5] Sanni, K.M., Hussain, Q., & Asghar, S. (2020). Heat transfer analysis for non-linear boundary driven flow over a curved stretching sheet with a variable magnetic field. *Frontiers in Physics*, 8, 00113. doi: 10.3389/fphy.2020.00113

[6] Hayat, T., Saif, R.S., Ellahi, R., Muhammad, T., & Ahmad, B. (2017). Numerical study of boundary-layer flow due to a nonlinear curved stretching sheet with convective heat and mass conditions. *Results in Physics*, 7, 2601–2606. doi: 10.1016/j.rinp.2017.07.023

[7] Saranya, S., Ragupathi, P., & Al-Mdallal, Q. (2022). Analysis of bio-convective heat transfer over an unsteady curved stretching sheet using the shifted Legendre collocation method. *Case Studies in Thermal Engineering*, 39, 102433. doi: 10.1016/j.csite.2022.102433

[8] Abbas, N., & Shatanawi, W. (2022). Theoretical survey of time-dependent micropolar nanofluid flow over a linear curved stretching surface. *Symmetry*, 14(8), 1629. doi: 10.3390/sym14081629

[9] Majeed, A., Naeem, S., Zeeshan, A., Qayyum, A., & Alhodaly, M.S. (2024). Three-dimensional bio-convection mechanism and heat transportation of nanofluid induced by magnetic field. *International Journal of Modern Physics B*, 38(20), 2450258. doi: 10.1142/S0217979224502588

[10] Abbas, Z., Arslan, M.S., & Rafiq, M.Y. (2024). Numerical investigation of cilia beating modulated flow of magnetized viscous fluid

in a curved channel with variable thermal conductivity. *Alexandria Engineering Journal*, 97, 230–240. doi: 10.1016/j.aej.2024.04.018

[11] Mahesha, R., Nalinakshi, N., & Kumar, T.S. (2025). Numerical study of radiative MHD hybrid nanofluid flow through porous concentric cylinders. *Archives of Thermodynamics*, 46(1), 201–208. doi: 10.24425/ather.2025.154194

[12] Ahmad, S., Nadeem, S., & Muhammad, N. (2019). Boundary layer flow over a curved surface imbedded in porous medium. *Communications in Theoretical Physics*, 71(3), 344–348. doi: 10.1088/0253-6102/71/3/344

[13] Riaz, A., Khan, S.U.D., Zeeshan, A., Khan, S.U., Hassan, M., & Muhammad, T. (2021). Thermal analysis of peristaltic flow of nanosized particles within a curved channel with second-order partial slip and porous medium. *Journal of Thermal Analysis and Calorimetry*, 143, 1997–2009. doi: 10.1007/s10973-020-09454-9

[14] Adeyemo, A.S., Sibanda, P., & Goqo, S.P. (2024). Analysis of heat and mass transfer of a non-linear convective heat generating fluid flow in a porous medium with variable viscosity. *Scientific African*, 24, e02140. doi: 10.1016/ j.sciaf.2024.e02140

[15] Sonam & Yadav, R.S. (2024). Evaluating the mixed convection flow of Casson fluid from the semi-infinite vertical plate with radiation absorption effect. *Archives of Thermodynamics*, 45(4), 45–59. doi: 10.24425/ather.2024.151996

[16] Jagadha, S., Madhusudhan Rao, B., Durgaprasad, P., Gopal, D., Prakash, P., Kishan, N., & Muthunagai, K. (2024). Darcy-Forchheimer two-dimensional thin flow of Jeffrey nanofluid with heat generation/absorption and thermal radiation over a stretchable flat sheet. *Archives of Thermodynamics*, 45(2), 247–259. doi: 10.24425/ather.2024.150869

[17] Imtiaz, M., Nazar, H., Hayat, T., & Alsaedi, A. (2020). Soret and Dufour effects in the flow of viscous fluid by a curved stretching surface. *Pramana − Journal of Physics*, 94, 48. doi: 10.1007/s12043-020-1922-0

[18] Konwar, H., Bendangwapang, & Jamir, T. (2022). Mixed convection MHD boundary layer flow, heat, and mass transfer past an exponential stretching sheet in porous medium with temperature-dependent fluid properties. *Numerical Heat Transfer, Part A: Applications*, 83(12), 1346–1364. doi: 10.1080/10407782.2022.2104581

[19] Jamir, T., Konwar, H., & Tzudir, B. (2024). Soret and Dufour effects on unsteady non-linear mixed convection flow past a stretching sheet influenced by non-linear thermal radiation. *Numerical Heat Transfer, Part A: Applications*, 86(14), 4987–5005. doi: 10.1080/10407782.2024.2325675

[20] Krishnaveni, T.R., Reddy G.V.R., Anitha, J., Kumar G.C., Rajagopalan, N.R., Govindan, V., Byeon, H., Pimpunchat, B. (2025). Mechanism of thermal radiation, Soret-Dufour on ferromagnetic hybrid nanofluid through a permeable surface. *Case Studies in Thermal Engineering*, 68, 105919. doi: 10.1016/j.csite.2025.105919

[21] Haile, E., & Shankar, B. (2014). Heat and mass transfer through a porous media of MHD flow of nanofluids with thermal radiation, viscous dissipation and chemical reaction effects. *Chemical Science International Journal*, 4(6), 828–846. doi: 10.9734/acsj/2014/11082

[22] Oladapo, A.O., Akindele, A.O., Obalalu, A.M., & Ajala, O.A. (2024). Important of slip effects in non-Newtonian nanofluid flow with heat generation for enhanced heat transfer devices. *Defect and Diffusion Forum*, 431, 147–162. doi: 10.4028/p-baACr1

[23] Sademaki, L.J., Reddy, B.P., & Matao, P.M. (2025). Viscous dissipation effects on heat propagating MHD nanofluid flow induced by the Brownian motion and thermophoresis impacts in a vertical cone with convective surface conditions. *Partial Differential Equations in Applied Mathematics*, 13, 101143. doi: 10.1016/j.padiff.2025.101143

[24] Hanafy, H., & Tlili, I. (2025). Thermo-diffusion analysis for viscoelastic fluid due to stretching surface with viscous dissipation and radiative effects. *Case Studies in Thermal Engineering*, 67, 105848. doi: 10.1016/j.csite.2025.105848

[25] Shampine, L., Kierzenka, J., & Reichelt, M. (2000). Solving boundary value problems for ordinary differential equations in MATLAB with bvp4c. *Tutorial Notes*, 752751–27. https://classes.engineering.wustl.edu/che512/bvp_paper.pdf

Co-published by
Institute of Fluid-Flow Machinery
Polish Academy of Sciences
Committee on Thermodynamics and Combustion
Polish Academy of Sciences

http://www.imp.gda.pl/archives-of-thermodynamics/

ARCHIVES OF THERMODYNAMICS

Shape effects on steady flow and heat transfer of Cu-nanofluid over a nonlinear stretching surface with Joule heating

Ramzan Ali[a*], Ainura Mitalipova[b], Syed Wajeeh Ul Hussan[c], Abdikerim Kurbanaliev[b], Azeem Shahzad[c], Mukhammadmuso Abduzhabbarov[d]

[a]University of Doha for Science and Technology, 68 Al Tarafa, Jelaiah Street, Duhail North, 24449, Doha, Qatar
[b]Osh State University Kyrgyz Republic, Lenina Street 331, 714000, Kyrgyzstan
[c]University of Engineering and Technology, Department of Mathematics, Faculty of Basic Sciences, Taxila, HMC Link Rd, Taxila, 47050, Pakistan
[d]Westminster International University in Tashkent, School of Law, Technology & Education, Istiqbol 12, Tashkent, 100047, Uzbekistan
*Corresponding author email: ramzan.ali@udst.edu.qa

Received: 03.07.2024; revised: 22.05.2025; accepted: 27.05.2025

Abstract

Nanofluids have garnered significant interest in various fields due to their numerous advantages and potential applications. The appeal of ethylene glycol (EG)-based Cu-nanofluid lies in its excellent thermal conductivity, stability, and ability to enhance heat transfer properties, making it a promising candidate for diverse industrial applications. In this study, we analyse the flow behaviour of EG-based copper (Cu) nanofluid over a nonlinear stretching surface under the influence of Joule heating effects. The research involves the development of a mathematical model and formulating of governing equations represented as system of partial differential equations, which are subsequently transformed into nonlinear ordinary differential equations through suitable transformations. A numerical framework based on MATLAB bvp4c solver technique is employed to obtain approximate solutions. The study examines the influence of dimensionless parameters on velocity and thermal distributions. The findings for the local Nusselt number and skin friction are presented in tabular form, highlighting the effects of key parameters. The results are benchmarked against three different sources from existing literature, showing strong agreement in the case of reduced Nusselt number.

Keywords: Joule heating; MHD flow; Cu-nanofluid; Stretching surface

Vol. 46(2025), No. 3, 89–104; doi: 10.24425/ather.2025.156581

Cite this manuscript as: Ali, R., Mitalipova, A., Ul Hussan, S.W., Kurbanaliev, A., Shahzad, A., & Abduzhabbarov, M. (2025). Shape effects on steady flow and heat transfer of Cu-nanofluid over a nonlinear stretching surface with Joule heating. *Archives of Thermodynamics*, 46(3), 89–104.

1. Introduction

Nanofluids are stable dispersions of nanoparticles in a base fluid, in which the thermophysical properties, such as thermal conductivity, are enhanced several times compared to those of the pure liquid. On the other hand, these nanofluids are used in various sectors such as heat transfer, lubrication, biomedicine, and solar panels to have better optical characteristics and absorption ability of CO_2. Although nanofluids have many advantages over other types of fluids, their stability is still a major hurdle when using them in diverse engineering fields. To overcome the issue, different stabilization strategies combined with numerous performance evaluation approaches have been introduced. It is

Nomenclature

A – proportionality constant
$\boldsymbol{B}$ – magnetic field, T
B_0 – constant magnetic field, T
c – dimensional constant
C_p – specific heat capacity, (J/kg K)
Ec – Eckert number
$f'(\eta)$– dimensional velocity distribution
$\boldsymbol{J}$ – current density vector, A/m^2
k – thermal conductivity, W/(m K)
K – slip parameter
$\boldsymbol{L}$ – velocity gradient tensor, 1/s
m – shape factor
n – stretching parameter
M – magnetic parameter
Nu – Nusselt number
Pr – Prandtl number
$\boldsymbol{q}$ – electric charge, C
Re – Reynolds number
T – temperature parameter, K
u, v – velocity components in the x- and y-axis directions, m/s
U – surface velocity, m/s
$\boldsymbol{V}$ – velocity vector, m/s
x, y – Cartesian coordinates, m

Greek symbols

α – thermal diffusivity, m^2/s
ε_i – constants (i = 1,2,3,4,5)
η – similarity variable
$\theta(\eta)$– dimensionless temperature distribution
μ – dynamic viscosity, Pa·s
υ – kinematic viscosity, m^2/s
ρ – density, kg/m^3
σ – electrical conductivity, S/m
ϕ – volume fraction

Subscripts and Superscripts

f – fluid
nf – nanofluid
s – solid particles
w – wall
∞ – surrounding fluid
$(\cdot)'$, $(\cdot)''$, $(\cdot)'''$ – differentiation with respect to η

Abbreviations and Acronyms

EG – ethylene glycol
MHD– magnetohydrodynamics
ODE – ordinary differential equation
PDE – partial differential equation

generally accepted that the nanoparticle and base fluid characteristics, preparation methods, external factors and stabilizer content play critical roles in assessing nanofluid stability over time.

Literature review reveals that nanofluids are a rapidly growing field of research that is currently applied in many different fields. Several attempts have been made simultaneously to create stable nanofluids.

Copper (Cu) nanofluid can be defined as a liquid that comprises copper nanoparticles suspended in the base fluid, which can be, among others, water, ethylene glycol, or oil. The following properties of copper are some of the reasons why copper nanofluids are applied in heat exchangers, solar collectors, cooling of electronic devices, and some other loads where the process of heat transfer needs improvement, high thermal conductivity and electrical conductivity. This is because the conduction of the copper within the nanofluids is high, hence improving the energy and overall performance of the nanofluids. Copper is also less expensive to incorporate into other nanomaterials and other related compounding materials to which it can be added. Copper nanoparticles are also known to have an antimicrobial property that makes these fluids useful in reducing biofouling in systems where water is used as the heat transfer medium. Hence, copper is employed in nanofluids due to its thermal/electrical conductivity, reasonable cost, and bacteriostatic properties. Eastman et al. [1] investigated that the nanofluid of copper nanoparticles in ethylene glycol has significantly higher effective thermal conductivity than pure or oxide nanoparticles. This increase can be up to 40%, contradicting previous predictions of particle shape and size having no effect on thermal conductivity. Chakraborty and Panigrahi [2] discussed the stability of nanofluid and its significance in industrial applications, and offer recommendations for its wider practical adoption. Patel et al. [3] explored thermal conductivities of nanoparticles in water and toluene media, revealing variations based on particle type and stabilization, with additional factors influencing the thermal conductivity mechanism in nanofluids. Liu et al. [4] examined the flow and heat transfer near a rotating disk containing nanofluids, showing variations in boundary layer thicknesses and heat transfer rates with different nanoparticle volume fractions and materials. The flow and heat transfer properties of nanofluids in a rotating frame were studied by Das [5], who considered two types of nanofluids and analysed the effects of different parameters. Nanofluid flow and heat transfer are extensively studied for various industrial and engineering applications.

Utilizing the Buongiorno model, the work [6] investigates mass and heat transfer in nanofluid-connected flow and discovers that heat transmission diminishes as thermal radiation and convection parameters grow. Research [7] explores the impact of external forces like natural convection, thermal radiation, and chemical reactions on heat and mass transfer. Nanofluid combinations can minimize the skin friction coefficient and maximize heat transfer rates. Magnetic fields and thermal radiation influence hybrid nanofluids, enhancing thermal conductivity. The study of Sakiadis [8] offers valuable insights into optimizing nanofluid flow and heat transfer processes. Ferdows et al. [9] analysed the effects of MHD flow and Hall currents on boundary layer flow over a three-dimensional extending surface to demonstrate improvements in velocity, profile and heat flux, and transfer rates.

Ahmad et al. [10] examined the mixed convection flow of hybrid nanofluid over a nonlinear stretching sheet, showing that the magnetic field velocity decreases and thermal radiation temperature increases. The influence of a magnetic field and nanoparticles on Carreau fluid flow and heat, and mass transfer over a porous nonlinear stretching surface was studied by Eid et al. [11]. Hayat et al. [12] present a numerical simulation study on boundary layer flow over a nonlinear curved stretchable surface, examining various parameters. Zaimi et al. [13] present a mathematical study on boundary layer flow and heat transfer in a nanofluid, examining the effects of parameters and identifying dual solutions. When dust particles and polymers combine in a viscous liquid, Athar et al. [14] observed that the polymers undergo deformation inside the boundary layer but not outside of it. Shah et al. [15] used graphs and the homotopy analysis approach to analyse the heat transfer and boundary layer flow of couple stress fluid at the stagnation point over an exponentially extending surface.

Venkateswarlu et al. [16] and Vidya et al. [17] conducted a study on the incompressible stagnation point flow of a conductive hyperbolic radiative nanoliquid past a stretching surface. They found that increasing Weissenberg's number reduced fluid velocity. Hashim et al. [18] extended the mathematical formulation for the aligned magnetic field on Williamson fluid over a stretching sheet with Newtonian heating, analysing the effects of various parameters on temperature and velocity profiles.

Chen [19] examined both Joule heating and viscous dissipation on MHD (magnetohydrodynamic) flow over a stretching sheet, considering the influence of free convection, thermal radiation, and surface suction/blowing. The study of Khashi'ie et al. [20] reveal the variation of flow and heat transfer characteristics of a hybrid nanofluid of a shrinking cylinder with Joule heating with distinct types of nanofluids. Joule heating effects on fluid movement and heat transmission over an exponentially extending sheet are explored by Srinivasacharya and Jagadeeshwar [21] mainly in view of its relevance to industrial applications and magnetohydrodynamic flows. Ganesh Kumar et al. [22] discuss the effect of viscous dissipation and Joule heating on Jeffrey nanofluid and how the temperature profile and the thickness of the thermal boundary layer are affected by it. Ghaffarpasand [23] investigates MHD natural convection in a cavity filled with Fe_3O_4-water nanofluid, revealing improved heat transfer with ferrite nanoparticles and increased entropy generation under Joule heating and Lorenz force. Mutuku et al. [24] analyse the impact of Joule heating and viscous dissipation on nanofluid flow past an inclined plate, highlighting the significant influence of controlling parameters on flow fields. Ali et al. [25] conducted a study on the impact of various forces and parameters on ethylene glycol-based nanofluids suspended above a thin vertical needle.

Shankar Goud et al. [26] investigated the effects of Joule heating on surfaces that stretch exponentially, and Khashi'ie et al. [27] communicated about the Joule heating effect of hybrid nanofluid. According to the research of Rana et al. [28] on an exponentially stretched surface, the thermal boundary layer structure is improved by both Joule and viscous heating mechanisms, which lowers nano-liquid velocity. Viscoelastic nanofluid has greater momentum, according to research by Tarakaramu et al. [29] on the effects of different physical parameters on MHD nanofluid flow to a stretched surface.

The research community in engineering and modelling has extensively investigated the boundary layer flow and heat transfer of nanofluids under Joule heating, focusing on factors like hydromagnetic forces, mixed convection, thermal stratification, chemical reactions, and viscous dissipation. Saleem et al. [30] investigated the impact of various copper nanoparticle shapes on the flow and heat transfer characteristics of a water-based nanofluid over a flat surface. Fakour et al. [31] studied the flow and heat transfer characteristics of nanofluid thin films over an unsteady stretching elastic sheet using the lattice Boltzmann method (LBM). Using aluminum and copper with water, Mathews and Tallab [32] discussed the nonlinearity of the stretching sheet. Triveni et al. [33] analyse the heat transfer of MHD Casson nanofluid flow over a nonlinear stretching sheet in the presence of a nonuniform heat source. Hayat et al. [34] analysed MHD thin film flow with viscous dissipation and slip effects for nanofluids of various nanoparticle shapes on an unsteady radially stretching surface.

A numerical study using a vertical cone and Williamson nanofluid flow has been discussed by Sathyanarayana and Goud [35]. Joachimiak et al. [36] investigated the effects of different physical criteria on thermochemical attitudes while conducting a numerical study of an aluminum alloy. In his discussion of the various nanoparticle shape parameters, Hayat and Shahzad [37] included a numerical study and analysis of the impacts of heat transmission and thin film flow for various gold nanoparticle shapes on a vertically stretched sheet. In another study [38], authors considered gold nanoparticles and the effects of different shape factors on a radial stretching sheet. Ali et al. [39] proposed a model for the unsteady flow of silica nanofluid over a stretching cylinder and considered the shape effects of the nanoparticles. Gangadhar et al. [40] investigated the flow performance of silver-engine oil-based nanofluids with different non-Newtonian models through a Riga plate. In [41], Gangadhar and coauthors presented a numerical study on the performance of an HVAC (heating, ventilation, and air conditioning) system utilizing Sutterby flow ternary nanofluids, with a focus on a Cu-Ag-AA7075/$C_6H_9NaO_7$ nanofluid. In other works [42−44], Gangadhar et al. provided the PDEs (partial differential equations) model-based Williamson fluid over a heated cylinder with convective heating. Furthermore, they considered thermal radiation and Cattaneo-Christov energy diffusion. They incorporated graphene and magnetic oxide nanoparticles to improve thermal conductivity. Their studies showed that enhanced thermal radiation increases the temperature of the fluid, while suction reduces skin friction coefficients but enhances heat and mass transfer rates. Their model was validated by comparing results with existing literature. Furthermore, Gangadhar et al. [45] explored the self-propelled movement of gyrotactic swimming microorganisms in a Casson nanofluid slip flow over a stretching cylinder with a strong magnetic field, using a non-dimensional numerical model and bvp4c technique. In another work [46], Gangadhar et al. examined the effect of a strong magnetic field and thermal radiation on the free convective flow of a ternary nanofluid over a moving wedge surface.

The PDE model provided in the manuscript has potential applications in heat transfer enhancement. It is evident that the copper-based nanofluid has extraordinary thermal conductivity.

This peculiar property makes them an ideal candidate for enhancing heat transfer for real-life applications, including cooling microelectronics and solar collectors. The proposed model, which includes PDEs with complex boundary conditions and the study of different particle shapes, is the first of its kind. Nanofluidic models with nonlinear stretching surfaces are highly applicable in industrial processes like sheet drawing, sustainable polymer production. The literature suggests studying efficient cooling and uniform heat distribution for high-quality engineering products. Nanofluid models are used for controlled heating processes in aerospace, automation and renewable energy. A better PDE model with realistic boundary conditions will enable the research community to design efficient devices.

This article investigates the steady heat transfer and flow in Cu nanoparticles with the added effects of thermal radiation, Joule heating, magnetohydrodynamics, and velocity slip over time-independent nonlinear stretching surfaces. It is the first study to investigate steady-state heat transfer and flow over a time-independent stretching surface with ethylene glycol (EG) as the base liquid. Here, we utilize a Cartesian coordinate system for the mathematical description of the problem and solve the obtained system of simplified nonlinear ordinary differential equations (ODEs) by utilizing an effective and convergent technique bvp4c. All the necessary calculations are performed in MATLAB. Additionally, a graph is included to explain the impact of physical parameters on temperature, velocity, skin friction number and Nusselt number.

2. Materials and methods

Heat and mass transfer analysis of a steady, viscous, incompressible nanofluid under laminar flow through a stacking and two-dimensional, regulated, nonlinear and stretching surface is depicted in Fig. 1. Parameter T_w represents the surface temperature and T_∞ denotes the temperature of the surrounding fluid. The x-axis is taken along the surface and the y-axis is taken perpendicular to it.

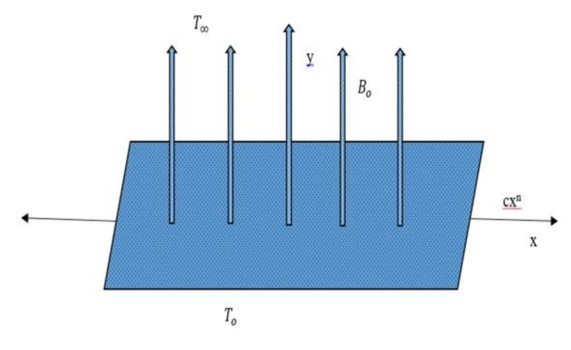

Fig. 1. Schematic diagram of the problem.

It is further assumed that the stretching velocity of the surface is given by

$$U = cx^n, \tag{1}$$

where n is the stretching parameter, and the magnetic field applied perpendicular to the surface is equal to

$$\boldsymbol{B} = B_0 x^{\frac{n-1}{2}}, \tag{2}$$

where B_0 is a constant magnetic field. It was also assumed that any generated magnetic field component is much smaller than the external magnetic field and the base fluid is ethylene glycol containing copper nanoparticles. These nanoparticles exist in various shapes and have a uniform size without any distortions, remaining in thermodynamic equilibrium with the fluid in which they are suspended.

In light of the above assumptions, the governing equations of continuity, momentum and energy for the current study are expressed as follows:

$$\nabla \cdot \boldsymbol{V} = 0, \tag{3}$$

$$\rho_{nf}(\boldsymbol{V} \cdot \nabla)\boldsymbol{V} = \nabla \cdot \boldsymbol{\tau} + \boldsymbol{J} \times \boldsymbol{B}, \tag{4}$$

$$\rho_{nf}\frac{dT}{dt} = \boldsymbol{\tau} \cdot \boldsymbol{L} - \nabla \cdot \boldsymbol{q} + \frac{J^2}{\sigma_{nf}}, \tag{5}$$

where $\boldsymbol{V}$ is the velocity vector, $\boldsymbol{\tau}$ is the stress tensor, $\boldsymbol{J}$ is the current density vector, T is the temperature, t is the time, ρ_{nf} is the density of the nanofluid, $\boldsymbol{L}$ is the velocity gradient tensor, $\boldsymbol{q}$ is the electric charge of particles. In the case of a two-dimensional nanofluid model, the vector form reduces to the following system of equations [39,40]:

$$\frac{\partial u}{\partial x} + \frac{\partial v}{\partial y} = 0, \tag{6}$$

$$\left(u\frac{\partial u}{\partial x} + v\frac{\partial u}{\partial y}\right) = \frac{\mu_{nf}}{\rho_{nf}}\left(\frac{\partial^2 u}{\partial y^2}\right) - \frac{\sigma_{nf}B^2}{\rho_{nf}}u, \tag{7}$$

$$\left(u\frac{\partial T}{\partial x} + v\frac{\partial T}{\partial y}\right) = \alpha_{nf}\frac{\partial^2 T}{\partial y^2} + \frac{\mu_{nf}}{(\rho C_p)_{nf}}\left(\frac{\partial u}{\partial y}\right)^2 + \frac{\sigma_{nf}B^2}{(\rho C_p)_{nf}}u^2, \tag{8}$$

where μ_{nf} is the dynamic viscosity of the nanofluid and α_{nf} is the thermal diffusivity of the nanofluid, B is the strength of the magnetic field and C_p is the specific heat.

The boundary conditions for the problem under consideration at $y = 0$ are:

$$\begin{cases} u = U + A\,\nu_f\dfrac{\partial u}{\partial y}, \\ v = 0, \\ T = T_w, \end{cases} \tag{9}$$

as $y \to \infty$, u approaches 0 and T approaches T_∞.

The pertinent physical parameters from literature are defined as [31]:

$$\begin{gathered} \alpha_{nf} = \frac{k_{nf}}{(\rho C_p)_{nf}}, \\ \rho_{nf} = (1-\phi)\rho_f + \phi\rho_s, \\ \mu_{nf} = \mu_f(1 + A_1\phi + A_2\phi^2), \\ \sigma_{nf} = \sigma_f(1-\phi)\sigma_f + \phi\sigma_s, \end{gathered} \tag{10}$$

$$(\rho C_p)_{nf} = (1-\phi)(\rho C_p)_f + \phi\,(\rho C_p)_s,$$

$$\frac{K_{nf}}{K_f} = \left[\frac{K_s + (m-1)K_f + (m-1)(K_s - K_f)\phi}{K_s + (m-1)K_f - (K_s - K_f)\phi}\right]$$

where ϕ is the volume fraction, m is the shape factor, K_{nf}, K_f, and K_s are slip parameters of nanofluid, base fluid and solid particles, respectively.

Using the similarity transformation [30] mentioned below, we will obtain the dimensionless form of the governing equations:

$$\begin{aligned} \psi &= \mathrm{e}^{-\frac{1}{2}} f(\eta), \\ \eta &= \frac{y}{x}\mathrm{Re}^{\frac{1}{2}}, \\ \theta(\eta) &= \frac{T - T_\infty}{T_w - T_\infty}, \end{aligned} \tag{11}$$

where ψ is the stream function, η is the similarity variable, and θ is the dimensionless temperature. Function f represents a dimensionless similarity function that describes the velocity distribution within the boundary layer. The pattern of flow is defined by the stream function, and the components of velocity can be obtained as follows:

$$\begin{aligned} u &= \frac{\partial\psi}{\partial y} \\ v &= -\frac{\partial\psi}{\partial x} \end{aligned} \tag{12}$$

Here

$$\mathrm{Re} = \frac{xU}{\vartheta_f} \tag{13}$$

is the Reynolds number. From the above transformation, we have

$$\begin{aligned} u &= Uf(\eta), \\ v &= -U\mathrm{Re}^{\frac{1}{2}}\left[\frac{n+1}{2}f(\eta) + \frac{n-1}{2}\eta f'(\eta)\right]. \end{aligned} \tag{14}$$

By using the above transformation, the continuity Eq. (6) holds automatically, and Eqs. (7) and (8) take the following non-dimensional forms, respectively:

$$\begin{aligned} \varepsilon_1 f''' - nf'^2 - \frac{n+1}{2}ff'' - \varepsilon_3 Mf' \\ - (n-1)\,\eta f' f'' = 0, \end{aligned} \tag{15}$$

$$\begin{aligned} \theta''(\eta) + \frac{\mathrm{Pr}}{\varepsilon_2}\Big(\frac{n+1}{2}f\theta'(\eta) + \varepsilon_4 \mathrm{Ec} f''^2 \\ + \varepsilon_5 \mathrm{Ec}\, Mf'^2\Big) = 0. \end{aligned} \tag{16}$$

Now, the boundary conditions in terms of the transformed variable become:

$$\begin{cases} f(0) = 0, \\ f'(0) = 1 + Kf''(0), \\ f'(\infty) = 0, \\ \theta(0) = 1, \\ \theta(\infty) = 0. \end{cases} \tag{17}$$

The dimensionless constants are defined as follows:

Prandtl number	$\mathrm{Pr} = \frac{(\rho C_p \nu)_f}{kf}$,
slip parameter	$K = A\sqrt{\frac{\nu\, U_w}{x}}$,
Eckert number	$\mathrm{Ec} = \frac{U^2}{C_p(T_w - T_\infty)}$,
magnetic parameter	$M = \frac{B_0^2\, \sigma_f}{c\, \rho_{nf}}$.

Since the Nusselt number (Nu) and skin friction coefficient (C_f) are significant in engineering, they can be defined as:

$$\begin{aligned} C_f &= \frac{\tau_w}{\rho_f U^2}, \\ \mathrm{Nu} &= \frac{x\, q_w}{k_f(T_w - T_\infty)}. \end{aligned} \tag{18}$$

Further the constants ε_i, for $i = 1, \ldots, 5$ are defined as:

$$\begin{aligned} \varepsilon_1 &= \frac{1 + A_1\phi + A_2\phi^2}{1 - \phi + \phi\left(\frac{\rho_s}{\rho_f}\right)}, \\ \varepsilon_2 &= \frac{\frac{K_{nf}}{K_f}}{1 - \phi + \phi\left[\frac{(\rho C_p)_s}{(\rho C_p)_f}\right]}, \\ \varepsilon_3 &= \frac{1 - \phi + \phi\left(\frac{\sigma_s}{\sigma_f}\right)}{1 - \phi + \phi\left(\frac{\rho_s}{\rho_f}\right)}, \\ \varepsilon_4 &= \frac{1 + A_1\phi + A_2\phi^2}{1 - \phi + \phi\left[\frac{(\rho C_p)_s}{(\rho C_p)_f}\right]}, \\ \varepsilon_5 &= \frac{1 - \phi + \phi\left(\frac{\sigma_s}{\sigma_f}\right)}{1 - \phi + \phi\left[\frac{(\rho C_p)_s}{(\rho C_p)_f}\right]}. \end{aligned} \tag{19}$$

3. Numerical solution

This article uses the bvp4c [31] in MATLAB to get the mathematical solution of the reduced Eqs. (15) and (16) along with the boundary conditions Eq. (17). The main characteristics of the suggested bvp4c technique, which include handling single boundary value problems (BVPs), direct acceptance of both two-point and multipoint BVPs with improved accuracy, and faster convergence with reduced error, are well recognized in the research community. The basic numerical method implemented in bvp4c is a form of Simpson's method that is rather generic and can be found in numerous programs. To apply this strategy, the third-order ODE (15) and the second-order ODE (16) are transformed into the first-order differential equations as follows:

$$f = y_{(1)}. \tag{20}$$

Then we can write

$$f' = y'_{(1)} = y_{(2)},$$

$$f'' = y'_{(2)} = y_{(3)},$$

$$f''' = y'_{(3)} = \frac{1}{\varepsilon_1}\left(n y_{(2)}^2 + \frac{n+1}{2} y_{(1)} y_{(3)} + \varepsilon_3 M y_{(2)} + +n\eta y_{(2)} y_{(3)}\right), \tag{21}$$

$$\theta = y_{(4)},$$

$$\theta' = y'_{(4)} = y_{(5)},$$

$$\theta'' = y'_{(5)} = \frac{\Pr}{\varepsilon_2}\left[-\left(\frac{n+1}{2}\right) y_{(1)}\, y_{(5)} - \mathrm{Ec}\,\varepsilon_4 y_{(3)}^2 + -\varepsilon_5\,\mathrm{Ec}\, M y_{(2)}^2\right].$$

Boundary conditions are:

$$\begin{cases} y_{(2)}(0) = 1 + K y_{(3)}(0), \\ y_{(1)}(0) = 0, \\ y_{(2)}(\infty) = 0, \\ y_{(4)}(\infty) = 0. \end{cases} \tag{22}$$

4. Results and discussion

In this research, we explore a model that investigates how nanofluids, containing copper nanoparticles of various shapes, behave in two-dimensional boundary layer flow. By employing similarity transformations, we transform the given differential equations into simpler ordinary differential equations. Afterward, we analyse how factors like the magnetic parameter, slip parameter, volume fraction, stretching parameter and Eckert number impact the velocity and temperature profiles within the layer, considering various shapes of copper nanoparticles. These influences are illustrated through graphs shown in Figs. 2 to 12.

The pertinent impact of the magnetic parameter, which occurs through the modelling of Maxwell's equations on the velocity profile within the boundary layer, is comprehensively analysed and illustrated in Fig. 2 for EG-Cu nanofluid for various nanoparticle shapes. The results are presented for blade, brick, cylinder, platelets, and sphere, highlighting the influence of the shape factor on the velocity profile. Increasing the magnetic parameter leads to a noticeable reduction in the velocity of copper

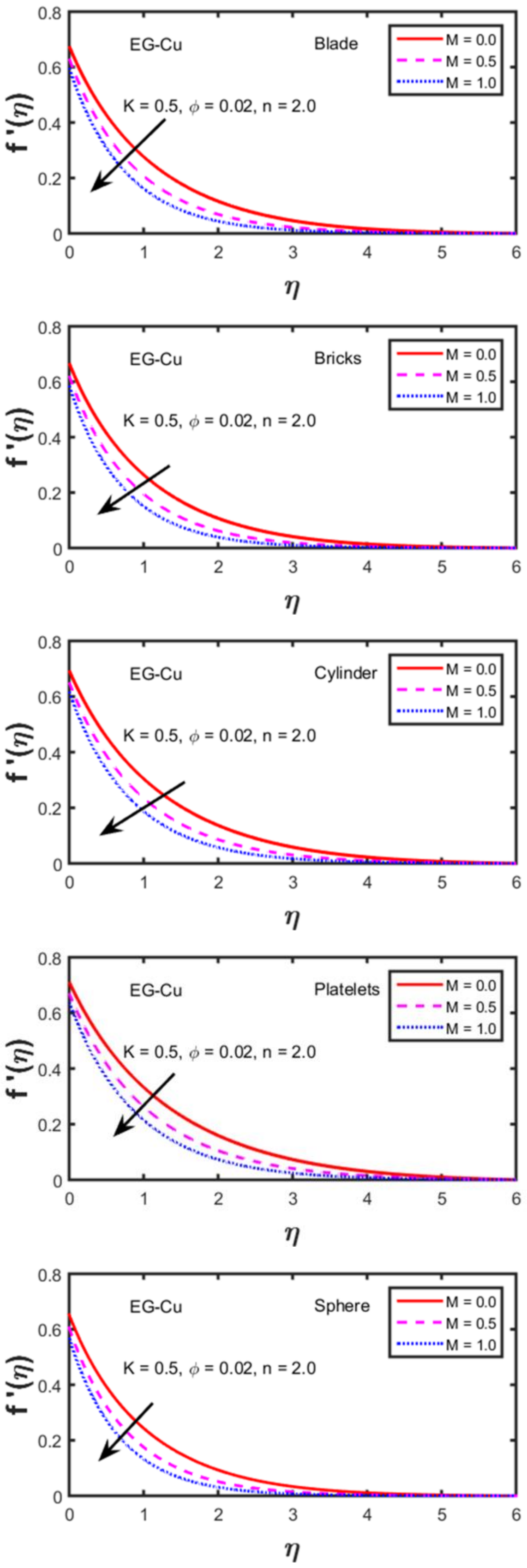

Fig. 2. Impact of the magnetic parameter (M) on the velocity profile of EG-Cu nanofluid for various nanoparticle shapes: blade, brick, cylinder, platelets, and sphere.

nanofluids across various nanoparticle shapes. This effect is attributed to the enhancement of Lorentz forces, which act as resistive forces opposing the fluid's motion, thereby decreasing the velocity profile.

From the graphical representation of the velocity profile, it is clear that an increase in the magnetic parameter (*M*) leads to a noticeable reduction in the velocity of the copper nanofluid across all nanoparticle shapes. This peculiar behaviour can be attributed to the presence of the Lorentz force, which arises from the interaction between the externally applied magnetic field and the induced electrical currents within the nanofluid. The Lorentz force acts as a resistive drag force, opposing the motion of the fluid and thereby reducing its velocity profile.

This effect is particularly significant within the boundary layer, where the interplay between magnetic forces and viscous forces becomes more pronounced. The reduction in velocity due to the magnetic parameter highlights the potential for controlling fluid dynamics in magnetohydrodynamic applications, where the magnetic field is utilized to manipulate the flow properties of conducting fluids, such as nanofluids, for engineering and industrial purposes.

Figure 3 presents the relationship between the magnetic parameter *M* and the fluid temperature of EG–Cu nanofluid for different nanoparticle shapes, including blade, brick, cylinder, platelets and sphere. The results clearly demonstrate that fluid temperature increases as *M* rises, emphasizing the critical role of nanoparticle geometry in dictating thermal behaviour. This trend is explained by the Lorentz force, which is induced when a magnetic field interacts with an electrically conducting nanofluid. The Lorentz force resists the motion of nanofluid particles, thereby dissipating their kinetic energy and converting it into thermal energy. This process enhances the overall heat transfer rate of the fluid. Importantly, the results highlight a dual effect: while the Lorentz force restricts particle movement and slows fluid motion, it simultaneously boosts thermal energy generation through dissipation. Consequently, higher values of *M* lead to a substantial rise in fluid temperature, as depicted in Fig. 3. These observations underscore not only the impact of magnetic fields on thermal transport but also the significance of nanoparticle shape in modifying velocity and temperature distributions within nanofluids.

Figure 4 illustrates the influence of the slip parameter *K* on the velocity profile of EG–Cu nanofluid for various nanoparticle shapes. As *K* increases, the velocity decreases for all particle geometries due to reduced momentum transfer at the fluid–wall interface under partial slip conditions. The results also highlight that nanoparticle shape strongly influences this behaviour: particles with larger surface areas, such as blades or platelets, exhibit more pronounced velocity reductions, while smoother geometries, like spheres, show smaller variations. These observations emphasize the importance of nanoparticle shape in governing flow characteristics under slip conditions.

Figure 5 depicts the influence of the partial slip condition (*K*) on the thermal field in EG-Cu nanofluid for five distinct nanoparticle shapes: blade, brick, cylinder, platelets, and sphere.

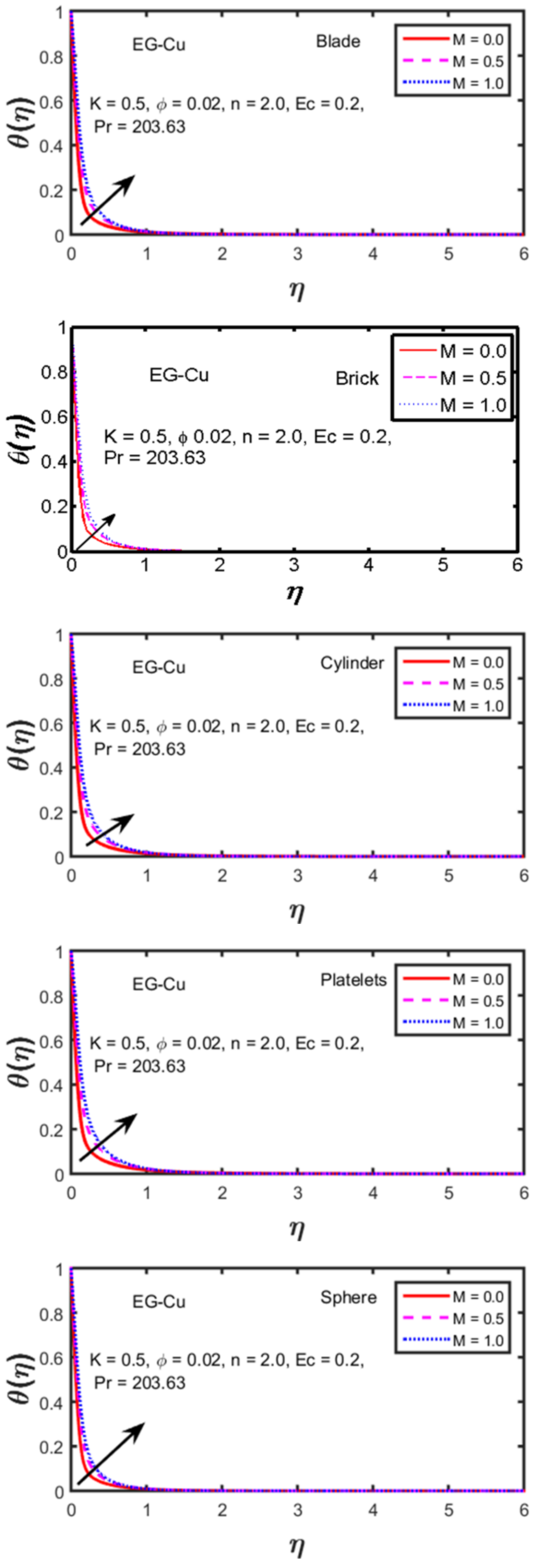

Fig. 3. Influence of magnetic parameter (*M*) on temperature profile of EG-Cu nanofluid for various nanoparticle shapes: blade, brick, cylinder, platelets, and sphere.

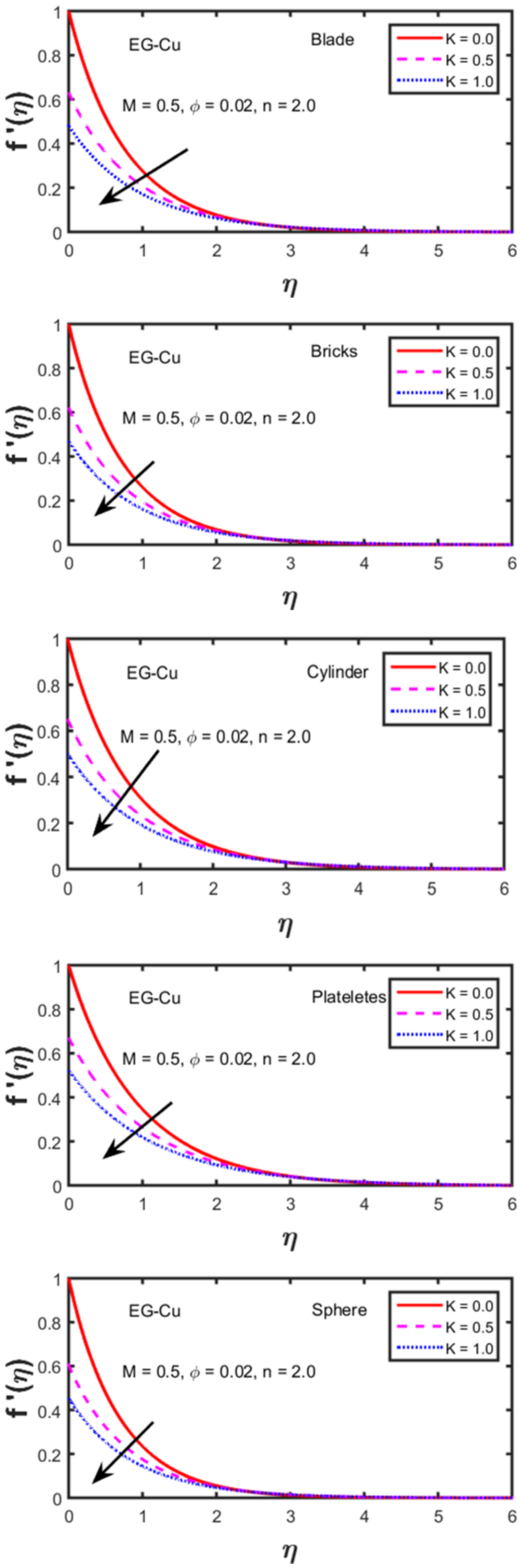

Fig. 4. Impact of slip parameter (*K*) on the velocity profile of EG-Cu nanofluid for various nanoparticle shapes: blade, brick, cylinder, platelets, and sphere.

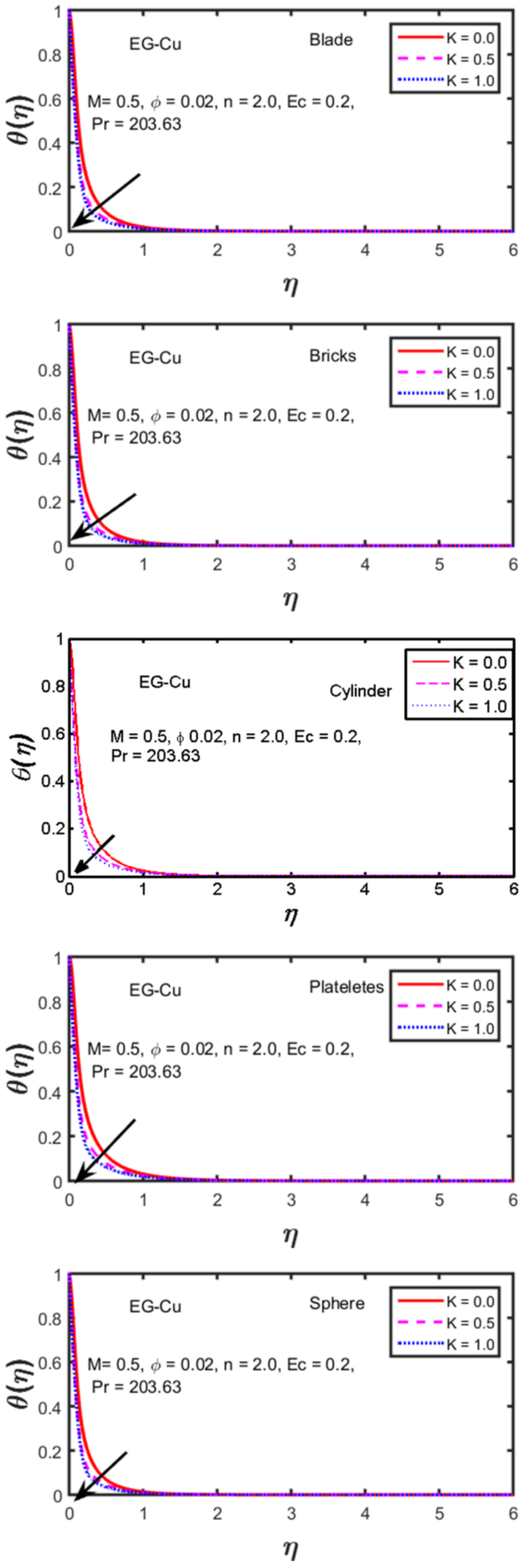

Fig. 5. Impact of the slip parameter (*K*) on the temperature profile of EG-Cu nanofluid for various nanoparticle shapes: blade, brick, cylinder, platelets, and sphere.

Increasing the slip parameter K reduces the friction at the boundary, which in turn reduces the rate of convective heat transfer. This reduction in heat transfer efficiency leads to a decrease in the temperature distribution within the EG-Cu nanofluid, regardless of the nanoparticle shape (blade, brick, cylinder, platelets, or sphere). Different shapes will exhibit different magnitudes of this effect due to their varying thermal conductivity and interaction with the base fluid, but the overall trend with respect to *K* will be the same.

Figure 6 demonstrates the influence of the nanoparticle volume fraction (ϕ) on the velocity profile for EG-Cu nanofluid for five nanoparticle shapes: blade, brick, cylinder, platelets, and sphere. The results demonstrate how the concentration of nanoparticles affects fluid flow, with each shape exhibiting unique flow characteristics. For instance, blade-shaped nanoparticles, with their sharp and elongated design, tend to increase resistance and turbulence, causing noticeable changes in the velocity profile. In contrast, spherical particles, due to their smooth and symmetrical shape, enable more uniform and stable flow. Platelet-shaped particles, with their flat and wide structure, enhance the velocity profile, while cylindrical and brick-shaped particles show intermediate flow patterns. Notably, increasing ϕ enhances the velocity for most copper nanoparticle shapes, including cylinders, platelets, blades, and bricks. However, a unique exception is observed for spherical nanoparticles, where increasing ϕ leads to a velocity decrease. This contrasting behaviour can be attributed to the interplay between various factors such as particle shape, interparticle interactions, and heat transfer mechanisms. Figure 7 delves into the influence of nanoparticle volume fraction (ϕ) on the temperature for EG-Cu nanofluid for various nanoparticle shapes. The results are presented for blade, brick, cylinder, platelets, and sphere, highlighting the influence of shape factor on the temperature profile. Interestingly, increasing ϕ generally leads to a temperature increase for most copper nanoparticle shapes, including cylinders, platelets, blades, and bricks. This can be attributed to enhanced heat generation within the nanofluid due to higher particle concentration.

The impact of the stretching parameter (n) on the velocity profile with different shapes of copper nanoparticles is shown in Fig. 8 for the EG-Cu nanofluid for five nanoparticle shapes: blade, brick, cylinder, platelets, and sphere. The results demonstrate how the rate of surface stretching influences fluid flow, with each nanoparticle shape showing unique flow characteristics. These findings highlight the significant role of nanoparticle geometry in determining fluid dynamics during stretching, providing critical insights for applications, such as industrial coating, polymer processing, or flexible electronics, where controlling flow behaviour under deformation is essential for optimizing performance. The velocity profile also tends to reduce with a rise in n values, as mentioned earlier; a rise in the values of n reduces the boundary layer thickness.

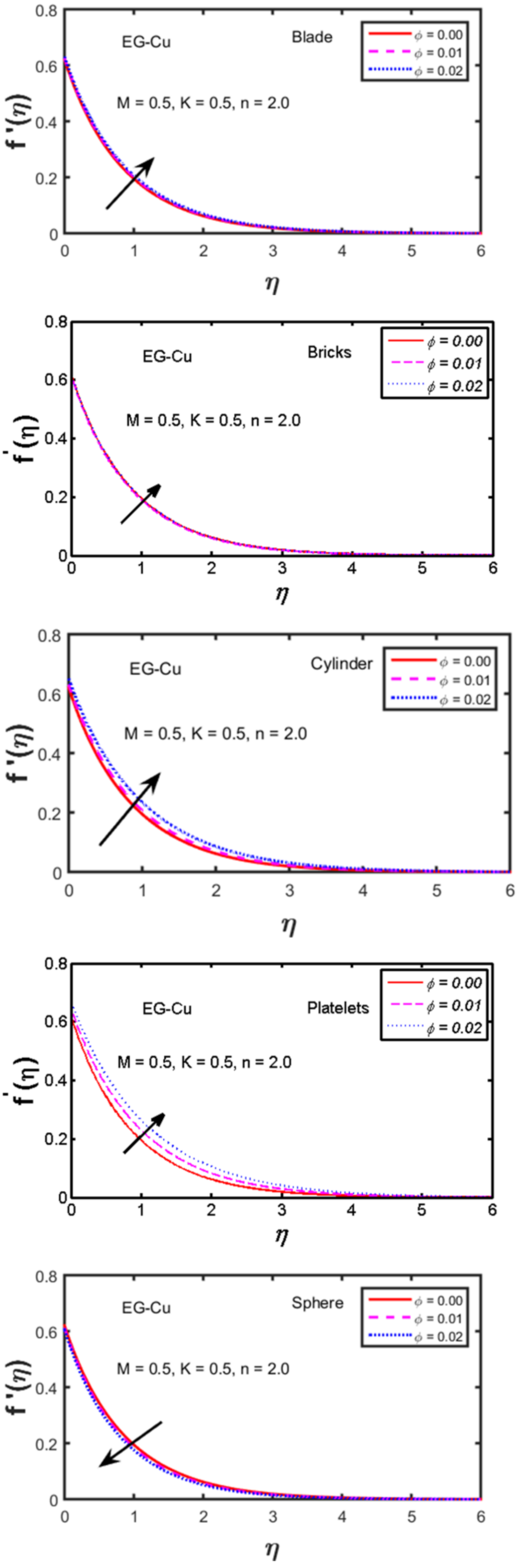

Fig. 6. Impact of volume fraction (ϕ) on the velocity profile of EG-Cu nanofluid for various nanoparticle shapes: blade, brick, cylinder, platelets, and sphere.

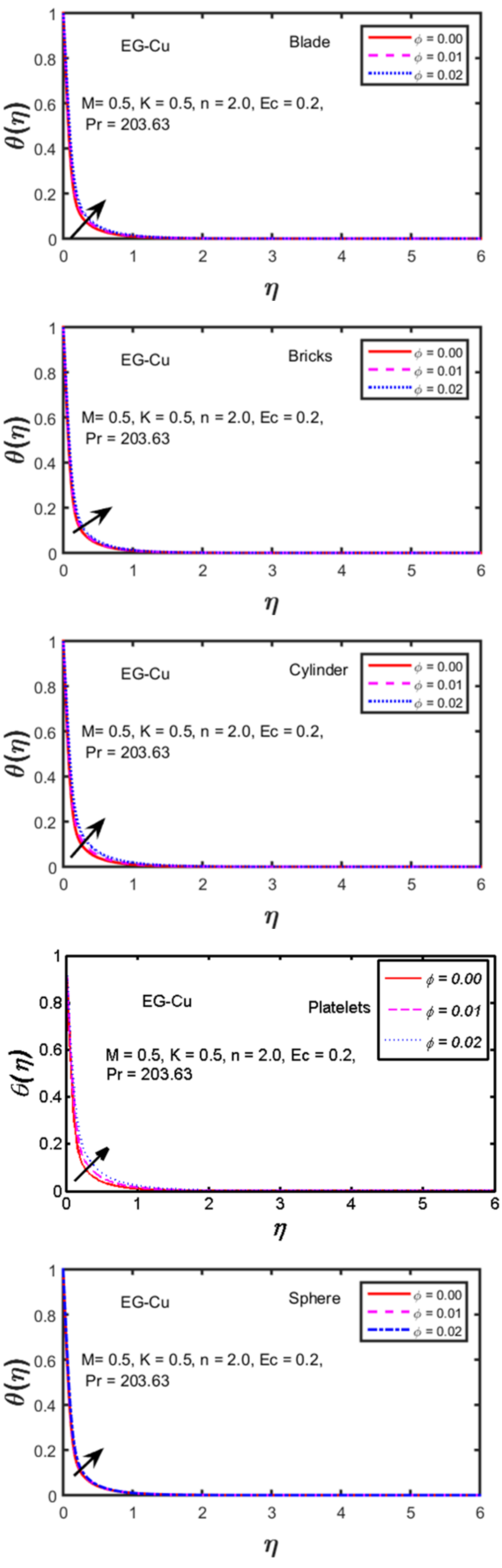

Fig. 7. Impact of volume friction (ϕ) on the temperature profile of EG-Cu nanofluid for various nanoparticle shapes: blade, brick, cylinder, platelets, and sphere.

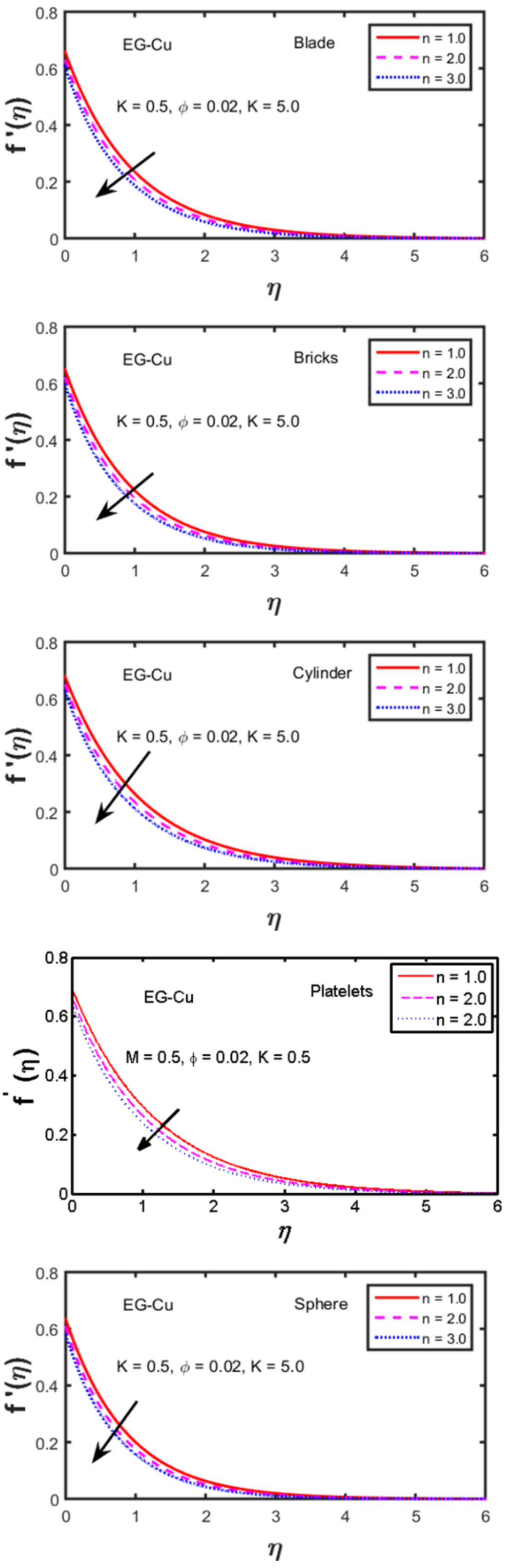

Fig. 8. Effect of the stretching parameter (n) on the velocity profile of EG-Cu nanofluid for various nanoparticle shapes: blade, brick, cylinder, platelets, and sphere.

Figure 9 portrays the impact of stretching parameter (n) on the temperature profile for EG-Cu nanofluid for five nanoparticle shapes: blade, brick, cylinder, platelets, and sphere. The results illustrate how the rate of surface stretching influences thermal behaviour, with each nanoparticle shape displaying distinct heat transfer characteristics.

The findings emphasize the importance of optimizing nanoparticle shape to achieve desired thermal performance in systems, where stretching and heat transfer are interconnected. It is noted that the temperature also reduces with a rise in the stretching parameter.

Figure 10 sheds light on the role of the Eckert number (Ec) in shaping the temperature profile. As Ec increases, we observe a further enhancement in temperature. This signifies the growing importance of viscous dissipation with increasing fluid velocity.

Figure 11 provides an intriguing comparison of the velocity profiles for different copper nanoparticle shapes. We observe that the velocity ranking, from highest to lowest, is as follows: platelets, cylinders, blades, bricks and spheres. This suggests that platelet-shaped nanoparticles offer the strongest enhancement in nanofluid velocity, while spherical nanoparticles exhibit the least impact.

Finally, Fig. 12 offers a scientifically compelling results for comparison of temperature profiles for different copper nanoparticle shapes. We can discern that the temperature ranking, from highest to lowest, follows the order: platelets, cylinders, blades, bricks and spheres. This suggests that platelet-shaped nanoparticles have the most significant impact on heat generation, while spherical nanoparticles contribute the least. These findings unveil the intricate relationships between various parameters and their impact on the thermal behaviour of copper nanofluids. Such insights can guide the design and optimization of nanofluid-based systems for diverse applications in thermal management, energy harvesting, and beyond.

Table 1 shows the physical and thermal characteristics of base fluids and copper nanoparticles [32] and Table 2 exhibits the varying values of the shape factor and viscosity of fluid under consideration [31]. In Table 3, the current result is contrasted with the findings of Khan and Pop [47], Wang [48], and Reddy Gorla and Sidawi [49] across a range of Prandtl numbers. We noticed that our results are in great agreement with existing literature for specific values. In Table 4, numerical values of skin friction are listed for different shapes of copper nanoparticles under various physical conditions. The data show that an increase in volume fraction (ϕ), magnetic field strength (M) and stretching parameter (n) leads to an increase in the skin friction coefficient for multi-shaped copper nanoparticles. However, the trend is reversed for the slip parameter (K). In Table 5, the heat transfer coefficient (Nusselt number, Nu) is computed for parameters such as magnetic field strength (M), volume fraction (ϕ) stretching parameter (n) and slip parameter (K). The Nusselt number reduces with increasing values of magnetic field strength (M), volume fraction (ϕ) and Eckert number (Ec), for multi-shaped copper nanoparticles. Conversely, a different pattern is observed for the slip parameter (K) and stretching parameter (n).

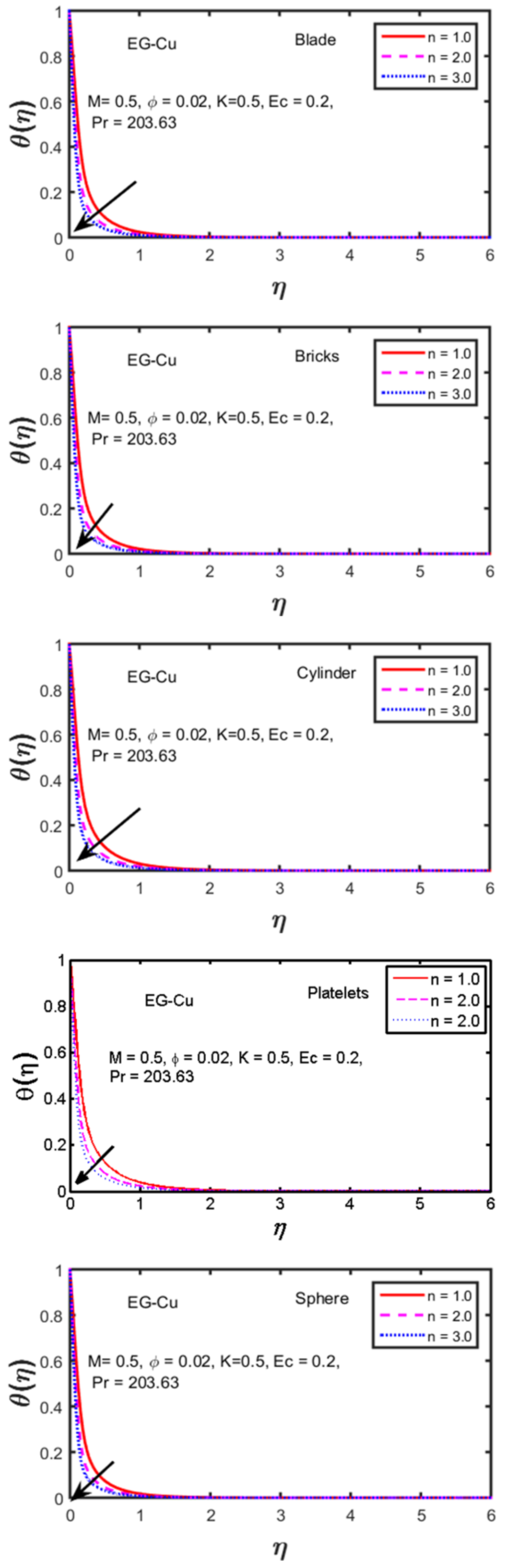

Fig. 9. Effect of the stretching parameter (n) on the temperature profile of EG-Cu nanofluid for various nanoparticle shapes: blade, brick, cylinder, platelets, and sphere.

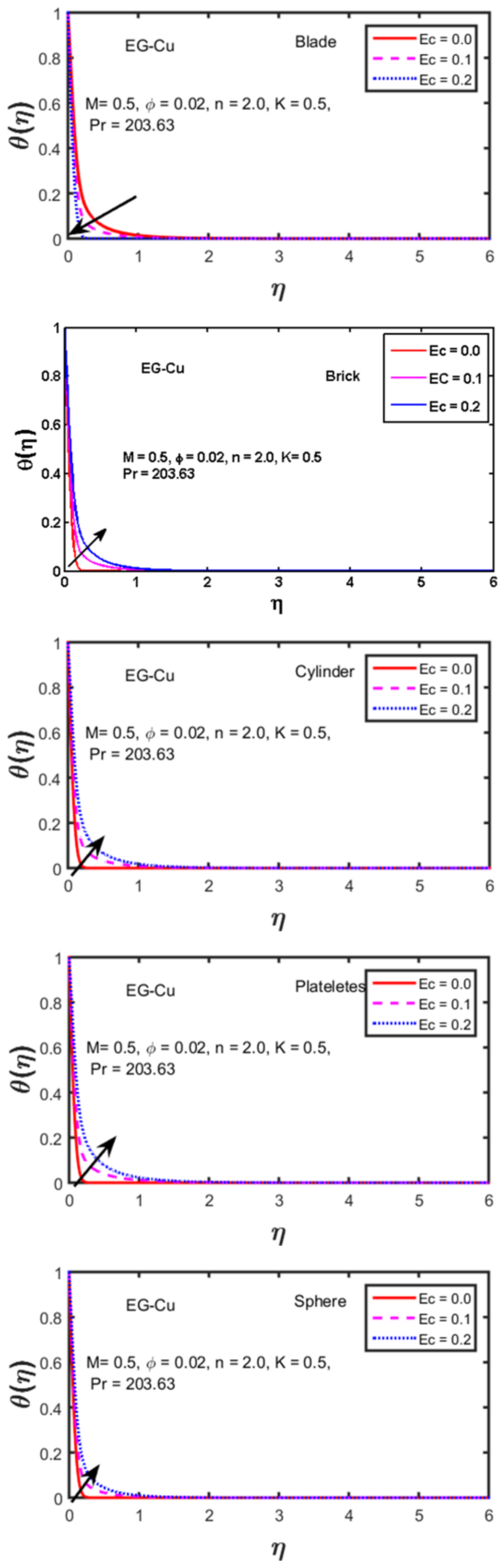

Fig. 10. Impact of the Eckert number (Ec) on the temperature profile of EG-Cu nanofluid for various nanoparticle shapes: blade, brick, cylinder, platelets, sphere.

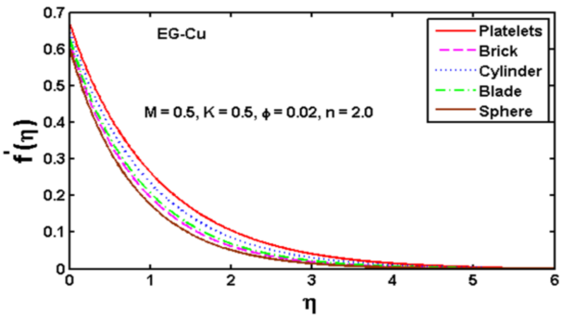

Fig 11. Impact of nanoparticle shape on the velocity profile.

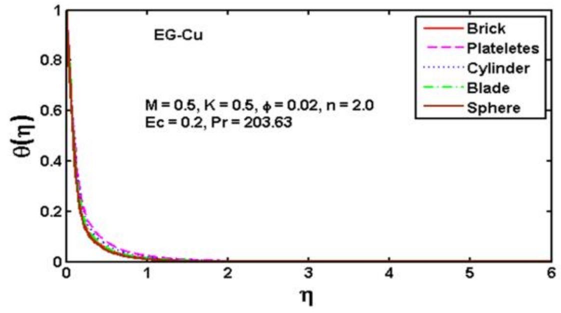

Fig. 12: Impact of nanoparticle shape on the temperature profile.

Table 1. Physical and thermal characteristics of base fluids and copper nanoparticles [32].

Nanoparticles / Base fluid	Specific heat, C_p (J/kgK)	Thermal conductivity, *k* (W/m K)	Density, *ρ* (kg/m^3)
Copper	385	401.0	8933
Ethylene glycol	2430	0.253	1115

Table 2. Varying values of the shape factor and viscosity [31].

Parameters / Nanoparticles	A_1	A_2	*m*
Blade	14.6	123.3	8.26
Brick	1.0	471.4	3.72
Cylinder	13.5	904.4	4.82
Platelets	37.1	612.6	5.72
Sphere	2.5	6.5	3.00

Table 3. Comparison of results for the reduced Nusselt number $\theta'(0)$ considering: $K = 0,\ M = 0,\ \phi = 0,\ \mathrm{Ec} = 0,\ n = 1$.

Pr	**Khan [1]**	**Wang [2]**	**Sidawi [50]**	**Present**
0.7	0.4539	0.4539	0.53	0.4544
2.0	0.9113	0.9114	0.9114	0.9114
7.0	1.8954	1.8954	1.8905	1.8954
20.0	3.3539	3.3539	3.3539	3.3539
70.0	6.4621	6.4622	6.4622	6.4622

Table 4. Values of skin-friction coefficient for multi-shape nanoparticles.

M	K	ϕ	n	$C_f\mathrm{Re}^{\frac{1}{2}}$				
				Cylinder	**Platelets**	**Sphere**	**Blade**	**Brick**
0.5	0.5	0.02	2	-1.138160	-1.306940	-0.830585	-0.989867	-0.928154
0.0	–	–	–	-0.998848	-1.145640	-0.731201	-0.869857	-0.816152
1.0	–	–	–	-1.246380	-1.433560	-0.906007	-1.082130	-1.013850
.5	0.0	–	–	-2.023270	-2.232800	-1.624970	-1.834350	-1.754120
–	1.0	–	–	-0.811870	-0.945852	-0.573870	-0.696044	-0.648416
–	0.5	0.00	–	-0.758920	-0.758920	-0.758920	-0.758920	-0.758920
–	–	0.01	–	-0.903964	-1.010440	-0.794841	-0.868059	-0.817518
–	–	0.02	1	-1.046630	-1.197250	-0.770443	-0.913785	-0.858335
–	–	–	3	-1.210200	-1.393640	-0.877531	-1.049520	-0.982801

Table 5: Comparison of the numerical values of Nusselt number for multi-shape nanoparticles.

M	K	Ec	ϕ	n	$\mathrm{NuRe}^{-\frac{1}{2}}$				
					Cylinder	**Platelets**	**Sphere**	**Blade**	**Brick**
0.5	0.5	0.2	0.02	2	5.797680	5.45369	6.40553	6.41026	6.22636
0.0	–	–	–	–	8.654940	8.54567	8.79801	9.11713	8.77341
1.0	–	–	–	–	3.635770	3.07073	4.66863	4.40239	4.3504
0.5	0.0	–	–	–	0.340441	−0.13803	1.35575	1.03829	1.0155
–	1.0	–	–	–	6.716180	6.57152	6.89114	7.12693	6.8602
–	0.5	0.0	–	–	11.574800	11.8706	10.91440	11.7129	11.1567
–	–	0.1	–	–	8.686250	8.66215	8.65996	9.06153	8.69152
–	–	0.2	0.00	–	6.892040	6.89204	6.89204	6.89204	6.89204
–	–	–	0.01	–	6.472940	6.26860	6.64252	6.68574	6.62141
–	–	–	0.02	1	3.334780	2.91268	4.12472	3.94395	3.87874
–	–	–		3	7.679450	7.39147	8.15487	8.29984	8.02463

5. Conclusions

In this article, heat transfer enhancement due to variation in copper nanoparticle shape factor for blades, spheres, bricks, cylinders and platelets in a nanofluid over stretching surfaces has been studied theoretically. Additionally, the effect of thermophysical quantities like volume fraction on heat transfer rates has been investigated. It is observed in this study that the surface area of nanoparticles greatly influences the thermal conductivity and all other properties of the nanofluid, and the increase in shape factor values enhances the heat transfer rate. Hence, the heat transfer rate for bricks is the highest in comparison to all other shapes of nanoparticles due to the large interfacial contact area. Regarding the role of the shape factors in heat transfer, it has been concluded that brick-shaped nanoparticles can be considered a good choice for future nanofluid applications in heat exchangers.

Based on the obtained results, the new findings are as follows:

- Nanoparticles in the shape of platelets offer excellent flow and bricks offer excellent heat transfer properties.
- Spherical nanoparticles have poor flow and heat transfer rates as compared to other shapes.
- An increase in the magnetic parameter M reduces velocity and hence decreases the boundary layer thickness.
- The interaction of the magnetic field and the conducting fluid causes Joule heating, which occurs when electrical energy is transformed into heat by flow-induced currents. This increased heat generation influences the temperature distribution and results in an increase in temperature.
- Increasing the slip parameter reduces both velocity and temperature profiles.
- Increasing the stretching parameter value reduces both the velocity distribution and the temperature of the copper nanofluid.
- An increase in the volume fraction enhances velocity and temperature profiles.
- Nusselt number enhances with increasing values of all parameters, such as the slip parameter and stretching parameter.
- Comparing the impact of the Eckert number, volume fraction and magnetic parameter, it was found that the Nusselt number decreases as these parameters increase.
- Skin fraction magnitude increases for increasing values of volume fraction, stretching parameter, and magnetic parameter, and decreases for increasing values of slip parameter.

References

[1] Eastman, J.A., Choi, S.U.S., Li, S., Yu, W., & Thompson, L.J. (2001). Anomalously increased effective thermal conductivities of ethylene glycol-based nanofluids containing copper nanoparticles. *Applied Physics Letters*, 78(6), 718−720. doi: 10.1063/1.1341218

[2] Chakraborty, S., & Panigrahi, P.K. (2020). Stability of nanofluid: A review. *Applied Thermal Engineering*, 74, 115259. doi: 10.1016/j.applthermaleng.2020.115259

[3] Patel, H.E., Das, S.K., Sundararajan, T., Sreekumaran Nair, A., George, B., & Pradeep, T. (2003). Thermal conductivities of naked and monolayer protected metal nanoparticle based nanofluids: Manifestation of anomalous enhancement and chemical effects. *Applied Physics Letters*, 83(14), 2931−2933. doi: 10.1063/1.1602578

[4] Liu, I.C., Wang, H.H., & Liu, C.N. (2013). Flow and heat transfer of nanofluids near a rotating disk. *Advanced Materials Research*, 664, 859−865. doi: 10.4028/www.scientific.net/AMR.664.859

[5] Das, K. (2014). Flow and heat transfer characteristics of nanofluids in a rotating frame. *Alexandria Engineering Journal*, 53(3), 757−766. doi: 10.1016/j.aej.2014.04.003

[6] Pandey, A.K., & Upreti, H. (2023). Heat and mass transfer in convective flow of nanofluid. In *Advances in Mathematical and Computational Modeling of Engineering Systems* (pp. 295−313). CRC Press. doi: 10.1201/9781003367420-14

[7] Srisailam, B., Reddy, K.S., Narender, G., & Malga, B.S. (2022). Flow and heat transfer analysis of MHD nanofluid due to convective stretching sheet. *Indian Journal of Science and Technology*, 15(44), 2393−2402. doi: 10.17485/ijst/v15i44.1006

[8] Sakiadis, B.C. (1961). Boundary-layer behavior on continuous solid surfaces: II. The boundary layer on a continuous flat surface. *AIChE Journal*, 7(2), 221−225. doi: 10.1002/aic.690070211

[9] Ferdows, M., Ramesh, G.K., & Madhukesh, J.K. (2023). Magnetohydrodynamic flow and Hall current effects on a boundary layer flow and heat transfer over a three-dimensional stretching surface. *International Journal of Ambient Energy*, 44(1), 938−946. doi: 10.1080/01430750.2022.2157873

[10] Ahmad, B., Abbas, T., Fatima, K., Duraihem, F.Z., & Saleem, S. (2024). Nonlinear flow of hybrid nanofluid with thermal radiation: A numerical investigation. *ZAMM Journal of Applied Mathematics and Mechanics*, 104(1), e202200170. doi: 10.1002/zamm.202200170

[11] Eid, M.R., Mahny, K.L., Muhammad, T., & Sheikholeslami, M. (2018). Numerical treatment for Carreau nanofluid flow over a porous nonlinear stretching surface. *Results in Physics*, 8, 1185−1193. doi: 10.1016/j.rinp.2018.01.070

[12] Hayat, T., Saif, R.S., Ellahi, R., Muhammad, T., & Ahmad, B. (2017). Numerical study of boundary-layer flow due to a nonlinear curved stretching sheet with convective heat and mass conditions. *Results in Physics*, 7, 2601−2606. doi: 10.1016/j.rinp.2017.07.023

[13] Zaimi, K., Ishak, A., & Pop, I. (2014). Boundary layer flow and heat transfer over a nonlinearly permeable stretching/shrinking sheet in a nanofluid. *Scientific Reports*, 4, 4404. doi: 10.1038/srep04404

[14] Athar, M., Ahmad, A., & Khan, Y. (2023). Polymer presence in boundary layer flow and heat transfer of dusty fluid over a stretching surface. *Multidiscipline Modeling in Materials and Structures*, 19(4), 617–633. doi: 10.1108/mmms-09-2022-0167

[15] Shah, G., Rehman, A., & Sheikh, N. (2022). Heat transfer analysis over the boundary layer stagnation-point flow of couple stress fluid over an exponentially stretching sheet. *American Journal of Applied Mathematics*, 10(3), 100−105. doi: 10.11648/j.ajam.20221003.13

[16] Venkateswarlu, S., Varma, S., & Kumar, R.K. (2022). Boundary layer flow of a conducting hyperbolic nanofluid over a stretching surface with chemical reaction and heat source/sink. *Journal of Theoretical and Applied Mechanics*, 52(2), 179–196. doi: 10.55787/jtams.22.52.2.179

[17] Vidhya, M., Juliet, S.S., Govindarajan, A., & Priyadarshini, E. (2022). An axisymmetric flow over non-linear radially stretching surface with heat transfer and chemical reaction effects. *AIP Conference Proceedings*, 2516(1), 170027. doi: 10.1063/5.0108677

[18] Hashim, H., Sarif, N.M., Salleh, M.Z., & Mohamed, M.K.A. (2020). Aligned magnetic field on Williamson fluid over a stretching sheet with Newtonian heating. *Journal of Physics: Conference Series*, 1529, 052085. doi: 10.1088/1742-6596/1529/5/052085

[19] Chen, C.H. (2010). Combined effects of Joule heating and viscous dissipation on magnetohydrodynamic flow past a permeable, stretching surface with free convection and radiative heat transfer. *Journal of Heat Transfer*, 132(6), 064503. doi: 10.1115/1.4000946

[20] Khashi'ie, N.S., Arifin, N.M., Pop, I., & Wahid, N.S. (2020). Flow and heat transfer of hybrid nanofluid over a permeable shrinking cylinder with Joule heating: A comparative analysis. *Alexandria Engineering Journal*, 59(3), 1787−1798. doi: 10.1016/j.aej.2020.04.048

[21] Srinivasacharya, D., & Jagadeeshwar, P. (2019). Effect of Joule heating on the flow over an exponentially stretching sheet with convective thermal condition. *Mathematical Sciences*, 13(3), 201−211. doi: 10.1007/s40096-019-0290-8

[22] Ganesh Kumar, K., Rudraswamy, N.G., Gireesha, B.J., & Krishnamurthy, M.R. (2017). Influence of nonlinear thermal radiation and viscous dissipation on three-dimensional flow of Jeffrey nano fluid over a stretching sheet in the presence of Joule heating. *Nonlinear Engineering*, 6(3), 207−219. doi: 10.1515/nleng-2017-0014

[23] Ghaffarpasand, O. (2016). Numerical study of MHD natural convection inside a sinusoidally heated lid-driven cavity filled with FeO-water nanofluid in the presence of Joule heating. *Applied Mathematical Modelling*, 40(21-22), 9165–9182. doi: 10.1016/j.apm.2016.05.038

[24] Mutuku, W.N., Makinde, O.D., & Theuri, D. (2017). Hydromagnetic mixed convection flow of nanofluid with slip, viscous dissipation and Joule heating past an inclined plate. *Journal of Nanofluids*, 6(6), 1065−1073. doi: 10.1166/jon.2017.1404

[25] Ali, B., Jubair, S., Al-Essa, L. A., Mahmood, Z., Al-Bossly, A., & Alduais, F.S. (2023). Boundary layer and heat transfer analysis of mixed convective nanofluid flow capturing the aspects of nanoparticles over a needle. *Materials Today Communications*, 35, 106253. doi: 10.1016/j.mtcomm.2023.106253

[26] Shankar Goud, B., Dharmendar Reddy, Y., & Mishra, S. (2023). Joule heating and thermal radiation impact on MHD boundary layer Nanofluid flow along an exponentially stretching surface with thermal stratified medium. *Proceedings of the Institution of Mechanical Engineers, Part N: Journal of Nanomaterials, Nanoengineering and NanoSystems*, 237(3-4), 107−119. doi: 10.1177/23977914221100961

[27] Khashi'ie, N.S., Arifin, N.M., & Pop, I. (2022). Magnetohydrodynamics (MHD) boundary layer flow of hybrid nanofluid over a moving plate with Joule heating. *Alexandria Engineering Journal*, 61(3), 1938−1945. doi: 10.1016/j.aej.2021.07.032

[28] Rana, P., Mahanthesh, B., Nisar, K. S., Swain, K., & Devi, M. (2021). Boundary layer flow of magneto-nanomicropolar liquid over an exponentially elongated porous plate with Joule heating and viscous heating: a numerical study. *Arabian Journal for Science and Engineering*, 46, 12405−12415. doi: 10.1007/s13369-021-05926-8

[29] Tarakaramu, N., Satya Narayana, P.V., Babu, D.H., Sarojamma, G., & Makinde, O.D. (2021). Joule Heating and dissipation effects on magnetohydrodynamic couple stress nanofluid flow over a bidirectional stretching surface. *International Journal of Heat and Technology*, 39(1), 205−212. doi: 10.18280/ijht.390122

[30] Saleem, S., Qasim, M., Alderremy, A., & Noreen, S. (2020). Heat transfer enhancement using different shapes of Cu nanoparticles in the flow of water based nanofluid. *Physica Scripta*, 95(5), 055209. doi: 10.1088/1402-4896/ab4ffd

[31] Fakour, M., Rahbari, A., Khodabandeh, E., & Ganji, D.D. (2018). Nanofluid thin film flow and heat transfer over an unsteady stretching elastic sheet by LSM. *Journal of Mechanical Science and Technology*, 32, 177−183. doi: 10.1007/s12206-017-1219-5

[32] Mathews, J., & Tallab, H. (2024). Unsteady magnetohydrodynamic free convection and heat transfer flow of Al_2O_3-Cu/water nanofluid over a non-linear stretching sheet in a porous medium. *Archives of Thermodynamics*, 45(3), 165–173. doi: 10.24425/ather.2024.150449

[33] Triveni, B., Rao, M.V.S., Gangadhar, K., & Chamkha, A.J. (2024). Heat transfer analysis of MHD Casson nanofluid flow over a nonlinear stretching sheet in the presence of nonuniform heat source. *Numerical Heat Transfer, Part A: Applications*, 85(13), 2145−2164. doi: 10.1080/10407782.2023.2219831

[34] Hayat, U., Ali, R., Shaiq, S., & Shahzad, A. (2023). A numerical study on thin film flow and heat transfer enhancement for copper nanoparticles dispersed in ethylene glycol. *Reviews on Advanced Materials Science*, 62(1), 20220320. doi: 10.1515/rams-2022-0320

[35] Sathyanarayana, M., & Goud, T.R. (2023). Numerical study of MHD Williamson-nano fluid flow past a vertical cone in the presence of suction/injection and convective boundary conditions. *Archives of Thermodynamics*, 44(2), 115−138. doi: 10.24425/ather.2023.146561

[36] Joachimiak, D., Judt, W., & Joachimiak, M. (2023). Numerical analysis of the heating of a die for the extrusion of aluminium alloy profiles in terms of thermochemical treatment. *Archives of Thermodynamics*, 44(2), 159−175. doi: 10.24425/ather.2023.146563

[37] Hayat, U., & Shahzad, A. (2023). Thin film flow, heat transfer and viscous dissipation effects on vertical stretching sheet for different shapes of (Au-Np) dispersed in water. *Physica Scripta*, 98(10), 105251. doi: 10.1088/1402-4896/acfb4e

[38] Hayat, U., & Shahzad, A. (2023). Analysis of heat transfer and thin film flow of Au-Np over an unsteady radial stretching sheet. *Numerical Heat Transfer, Part A: Applications*, 84(11), 1338−1351. doi: 10.1080/10407782.2023.2175746

[39] Ali, R., Iqbal, A., Abbass, T., Arshad, T., & Shahzad, A. (2024). Unsteady flow of silica nanofluid over a stretching cylinder with effects of different shapes of nanoparticles and Joule heating. *Archives of Thermodynamics*, 45(3), 115–126. doi: 10.24425/ather.2024.151222

[40] Gangadhar, K., Naga Chandrika, G., & Dinarvand, S. (2025). Investigation into silver-engine oil nanoliquid convinced by Riga surface: Deviations in three binary nanofluids. *Modern Physics Letters B*, 39(01), 2450385. doi: 10.1142/s0217984924503858

[41] Gangadhar, K., Vardhana, K.A., & Wakif, A. (2024). HVAC-solar energy performance exploiting Sutterby (AA7075–Ag–Cu/$C_6H_9NaO_7$) ternary magnetic nanofluid through spinning flow with joule heating. *Modern Physics Letters B*, 39(14), 2450493. doi: 10.1142/S0217984924504931

[42] Gangadhar, K., Sangeetha Rani, M., & Wakif, A. (2024). Non-Fourier heat flux and Joule dissipation in hybrid nanoparticles suspension with Williamson fluid. *The European Physical Journal Plus*, 139, 306. doi: 10.1140/epjp/s13360-024-05054-w

[43] Gangadhar, K., Sree, T. S., Wakif, A., & Subbarao, K. (2024). Stefan blowing impact and chemical response of Rivlin-Reiner fluid through rotating convective disk. *Pramana Journal of Physics*, 98, 160. doi: 10.1007/s12043-024-02836-w

[44] Gangadhar, K., Rao, M.V.S., Kumari, M.A., & Wakif, A. (2024). Impact of the Stefan gusting on a bioconvective nanofluid with the various slips over a rotating disc and a substance-responsive specie. *Modern Physics Letters B*, 39(1), 2450406. doi: 10.1142/s0217984924504062

[45] Gangadhar, K., Sujana Sree, T., & Wakif, A. (2024). Generalized slip impact of Casson nanofluid through cylinder implanted in swimming gyrotactic microorganisms. *International Journal of Modern Physics B*, 38(28), 2450380. doi: 10.1142/s0217979224503806

[46] Gangadhar, K., Rani, M.S., & Wakif, A. (2024). Ternary nanofluids due to moving wedge with strong magnetic field and convective condition. *International Journal of Modern Physics B*, 39(03), 2550026. doi: 10.1142/s0217979225500262

[47] Khan, W.A., & Pop, I. (2010). Boundary-layer flow of a nanofluid past a stretching sheet. *International Journal of Heat and Mass Transfer*, 53(11-12), 2477–2483. doi: 10.1016/j.ijheatmasstransfer.2010.01.032

[48] Wang, C.Y. (1989). Free convection on a vertical stretching surface. *ZAMM Journal of Applied Mathematics and Mechanics*, 69(11), 418–420. doi: 10.1002/zamm.19890691115

[49] Reddy Gorla, R.S., & Sidawi, I. (1994). Free convection on a vertical stretching surface with suction and blowing. *Applied Scientific Research*, 52, 247–257. doi: 10.1007/bf00853952